5-2022

Materials and interfaces for electrocatalytic hydrogen production and utilization.

Alexander Jiya Gupta
University of Louisville

MATERIALS AND INTERFACES FOR ELECTROCATALYTIC HYDROGEN PRODUCTION AND UTILIZATION

By

Alexander Jiya Gupta
B.S., University of Louisville, 2016

A Dissertation
Submitted to the Faculty of the
J.B. Speed School of Engineering of the University of Louisville
in Partial Fulfillment of the Requirements
for the Degree of

Doctor of Philosophy
in Chemical Engineering

Department of Chemical Engineering
University of Louisville
Louisville, Kentucky

May 2022

MATERIALS AND INTERFACES FOR ELECTROCATALYTIC HYDROGEN PRODUCTION AND UTILIZATION

By

Alexander Jiya Gupta
B.S., University of Louisville, 2016

A Dissertation Approved on

January 21, 2022

by the following Dissertation Committee:

_____
Gautam Gupta, PhD

_____
Robert Buchanan, PhD

_____
Vance Jaeger, PhD

_____
Gerold Willing, PhD

DEDICATION

This dissertation is dedicated to Juniper.

My heart.

My hope.

My light at the end of the tunnel.

ACKNOWLEDGMENTS

I would like to thank my advisor Dr. Gautam Gupta for his guidance, patience, friendship, and belief in me. I would not be in this position without him. I would also like to thank the other committee members Drs. Vance Jaeger, Robert Buchanan, and Gerold Willing for their assistance over the last several years. Thanks to Drs. Ulises Martinez, Rod Borup, Jacob Spendelow, Sid Komini-Babu, and Joseph Dumont for their guidance and support, and thanks to my many coauthors, coworkers, and lab-mates for their camaraderie and collaborative spirits. I also owe a debt of gratitude to my parents Wendy and Mukesh Gupta for providing me with invaluable educational opportunities. Many thanks to my extended family as well. Thank you to my friends for giving me warm hugs and hearty laughter. Lastly, I want to express my sincerest appreciation to my wife Jill for her unwavering support and love even during the darkest times. She made me realize that I could be a better man.

ABSTRACT

MATERIALS AND INTERFACES FOR ELECTROCATALYTIC HYDROGEN PRODUCTION AND UTILIZATION

Alexander J. Gupta

January 21, 2022

Mass industrialization over the last few centuries has created a global economy which is dependent upon fossil fuels to satisfy an exponentially increasing demand for energy. Aside from the possible depletion of this finite resource, the combustion of fossil fuels releases greenhouse gases into the atmosphere which cause the global temperature to rise – a phenomenon which has already begun to create geologic and geopolitical instability and shows no signs of abatement. One proposed method to rid humanity of its dependence on fossil fuels is to use green hydrogen as an energy carrier. In this scheme, excess electricity from a robust renewable energy generation infrastructure is diverted to grid-scale electrolyzers which split water into hydrogen and oxygen. The hydrogen is in turn distributed via supply chain to end users who employ fuel cells to locally convert the energy stored in the chemical bond of hydrogen into electricity on-demand.

This vision for an alternative global energy economy has been inhibited by several factors including the low utilization of renewable energy generating technologies, the considerable cost of precious metals required for electrolyzer electrodes, and the relatively low efficiency of the cathodic fuel cell reaction. This

dissertation is a compilation of experimental work related to the development of materials and interfaces for enhanced electrocatalytic hydrogen evolution using non-precious materials and hydrogen utilization in highly-efficient proton exchange membrane fuel cells. Chapter 1 begins with an overview of the global energy diet and the problem of climate change followed by a discussion of renewable energy technologies, ending with a proposal of how the large-scale implementation of green hydrogen technologies may fit into the futuristic energy landscape. Chapter 2 presents a brief review of the mechanism of hydrogen evolution electrocatalysis including its thermodynamic, kinetic, and mass transport limitations.

In Chapter 3, we demonstrate a simple and scalable fabrication process for highly-active non-precious molybdenum sulfide electrolyzer cathodes. Molybdenum sulfide and other transition metal dichalcogenides have received considerable attention in recent years as electrolyzer catalysts due to their environmental benignity, high stability, good catalytic activity, and low cost. Aside from the issue of low efficiency, industrial implementation of most reported molybdenum sulfide fabrication procedures is complicated by extreme and/or lengthy processing conditions. Our process is roll-to-roll amenable and produces a catalyst film in milliseconds without the use of harsh processing conditions or excessive chemicals. Ex-situ characterization of the resulting electrode confirms transformation of the precursor to molybdenum sulfide and reveals a hydrogen evolution reaction overpotential of 200 mV at 10 mA cm^{-2} which is comparable to that of other reported highly-active molybdenum sulfide catalysts.

Chapter 4 deals with the development and ex-situ characterization of a novel non-precious electrocatalyst platform for hydrogen evolution based upon a nickel-centered thiosemicarbazone molecular framework. The enzyme hydrogenase, found in most forms of life, has served as a source of inspiration for researchers due to its ability to reversibly catalyze hydrogen evolution efficiently. However, efforts to translate the activity of the hydrogenase active site to an electrode have been limited in their success. We report a class of molecular catalysts inspired by previous work on hydrogenase active site analogues. Successful translation and retention of the catalyst to the electrode surface is confirmed, and ex-situ testing reveals a hydrogen evolution reaction overpotential of 450 mV at 10 mA cm^{-2} with remarkable stability – a promising milestone which lays the foundation for further development of this class of materials.

Beginning in Chapter 5, the focus of the dissertation is shifted away from materials for hydrogen evolution and toward the development of highly-efficient proton exchange membrane fuel cell devices. Chapter 5 details the interplay between chemical transport, catalytic kinetics, thermodynamic considerations, and Ohmic losses which influence fuel cell efficiency. In Chapter 6, we introduce a structured proton exchange membrane fuel cell cathode which utilizes an array of bulk-like ionomer channels to improve the interface between the catalyst layer and membrane. The channels serve as conduits for rapid proton transport, dramatically decreasing the cathode sheet resistance and enabling a reduction in electrode ionomer content which attenuates active site inhibition from sulfonate adsorption. Using this approach, the mass activity of Vulcan carbon-based Pt

catalyst is improved by up to 80 %, and the power density is improved by up to hundreds of mW cm^{-2} at benchmark cell potentials – particularly under arid conditions. Further performance gains may be realized by tuning the electrode geometry and/or applying this technology to other catalyst types including those based upon high-surface-area carbon.

The results described in this dissertation 1) advance the understanding of materials and fabrication processes for hydrogen evolution electrodes and 2) provide a simple tool for mitigating chemical transport and catalyst poisoning limitations in the proton exchange membrane fuel cell cathode.

TABLE OF CONTENTS

PAGE

LIST OF TABLES

TABLE PAGE

LIST OF FIGURES

FIGURE PAGE

1. MOTIVATION

1.1. THE GLOBAL ENERGY DIET

Since the beginning of the industrial revolution in the eighteenth century, humanity has developed an increasingly voracious appetite for energy. As shown in Figure 1, energy consumption in the US alone has increased 168 %[1] over the last 70 years, although it has decreased somewhat from 2018 to the present due to efforts to improve energy efficiency[2]. Other wealthy countries have also enjoyed a decrease in consumption due to similar efforts, but these efforts have been insufficient to attenuate global energy consumption. Ritchie and Roser report a globally-averaged growth in energy consumption of approximately 500 % over the same period of time (Figure 2) which is largely attributed to rapid population and income growth in developing nations[2]. The US Energy Information Administration projects a further 50 % increase in global energy consumption by 2050, led primarily by growth in Asia.[3]

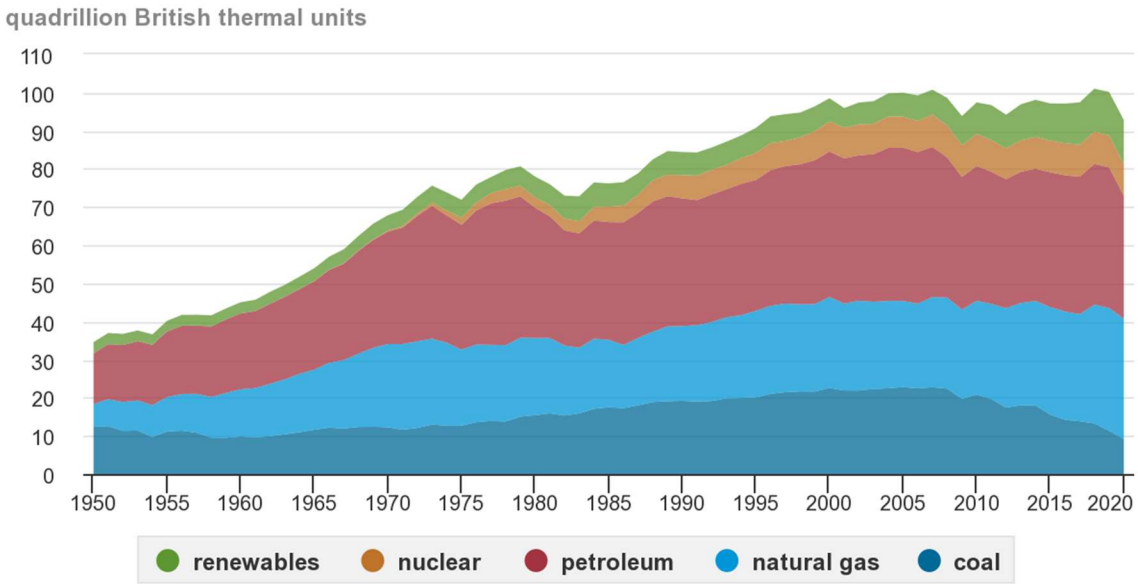

Figure 1. U.S. primary energy consumption by major sources, 1950 – 2020.

Source: U.S. Energy Information Administration (May 2021)[1].

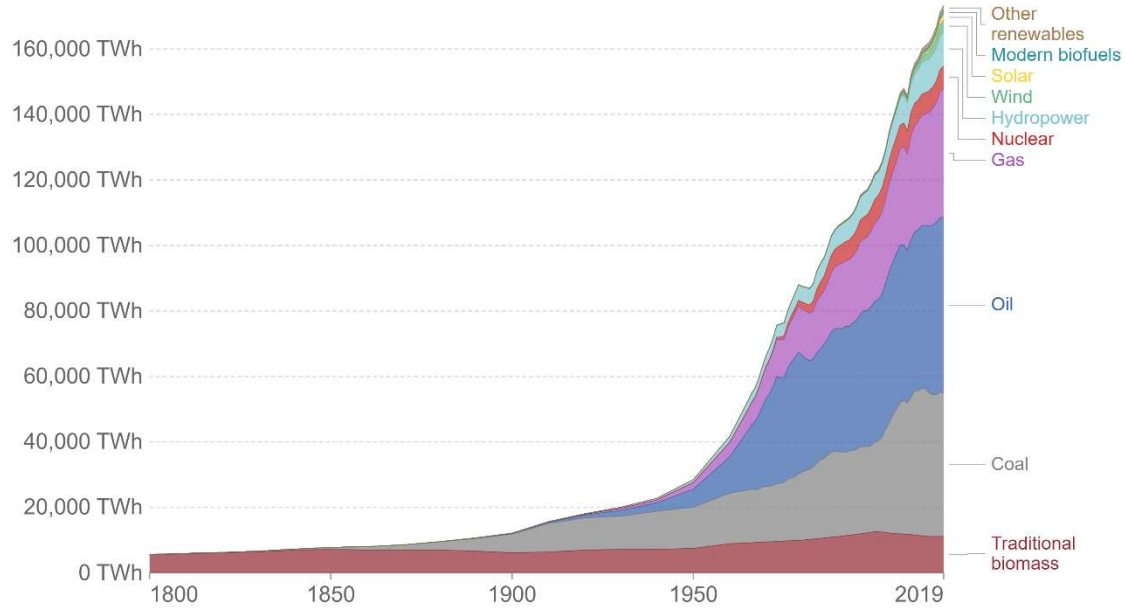

Figure 2. Global primary energy consumption by source. Primary energy is calculated based on the 'substitution method' which takes account of the

inefficiencies in fossil fuel production by converting non-fossil energy into the energy inputs required if they had the same conversion losses as fossil fuels. Reproduced from [2].

Presently, 85 % of global primary energy is derived from the combustion of fossil fuels and traditional biomass[2]. An area of concern regarding the use of fossil fuels as the single largest component in our global energy mix is the issue of scarcity. Fossil fuels are finite; the transformation of organic matter to energy-rich fossil fuels is a very slow geologic process estimated to take place over hundreds of millions of years[4]. Recently, BP's Statistical Review of World Energy estimated that at the current levels of production/consumption, there are sufficient known reserves of coal, oil, and natural gas to last another 115, 53, and 51 years respectively[2,5]. It is important to note that this report includes only known available reserves – not undiscovered/untapped resources. Advances in technology have in the past, and are expected to continue to, increase fossil fuel recovery rates, enable utilization of lower-grade fossil fuels, and make available new reserves which are currently either unknown or are deemed to be inaccessible[6]. However, rising energy demand will likely offset the increasing availability of fossil fuel reserves to some degree. Although the market price of a given fossil fuel is difficult to predict in the long-term, a future world economy dependent upon fossil fuels, at a time when scarcity and high prices render their use unaffordable for a large portion of the population, would likely suffer from instability.

1.2. CLIMATE CHANGE

Aside from the uncertain longevity of global fossil fuel reserves, the prolific use of fossil fuels exacerbates the problem of climate change. In the mid-19th century, Tyndal reported that a portion of solar radiation is absorbed by the atmosphere and Earth's surface and then re-emitted as infrared radiation[7]. Atmospheric gases, including CO_2, CH_4, N_2O, and water vapor (greenhouse gases), absorb this infrared radiation and re-emit it in all directions, effectively trapping a portion within the Earth's atmosphere and preventing its release into space. This phenomenon, known as the Greenhouse Effect[8], is depicted in Figure 3.

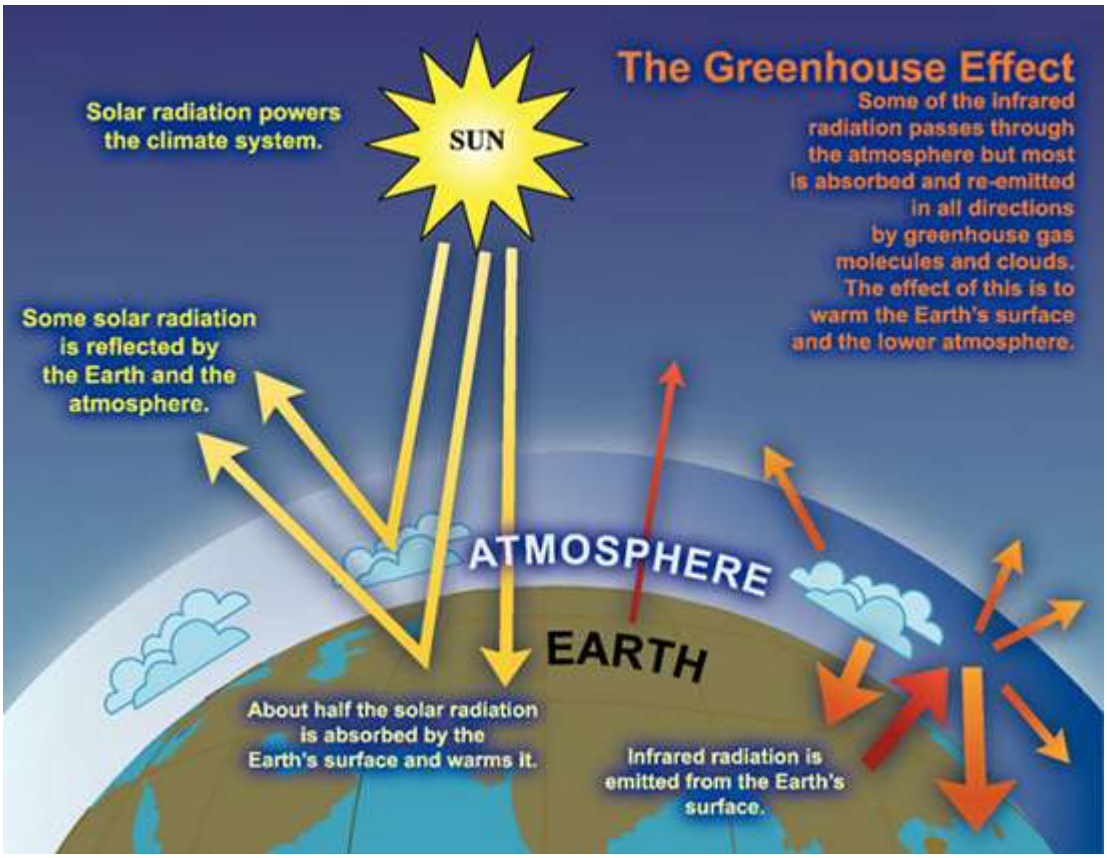

Figure 3. An idealized model of the greenhouse effect. Reproduced with permission from [8].

In the absence of the Greenhouse Effect, it is estimated that the surface temperature of Earth would be below the freezing point of water[8], making life as we know it impossible. However, several studies[9–11] have determined that human activities have augmented the greenhouse effect by increasing the atmospheric concentration of greenhouse gases, resulting in a global temperature increase of roughly 1 °C since pre-industrial times with rapid acceleration in recent years[12]. The consensus model for climate change[8,13,14] is a feedback loop beginning with elevated atmospheric concentrations of CO_2, CH_4, nitrogen oxides, and fluorinated gases due to anthropogenic activities such as industrial-scale fossil fuel combustion and deforestation. The additional atmospheric heat retention provided by these molecules increases the average temperature which in turn causes the atmospheric saturation pressure of water to rise. Additional atmospheric water intensifies the Greenhouse Effect, causing a self-reinforcing process.

The Intergovernmental Panel on Climate Change (IPCC) predicts grave consequences for much of the global population associated with 2 °C of average atmospheric warming above pre-industrial levels[15]. At this level of warming, roughly 37 % of Earth's population will experience severe heatwaves at least once every 5 years. About 61 million additional people in urban areas will be exposed to severe drought. 50 % more people on Earth will experience lack of water availability. Several locations will experience an increase in the frequency and/or intensity of severe weather events. The sea level will rise more than 0.2 m

over 70 % of Earth's coastlines. Ocean acidification will create additional marine "dead zones," eliminating commercial fisheries and restricting food supplies. These, and other consequences of unabated global warming, would be detrimental to the global economy and geopolitical stability. Although, as mentioned previously, several decades of fossil fuel reserves remain available to humanity, burning just one-third of these currently-known reserves is 50 % likely to cause global warming of 2 °C[11]. According to one analysis[16] based on climate models in the latest IPCC report[17], at current emission levels, Earth will exceed 1.5 °C of warming over pre-industrial levels around 2032 with 2 °C of warming to follow around 2052. Therefore, the problem of potential long-term fossil fuel depletion is dwarfed by the more immediate consequences of allowing global warming to proliferate.

In 2015, several countries became signatories to the Paris Climate Accord[18] – an international treaty on climate change aimed at limiting global warming to below 2 °C compared to pre-industrial levels. To achieve this goal, the IPCC estimates that anthropogenic greenhouse gas emissions must decline by 25 % by 2030 and reach net-zero by 2070 [15]. This timeline demands aggressive innovation and implementation of technologies for increased energy efficiency and green energy production and distribution.

1.3. RENEWABLE ENERGY

Except for nuclear, green energy sources have grown as a portion of the global energy diet in recent years (Figure 2). Recently, the cost of onboarding new power generation capacity based upon wind and solar undercut the cost of

bringing on new fossil fuel generation capacity[19]. As older power generation facilities are retired and new demand for electricity is created over time, investors will be incentivized to utilize renewable energy technologies in new energy generation projects if these technologies can maintain or improve upon their downward cost trajectory. However, it remains to be seen whether this trend of market-oriented adoption will be sufficient to meet emission-reduction timelines without aggressive public sector intervention.

Beyond the uncertain adoption of these technologies, renewable energy sources largely suffer from the problem of temporal inflexibility. Nuclear, hydroelectric, and geothermal power plants are not amenable to flexible operation. In other words, these sources deliver a static base load without the ability to easily dial up or down the power output. These technologies can supplement our current energy mix because the output of fossil fuel power plants can easily be modulated to match demand. On the other hand, wind and solar power sources suffer from the issue of intermittency – they only produce electricity when the wind is blowing or the sun is shining. Relying solely on these intermittent renewable energy generation methods creates the likelihood of recurring blackouts at night time during periods of peak demand and a wasted surplus of energy during the day time and/or on windy days. Further, none of these energy sources alone are readily applicable to modern transportation applications. To implement an energy portfolio derived only from renewable sources, a means of storing and transporting energy for use in another time or place is needed. In

other words, the world needs an emission-free energy vector with the convenience and portability of gasoline.

To this end, battery systems have received considerable attention in recent years[20]. In principle, excess generated renewable energy could be diverted to charge a system of batteries which could be discharged during periods of peak demand or used for transportation (i.e. in cars, trucks, trains, airplanes, etc.). Recently, battery technology has progressed significantly, and battery-operated electric vehicles (BEVs) are a common sight on America's roadways today. However, batteries suffer from inherent issues including cumbersome charging times required to prevent degradation and prolong lifecycle[21]. Additionally, batteries have relatively low specific energy[22,23] necessitating impractically large batteries to be useful for grid-scale applications. Furthermore, any battery large enough for use in long-haul transportation would detract from a significant amount of cargo weight, rendering its use uneconomical. Lastly, batteries are prone to self-discharge over time which limits their reliability.

1.4. HYDROGEN AS A GREEN ENERGY VECTOR

An alternative to using batteries as carriers for renewable energy is to use hydrogen (H_2) instead. Excess energy from renewable power generation can be diverted to an electrolyzer which splits water into H_2 and oxygen (O_2). The H_2 is subsequently stored and transported to the end user where it is oxidized in a device called a fuel cell which converts the chemical energy stored in the H-H bond to an electric current. Water electrolysis produces H_2 at a much higher degree of purity than other techniques which is a benefit for utilization in low-

temperature fuel cells where impurities poison catalytic active sites. H_2 is uniquely suited as an energy carrier because it can be quickly refueled, has a higher specific energy than batteries[22,23], and its oxidation is a carbon-neutral process which produces water as the sole byproduct. The means of storing energy derived from renewable sources in hydrogen by splitting water is depicted in Figure 4.

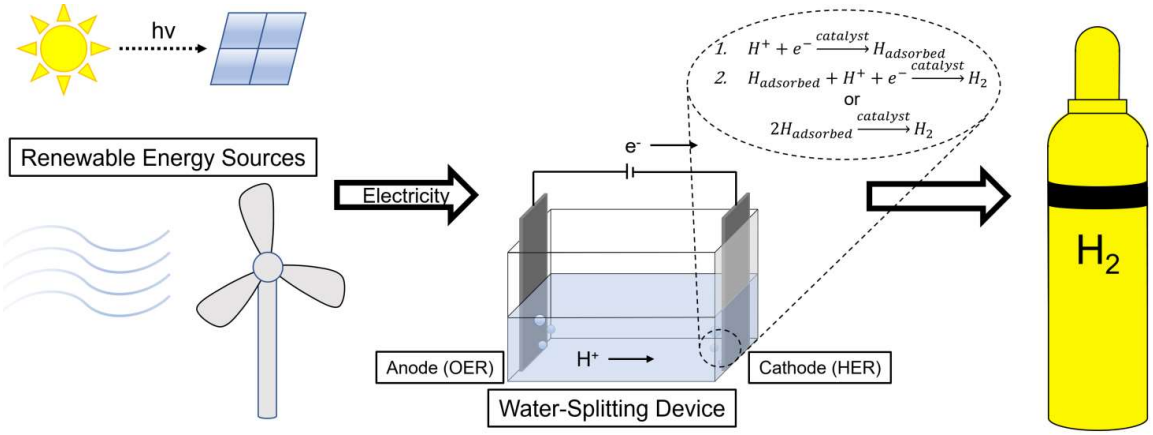

Figure 4. Means of storing excess renewable energy in H_2 using an electrolyzer.

In addition to its prospective use as an energy carrier, H_2 is an important industrial feedstock[24] in the processes of fossil fuel refining, Haber-Bosch ammonia production, food processing, steel making, cosmetics manufacturing, and biomass upgrading. Its use for these purposes has become more common over time (Figure 5). The vast majority of H_2 is produced via processes which use fossil fuels as feedstock and generate greenhouse gases as byproducts, such as steam reformation or coal gasification, with only 2 % derived from water electrolysis[24] (Figure 6). The under-utilization of electrolysis for this purpose is

attributed to cost. As shown in Figure 7, electrolysis is expected to remain the single most expensive route for hydrogen production in the near term[24].

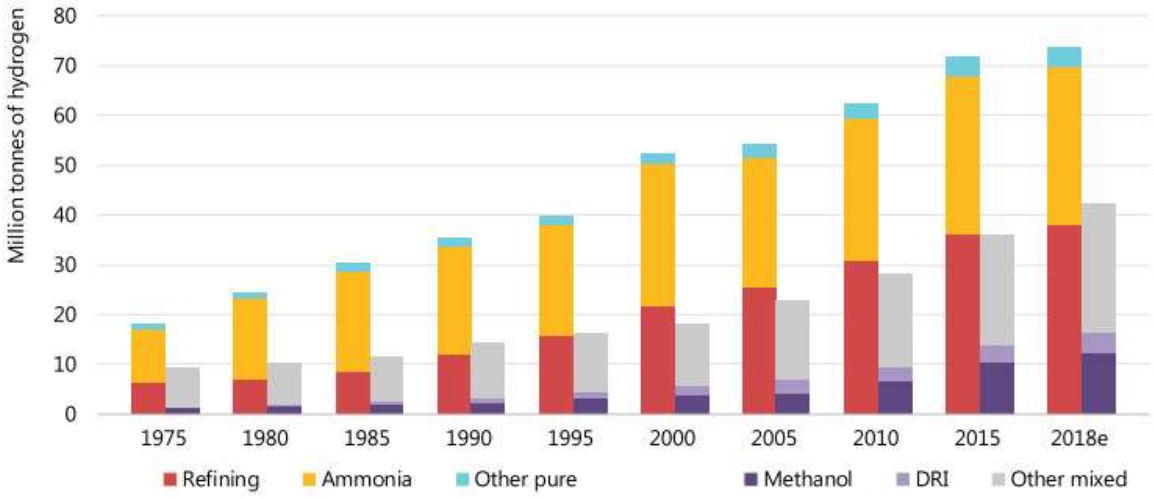

Figure 5. Global annual demand for hydrogen since 1975. DRI = direct reduced iron steel production. Refining, ammonia and “other pure” represent demand for specific applications that require hydrogen with only small levels of additives or contaminants tolerated. Methanol, DRI and “other mixed” represent demand for applications that use hydrogen as part of a mixture of gases, such as synthesis gas, for fuel or feedstock. Reproduced from IEA 2019[24]. All rights reserved.

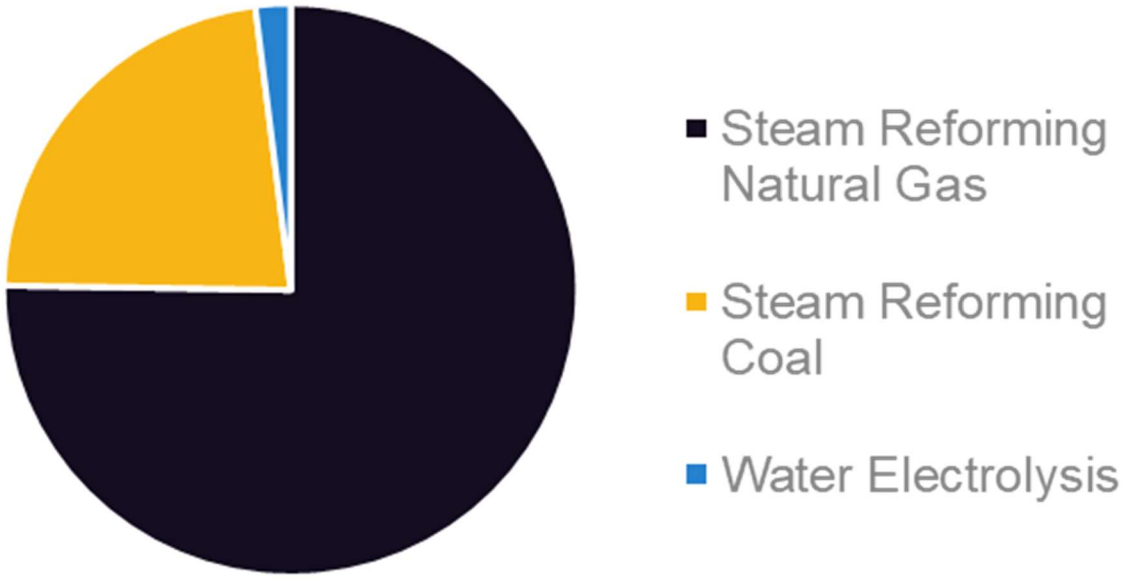

Figure 6. Relative portions of global H_2 supply from various processes.

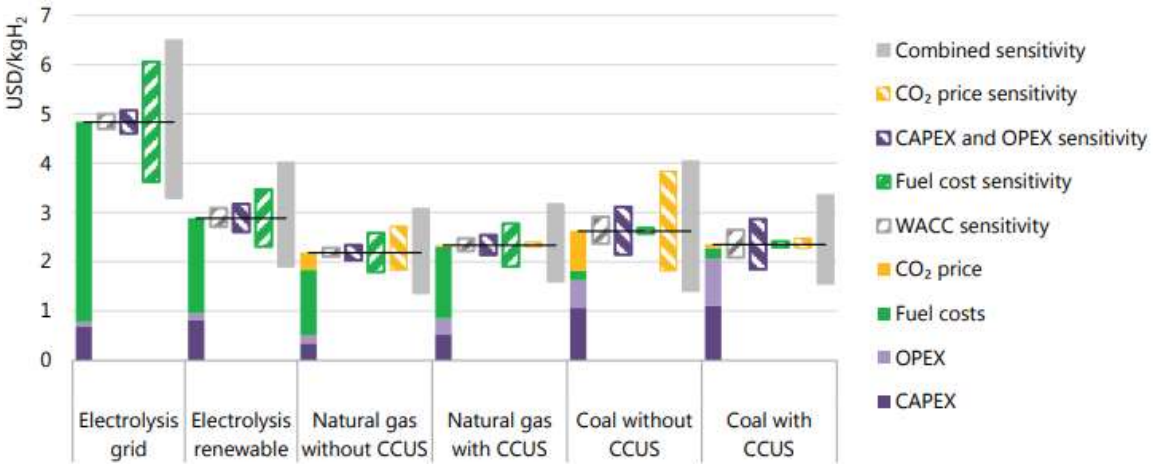

Figure 7. Hydrogen production costs for different technology options, 2030. WACC = weighted average cost of capital. Assumptions refer to Europe in 2030. Renewable electricity price = USD 40/MWh at 4000 full load hours at best locations; sensitivity analysis based on +/-30% variation in CAPEX, OPEX and fuel costs; +/-3% change in default WACC of 8% and a variation in default CO_2 price of USD 40/tCO_2 to USD 0/tCO_2 and USD 100/tCO_2. More information on the underlying assumptions is available at www.iea.org/hydrogen2019. Reproduced from IEA 2019[24]. All rights reserved.

For H_2 sourced from electrolysis to gain traction as an energy carrier or industrial feedstock, it is imperative to reduce its cost. In this case, the *fuel cost* which dominates the cost of H_2 from electrolysis in Figure 7 is representative of the combined cost and utilization of electricity that goes into the process as well as the efficiency of electrolyzer systems. As mentioned previously, the cost of electricity from renewable sources is on a downward trajectory. However, both electrolyzer and fuel cell systems suffer from significant irreversible losses which

limit their efficiency. Another significant contributor to the cost of electrolysis is the capital expenditure (CAPEX) or the upfront cost of the electrolyzer system itself. Figure 8 shows that the single largest contributor to the cost of the electrolyzer stack is the catalyst-coated membrane (CCM). The significant CCM cost is mainly driven by expensive platinum-group metals used in the electrodes. This is also true for fuel cell stacks. To attenuate this expense, much effort has been expended in the research and development of efficient electrocatalysts comprised of earth-abundant non-precious elements[25].

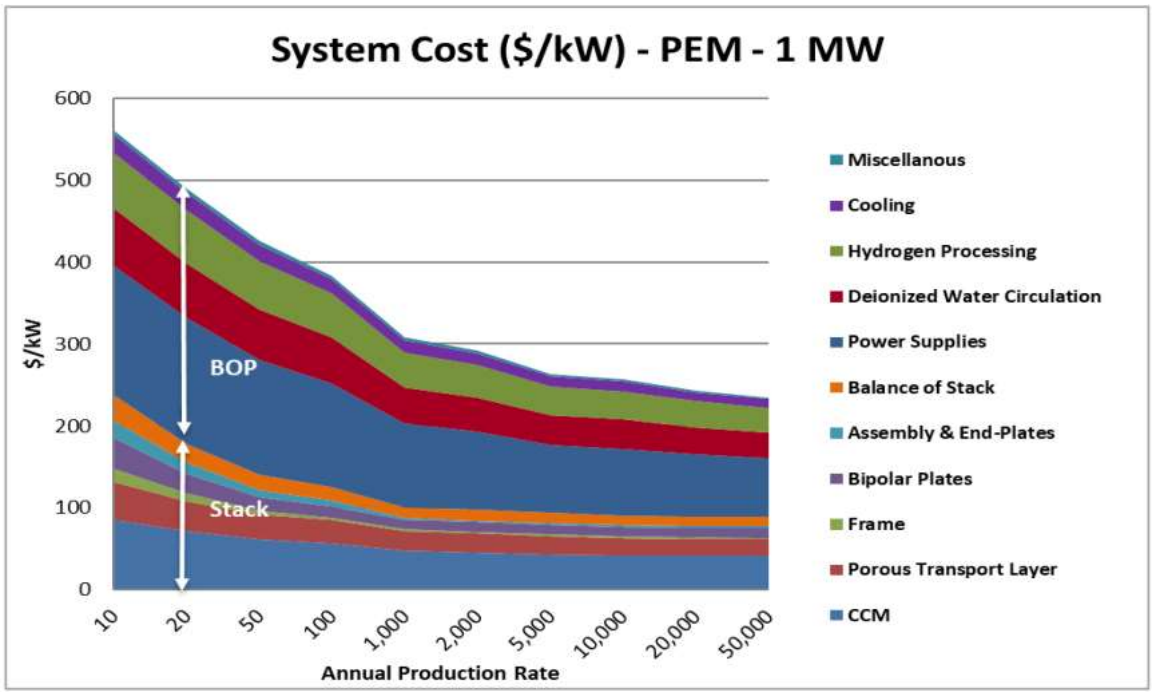

Figure 8. 1-MW PEM electrolyzer system cost at different annual production rates. Shows breakdown of cost contribution for each component. Reproduced from [26].

Figure 9 presents an overview of a hypothetical energy economy which uses green H_2 as the predominant energy carrier. This scheme, known as H2@Scale, is a U.S. Department of Energy initiative aimed at advancing technologies for H_2 production, transport, storage, and utilization to enable decarbonization and revenue opportunities across multiple sectors[27]. As shown in Figure 9, renewable energy and green H_2 are not silver bullets; roles exist for other energy sources and carriers including batteries and even fossil fuels (with carbon capture and storage technology). However, several areas in this scheme demand advanced and application-specific electrolyzer and fuel cell technology. The work presented in subsequent chapters of this dissertation aims to address needs in various areas of this scheme. Chapter 2 outlines the fundamentals of hydrogen evolution electrocatalysis. Chapter 3 presents a rapid fabrication technique for an electrode based on non-precious molybdenum sulfide for hydrogen evolution – the cathodic electrolyzer reaction. This work contributes to the development of techniques for the rapid fabrication of highly-active electrodes based upon cost-effective materials. Chapter 4 introduces and characterizes a class of hydrogen evolution electrocatalysts based on the thiosemicarbazone molecular framework. This work contributes to efforts to translate the remarkable activity and stability of biomimetic nickel-based hydrogen catalysts to electrode surfaces. Both Chapters 3 and 4 contribute to the body of work which ultimately seeks to lower electrolyzer CAPEX by utilizing non-precious materials. Chapter 5 outlines the fundamentals of proton exchange membrane fuel cells. Chapter 6 details the development and *in-situ* testing of advanced structured electrodes for oxygen

reduction – the cathodic (rate-limiting) fuel cell reaction. This approach constitutes an improvement of fuel cell activity beyond the current state of the art and seeks to reduce technological barriers to widespread fuel cell adoption and implementation in the “Power Generation” and “Hydrogen Vehicle” areas of Figure 9.

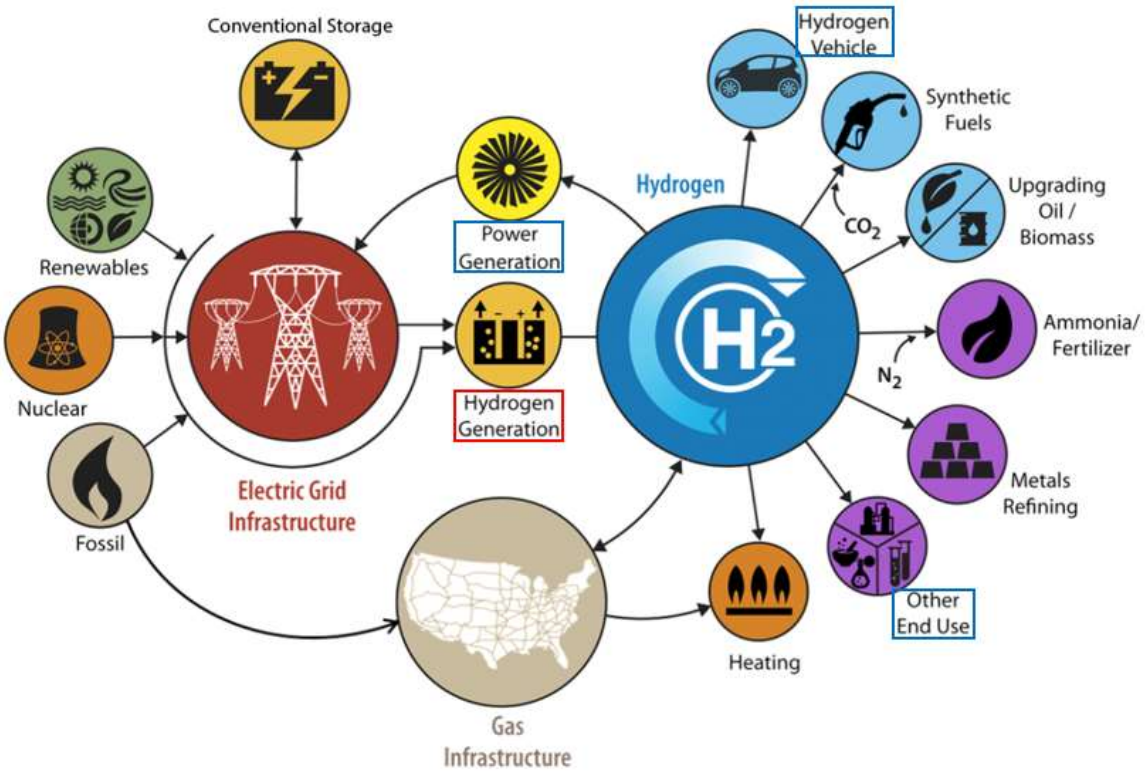

Figure 9. Overview of the H2@Scale scheme for an energy economy based upon green hydrogen. Areas outlined in red represent electrolyzer applications, and areas outlined in blue outline fuel cell applications. Source: U.S. Department of Energy[27].

2. HYDROGEN EVOLUTION ELECTROCATALYSIS

2.1. PROTON EXCHANGE MEMBRANE WATER ELECTROLYSIS

Water electrolysis (Equation 1) is an electrochemical reaction comprised of the cathodic H_2 evolution reaction (HER, Equation 2) and anodic O_2 evolution reaction (OER, Equation 3) half-reactions.

$$2H_2O \rightarrow 2H_2 + O_2 \qquad \textit{Equation 1}$$

$$4H^+ + 4e^- \rightarrow 2H_2 \qquad \textit{Equation 2}$$

$$2H_2O \rightarrow O_2 + 4H^+ + 4e^- \qquad \textit{Equation 3}$$

The above equations reference an electrolyzer reaction based upon protons as charge carriers. Several types of electrolyzers exist including proton exchange membrane, alkaline, and solid oxide[28]. However, electrolyzers aside from the proton exchange membrane water electrolyzer (PEMWE) type fall outside of the scope of this work and will not be discussed herein. Additionally, balance of plant components needed to support practical electrolyzer operation (e.g. pump, sensor, heat exchanger, compressor, blower, humidifier) are beyond the scope of this dissertation.

Myriad challenges exist regarding the current technological limitations of PEMWE components[29]. Briefly, modern devices which utilize precious metal-based electrodes are limited by the sluggish kinetics of OER. IrO_2 provides a balance of activity and stability and is thus considered the best anode catalyst despite its mass-specific kinetic limitations[30]. However, its cost and scarcity pose a

significant problem for large-scale manufacturing. Clearly, a need exists to either increase the activity of the anode catalyst while reducing loading or to develop new materials with superior activity and stability at a lower price point. The chemical stability, Ohmic losses, and hydrogen permeability of the perfluorosulfonic acid (PFSA) membrane which separates anode and cathode is also a source of concern and motivation for ongoing research[29]. Diffusion media (DM) and bipolar plates (BPPs) are typically comprised of expensive corrosion-resistant materials such as titanium (Ti) because of the corrosive environment in the PEMWE. These materials are significant contributors to the CAPEX of a PEMWE stack (Figure 8), and much work focuses on developing cheaper materials for these components[30].

Lastly, the Pt catalyst used in the cathode CL is generally able to catalyze HER with low overpotentials at relatively low loading[31]. However, as noted in Figure 8, the CCM represents the plurality of an electrolyzer stack cost. The CCM cost is driven by the precious metals on both the anode and cathode. Even at the low loading of platinum conventionally used for PEMWE cathode CLs, large-scale implementation of conventional PEMWE devices sufficient to satisfy global energy conversion demands runs the risk of further driving Pt costs up to prohibitive levels. To ensure that PEMWE manufacture is economical at scale, development of cost-effective cathode CL materials based upon earth-abundant elements is a necessity. To contribute to the ultimate goal of developing a cost-effective and efficient electrolyzer stack, Chapters 3 and 4 present work which focuses exclusively on the development and implementation of non-precious

catalysts for HER. The remainder of this chapter outlines scientific aspects of HER.

2.2. EX-SITU HYDROGEN EVOLUTION ELECTROCATALYSIS EXPERIMENTATION

As will be shown in Chapters 3 and 4, replacing Pt-based materials with non-PGM HER catalysts currently confers considerable HER overpotentials. In order to study these losses with the goal of furthering non-precious catalyst design, a model experimental system is required to isolate the cathode properties from the whole-system losses encountered in a PEMWE cell. To this end, a rotating (ring)-disk electrode (RRDE) setup is employed (Figure 10).

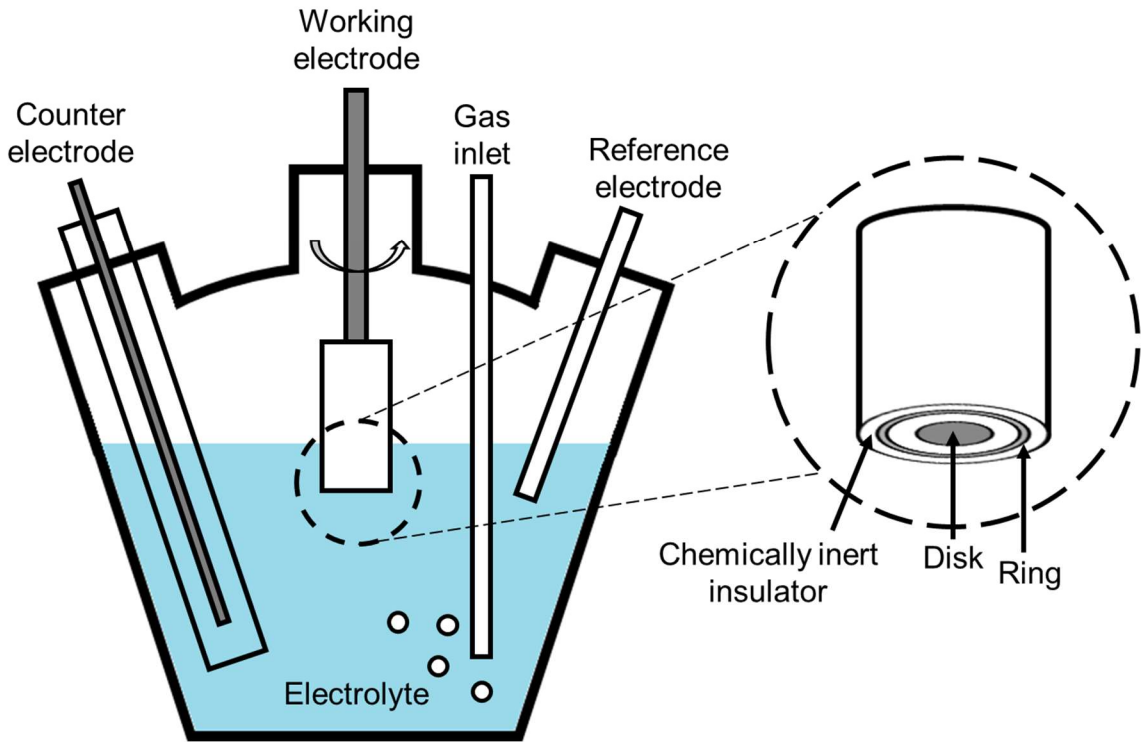

Figure 10. RRDE cell setup. Reproduced with permission from [32].

The RRDE setup uses a glass cell filled with an electrolyte medium. In the studies presented here, a glass electrochemical cell is filled with mildly acidic aqueous electrolyte (0.5 M H_2SO_4) which emulates the acidic conditions within the PFSA medium in a PEMWE. The catalyst to be studied is deposited on the disk, allowing for a controlled loading over a defined geometric surface area. The catalyst is typically mixed with an aqueous suspension of Nafion before deposition to serve as both a binder and proton conduit. During operation, the disk is rotated to remove evolved hydrogen bubbles from the electrode, mitigating mass transport losses (discussed more below). Losses from the electrode not under study (in this work, the anode where OER takes place) are eliminated by using a counter electrode with surface area several orders of magnitude higher than that of the disk to force HER on the disk to act as the rate limiting half-reaction in the cell. For the study of HER, inert N_2 gas is bubbled into the cell to prevent the more energetically-favorable oxygen reduction reaction (ORR, discussed beginning in Chapter 5) from occurring at the disk. A reference electrode is employed to standardize the working electrode (disk) potential. Lastly, a platinum ring concentric to the disk is used in some cases for oxidation and thus Faradaic quantification of product H_2. Physical considerations of HER studied with this system are outlined in the following sections.

2.3. THERMODYNAMIC CONSIDERATIONS

The Gibbs free energy of a system describes the maximum reversible work that may be performed by said system at constant temperature and pressure. For an

electrochemical reaction at equilibrium (e.g. a HER electrode at open-circuit – the condition of zero current flow), it is given by Equation 4.

$$\Delta G = \Delta G^0 + RTlnQ \qquad \textit{Equation 4}$$

where ΔG^0 is the reference free energy at standard conditions, R is the gas constant, T is the temperature, and Q is the reaction quotient. By definition, free energy is related to electrical potential as in Equation 5.

$$\Delta G = -zFE \qquad \textit{Equation 5}$$

Combining and rearranging, the Nernst equation (Equation 6) is obtained which describes the ideal (thermodynamic) reversible voltage as a function of temperature where E^0 is the standard reaction potential, F is Faraday's constant, and a_i is the activity of the i^{th} component. The left-hand expression is general for electrochemical systems, and the right-hand expression is specific to HER (Equation 2)

$$E = E^0 - \frac{RT}{zF} lnQ = E^0 - \frac{RT}{F} ln \frac{{a_{H_2}}^{\frac{1}{2}}}{a_{H^+}} \qquad \textit{Equation 6}$$

where $E^0 = 0$ at standard conditions (1 atm, pH = 0, 298 K, open circuit). The activities a_{H_2} and a_{H^+} are related to the pressure of H_2 and concentration of H^+ respectively. Solving for E gives the reversible open-circuit potential of the hydrogen electrode versus *reversible hydrogen electrode* (RHE). Further, E vs. RHE can be determined at any overpotential by substituting the measured potential vs. *normal hydrogen electrode* (NHE, after reference electrode correction) for E^0. This allows for standardization of polarization behavior over a

variety of experimental conditions. Equation 6 represents the thermodynamic maximum potential for HER (HER cannot take place above this value).

2.4. KINETIC LOSSES

Several irreversible losses which limit the actual rate of H_2 production at a given operating potential are present in HER systems. The potential loss required to reach a given current density is referred to as *overpotential* or overvoltage. The first of these losses is related to activation of the electrode (kinetic losses) and shall be described herein. Kinetic losses refer to the use of some additional amount of potential needed to drive the electrochemical reaction at the catalyst surface. In other words, some amount of electrical potential is used to achieve the transition state between reactant and product. A good electrocatalyst lowers this potential barrier. Electrode kinetics is the primary area of consideration in the design and ex-situ evaluation of novel HER catalysts/electrodes – the focus of Chapters 3 and 4. Therefore, kinetic losses will be covered more extensively than other losses in this chapter. The relationship between reaction rate and kinetic losses is derived below.

Consider the redox reaction in Equation 7 (general form of Equation 2).

$$O^+ + e^- \underset{k_r}{\overset{k_f}{\rightleftharpoons}} R \qquad \textit{Equation 7}$$

where O^+ is the oxidized reactant (H^+ in this case), R is the reduced product (H_2), k_f is the forward rate constant, and k_r is the reverse rate constant. Equation 8 describes the rate of the reaction in Equation 7.

$$-r_{O^+} = k_f C_{O^+} - k_r C_R \qquad \textit{Equation 8}$$

where C_{O^+} and C_R are the concentrations of the reactant and product respectively. At equilibrium, $-r_{O^+} = 0$, and $k_f C_{O^+} = k_r C_R$. Equation 9 is the form of the Nernst equation (Equation 6) for this system.

$$(E^0 - E)\frac{zF}{RT} = lnk_f - lnk_r \qquad \textit{Equation 9}$$

$z = 1$ electrons are transferred per H^+ for HER. The rate constants are both functions of E. Taking the derivative of Equation 9 with respect to E yields Equation 10.

$$1 = \frac{RT}{F}\left[\frac{d(lnk_r)}{dE} + \frac{d\left(ln\frac{1}{k_f}\right)}{dE}\right] \qquad \textit{Equation 10}$$

At this point, the dimensionless constant α may be introduced. α, known as the charge transfer coefficient, is the material-dependent proportion of electrical energy used to drive the electrochemical reaction[28] at the catalyst surface. For a hydrogen electrode, α is defined by Equation 11 and Equation 12.

$$\frac{RT}{F}\frac{d(lnk_r)}{dE} = 1 - \alpha \qquad \textit{Equation 11}$$

$$\frac{RT}{F}\frac{d\left(ln\frac{1}{k_f}\right)}{dE} = \alpha \qquad \textit{Equation 12}$$

Integrating Equation 12 with respect to E, applying the boundary conditions $k_f = k_f^0$ and $k_r = k_r^0$ at $E = E^0$, and recognizing that the overpotential $\eta = E - E^0 =$

$\frac{-E_a}{F}$, Equation 13 is obtained. Equation 13 is the form of Arrhenius' Law which describes the kinetics of HER.

$$k_f = k_f^0 e^{\frac{-\alpha E_a}{RT}} \qquad \textit{Equation 13}$$

The cell current is defined by $i = nF(-r_{O^+})$. If the cell voltage is close to open circuit (i.e. $E \approx E^0$), assume that $C_{O^+} = C_R$ thus $k_f = k_r = k^0$. Therefore, the kinetically limited hydrogen electrode current is described by Equation 14.

$$i = i_0 \left(e^{\frac{-\alpha \mathrm{F} \eta}{RT}} - e^{\frac{(1-\alpha)\mathrm{F}\eta}{RT}} \right) \qquad \textit{Equation 14}$$

Equation 14 is known as the Butler-Volmer equation and describes the reaction kinetics at the electrode surface. As the reaction is driven in the forward direction away from open circuit, the second term becomes insignificant, and the current can be approximated with Equation 15.

$$i = i_0 e^{\frac{-\alpha \mathrm{F} \eta}{RT}} \qquad \textit{Equation 15}$$

Equation 15 is known as the Tafel equation. i_0, the exchange current density, reflects the inherent activity of the electrode surface. Intrinsic electrocatalytic activity is directly correlated with i_0. Therefore, i_0 serves as a powerful metric for evaluating the utility of electrocatalysts. Additionally, a commonly reported empirical parameter called the Tafel Slope which relates to α is defined by Equation 16.

$$A = \frac{\lambda k_B T}{e\alpha}$$ *Equation 16*

where A is the Tafel Slope, k_B is the Boltzmann constant, T is the temperature, and e is the electric elementary charge of the electron. In summary, HER overpotentials due to kinetic losses at the cathode are described by Equation 17.

$$\eta_{kinetic} = \frac{-RT}{\alpha \mathrm{F}} ln\left(\frac{i}{i_0}\right)$$ *Equation 17*

The intrinsic kinetic efficiency of a HER electrocatalyst can be qualitatively predicted by the Sabatier principle which dictates that an optimal electrocatalyst should interact with reagents and intermediates strongly enough that they bind the catalyst surface but not interact with intermediates or products so strongly that the active site is inhibited for an excessive period of time[33,34]. For electrochemical applications, this principle is depicted in the so-called Sabatier plot, or volcano plot, which plots the benchmark catalytic current density (corresponding to reaction rate) as a function of the binding energy between the reactant and catalyst. Such a plot is exhibited in Figure 11[35,36]. Here, i_0 of the hydrogen electrode is plotted as a function of the energy of metal hydride formation. Metals on the ascending branch of the plot bind hydrogen weakly, resulting in a relatively low reaction rate due to the escape of intermediates before conversion. On the other hand, materials on the descending branch of the plot bind hydrogen strongly, resulting in occupation of catalytic active sites for extended periods of time. PGMs sit at the top of the volcano plot for HER due to their unique electronic structure, making this the best class of natural materials to catalyze HER. The modification of non-PGM materials to give PGM-like volcano

plot behavior is the greatest source of effort in the field of non-precious hydrogen electrocatalysis.

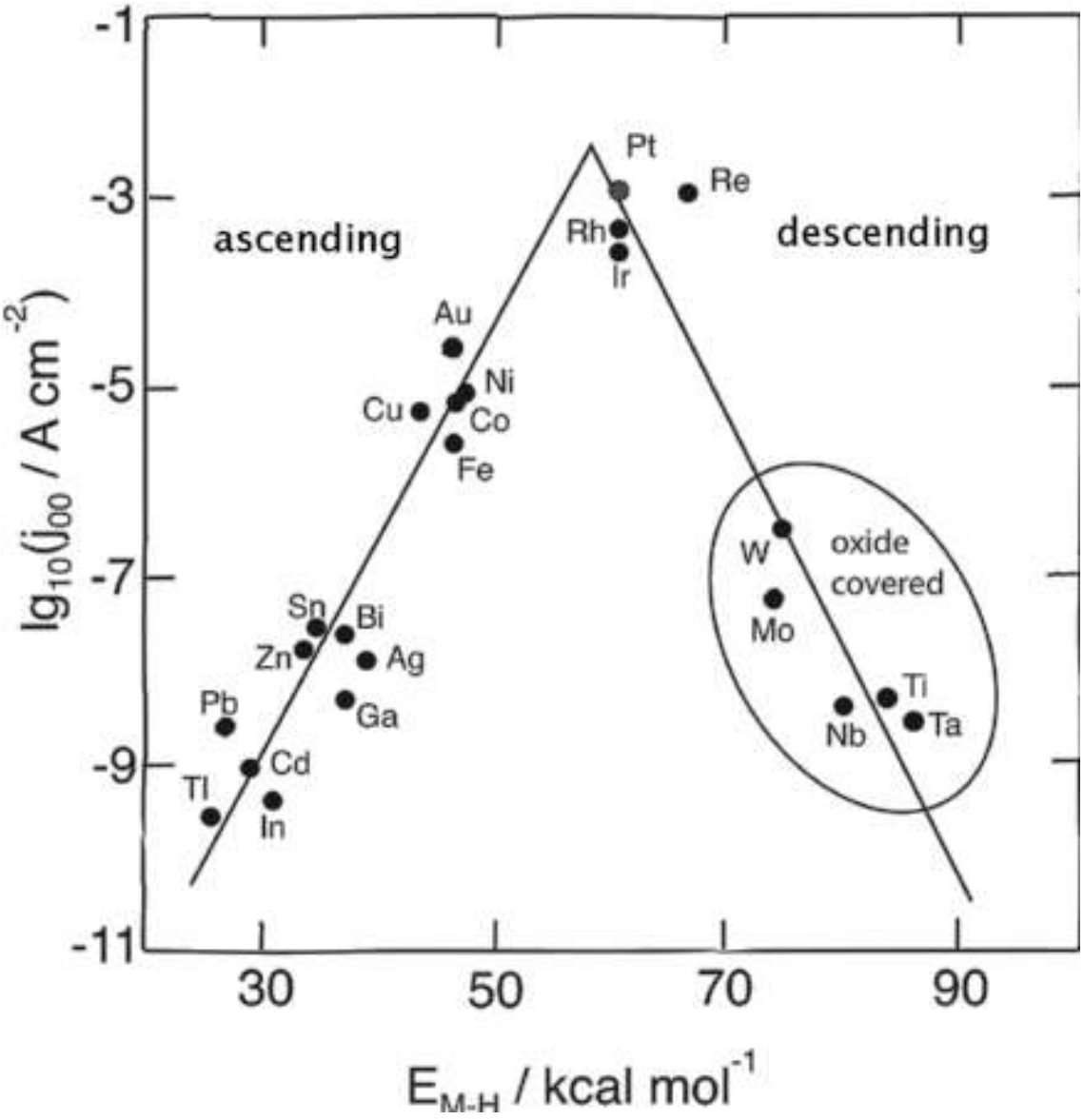

Figure 11. Sabatier plot of various metals for HER. Reproduced from [36] using data from [35].

It is generally accepted that HER proceeds mechanistically through two of three steps[37]. The *Volmer* step (Equation 18) constitutes the adsorption of a solvated proton onto the catalyst surface as a hydride and must occur before either of the other steps.

$$H^+ + M + e^- \underset{k_{-1}}{\overset{k_1}{\rightleftharpoons}} MH_{ads} \qquad \textit{Equation 18}$$

where M represents the catalyst active site and k_1 and k_{-1} are the forward and reverse rate constants respectively for the Volmer step. The next step, which yields H_2, can occur through one of two pathways. Equation 19 shows the first option: electrochemical desorption via the *Heyrovsky* step.

$$MH_{ads} + H^+ + e^- \underset{k_{-2}}{\overset{k_2}{\rightleftharpoons}} M + H_2 \qquad \textit{Equation 19}$$

In Equation 19, the adsorbed hydride from the Volmer step reacts with another solvated proton, forming H_2. Alternatively, the *Tafel* step (Equation 20) can take place instead.

$$2MH_{ads} \underset{k_{-3}}{\overset{k_3}{\rightleftharpoons}} 2M + H_2 \qquad \textit{Equation 20}$$

In Equation 20, two adsorbed hydrides combine chemically, yielding H_2. The measured HER Tafel slope (Equation 16) is commonly used to ascribe a HER mechanism to a catalyst. In the case where HER is limited by the Volmer step (Volmer mechanism), the Tafel slope is approximately 120 mV dec^{-1} [37]. For reactions limited by the Heyrovsky step (Volmer-Heyrovsky mechanism), the Tafel slope is approximately 40 mV dec^{-1}. Reactions limited by the Tafel step

(Volmer-Tafel mechanism) have a characteristic Tafel slope of approximately 30 mV dec^{-1}. Electrodes which give Tafel slopes that don't fit cleanly within the confines of the above criteria are considered to have a *mixed* HER mechanism. The Tafel slope is largely dependent upon the material, although electrode properties can play a role as well. Because the Tafel slope represents the amount of additional potential input required to raise the reaction rate by an order of magnitude in the kinetic region, a superior electrocatalyst generally has a lower Tafel slope, and the Volmer-Tafel mechanism is the most desirable. Pt possesses a Tafel slope of roughly 30 mV dec^{-1} for HER[38], placing it squarely in Volmer-Tafel territory and positioning it as the ultimate benchmark for HER electrocatalysis.

2.5. OHMIC LOSSES

In any electrical system, some amount of charge carrier kinetic energy is lost as heat as the charge carriers traverse circuit elements. In the RRDE cell, the majority of Ohmic losses occur as protons are conducted through the liquid electrolyte, but a small amount of energy is also lost due to imperfect contact at the interfaces between various cell components and within wires and other elements which make up the balance of the system. Overpotentials due to these losses are described by Ohm's Law (Equation 21).

$$\eta_{Ohmic} = ir \qquad \textit{Equation 21}$$

Additionally, some energy is lost as heat due to the resistance within the percolating network which transports protons and electrons throughout the catalyst layer. Some of this heat is actually recovered by increasing the local

energy of the reactants and effectively decreasing ΔG_{rxn}. However, these losses are minimal in a RRDE system where the electrode is in direct contact with a liquid electrolyte, so this consideration is neglected in subsequent discussion.

2.6. MASS TRANSPORT LOSSES

At the voltages considered in the following studies, mass transport limitations are not particularly significant due to the rapid removal of H_2 bubbles from the electrode surface via rotation of the disk. However, mass transport limitations deserve consideration in PEMWE systems – particularly on the oxygen electrode at high potentials. Since the studies in Chapters 3 and 4 do not deal with devices, PEMWE mass transport limitations will be addressed briefly here. The PEMWE mass transport overpotential is expressed by Equation 22.

$$\eta_{mt} = \frac{RT}{zF} ln\left(\frac{1}{1 - \frac{i}{i_{lim}}}\right) \qquad \textit{Equation 22}$$

where i_{lim} represents the mass transport-limited current. i_{lim} is itself a function of current; electrode properties including thickness, surface area, and double layer; and gas properties including diffusivity and local concentration[39,40].

2.7. SUMMARY

The operating potential for the HER half-cell RRDE setup considered in the following chapters is approximated in Equation 23 where mass transport limitations at relevant potentials are neglected.

$$V_{cell} = E + \eta_{kinetic} + \eta_{Ohmic}$$ *Equation 23*

In the following two chapters, electrode films based upon non-precious HER catalysts are prepared and characterized using the RRDE system. Measured electrode potentials are corrected for Ohmic losses (iR compensation) to highlight kinetic properties of the catalyst.

3. INTENSE PULSED LIGHT, A PROMISING TECHNIQUE TO DEVELOP MOLYBDENUM SULFIDE CATALYSTS FOR HYDROGEN EVOLUTION

We have demonstrated a simple and scalable fabrication process for defect-rich MoS_2 directly from ammonium tetrathiomolybdate precursor using intense pulse light treatment in milliseconds durations. The formation of MoS_2 from the precursor film after intense pulsed light exposure was confirmed with XPS, XRD, electron microscopy and Raman spectroscopy. The resulting material exhibited high activity for the hydrogen evolution reaction (HER) in acidic media, requiring merely 200 mV overpotential to reach a current density of 10 mA cm^{-2}. Additionally, the catalyst remained highly active for HER over extended durability testing with the overpotential increasing by 28 mV following 1000 cycles. The roll-to-roll amenable fabrication of this highly-active material could be adapted for mass production of electrodes comprised of earth-abundant materials for water splitting applications.

Alexander Gupta[2], Krishnamraju Ankireddy[2], Bijendra Kumar[2], Adel Alruqi[3], Jacek Jasinski[2], Gautam Gupta[1], and Thad Druffel[1]

[1] University of Louisville, Department of Chemical Engineering, Louisville, KY 40292, United States of America

[2] University of Louisville, Conn Center for Renewable Energy Research, Louisville, KY 40292, United States of America

[3] University of Louisville, Department of Physics and Astronomy, Louisville, KY 40292, United States of America

This material is based upon work supported by the National Science Foundation under Grant No. 1800245. The authors acknowledge the Conn Center for Renewable Energy Research at the University of Louisville for their financial support and research facilities.

3.1. INTRODUCTION

Hydrogen production via electrocatalysis is a promising route for storing excess energy from renewable sources (such as wind or solar) during off-peak energy consumption hours. In addition to its use as an energy carrier, molecular hydrogen is an important chemical feedstock with applications in ammonia production, hydrocracking, hydrodesulfurization, and other industries. Platinum and other noble metals are efficient catalysts for the hydrogen evolution reaction (HER)[41]; however, they are scarce and expensive[42]. Earth-abundant alternative catalysts[43], including metal carbides, nitrides, and sulfides[44,45], are promising candidates to achieve electrocatalytic hydrogen production[25].

Among these catalysts, molybdenum disulfide (MoS_2) has been explored widely for hydrogen production[46,47] due to its environmental benignity, high stability in acidic environments, and good catalytic activity. MoS_2 is a transition metal dichalcogenide with an Mo layer sandwiched between two sulfur layers with weak Van der Waals forces in a trigonal prismatic arrangement[48,49]. The edges of sheet-like MoS_2 are active sites for HER, with the basal plane being catalytically inert, so a greater concentration of edge sites is associated with better catalytic activity[50]. There has been tremendous effort put into the preparation of active MoS_2 structures via solvent- assisted exfoliation[51], chemical exfoliation[52,53], hydrothermal synthesis[54], intercalation-aided exfoliation[55], chemical vapor deposition[56,57], thermal annealing of MoS_2 precursor materials[58], and electrochemical synthesis[59]. The large-scale preparation of MoS_2 films by chemical vapor deposition, and nanosheets by solution-based chemical

exfoliation, has also been reported[60]. Industrial implementation of most of these fabrication methods is somewhat impractical due to sophisticated synthesis procedures with processing steps including high vacuum, high temperature, H_2S gas flow, and/or inert atmosphere conditions. Here, we report a novel one-step, extremely fast, and scalable fabrication method for defect-rich MoS_2 using the intense pulsed light (IPL) technique.

IPL, also known as photonic sintering, imparts rapid intense pulses of light to provide localized heating and/or induce chemical reactions in an absorbing thin film. The IPL unit essentially contains a xenon flash lamp, a capacitor bank, and coil circuitry which cooperatively generate a burst of intense light. The treatment is carried out within a millisecond time frame which is desirable from a processing standpoint. The light energy is absorbed by the thin film and almost immediately released as heat, inducing very localized temperatures of several hundred degrees centigrade. Process parameters include the input energy density, pulse duration, and number of pulses. The IPL technique has been utilized for processing metal nanoparticles and semiconductor materials for various applications[61].

This study highlights the rapid means of preparing MoS_2 structures with high edge site concentration from precursor-coated films using IPL for the first time. The structural properties of the resulting material (IPL-MoS_2) were analyzed using x-ray diffraction (XRD), Raman, scanning electron microscopy, transmission electron microscopy (TEM) and x-ray photoelectron spectroscopy (XPS) and compared with those of bulk MoS_2. IPL-MoS_2 was further

characterized in terms of its electrochemical activity for HER and compared with bulk MoS_2. Electrochemical characterization reveals that IPL-MoS_2 exhibits catalytic activity superior to bulk crystalline MoS_2 and is among the most highly active reported MoS_2 catalysts obtained from various treatments for HER[25].

3.2. METHODS

3.2.1. MATERIALS

Bulk molybdenum sulfide powder with an average particle size of 6 μm was purchased from Sigma Aldrich. Ammonium tetrathiomolybdate powder was supplied by Beantown Chemical. Ethanol (200 proof) was obtained from Decon Labs. Twice-deionized Millipore water (18MΩ cm) was used. FTO-coated glass was obtained from Hartford Glass Company, Hartford City, IN. Sulfuric acid (ACS grade) was purchased from VWR. Compressed nitrogen and hydrogen gases were provided by Welders Supply, Louisville, KY.

3.2.2. MoS_2 FILM PREPARATION AND IPL PROCESSING

The precursor solution was prepared by mixing 0.157 g of ammonium tetrathiomolybdate in 2:1 v/v water and ethanol solvent for a total of 6 ml. The solution was sonicated for two hours and subsequently filtered through a 250 nm nylon filter. The same procedure was used to prepare the bulk crystalline MoS_2 solution. The filtered solution was drop casted on FTO-coated glass substrates (for material characterization) or glassy carbon electrodes (GCE, for electrochemical testing) with a loading of approximately 1.3 mg cm^{-2}. The GCEs were rotated (~400 RPM) during dropcasting to obtain a relatively uniform film, while the FTO substrates were not. The air-dried films were IPL treated with a

total number of 10 repeated pulses with each pulse producing 25 J cm^{-2} energy density and having a 2 ms duration. The Sinteron 2000-L IPL apparatus and full-spectrum UV-to-near-IR lamp were purchased from xenon.

3.2.3. EXPERIMENTAL SET-UP FOR HER

Electrochemical characterization was carried out using a Metrohm Autolab PGSTAT302N potentiostat/galvanostat in potentiostat mode with a MSR electrode rotator from Pine Research. Replaceable-tip glassy carbon working electrodes were purchased from Pine Research (E4TQ Changedisk series). A five-neck electrochemical cell from Pine Research was filled with 0.5 MH_2SO_4 electrolyte. A graphite rod inside a glass frit (Pine Research) was used as the counter electrode. An Ag/AgCl reference electrode, calibrated versus RHE (223.1 mV versus RHE), was used to determine the absolute potential throughout electrochemical experiments. A glass diffuser (Pine Research) was used to bubble gas into the electrolyte. Platinum meshes (Alfa Aesar, 99.9% metals basis) were used to calibrate measured potentials versus RHE. A platinum ring (Pine Research, E6R2 Fixed-Disk RRDE Tip) was used to measure the HER activity of platinum.

3.2.4. CHARACTERIZATION OF MoS_2 FILMS

XRD was carried out using a Bruker Discovery D8 x-ray diffractometer equipped with an x-ray source of Cu Kα (λ = 0.1548 nm) and operated at a scan rate of 2 s/step and a step size of 0.02°. Raman spectroscopy was performed using a Renishaw Raman Spectrometer equipped with a red laser of 632 nm. The power of the red laser was kept below 1 mW to prevent over heating of the sample, and

the emission was collected with an integrated CCD camera by dispersing with a 1800 lines mm^{-1} grating. TEM analysis was carried out using a FEI Tecnai F20 TEM equipped with a field emission gun (FEG) and operated at 200 kV of accelerating voltage. Microstructures of the films were characterized using a FEI Nova NanoSEM 600 with an accelerating voltage of 10 kV and a working distance of 5 mm. XPS was carried out using a VG Scientific MultiLab 3000 ultra-high vacuum surface analysis system with CLAM4 hemispherical electron energy analyzer and a dual-anode Mg/Al x-ray source. All mea- surements were performed using non-monochromatic Al Kα (hv = 1486.6 eV) x-ray radiation under a base chamber pressure in the low 10−8 Torr range. For each sample, a survey scan from 0 to 1000 eV was collected to identify all elemental peaks. This was followed by the acquisition of high-resolution Mo 3d, S 2p, C 1s and O 1s spectra. An intrinsic C 1s peak at 284.5 eV was used for the binding energy calibration. The analysis of XPS spectra (background subtraction and peak deconvolution) was performed using XPSPEAK4.1 software. The background curves were fitted with a Shirley function.

Electrochemical characterization was done using linear sweep voltammetry, cyclic voltammetry, and frequency response analysis techniques. To obtain polarization/Tafel plots, the potential was swept from 0.1 to −0.6 V versus RHE at a rate of 5 mV s^{-1}. For activation/durability testing, the potential was swept from 0.1 to −0.35 and back to 0.1 V versus RHE at 50 mV s^{-1} repeatedly. All measured potentials were calibrated to the RHE scale after the experiment (to avoid platinum contamination) by saturating the electrolyte with H_2 gas,

conducting cyclic voltammetry repeatedly between platinum working and counter electrodes, and taking the average potential versus the reference electrode at zero current.

3.3. RESULTS AND DISCUSSION

The surface morphology analysis of the ammonium tetrathiomolybdate precursor film before and after IPL exposure reveals an obvious morphological change after IPL treatment (Figure 12A and Figure 12B). The films consist of thick micron-scale assemblies. However, the larger features with smooth surface morphology transformed to aggregates after IPL, which is similar to sintering that has been demonstrated before with IPL[62–64]. The high-resolution images of IPL-treated film clearly exhibit rough surface morphology compared to as-deposited precursor film. To investigate whether this morphological change led to MoS_2 structure, XRD was carried out on IPL-MoS_2. The crystallographic structural analysis of IPL-MoS2 revealed the successful conversion of precursor material into MoS_2 structure. The XRD reflection peak at 14.4°, corresponds to hexagonal MoS_2 phase (JCPDS card No. 73-1508) (Figure 12C). The majority of the other reflections (26.5°, 33.5°, 37.7°, 51.6°, 54.4°, 61.6° and 65.5°) originate from the underlying FTO substrate. Comparative XRD patterns (Figure 41) show the presence of the reflection at 14.4° in IPL-MoS_2 and the absence of this reflection in the precursor. The calculated d-spacing, using the diffraction angle at 14.4° which corresponds to the (002) crystal plane, is 0.615 nm which is similar to that of 2H–MoS_2 (0.62 nm).

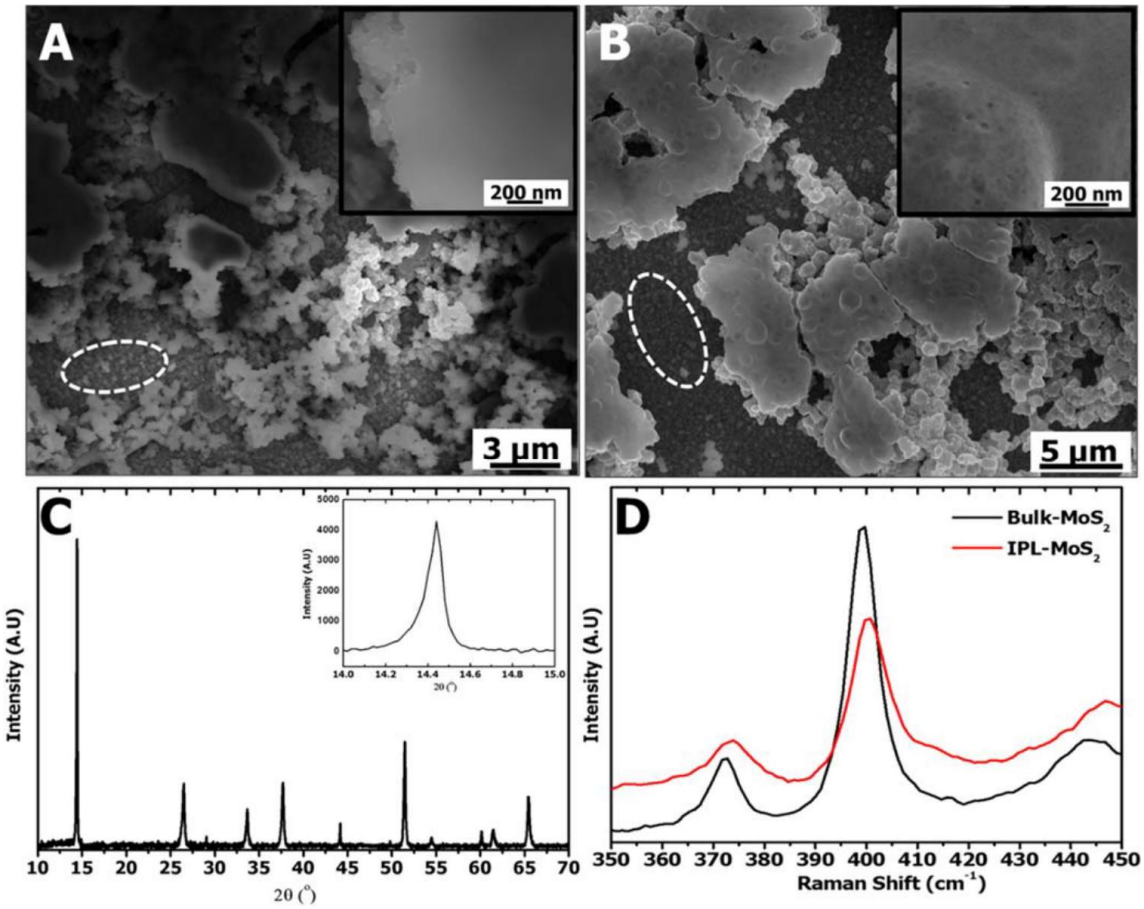

Figure 12. MoS_2 structural analysis (A) ammonium thiomolybdate precursor film on FTO-coated glass substrate (B) IPL treated MoS_2 film on FTO-coated glass substrates (white dotted circles display the FTO surface morphology)(C) XRD spectrum of IPL-MoS_2 film, (D) Raman spectra from bulk MoS_2 and IPL-MoS_2 structures.

Further investigation of structural transformation from precursor to MoS_2 nanosheets was carried out using Raman spectroscopy and compared with the spectra from bulk MoS_2 structures. The Raman spectra reveal that E2g (373.8 cm^{-1}) and A1g (400.2 cm^{-1}) peaks from IPL-MoS_2 match the corresponding E2g

(372.3 cm^{-1}) and A1g (399.2 cm^{-1}) peaks from bulk MoS_2, confirming the IPL-assisted conversion of precursor film to MoS_2 (Figure 12D). Raman spectra from 300 to 500 cm^{-1} are shown in Figure 42. The dominant phase exhibited by both IPL and bulk MoS_2 materials was 2H–MoS_2. There is a broad peak between 440 and 450 cm^{-1}, and attributing this peak to MoS_2 is an open question. The peak at 454 cm^{-1} was previously assigned to the double frequency of the LA(M) mode (227 cm^{-1}), and the peak at 440 cm^{-1} was predicted to be Mo–S vibrations for oxysulfide species[65–67]. However, further investigation is required to confirm if there is any oxysulfide species in IPL and bulk MoS_2 materials which is beyond the scope of this study.

Further probing of morphological and structural properties of the IPL-MoS_2 was conducted using TEM. Analysis of the films reveals that there are highly-corrugated lattice fringes across the sample. This implies that there are many defects and distortions within the structures. TEM images reveal mostly short clusters with discontinuous, bending, disjointed, and curved basal planes resulting in a highly defective MoS_2 structure (Figure 13A). The interlayer d-spacing is found to be 0.62 nm (Figure 13B), confirming the XRD results. The individual planes are curved or bent which indicates disordered atomic arrangement. This, together with the fact that most clusters are short segments, indicates high density of edge sites, which are responsible for improved HER performance. High-resolution TEM images were obtained at different areas of the sample (Figure 43); these micrographs exhibited very similar defect structure which signifies homogeneity of the sample. To investigate the mechanism of IPL-

assisted MoS_2 formation from the precursor materials, XPS analysis of molybdenum (Mo) and sulfur (S) elements in both bulk MoS_2 and IPL-MoS_2 was carried out.

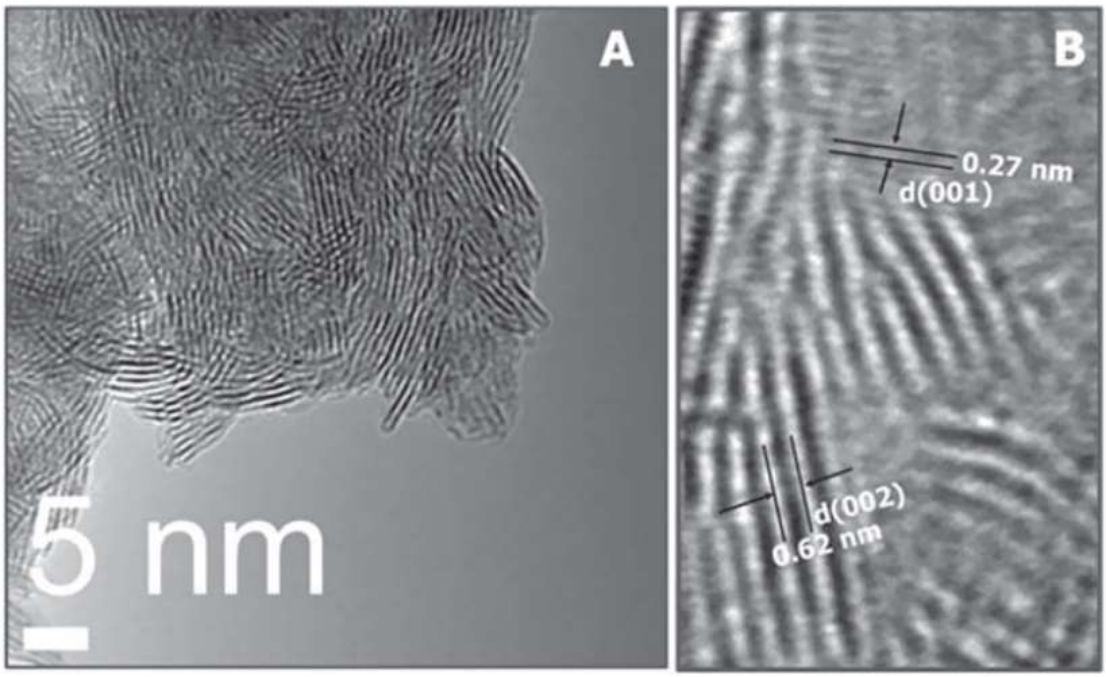

Figure 13. High-resolution TEM images of IPL-MoS_2 nanosheets (A) Defect-rich MoS_2 nanosheets (B) TEM image showing the interplanar spacing between (100) planes and layer-to-layer spacing.

A survey scan was acquired from 1 to 1000 eV. Detailed analysis on Mo and S elements was subsequently conducted by collecting high-resolution spectra of main Mo and S peaks. The survey spectra from IPL-MoS_2 and bulk MoS_2 are similar to each other (Figure 14).

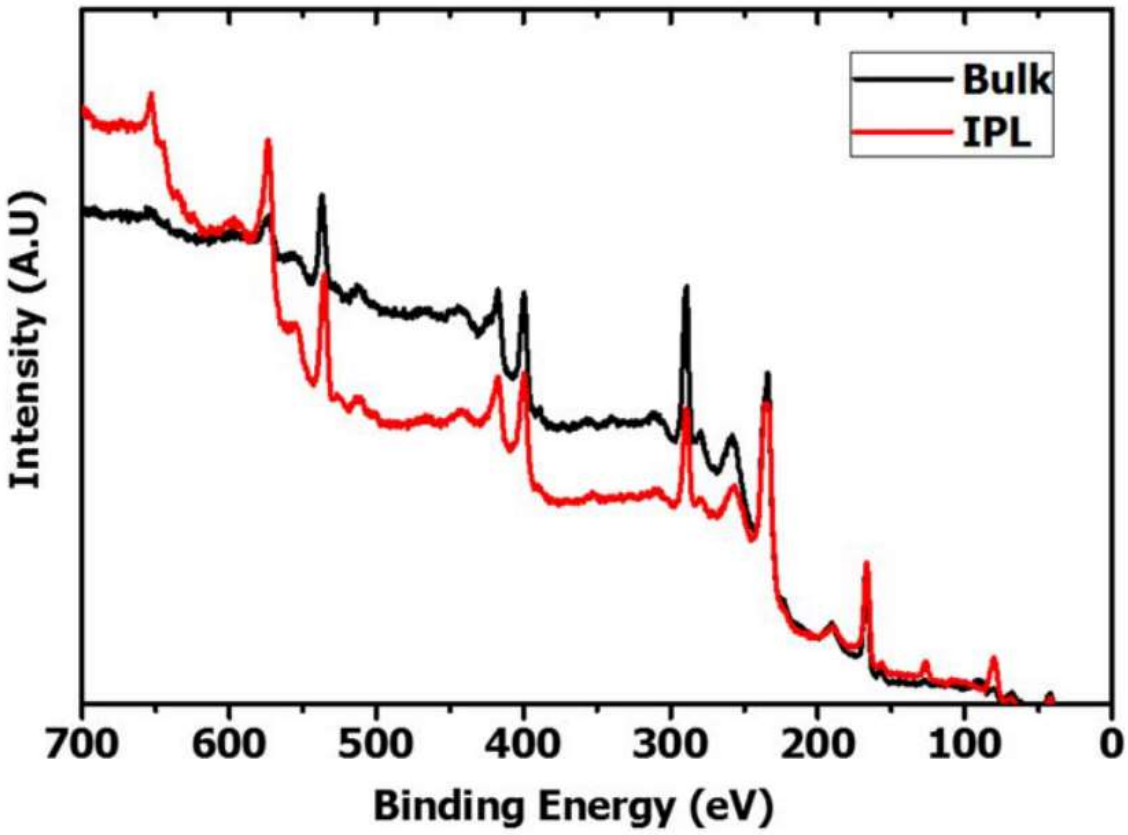

Figure 14. XPS spectrum of bulk MoS_2 and IPL-MoS_2 samples.

Mo and S peaks were detected in addition to C and O impurity peaks. The binding energies of Mo $3d_{5/2}$ are 228.9 and 229.3 eV for bulk MoS_2 and IPL-MoS_2 respectively, indicating +4 oxidation state for the Mo ion[68], whereas the binding energies for the Mo $3d_{3/2}$ are 232 and 232.4 eV for the bulk and IPL-MoS_2 samples respectively (Figure 15A and Figure 15B). The binding energy difference between Mo $3d_{5/2}$ and Mo $3d_{3/2}$ is 3.1 eV for the both bulk and IPL-MoS_2 samples. The energy difference of 3.1 eV is a characteristic of Mo species. The S 2p spectrum of IPL-MoS_2 exhibited a broad peak which was further

deconvoluted. This resulted in two doublets with the S $2p_{3/2}$ and S $2p_{1/2}$ states. The highest area doublet exhibited peaks at 162.0 and 163.3 eV for S $2p_{3/2}$ and S $2p_{1/2}$ states respectively, whereas the lowest area doublet displayed peaks at 163.5 and 164.6 eV for S $2p_{3/2}$ and S $2p_{1/2}$ states respectively. In case of bulk MoS_2, the S $2p_{3/2}$ and S $2p_{1/2}$ states showed peaks at 161.8 and 163 eV, respectively. The single doublet with S $2p_{3/2}$ around 161.8 eV is typical for S^{2-} ligands that form MoS_2. This suggests that the bulk MoS_2 powder might not have any other forms of S ligands, whereas the second doublet peak from IPL-MoS_2 with S $2p_{3/2}$ at 163.5 eV indicates the existence of S_2^{2-} ligands.

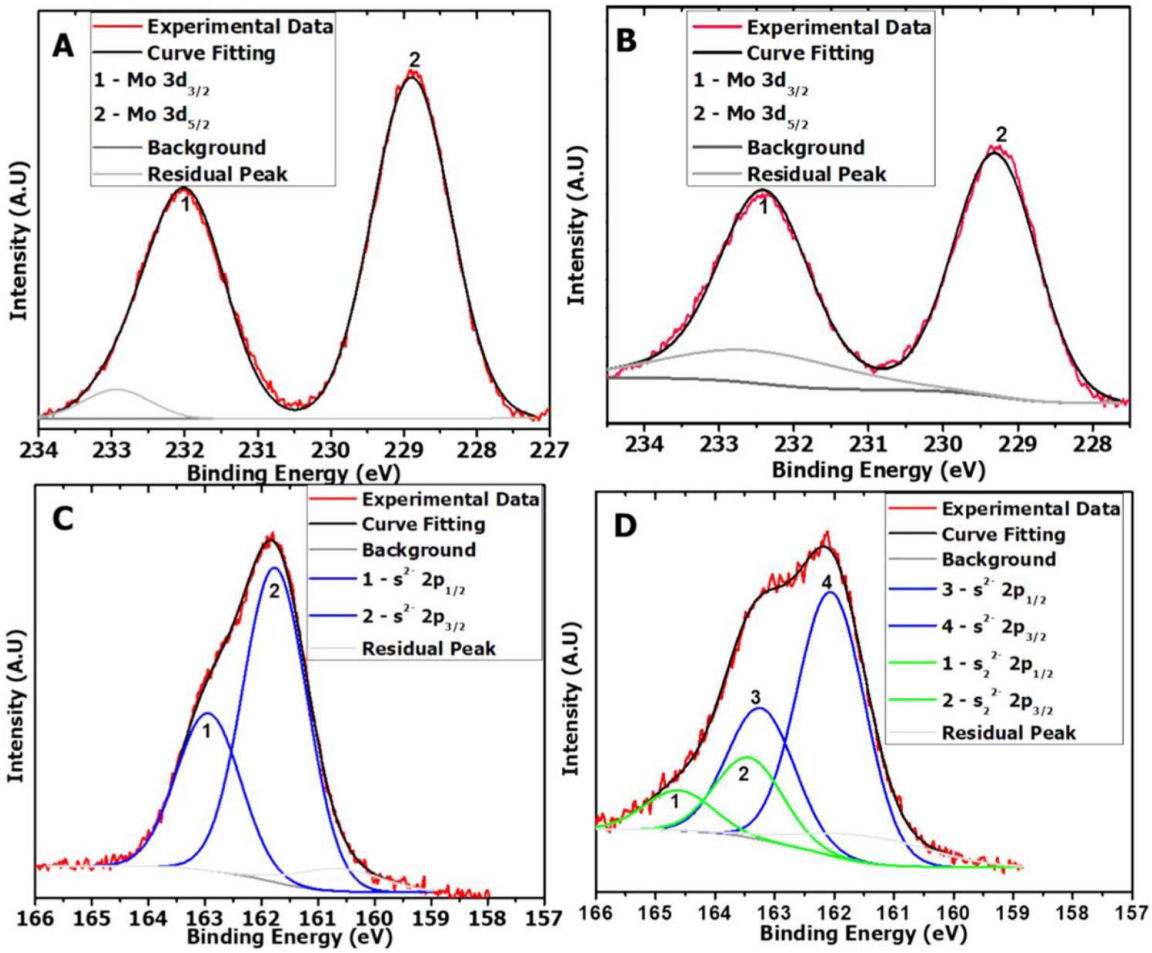

Figure 15. XPS elemental analysis of bulk MoS_2 (A) and (C) and IPL-MoS_2 (B) and (D) structures.

Muijsers et al conducted a sulfidation study on molybdenum oxide. The peak positions of S 2p for different intermediate compounds and the final MoS_2 structure after thermal decomposition has been assigned[68,69]. In the case of the IPL-MoS_2 sample, the S $2p_{3/2}$ peak at 163.5 eV can be attributed to bridging/apical S^{2-}. This indicates the existence of a small portion of intermediate complexes present in the IPL-MoS_2 sample. The area ratio of the lowest intensity

doublet to the highest intensity doublet is 0.3, which signifies that most of the precursor transformed to MoS_2 with minor amounts of intermediate complexes. The melting temperature of ammonium tetrathiomolybdate is approximately 155 °C, which is much lower than the temperature attained from the IPL process. This rapid thermal process might cause decomposition and sublimation of the sulfur and ammonium, which might create a large defect density in the film.

In addition, rapid heat treatment of the samples in milliseconds time scale might not fully reduce some of the sulfur atoms which can form bridging or terminal groups of MoS_2 structure. The IPL treated films still might have different forms of S atoms along with the S^{2-} basal plane.

Based on the preceding observations, and other observations reported in literature, we propose the following mechanism in Equation 24 for the conversion of tetrathiomolybdate to molybdenum disulfide[70].

$$MoS_4^{2-} + 2NH_4^+ \xrightarrow{\Delta} MoS_2 + H_2S + S + 2NH_3 \qquad \textit{Equation 24}$$

Electrochemical characterization was carried out on GCEs in a three-electrode cell. Dropcasting the precursor solution onto the GCE over rotation and then treating with IPL yields a rough IPL-MoS_2 film with thickness of approximately 20 μm (Figure 44). The diffusion length of a light pulse through a metal or semiconductor film has been shown to be on the order of hundreds of micrometers[61]. Therefore, local variations of film thickness should not significantly affect the conversion. Other factors affecting the conversion include number of pulses, energy density, and pulse duration[71]. Detailed mechanistic and

optimization studies on the IPL-assisted conversion of ammonium tetrathiomolybdate to IPL-MoS_2 are currently underway. All potentials have been iR compensated and calibrated versus RHE. A polarization plot comparing the activity of IPL-MoS_2 with other representative HER catalysts is depicted in Figure 16A. IPL-MoS_2 exhibits an onset overpotential for HER around 100 mV with an overpotential required to reach 10 mA cm^{-2} (a benchmark for solar water-splitting applications) of approximately 200 mV. IPL-MoS_2 shows similar activity on FTO-coated glass substrate (Figure 45). The low overpotential observed for IPL-MoS_2 is compared with overpotentials reported for other highly-active MoS_2 electrocatalysts in Table 1.

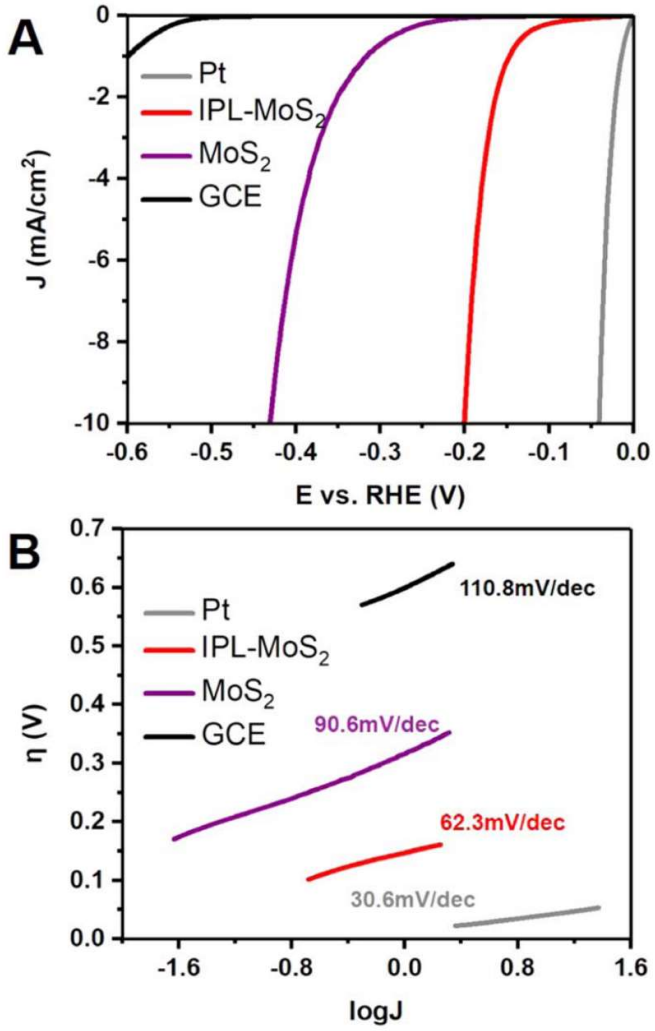

Figure 16. Electrochemical activity of the molybdenum sulfide catalyst following IPL treatment (IPL-MoS_2, red trace) in 0.5 M H_2SO_4. Included for comparison purposes are electrochemical activities of platinum metal (Pt, gray trace), bulk crystalline molybdenum sulfide (MoS_2, purple trace), and bare glassy carbon electrode (GCE, black trace) in 0.5 M H_2SO_4. The polarization plot (A) shows that the molybdenum sulfide catalyst exhibits high activity for HER, and the Tafel plot (B) compares kinetic attributes of various materials for HER.

Table 1

Comparison of HER overpotentials and Tafel slopes for IPL-MoS_2 and other reported molybdenum sulfide catalysts.

MoS_2 catalyst	Overpotential (mV) @ 10 mA cm^{-2}	Tafel slope (mV dec^{-1})
IPL-MoS_2 (this study)	200	62.3
Core-shell MoO_3-MoS_2 nanowires[72]	~250	50-60
MoS_2 NSs-550[73]	~200	68
Amorphous molybdenum sulfide[74]	200	60
1T-MoS_2[52]	187	43
Defect-rich MoS_2 nanosheets[75]	~150	50
MoS_2/RGO[76]	~150	41

The thermodynamics involved in the hydrogen evolution process for MoS_2 have previously been detailed extensively via density functional theory[50]. The active sites for hydrogen evolution in MoS_2 are the sulfur edges. At more positive potentials (>−80 mV versus RHE), proton coverage (number of protons bound to sulfur edges sites) is low and proton adsorption is thermodynamically downhill, but proton reduction is thermodynamically unfavorable due to the strength of S–H bonds. At more negative potentials (<−80 mV versus RHE), proton coverage is

higher, so both proton adsorption and proton reduction to yield H_2 are thermodynamically favorable. The −100 mV versus RHE onset of hydrogen evolution for IPL-MoS_2 is consistent with these calculations and suggests that IPL-MoS_2 effectively minimizes energetic and kinetic barriers for HER in contrast with bulk crystalline MoS_2 for which hydrogen evolution begins around −200 mV versus RHE.

HER kinetics can be expressed by the following three steps: the Volmer step (adsorption of proton onto the catalyst surface), the Heyrovsky step (combination of an adsorbed hydrogen with an electron and solution proton), or alternatively the Tafel step (combination of two adsorbed hydrogens). Combination of either the Volmer and Heyrovsky steps or the Volmer and Tafel steps yields H_2. Tafel slopes are used to give insights into the rate-limiting step for a given HER catalyst. However, determination of the HER mechanism from the Tafel slope alone is unfeasible as multiple mechanisms often occur simultaneously. Nevertheless, the significant difference between the Tafel slopes of IPL-MoS_2 and bulk crystalline MoS_2 (Figure 16) implies vastly different surface chemistry between the two materials with IPL-MoS_2 having faster reaction kinetics. The Tafel slope observed for IPL-MoS_2 is in line with Tafel slopes previously reported for other highly-active MoS_2 catalysts (~60mV dec^{-1})[72,74,77]. On other hand, the Tafel slope for bulk MoS_2 is around 90.6 mV dec^{-1}. These results indicate that the proton adsorption is the limiting step for the bulk MoS_2.

Included for comparison purposes in Figure 16 are the polarization curves and Tafel plots for platinum metal (Pt) and bare GCE substrate. Platinum, which is

currently regarded as the best HER catalyst, significantly outperforms both IPL-MoS_2 and bulk crystalline MoS_2 in terms of onset, overpotential, and Tafel slope. Although the performance gap between IPL-MoS_2 and Pt remains significant, IPL-MoS_2 represents significant progress when compared to bulk crystalline MoS_2.

In order to investigate the long-term durability of the IPL-MoS_2 material under reductive operating conditions, the material was cycled from 0.1 to −0.35 and back to 0.1 V versus RHE 1000 times. Throughout this extended cycling, an LSV was taken periodically in order to quantify the performance/degradation of the material at various points. Figure 17 compares polarization curves taken immediately after activation and after 1000 reductive cycles. The overpotential of the material increases by only 28 mV after 1000 cycles, implying high stability for HER in acidic media.

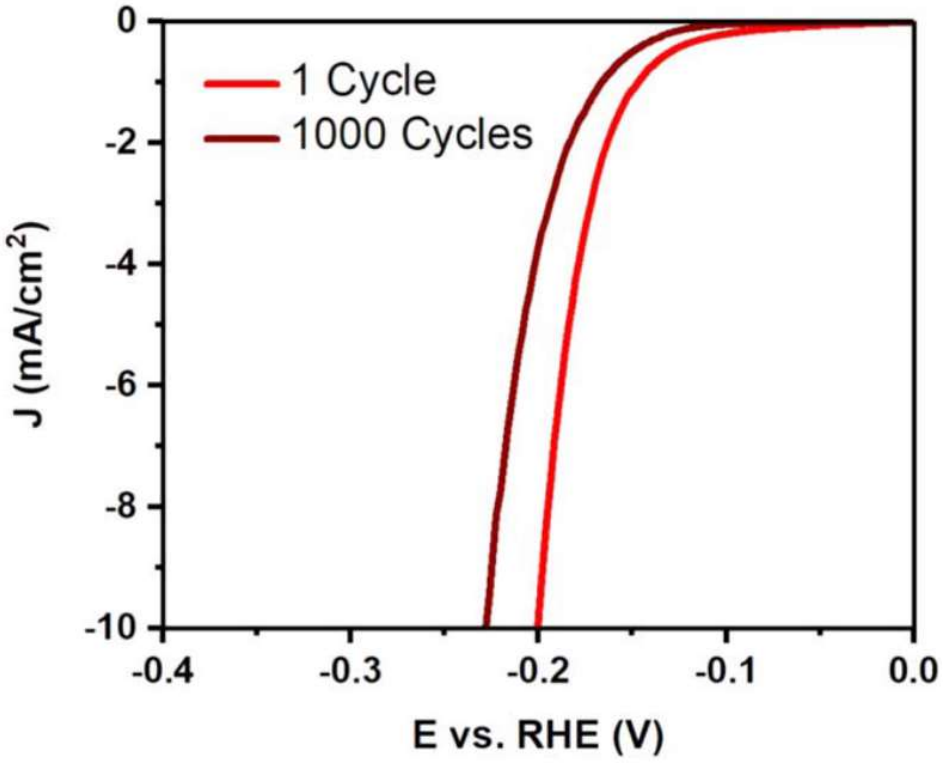

Figure 17. Polarization curves for IPL-MoS_2 after activation (1 Cycle, red trace) and after 1000 cycles at reductive potential (1000 cycles, brown trace).

3.4. CONCLUSIONS

In conclusion, we report an extremely rapid and benign way to prepare a class of MoS_2 catalysts using an IPL technique. The precursor can be readily converted to MoS_2 with short pulses of light in a few seconds. The conversion of the pre-cursor was demonstrated with XRD and Raman. TEM analysis confirmed that the IPL processed MoS_2 had multiple edge sites that would be beneficial to the HER reaction. A large amount of defect states presented by varying sulfur species at the defects was shown with XPS and confirms the mechanism of improved HER.

This presents a significant opportunity to prepare several classes of catalysts that are practically feasible and do not employ vacuum or hydrothermal techniques.

4. EFFECT OF STACKING INTERACTIONS ON THE TRANSLATION OF STRUCTURALLY RELATED BIS(THIOSEMICARBAZONATO)NICKEL(II) HER CATALYSTS TO MODIFIED ELECTRODE SURFACES

A series of crystalline nickel(II) complexes (**1** − **3**) based on inexpensive bis(thiosemicarbazone) ligands diacetylbis(4-methyl-3-thiosemicarbazone) (H2ATSM), diacetylbis(4,4-dimethyl-3-thiosemicarbazone) (H_2ATSDM), and diacetylbis[4-(2,2,2-trifluoroethyl)-3-thiosemicarbazone] (H_2ATSM-F_6) were synthesized and characterized by single-crystal X-ray diffraction and NMR, UV−visible, and Fourier transform infrared spectroscopies. Modified electrodes **GC-1** − **GC-3** were prepared with films of **1** − **3** deposited on glassy carbon and evaluated as potential hydrogen evolution reaction (HER) catalysts. HER studies in 0.5 M aqueous H_2SO_4 (10 mA cm^{-2}) revealed dramatic shifts in the overpotential from 0.740 to 0.450 V after extended cycling for **1** and **2**. The charge-transfer resistances for **GC-1** − **GC-3** were determined to be 270, 160, and 630 Ω, respectively. Characterization of the modified surfaces for **GC-1** and **GC-2** by scanning electron microscopy and Raman spectroscopy revealed

Alexander J. Gupta,[†,§] Nicholas S. Vishnosky,[‡,§] Oleksandr Hietsoi,[‡] Yaroslav Losovyj,[⊥] Jacob Strain,[‡] Joshua Spurgeon,[∥] Mark S. Mashuta,[‡] Rahul Jain,[‡] Robert M. Buchanan,[‡] Gautam Gupta,[*,†] and Craig A. Grapperhaus[*,‡]

[†]Department of Chemical Engineering, [‡]Department of Chemistry, [∥]Conn Center for Renewable Energy Research, University of Louisville, Louisville, Kentucky 40292, United States

[⊥]Department of Chemistry, Indiana University - Bloomington, Bloomington, Indiana 47405, United States

This research was supported, in part, by National Science Foundation Grants CHE-1665136 (to C.A.G.) and CHE- 1800245 (to G.G. and R.M.B.). M.S.M. thanks the Department of Energy (Grant DEFG02-08CH11538) and the Kentucky Research Challenge Trust Fund for an upgrade of our X-ray facilities.

similar crystalline coatings before HER that changed to surface-modified crystallites after conditioning (Figure 18). The surface of **GC-3** had an initial glasslike appearance before HER that delaminated after HER. The differences in the surface morphology and the effect of conditioning are correlated with crystal-packing effects. Complexes **1** and **2** pack as columns of interacting complexes in the crystallographic a direction with short interplanar spacings between 3.37 and 3.54 Å. Complex **3** packs as columns of isolated molecules in the crystallographic b direction with long-range interplanar spacings of 9.40 Å.

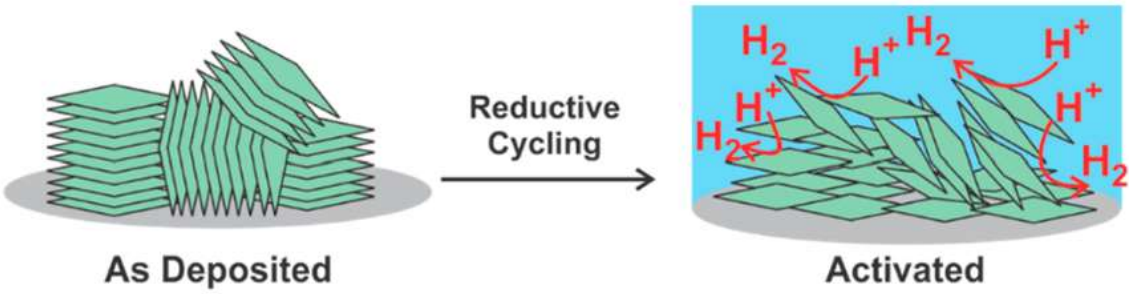

Figure 18. Effect of reductive cycling on morphology of catalyst films.

4.1. INTRODUCTION

Increasing worldwide demand for cheap energy has fueled the need to develop sustainable alternative energy sources[79]. Hydrogen offers great potential as a carbon-free alternative to fossil fuels[80]. One of the major challenges in this area is the development of artificial water-splitting catalysts based on solid-state materials and molecular electrocatalysts that efficiently produce O_2 and H_2 from water utilizing either solar energy[81–84] or electrolysis[42,85]. Platinum is the “gold standard” catalyst for H_2 production via the hydrogen evolution reaction (HER) in

aqueous acidic solutions. However, its practical widespread utility in electrocatalytic devices is limited by its scarcity and high cost[86,87]. This has stimulated the development of new electrocatalysts containing earth-abundant transition metals, such as iron[88], cobalt[89], nickel[90], copper[91], and molybdenum[76,92,93], as metal phosphides[89,94], selenides[95], sulfides[96,97], and small-molecule complexes[98–104]. Of these materials, molybdenum sulfides stand out as an economical alternative to platinum[77,105,106]. Their high activity is thought to arise from the location and number of cis-sulfur edge sites in their layered structures[77]. Moreover, Schaak and co-workers reported inexpensive and nonnoble nickel phosphide[94] and iron phosphide[107] nanoparticles that are highly effective for HER. Nickel−molybdenum nitride nanosheets have also demonstrated effectiveness in catalyzing HER[108].

There is consensus that most homogeneous molecular electrocatalysts generate reactive metal hydride intermediates during HER[98,109–112]. Several of these electrocatalysts display low overpotential, high turnover frequencies, and faradaic efficiencies in excess of 90%[112,113]. Noncovalent modification of electrode surfaces with catalysts has been studied for various applications[114–117]. There is an emerging interest in the modification of electrode surfaces with small-molecule HER catalysts[118–124]. Most notably, Fontecave and co-workers developed multiwalled carbon nanotube [Ni($P^{Ph}_2N^{Ph}_2$)$_2$] modified electrodes that display high catalytic activity at low overpotential[125]. We reported the translation of activity and mechanism of a rhenium thiolate HER catalyst from solution to modified electrodes[126]. Other examples of heterogeneous molecular catalysts for

HER include Co complexes of (dmgBF2)2 with carbon black on Nafion-coated glassy carbon[119] and cobaloxime-modified electrodes[119,120] as well as cobalt porphyrin[121,122,127], metal phthalocyanine[128–131], and an organometallic complex incorporated in a Nafion film[132]. However, these complexes either require high overpotentials and/or are unstable over prolonged electrolysis, reducing their practical use as HER catalysts.

The instability of surface-adsorbed electrocatalysts has been of concern since the observation that some cobalt[133–135] and nickel[136,137] complexes decompose to metal-containing nano- particles during HER. Studies by Dempsey and co-workers[138,139] and Wombwell and Reisner[140] highlight the importance of ligand design in catalyst preparation. These studies evaluated the stability of imine- and thiolate-containing chelates during HER and showed that Ni−S and ligand C=N bonds may be susceptible to hydrogenation, leading to catalyst degradation and electrodeposition of metal-based nanoparticles.

Recently, we, and others, have explored the use of thiosemicarbazone ligands in the design of new HER electrocatalysts. The thiosemicarbazone ligands are redox-noninnocent and can function as a reservoir for charge with hydrogen evolution at either the metal or ligand. The HER mechanism proceeds via ligand-assisted metal-centered[141], ligand-centered[142–144], or metal-assisted ligand-centered reactivity depending on the identity of the metal[103,143,145]. Herein, we report the synthesis, characterization, and electrocatalytic behavior of a series of structurally related bis-(thiosemicarbazonato)nickel(II) complexes (Figure 19) deposited on glassy carbon electrode (GCE) surfaces. The ligands are obtained

in high yields using readily available and inexpensive organic reagents according to literature methods[146,147]. The resulting nickel(II) complexes have been characterized by NMR, Fourier transform infrared (FT-IR), and UV−visible spectroscopies, X-ray crystallography, and cyclic voltammetry in acetonitrile prior to deposition on GCEs. Drop-casting acetonitrile inks of the nickel complexes on GCEs produce uniform coatings that were characterized by spectroscopy and microscopy methods before and after HER catalysis in aqueous acidic solutions.

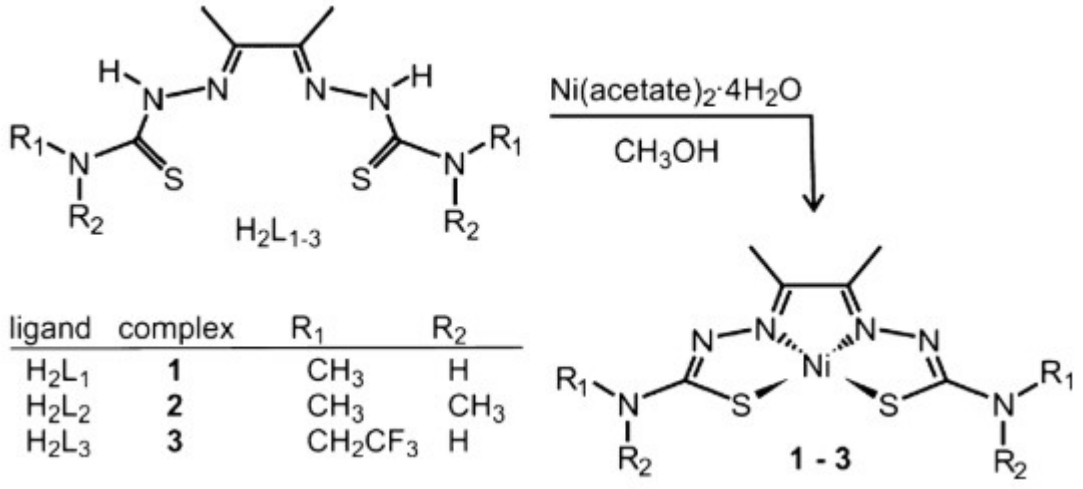

Figure 19. Synthesis and Labeling Scheme of Complexes **1 – 3**

4.2. METHODS

4.2.1. MATERIALS AND REAGENTS

All reagents and solvents were purchased from commercial sources and used as received unless otherwise indicated. Reactions were conducted open to air and under ambient conditions unless otherwise noted. Ni(ATSM)[146], H_2ATSDM[147], and H_2ATSM-F_6[147] were synthesized according to literature methods. Crystal

planarity analysis was done using PLATON[148]. All complexes were recrystallized via the evaporation of acetonitrile prior to dropcasting.

4.2.1.1. DIACETYLBIS(4,4-DIMETHYL-3-THIOSEMICARBAZONATO)NICKEL(II) (**2**)

The ligand H_2ATSDM (0.28 g, 0.96 mmol) was suspended in methanol (25 mL). To this suspension was added with stirring nickel(II) acetate tetrahydrate (0.25g, 1.0 mmol), immediately giving a color change to a dark-green-brown precipitate. This was stirred at reflux for 4 h. The suspension was allowed to cool to room temperature and then stored in a freezer overnight. The chilled suspension was then filtered cold and washed with water and ethanol, giving a red-brown solid. Yield: 0.29 g (88%). X-ray-quality crystals were obtained by dissolving Ni(ATSDM) in acetonitrile, which was then layered with ether and allowed to slowly evaporate. ^{1}H NMR (C_2D_6SO, 400 MHz): δ 1.87 (s, 3H) 3.10 (s, 6H). IR (cm^{-1}): 2910 (w) and 1501 (s) (CH), 1366 (vs) and 1082 (m) (C−N), 1322 (vs) and 1258 (s) (C=N), 1006 (w) (CS), 900 (m) (NiS), 783 (w) (NiN). Elem anal. Calcd for $C_{10}H_{18}N_6S_2Ni$: C, 34.80; H, 5.26; N, 24.35. Found: C, 34.57; H, 5.20; N, 24.12. MS. Calcd for $C_{10}H_{18}N_6S_2Ni$: m/z 344.03878. Found: m/z 343.80 (M^+), 344.80 ($M + H^+$). UV−visible [acetonitrile; λ_{max}, nm (ε, M^{-1} cm^{-1})]: 256 (23000), 411 (11000), 436 (11000).

4.2.1.2. DIACETYLBIS(4-2,2,2-TRIFLUOROETHYL)-3-THIOSEMICARBAZONATO)-NICKEL(II) (**3**)

The ligand H_2ATSM-F_6 (0.19 g, 0.48 mmol) was suspended in methanol (20 mL). To this suspension was added with stirring nickel(II) acetate tetrahydrate (0.15,

0.60 mmol), immediately giving a color change to a red-brown precipitate. This was stirred at reflux for 4 h. The suspension was allowed to cool to room temperature and then stored in a freezer overnight. The chilled suspension was then filtered cold and washed with water and ethanol, giving a red-brown solid. Yield: 0.0087 g (40%). X-ray-quality crystals were obtained by dissolving Ni(ATSM-F_6) in acetonitrile, which was then layered with ether and allowed to slowly evaporate. ^{1}H NMR (C_2D_6SO, 400 MHz): δ 1.94 (s, 3H) 4.00 (br, 2H) 8.29 (s, 1H). ^{13}C NMR: δ 178.1, 158.8, 124.9 (q, J = 280 Hz), 46.3 (q, J = 33 Hz) 14.4. IR (cm^{-1}): 3462 (m) (NH), 1514 (s) and 1476 (s) (CH), 1271 (s) and 1218 (m) (CN), 1138 (vs) (CF), 941 (w) (NiS), 832 (w) (NiN). Elem anal. Calcd for $C_{10}H_{12}N_6S_2F_6Ni$: C, 26.51; H, 2.67; N, 18.55; F, 25.16. Found: C, 26.36; H, 2.59; N, 18.29; F, 25.10. MS. Calcd for $C_{10}H_{18}N_6S_2Ni$: m/z 451.9822. Found: m/z 452.87 (M + H+). UV−visible [acetonitrile; λ_{max}, nm (ε, M^{-1} cm^{-1})]: 259 (24000), 328 (8200), 392 (9100).

4.2.2. HOMOGENEOUS ELECTROCHEMICAL CHARACTERIZATION

Electrochemical data were collected using a Gamry Interface 1000E potentiostat/galvanostat/ZRA. Complexes were dissolved in acetonitrile (1 mM) under air-free conditions in a standard three-electrode cell with 0.1 M TBAHFP as the supporting electrolyte. Glassy carbon was used as the working electrode with a platinum disk counter electrode and a silver wire pseudo reference electrode. Measured potentials were corrected for uncompensated resistance using the current-interrupt function. A small quantity of ferrocene was added as

an internal standard, and all potentials are referenced versus Fc^+/Fc (ΔE = 63 mV at a scan rate of 50 mV s^{-1}).

4.2.3. CRYSTALLOGRAPHIC STUDIES

An orange prism 0.40 × 0.34 × 0.18 mm^3 crystal of **2** grown from a solution of acetonitrile and diethyl ether was mounted onto a glass fiber for collection of the X-ray data on an Agilent Technologies/Oxford Diffraction Gemini CCD diffractometer. The CrysAlisPro[149] CCD software package (version 1.171.36.32) was used to acquire a total of 1026 20-s frame ω-scan exposures of data at 100 K to a $2\theta_{max}$ = 63.14° using monochromated Mo Kα radiation (0.71073 Å) from a sealed tube. Frame data were processed using CrysAlisPro[149] RED to determine the final unit cell parameters: a = 7.33437(16) Å, b = 8.5595(2) Å, c = 11.6784(3) Å, α = 103.865(2)°, β = 98.2102(19)°, γ = 91.7205(18)°, V = 702.92(3) Å3, D_{calc} = 1.631 Mg m^{-3}, and Z = 2 to produce raw hkl data that were then corrected for absorption (transmission min/max = 0.778/1.000; μ = 1.672 mm^{-1}) using SCALE3 ABSPACK[150]. The structure was solved by direct methods in the space group $P\bar{1}$ using SHELXS[151] and refined by least-squares methods on F^2 using SHELXL[151]. Non-hydrogen atoms were refined with anisotropic atomic displacement parameters. Hydrogen atoms were located by difference maps and refined isotropically. For all 4702 unique reflections [R(int) = 0.021], the final anisotropic full-matrix least-squares refinement on F^2 for 244 variables converged at R1 = 0.021 and wR2 = 0.055 with a goodness of fit (GOF) of 1.01.

Crystals of **3** suitable for X-ray analysis were grown from an acetonitrile and diethyl ether solution and mounted on a cryoloop for collection of the X-ray data

on an Agilent Technologies/Oxford Diffraction Gemini CCD diffractometer. X-ray structural analysis for **3** was performed on a 0.41 × 0.08 × 0.01 mm^3 red-brown plate using a 596-frame, 60-s frame ω-scan data collection strategy at 100 K to $2\theta_{max}$ = 53.20°. Complex **3** crystallized in the triclinic space group $P\bar{1}$ with the following unit cell parameters: a = 8.3598(10) Å, b = 9.4027(10) Å, c = 13.5112(17) Å, α = 109.467(10)°, β = 105.475(11)°, γ = 91.382(9)°, V = 957.53(19) Å3, Z = 2, and D_{calc} = 1.571 Mg m^{-3}. A total of 4447 independent data were corrected for absorption (transmission min/max = 0.678/1.000; μ = 1.291 mm^{-1}). The structure was solved by direct methods using SHELX[151]. All non-hydrogen atoms were refined with anisotropic atomic displacement parameters. Imine NH hydrogen atoms were located by difference maps and refined isotropically. Methyl hydrogen atoms were placed in their geometrically generated positions and refined as a riding model, and these atoms were assigned as U(H) = $1.5U_{eq}$. For reflections I > 2σ(I)[R(int) = 0.058], the final anisotropic full-matrix least-squares refinement on F^2 for 288 variables converged at R1 = 0.065 and wR2 = 0.119 with a GOF of 1.07.

4.2.4. HETEREOGENEOUS ELECTROCHEMICAL CHARACTERIZATION

A 4 mg sample of a given complex was dispersed in 1 mL of acetonitrile (VWR, ACS grade, dried using an MB-SPS from MBRAUN) using a vortex mixer (Vortex Genie 2, Scientific Industries). A 12.5 μL aliquot of a 10% aqueous Nafion solution was added to the resulting ink. The dispersion was further homogenized via ultrasonication (Cole-Parmer ultrasonic bath) for 2 h. After sonication, 10 μL of the resulting dispersion was dropped onto a GCE (E4TQ ChangeDisk, Pine

Research), rotating at 50 rpm, affixed to a rotator (MSR Rotator, Pine Research). The rotation speed was subsequently increased to 300 rpm, and this speed was maintained until the film was dried.

Evaluation of the materials' activities for HER was carried out in a three-electrode glass electrochemical cell (RDE/RRDE Cell Without Water Jacket, Pine Research) with 0.5 M H_2SO_4 (VWR, ACS grade) in twice-deionized Millipore water (18.2 Ω cm). A graphite rod (Pine Research), in a protective fritted glass tube (Pine Research), was used as the counter electrode. Ag/AgCl (1 M KCl, CH Instruments) was used as the reference electrode. Measured potentials were calibrated versus RHE after experiments were conducted (to prevent platinum contamination) by measuring the potential difference between a pristine platinum electrode (Standard Platinum Counter Electrode, Pine Research) and the reference electrode in H_2-saturated H_2SO_4. High-purity H_2 and N_2 gases used throughout these experiments were provided by Welders Supply, Louisville, KY.

A Metrohm Autolab PGSTAT302N potentiostat/galvanostat, operating in potentiostat mode, was used to obtain polarization and frequency response analysis (FRA) data. Reductive cycling to activate the catalyst and evaluate its stability was carried out between 0 and −0.8 V versus RHE at 50 mV s^{-1}. LSV was carried out intermittently throughout the cycling process, from 0 to −0.8 V versus RHE at 2 mV s^{-1}, to evaluate the activity of the catalyst, at a relatively high resolution, after various amounts of usage at reductive potentials. FRA data were collected with an applied direct-current bias of −0.3 V versus RHE, starting at 100 kHz and finishing at 0.02 Hz, with 5 mV_{RMS} amplitude. The working

electrode was rotated at 800 rpm throughout electrochemical characterization to assist the diffusion of H_2 gas away from the catalyst surface. Measured values were iR-compensated by multiplying the measured current at each point by the real component of resistance measured at 100 kHz and then subtracting these values from the corresponding applied potentials.

For determination of the electrochemical surface area, cyclic voltammetry was conducted over the potential range of 0.15−0.35 V versus RHE, where no faradaic processes were observed to occur. Six scan rates were used: 10, 20, 40, 80, 160, and 320 mV s^{-1}. At each vertex (0.15 or 0.35 V vs RHE), a constant potential was maintained for 30 s to allow time for the system to reach a steady state. Three scans were taken for each scan rate, and the measured currents were averaged. The average current at 0.3 V versus RHE during the anodic sweep was plotted as a function of the scan rate. The slope of this curve gives the approximate capacitance of the electrode per geometric surface area. To determine relative electrochemical surface areas, these values were compared to the value obtained for a bare GCE. Ferricyanide redox experiments were carried out in a 0.1 M potassium nitrate and 5 mM potassium ferricyanide solution. The potential was cycled from 0.4 to 1.2 V versus RHE at varying scan rates. Data were taken for each scan rate in triplicate, and measured currents were averaged together. The potential was held at each vertex for 30 s.

For determination of the faradaic efficiencies, produced H_2 gas was measured by gas chromatography (GC; SRI 6810) via online automatic injection (1 mL sample) and a thermal conductivity detector. Nitrogen (99.99%, Specialty Gases)

was used as the carrier gas to enable accurate H_2 quantification. The gas was injected every 15 min, and each measured value for the faradaic efficiency was representative of the past 15 min of electrolysis. In the bulk electrolysis cell itself, nitrogen was diffused into the electrolyte at 10 sccm regulated by a mass flow controller (MKS Instruments, Inc.). The potentiostat was operated in galvanostatic mode at a constant current density of 10 mA cm^{-2} during faradaic efficiency measurements. The electrochemical cell was set up identically as described for all other heterogeneous electrochemical experiments except the joints were sealed with vacuum grease and an air outlet line was run from the cell to the GC apparatus. In order to maintain an airtight seal, the GCE was not rotated. Instead, a magnetic stirrer was rotated at 360 rpm underneath the GCE to remove H_2 bubbles from the electrode surface. Theoretical H_2 was determined by counting the coulombs of charge that passed, and measured H_2 was determined via GC. The faradaic efficiencies were determined by comparing these values.

4.2.5. XPS

The XPS experiments were carried out using a PHI VersaProbe II instrument equipped with a focused monochromatic Al Kα source. The instrument base pressure was ca. 8 × 10−10 Torr. An X-ray power of 25 W at 15 kV was used for the XPS spectral acquisition mode with a 100 μm beam size at an X-ray incidence and takeoff angle of 45°. Calibration of the instrument work function was set to give a BE of 84.0 eV for the Au $4f_{7/2}$ line for metallic gold. The spectrometer dispersion was adjusted to give BEs of 284.8, 932.7, and 368.3 eV

for the C 1s line of adventitious (aliphatic) carbon presented on the nonsputtered sample, Cu $2p_{3/2}$ and Ag $3d_{5/2}$, photoemission lines, respectively. The PHI dual-charge neutralization system was used on all samples. The high-resolution Ni 2p, N 1s, O 1s, C 1s, and S 2p spectra were taken with a minimum of 10−60 s scans using 0.1 eV steps and 93.9, 46.95, 23.5, and 93.9 eV pass energy, respectively. MultiPak version 9.3.0.3, PHI software was used for signal above background measurement and Shirley background subtraction. At the ultimate PHI Versa Probe II instrumental resolution, the temperature spread (at 14/86%) of the metallic silver Fermi edge was less than 120 meV. All XPS spectra were recorded using the PHI software SmartSoft−VP Version 2.6.3.4, and processed using MultiPak Version 9.3.0.3, and/or CasaXPS, version 2.3.14. The relative sensitivity factors from the MultiPack library were used to determine atomic percentages. Peaks were fitted using GL line shapes, a combination of Gaussians and Lorentzians. A given sample was examined at five or six different spots on the mounted specimen to ensure that consistent, reproducible results were obtained. Elemental mapping of the 1000 × 700 and 200 × 100 μm areas was acquired with a FAT analyzer mode using 0.2 eV steps and 187.85 eV pass energy. X-ray beam sizes of 35 and 9 μm were used for the 1000 × 700 and 200 × 100 μm areas, respectively. The last image was constructed of 133 × 66 pixels.

4.2.6. OTHER CHARACTERIZATION

SEM was carried out using a TESCAN VEGA3 microscope operating at 10 kV and 10 mA. Images of the catalyst materials were taken using the ejectable GCE disk tip as the substrate. As above, catalyst dispersion was dropped onto the

GCE and allowed to dry over rotation. At this point, either the disk was ejected and taken to the SEM or the material was cycled to peak activity (as described above) before disk ejection and characterization. EDS characterization was carried out concurrently with SEM studies using an energy-dispersive X-ray analysis system attached to the electron microscope. EDS studies were done at 20 kV with a 50 nm spot size on the deposited film. The beam current was increased until the detector registered approximately 1000 counts s^{-1}. Consistent spectra were obtained for various spots.

Raman spectra from 100 to 3200 cm^{-1} were collected with a Reva Educational Raman spectrometer (Hellma USA, Inc., Plainview, NY). Samples were excited with a 450 mW collimated laser beam at 785 nm, and spectra were obtained by averaging 10 scans with a 400 ms integration time per scan. Electrode samples were prepared for Raman, as described for SEM. Acetonitrile inks with complex **2** and Nafion were evaluated as-prepared using the probe Raman spectrometer. Acetonitrile and glassy carbon were each directly measured using the probe Raman spectrometer. A modified electrode with Nafion was prepared by dropcasting 10 μL of an acetonitrile solution with the same Nafion content as that described for the catalytic inks but without a complex onto a GCE.

UV−visible spectroscopy was carried out using an Agilent Technologies Cary 60 UV−visible spectrometer. Standard solutions of **2** were prepared via serial dilution from the original 4 mg mL^{-1} acetonitrile ink with Nafion and used to construct a calibration curve. The peak at 260 nm was chosen for quantification because it was the most intense. **GC-2** was conditioned to peak activity (200

cycles) in sulfuric acid as previously described, washed thoroughly with deionized water, and immersed in 3 mL of acetonitrile for 30 s over rotation at 800 rpm. The resulting yellow acetonitrile solution was evaluated via UV−visible, and its absorbance was used to interpolate the solution concentration based upon the calibration curve.

4.3. RESULTS AND DISCUSSION

4.3.1. SYNTHESIS AND CHARACTERIZATION

The ligands diacetylbis(4-methyl-3-thiosemicarbazone) (H_2ATSM)[146], diacetylbis(4,4-dimethyl-3-thiosemicarbazone) (H_2ATSDM)[147], and diacetylbis[4-(2,2,2-trifluoroethyl)-3-thiosemicarbazone] (H_2ATSM-F_6)[147] were prepared as previously reported. The nickel(II) complexes **1−3** were synthesized using the methodology established for the preparation of **1**[146] (Figure 19). The newly reported **2** and **3** were characterized by elemental analysis, cyclic voltammetry, mass spectrometry, NMR, FT-IR, and UV−visible spectroscopies, and X-ray crystallography. The ^{1}H NMR spectra of **2** and **3** (Figure 46 and Figure 47) are consistent with their proposed structures. The IR spectra (Figure 48 and Figure 49) show shifts of ν_{C-N} stretches relative to the free ligand associated with nickel(II) coordination. All of the complexes are green in color upon dissolution in acetonitrile. The ligand-to-ligand charge-transfer transitions[146] in the UV−visible spectrum slightly increase in energy from **2** to **1** to **3** (Figure 50).

The solid-state structures of **2** and **3** were determined by single-crystal X-ray diffraction for comparison with the known structure of **1**[152]. Crystals of **2** and **3** were obtained as orange prisms and red-brown plates, respectively, via slow

evaporation of an acetonitrile solution layered with ether. Crystallographic data and structure refinement details are listed in Table 3. The crystal lattices of **1** and **3** include an acetonitrile solvate molecule, while the lattice of **2** is not solvated.

The ORTEP[153] representations of **2** and **3** in Figure 20, top and bottom, respectively, show that each contains a square-planar nickel(II) in an N_2S_2 donor environment. Selected bond distances and angles for **1−3** are provided in Table 4. The Ni−N distances are statistically equivalent over the series with an average value of 1.856(5) Å. Further, there are no significant differences in the Ni−S bond distances, which have an average value of 2.1568(18) Å. The similarities in the metric parameters are also observed in the bond distances within the ligand framework. For all three nickel complexes, the bond distances are consistent with a conjugated π system of alternating single and double bonds[154]. Comprehensive lists of bond distances and angles can be found in Table 5 and Table 6.

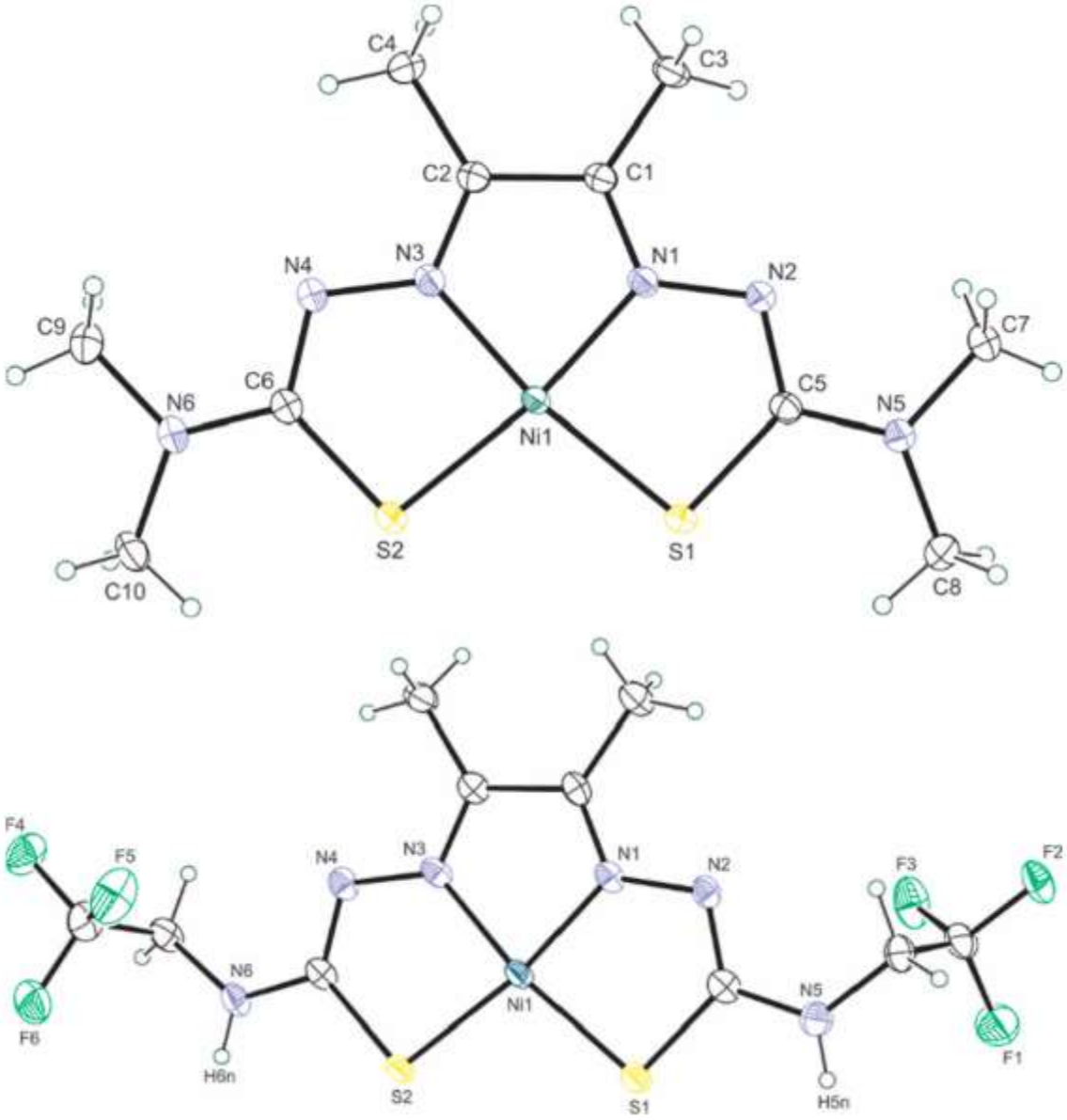

Figure 20. ORTEP[153] views (50% probability) of **2** (top) and **3** (bottom) showing atom labeling for non-hydrogen atoms in the asymmetric unit.

Overall, the structures of **1−3** are best described as square-planar. Both **1** and **2** are rigorously planar with all non- hydrogen atoms in or near the best-fit plane. For **1**, the best-fit plane of all 17 non-hydrogen atoms has a standard deviation of

±0.032 Å, with the largest deviation of ±0.067 Å for S2. Similarly, in **2**, the standard deviation from the best-fit plane of all 19 non-hydrogen atoms is ±0.053 Å, with the largest deviation of ±0.126 Å for C3. The pendant $-CH_2CF_3$ groups of **3** disrupt the overall planarity of that molecule. However, except for the $-CF_3$ moieties, the non-hydrogen atoms define a plane with a standard deviation of ±0.033 Å, with the largest deviation of ±0.083 Å for S2. The $-CF_3$ carbon atom C8 sits 1.46 Å above the best-fit plane for **3**, whereas C10 lies 1.43 Å below the plane.

The crystal-packing arrangements for the rigorously planar **1** and **2** display similar columns of paired complexes stacked along the *a* axes (Figure 21, top and middle, respectively). The bulkier $-CH_2CF_3$ groups in **3** preclude complex pairing, resulting in long-range stacking along the *b* axis (Figure 21, bottom). For **1**, the "inverse pair" of complexes containing Ni (*x*, *y*, *z*) and Ni′ (1 − *x*,1 − *y*,1 − *z*) stack with an interplanar distance of 3.48 Å. These inverse pairs form a column of complexes generated by translation along the *a* axis. The interplanar distance between Ni′ (*x*, *y*, *z*) and Ni″ (1 + *x*, *y*, *z*) is 3.47 Å. Neighboring columns, with equivalent spacings, are generated by the 2_1 screw axis (Ni‴) and *c* glide (Niⁱᵛ) associated with the space group $P2_1/c$. Complex **2**, which crystallizes in the space group $P\bar{1}$, displays similar columns generated by translation of the inverse pair Ni (*x*, *y*, *z*) and Ni′ (1 − *x*, 1 − *y*, 1 − *z*) along the *a* axis with interplanar distances of 3.54 and 3.37 Å for Ni/Ni′ and Ni′/Ni″, respectively. The crystal packing of **3** is unique because the bulkier $-CH_2CF_3$ groups prevent stacking of inverse pairs. As shown in Figure 21, Ni (*x*, *y*, *z*) and Ni′ (1 − *x*, 1 − *y*, 1 − *z*) are

contained in separate, neighboring columns directed along the *b* axis. In contrast to **1** and **2**, the interplanar distances for the columns of **3** are long, 9.40 Å, because each member of the column is generated by a translation in the *b* direction.

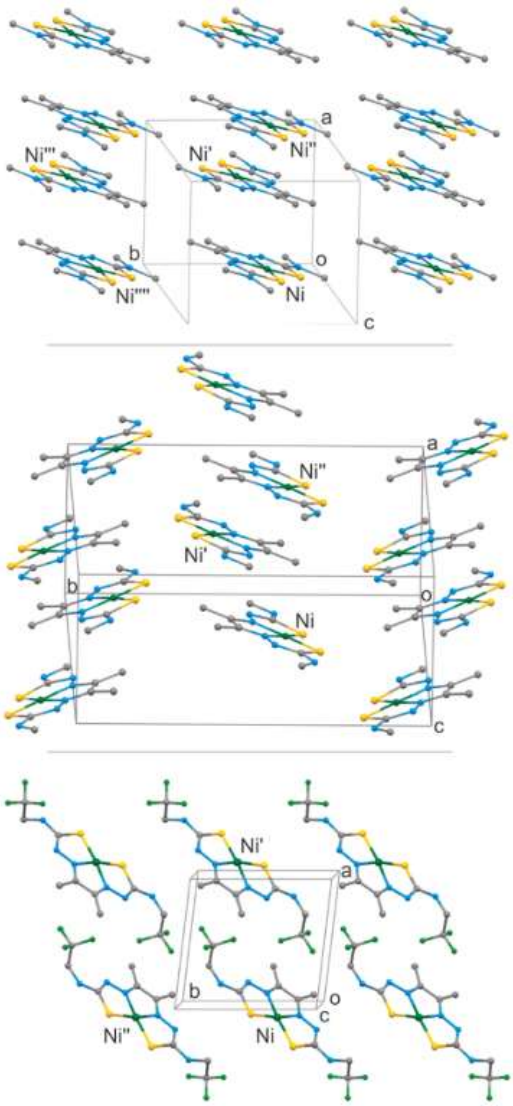

Figure 21. Packing diagrams for **1** (top), **2** (middle), and **3** (bottom). Individual labels are associated with the following symmetry operations: Ni, E (*x, y, z*); Ni′, i

(1 − *x*, 1 − *y*, 1 − *z*), Ni″, translation along *a* (1 + *x*, *y*, *z*) for **1** and **2** or along *b* (*x*, 1+ *y*, *z*) for 3; Ni‴, 2_1 (1 − *x*, 0.5 + *y*, 1.5 − *z*); Ni⁗, *c* glide (*x*, 1.5 − *y,* 0.5 + *z*).

4.3.2. HOMOGENEOUS ELECTROCHEMICAL CHARACTERIZATION

Cyclic voltammograms of **1−3** (Figure 22) show two reversible events at potentials more cathodic than −1.3 V versus ferrocenium/ferrocene (Fc^+/Fc) in acetonitrile containing 0.1 M tetrabutylammonium hexafluorophosphate (TBAHFP) as the supporting electrolyte. The more anodic event is assigned to a ligand-centered reduction, and the more cathodic event is assigned to the nickel(II/I) redox couple (Table 2). The locations of these reductive events were previously established by density functional theory calculations by our laboratory[155] and others[98]. The ligand- and metal-centered $E_{1/2}$ values for **1** occur at −1.73 and −2.31 V versus Fc^+/Fc, respectively. The pendant secondary amines of **1** are replaced with tertiary amines in **2**, resulting in an ∼30 mV cathodic shift in the ligand-centered reduction potential, −1.76 V. This is similar to the corresponding 20 mV shift observed for the related copper derivative of **2** relative to the related copper derivative of **1**[156]. The nickel(II/I) event of **2** does not shift significantly compared to that of **1**. The $-CH_2CF_3$ functionalities of **3** result in a 160 mV anodic shift of the ligand-centered event to −1.57 V. The nickel(II/I) couple of **3** is similarly shifted to −2.19 V. The magnitude of the shift is in good agreement with Que and co-workers' copper derivatives, which displayed a ∼70 mV anodic shift per $-CF_3$ group compared to CuATSM.

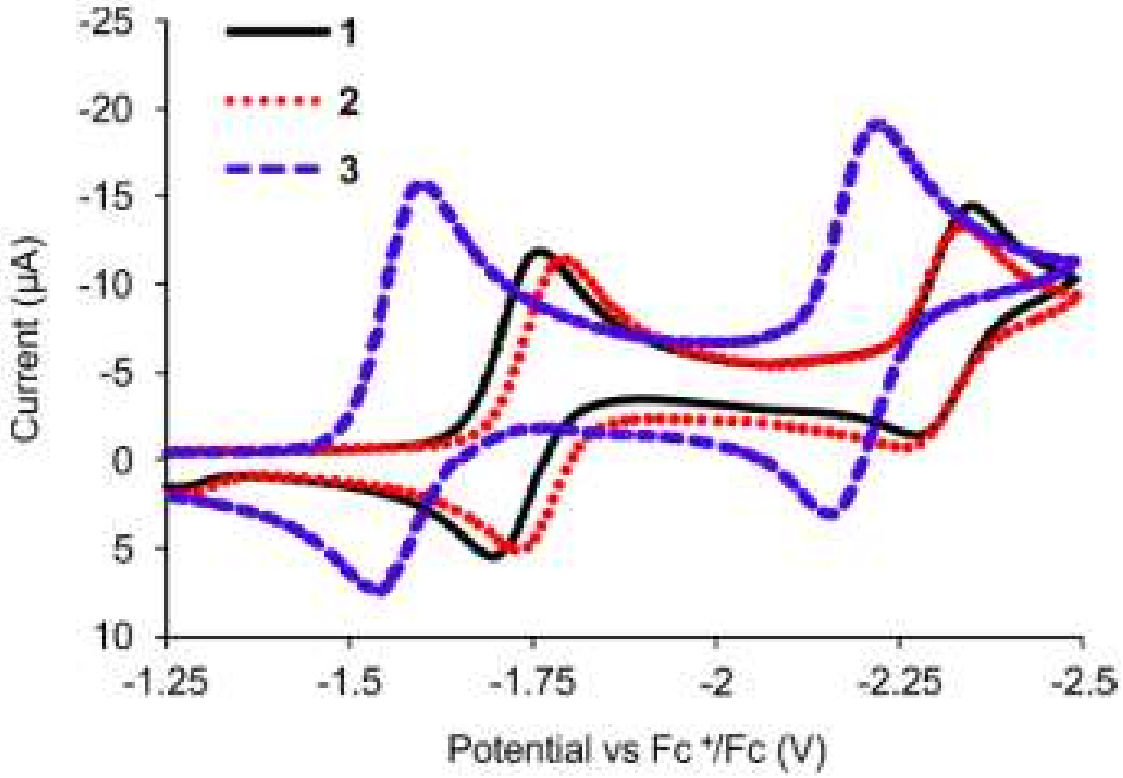

Figure 22. Cyclic voltammograms of **1** (black trace), **2** (red trace), and **3** (blue trace) in acetonitrile at 1 mM concentration with 0.1 M TBAHFP as the supporting electrolyte. Scan rate = 50 mV s^{-1}; potentials referenced versus Fc^{+}/Fc.

Table 2

Reduction Potentials versus Fc+/Fc and Peak Separation for **1−3** in Acetonitrile Containing 0.1 M TBAHFP as the Supporting Electrolyte

	$E_{1/2}$, V (ΔE, mV)	
complex	L/L^-	nickel(II/I)
1	−1.73 (64)	−2.31 (78)
2	−1.76 (62)	−2.30 (73)
3	−1.57 (59)	−2.19 (64)

Previously, our laboratory reported the homogeneous HER catalysis of **1**[155]. Under increasing additions of acetic acid in acetonitrile, there was a measurable and stable increase in the catalytic current at −2.35 V versus Fc^+/Fc. This current eventually plateaued, indicating acid saturation. The evolution of hydrogen was confirmed via bulk electrolysis. Overall, as a homogeneous HER catalyst in acetonitrile with acetic acid additions, **1** performed at an overpotential of 0.53 V with turnover frequency and faradaic efficiency values of 4200 s^{-1} and 87%, respectively. The proposed mechanism is a ligand-assisted metal-centered process in which the first reduction occurs on the ligand, followed by protonation on the ligand hydrazino nitrogen atom. Straistari et al. evaluated the *p*-anisole/NiATSM complex for homogeneous HER catalysis, further proving the viability of nickel bis(thiosemicarbazone) complexes for HER catalysis[98]. The bis(thiosemicarbazone) ligand class and metal chelates have been well established for their HER activity[99,102,142].

4.3.3. HER ACTIVITY OF MODIFIED ELECTRODES

Modified electrodes **GC-1−GC-3** were prepared by mixing 4 mg of **1**, **2**, or **3** with 1 mL of acetonitrile and 12.5 μL of a 10% aqueous Nafion solution. The resulting suspension was homogenized via ultrasonication, and 10 μL of the suspension was then dropped onto the surface of a GCE. The suspension was allowed to dry on the electrode over rotation at approximately 300 rpm. The freshly prepared modified electrodes required high over- potentials of ∼700−750 mV to reach a current density of 10 mA cm^{-2} (the metric for comparing catalysts for water-splitting applications[157,158]) upon immersion in 0.5 M H_2SO_4, indicating poor initial catalytic activity.

The modified electrodes were then conditioned by reductive cycling. The potential was swept between 0 and −0.8 V versus reversible hydrogen electrode (RHE) at 50 mV s^{-1}; electrochemical impedance spectroscopy (EIS) and linear-sweep voltammetry (LSV) at 1 mV s^{-1} over the same potential range were done prior to any cycling and every 100 cycles thereafter to accurately measure the activity of the electrode. It is important to note that chronoamperometry was not used to condition the electrodes, so the activities of the electrodes at various points are quantified after a given number of cycles, not after a certain period of time. For **GC-1**, the overpotential decreases from 0.697 to 0.451 V (Figure 23A). Similarly, the overpotentials for **GC-2** and **GC-3** decrease from 0.703 V to a minimum of 0.446 V and from 0.740 to 0.514 V (parts B and C of Figure 23, respectively). The vertical scale of Figure 23 was truncated at 10 mA cm^{-2} to directly compare the overpotentials required to reach 10 mA cm^{-2}, a commonly

used benchmark for water-splitting catalysts. The full ranges of current densities achieved before and after conditioning to the peak activity via cathodic polarization are depicted for **GC-1−GC-3** in parts A−C of Figure 51, respectively. The large shift of ~0.250 V represents a dramatic improvement in the catalytic efficiency. Prior to conditioning, the Tafel slopes for **GC-1−GC-3** are 91, 72, and 54 mV dec^{-1}, respectively. Following conditioning, for **GC-1** and **GC-2**, the Tafel slopes increase only slightly (Figure 23D,E), suggesting that the mechanism has not significantly changed. The Tafel slope for **GC-3** after reductive cycling did exhibit a significant change (Figure 23F). However, Tafel slopes between 50 and 120 mV dec^{-1} generally indicate a mixed HER mechanism, with proton adsorption being more limiting for higher Tafel slopes.

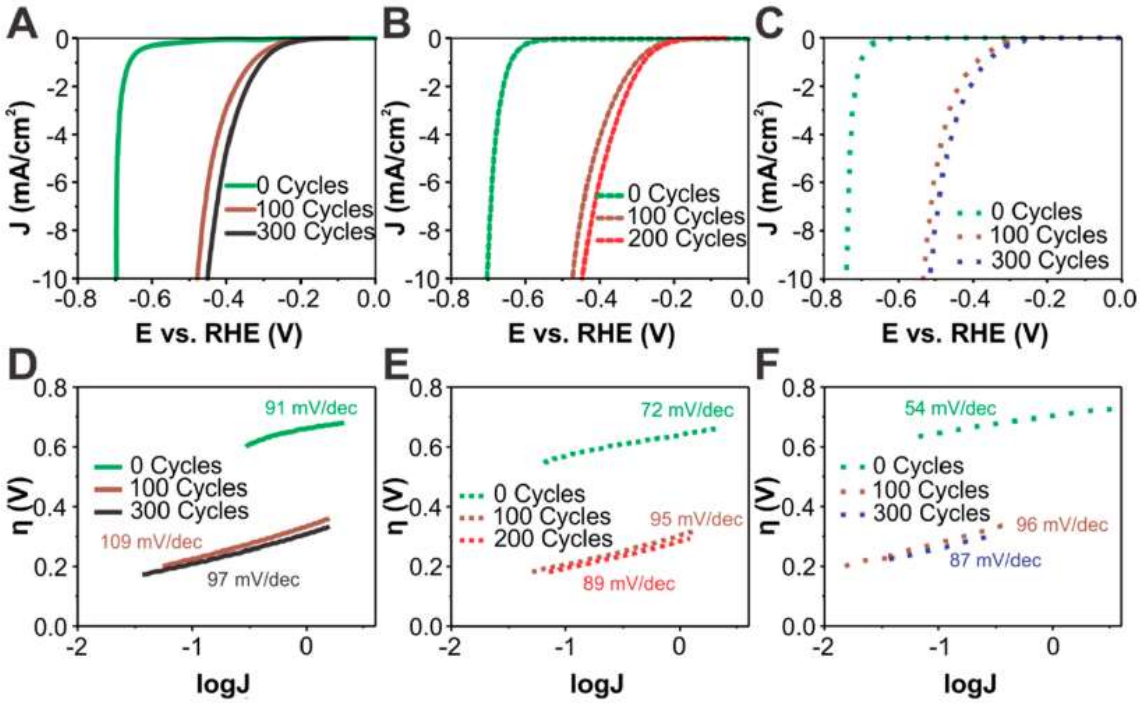

Figure 23. Effects of reductive cycling from 0 to −0.8 V vs RHE at 50 mV s^{-1} on the performance of the three modified electrodes. (A) polarization curves for **GC-1** which exhibits peak HER performance after 300 cycles. (B) polarization curves for **GC-2** which exhibits peak HER performance after 200 cycles. (C) polarization curves for **GC-3** which exhibits peak performance after 300 cycles. (D) Tafel slopes for **GC-1** before and after 300 cycles. (E) Tafel slopes for **GC-2** before and after 200 cycles. (F) Tafel slopes for **GC-3** before and after 300 cycles.

Extended reductive cycling beyond the point of peak activity was used to probe the stability of **GC-1 − GC-3**. LSV plots are shown in Figure 24A - Figure 24C respectively and Tafel plots are shown in Figure 24D - Figure 24F respectively. For all three modified electrodes, only minor increases in overpotentials were

observed. The relative consistencies of the overpotentials over extended reductive cycling indicates that this class of modified electrodes exhibits high durability for HER catalysis. A comparison of modified electrode performance for **GC-1 − GC-3** at peak electrochemical activity is summarized in Figure 25. The polarization curves, Figure 25A, show small differences in HER overpotential for **GC-1 – GC-3**. The Tafel slope plots, Figure 25B, show small differences in the Tafel slopes for **GC-1 – GC-3** at peak activity.

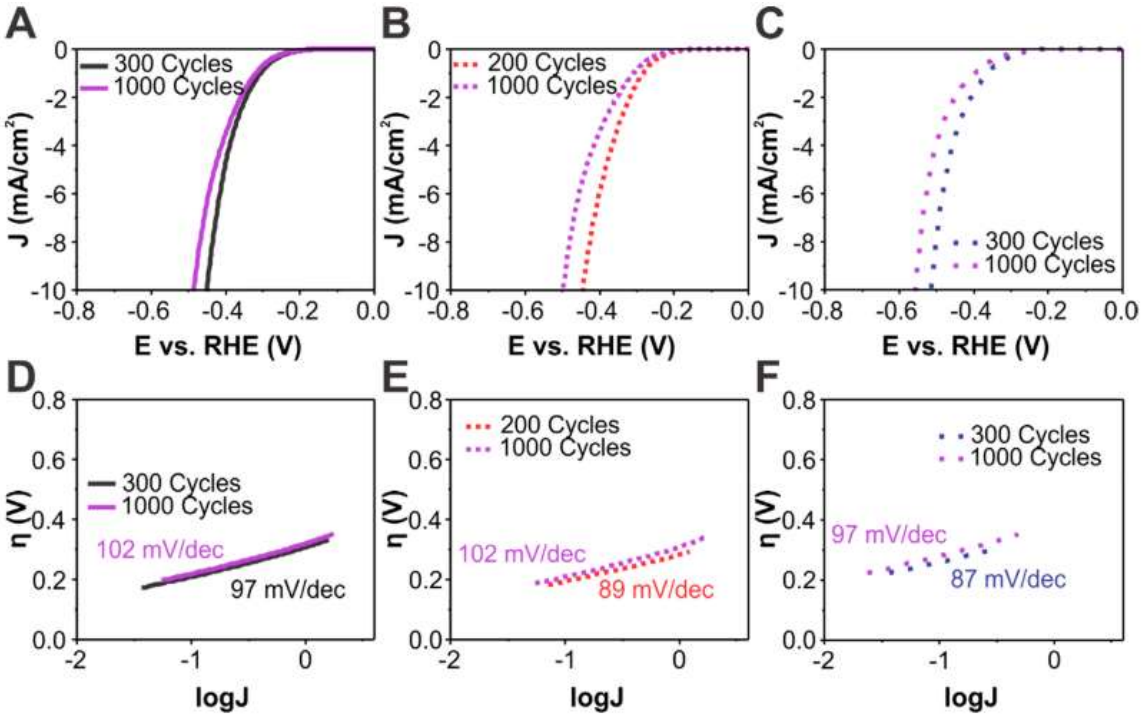

Figure 24. Effects of reductive cycling from 0 to −0.8 V vs RHE at 50 mV s^{-1} on the performance of the three modified electrodes past peak activity. (A) polarization curves for **GC-1**, revealing that its performance diminishes following 300 cycles. (B) polarization curves for **GC-2**, revealing that its performance diminishes following 200 cycles. (C) polarization curves for **GC-3**, revealing that its performance diminishes following 300 cycles. (D) Tafel slopes for **GC-1** at 300

and 1000 cycles. (E) Tafel slopes for **GC-2** at 200 and 1000 cycles. (F) Tafel slopes for **GC-3** at 300 and 1000 cycles.

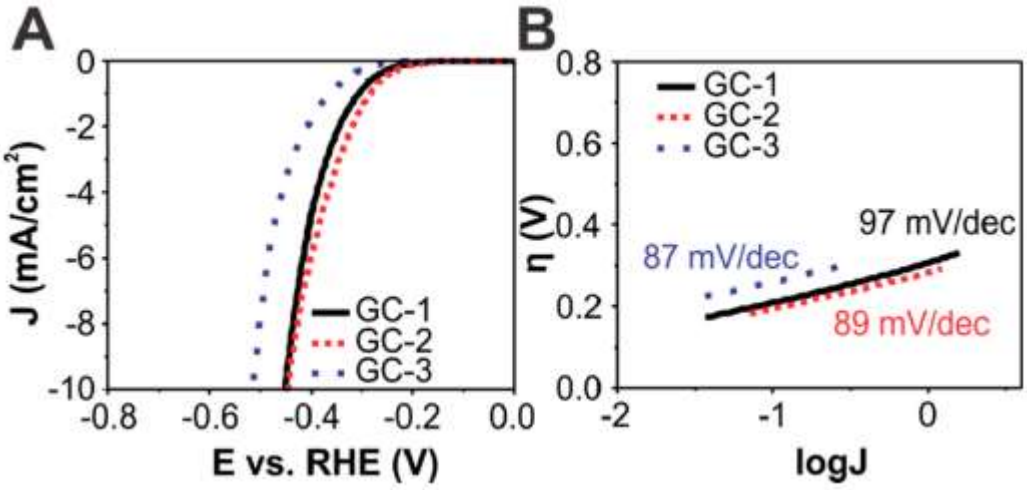

Figure 25. HER performance of three nickel compounds evaluated following reductive cycling to the point of peak catalytic activity. Polarization curves (A) show the onset of hydrogen evolution and the overpotential required for each modified electrode to reach a current density of 10 mA cm^{-2}. Tafel plots (B) show the current response to increasing overpotential throughout the onset period.

The effect of organic solvent on the modified electrodes is shown in Figure 52. Modified electrodes **GC-1** and **GC-2**, with and without conditioning through reductive cycling, were immersed in acetonitrile for 30 s while rotating at 800 rpm. Polarization curves were recorded for each modified electrode. After immersion in acetonitrile the conditioned **GC-1** electrode shows greatly diminished HER activity with only slightly lower overpotential compared to a bare

GCE (Figure 52A). A similar effect is observed for the conditioned **GC-2** electrode, Figure 52B. Clearly, acetonitrile treatment removes the active catalysts from the electrode. However, the ~100 mV improvement in overpotential (10 mA cm^{-2}) compared to a bare GCE indicates some catalyst remains on the electrode. For a nonconditioned **GC-1** electrode, immersion in acetonitrile (Figure 52C, black trace) actually decrease both the onset potential and the overpotential required to reached a current density of 10 mA cm^{-2}. Attempts to condition the **GC-1** electrode after acetonitrile immersion result in a diminished overpotential (Figure 52, red trace). Similar results are obtained for nonconditioned **GC-2** (Figure 52D). Pretreating the modified electrodes with acetonitrile prior to conditioning may work to roughen the films and expose more active sites for HER. However, the overpotential of the electrodes are ultimately poorer when treating with acetonitrile either before or after conditioning which suggests a net removal of active species from the electrode.

Recoverability of the catalysts after conditioning to peak activity is demonstrated in Figure 53. The absorbance spectra of acetonitrile solutions of **2** in various concentrations were measured in Figure 53A and used to construct a calibration curve in Figure 53B. Additionally, **GC-2**, conditioned to 200 cycles, was washed in acetonitrile, and the absorbance spectrum was recorded for the resulting solution. The absorbance spectrum of the recovered material matches those of the acetonitrile solutions of **2**, implying that the chemical structure of the catalyst is retained throughout the conditioning process. From the calibration curve, it was

determined that 0.03 mg **2** was recovered from the electrode due to the acetonitrile wash, a recovery of about 75%.

Washing the conditioned modified electrodes in acetonitrile for 30 s results in a substantial loss of activity (blue traces show higher HER overpotential than red traces, Figure 52A,B), consistent with removal of 75% of originally deposited material from the surface. However, the washed electrodes (Figure 52A,B, blue traces) still show lower overpotentials for HER than the bare GCE (Figure 52A,B, black traces), indicating that washing in acetonitrile for 30 s is not sufficient to remove 100% of the catalyst material from the electrode surface. Furthermore, a small amount of catalyst is lost during the conditioning process.

4.3.4. SURFACE CHARACTERIZATION OF MODIFIED ELECTRODES

To investigate the effect of conditioning by reductive cycling, we visually characterized the surfaces of **GC-1−GC-3** using scanning electron microscopy (SEM). Prior to conditioning, the images of **GC-1** (Figure 26A) and **GC-2** (Figure 26B) show similar microcrystalline coatings with boxlike crystals. The surface morphology of **GC-3** (Figure 26C), while still microcrystalline, has a morphology more akin to thin plates. This difference in the surface morphology is observed in the single crystals investigated by X-ray diffraction (Figure 21). After conditioning to 1000 cycles, the surface of **GC-1** lacks a crystalline appearance and resembles an amorphous micro-porous network (Figure 26D). A similar trend is observed for **GC-2**. Although the overall boxlike appearance remains intact after 1000 cycles (Figure 26E), there is observable degradation of the crystalline edges and faces. In both cases, conditioning disrupts the crystal packing and

reorders the catalyst on the electrode with an increase in the surface area, which results in more exposed active sites. Following conditioning to 1000 cycles, the surface structure of **GC-3** displays a fractured platelike appearance (Figure 26).

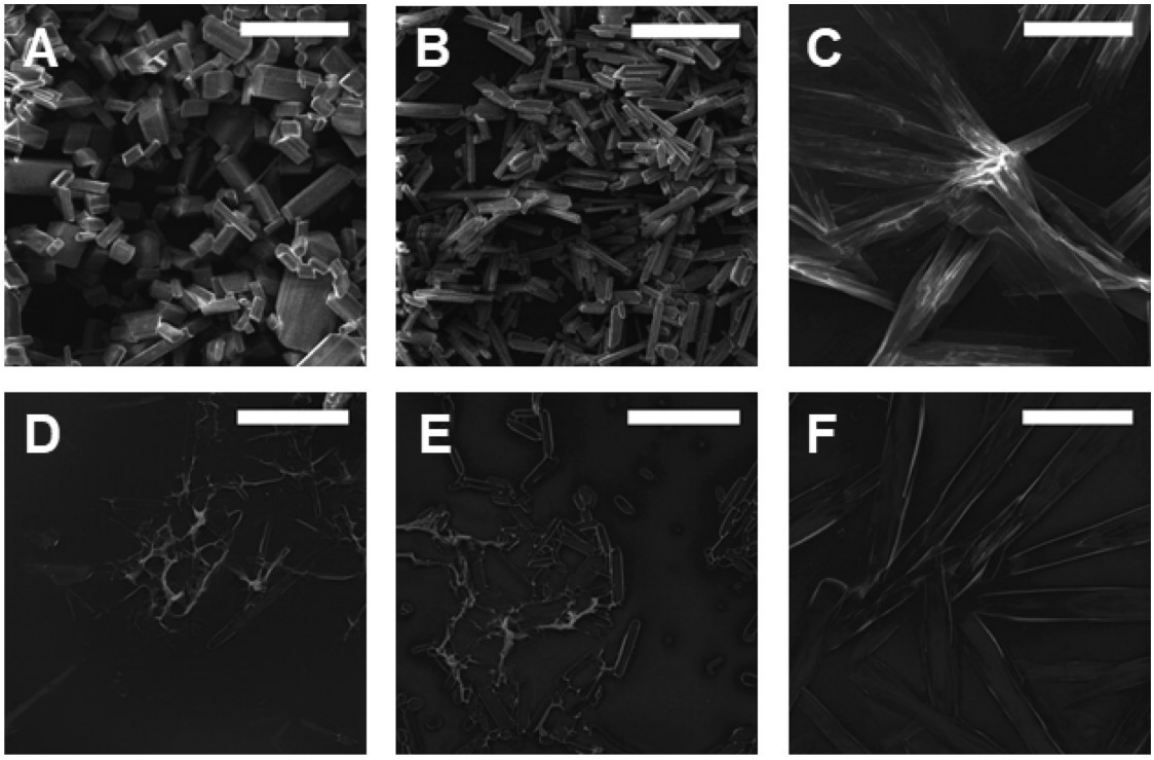

Figure 26. SEM characterization of nickel compound films on GCEs before and after 1000 reductive cycles (0 to −0.8 V vs RHE; 50 mV s^{-1}): (A) **GC-1** before reductive cycling; (B) **GC-2** before reductive cycling; (C) **GC-3** before reductive cycling; (D) **GC-1** after 1000 cycles; (E) **GC-2** after 1000 cycles; (F) **GC-3** after 1000 cycles. All scale bars correspond to 50 μm.

To analyze the retention of the material on the surface of the electrode after cycling to peak activity, a probe Raman system was employed to study modified electrodes and inks of **2**, the best-performing catalyst. Figure 54A shows a spectrum for a GCE with a Nafion film, and Figure 54B shows a spectrum for a bare GCE. This figure shows that Nafion cannot be detected via Raman in the quantities used in this study. Peaks corresponding to glassy carbon are marked

with black asterisks. Figure 55A shows a Raman spectrum for acetonitrile, and Figure 55B shows a spectrum for complex **2** in an acetonitrile solution with Nafion. Bands originating from acetonitrile (marked with blue asterisks) are observed in acetonitrile and are retained in the solution of **2**. A total of 10 peaks originating from unique chemical bonds in **2** are observed in Figure 55B and are marked with green asterisks. Figure 55C shows **GC-2** as-deposited. All 10 peaks originating from complex **2** are retained, confirming successful translation of the original complex to the electrode surface. Additionally, bands corresponding to glassy carbon, and some bands corresponding to acetonitrile, are observed. Figure 55D shows **GC-2** after conditioning to peak activity (200 cycles). All 10 peaks originating from **2** are retained, confirming that the original chemical structure of the catalyst is retained throughout the conditioning process.

The modified electrode **GC-2** was selected as a representative sample for surface characterization via energy-dispersive X-ray spectroscopy (EDS) and X-ray photoelectron spectroscopy (XPS) before and after 1000 cycles. EDS studies, performed for both catalyst samples (before and after cycling; (Figure 56 and Figure 57 respectively), reveal the presence of nickel and sulfur. Unfortunately, collected EDS data do not provide any information about the local distribution or oxidation state of detected elements. XPS studies were employed to examine the effect of conditioning on speciation of the complexes and to characterize a local distribution on the electrode surface. Survey scans of **GC-2** before and after conditioning to 1000 cycles (Figure 58A) show the presence of a large fluorine signal, attributed to Nafion, before and after conditioning. The

survey scan of the bare GCE (Figure 58B) shows that neither nickel nor sulfur is present before dropcasting **2** on the electrode. The atomic compositions of **GC-2** both before and after conditioning are described in Table 7. The peak corresponding to cationic nickel, 853.4 eV[159] (Figure 27A), is identified in the uncycled electrode. The presence of anionic sulfur, 163 eV[160,161], is concurrently detected in the uncycled electrode (Figure 27). Fitting parameters for Figure 27A,B can be found in Table 8 and Table 9, respectively. To confirm the presence of nickel and sulfur, as revealed by EDS, solely occurring from the deposition of our catalyst, secondary X-ray imaging (SXI) and elemental mapping were employed (Figure 28A). The contrast variation observed in SXI is related to lateral distribution of the catalyst (Figure 26) over the electrode surface. The bright-yellow areas correspond to the denser locations of the catalyst, while the dark spots are less covered by the catalyst. The inset of Figure 28A displays a red x in the yellow section and a blue x in the black section. The colors of the x relate to the traces in Figure 28B. In the blue trace, a weak nickel signal is detected; however, the red trace exhibits a distinct nickel signal at 853.4 eV. Elemental mapping of nickel and sulfur seen in Figure 28C follows the location of the bright features seen in SXI (Figure 28A). The green pixels are correlated to Ni $2p_{3/2}$ and the red S 2p (at ~163 eV). A comparison of the elemental mapping with SXI displays that the sulfur and nickel are present at the same location on the electrode surface and only in the areas of dense deposition, indicated by the bright-yellow pixels. Because the bright-yellow pixels are the areas of catalyst deposition, as proven in Figure 28B, we postulate that the observed nickel and

sulfur from the elemental mapping (Figure 28C) originates from our catalyst. Formation of NiS during conditioning can be ruled out because NiS is not stable below pH 3[162], and conditioning takes place in 0.5 M H_2SO_4 (pH 0.3). Nickel sulfides have been reported as catalysts for HER in neutral[163] or alkaline[164] media. Furthermore, no signals for NiS_2[165], NiS[166], or Ni_3S_2[167] were detected in the Raman spectrum of **2** in an acetonitrile solution (Figure 55B) or in Raman spectra for **GC-2** before or after conditioning (parts C and D of Figure 55, respectively).

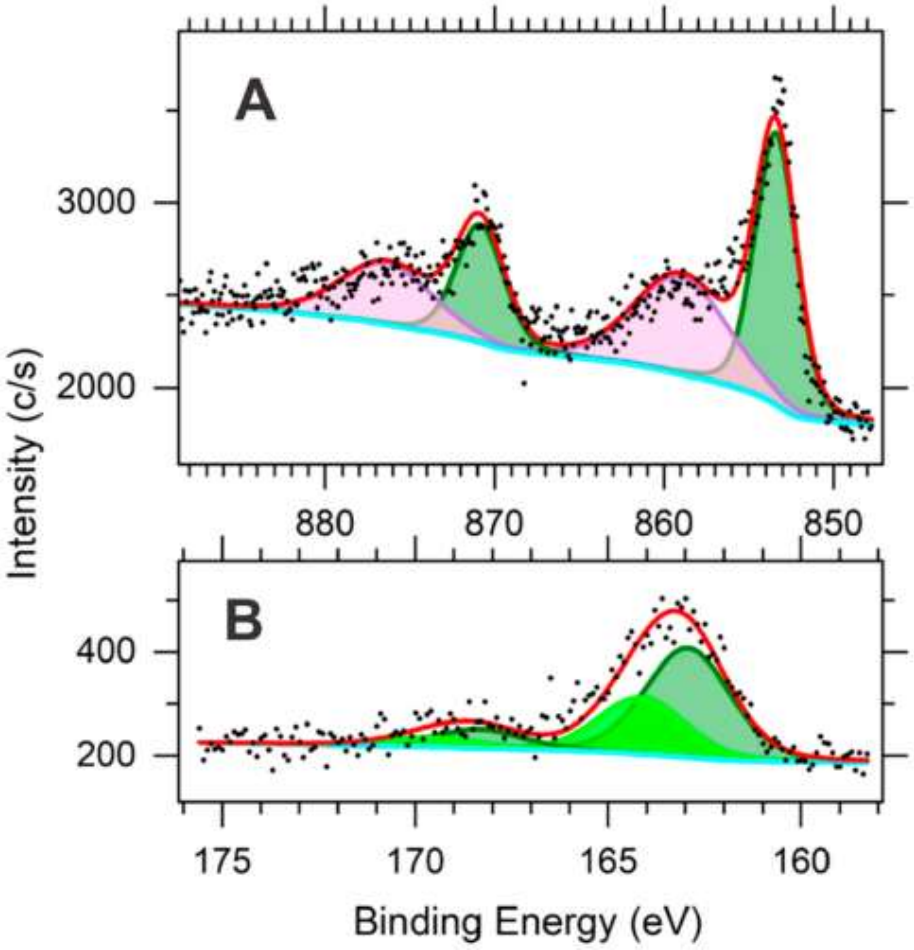

Figure 27. XPS spectra of the cationic nickel region (A) and anionic sulfur region (B) of the uncycled **GC-2** electrode surface. Black dots represent experimental spectra, while the red trace is the generated fit in parts A and B. The green color in part A represents a Ni 2p doublet, the violet color the signal from a F KLL Auger transition, and the cyan color in parts A and B the background. The green and lime colors in part B represent S 2p doublets.

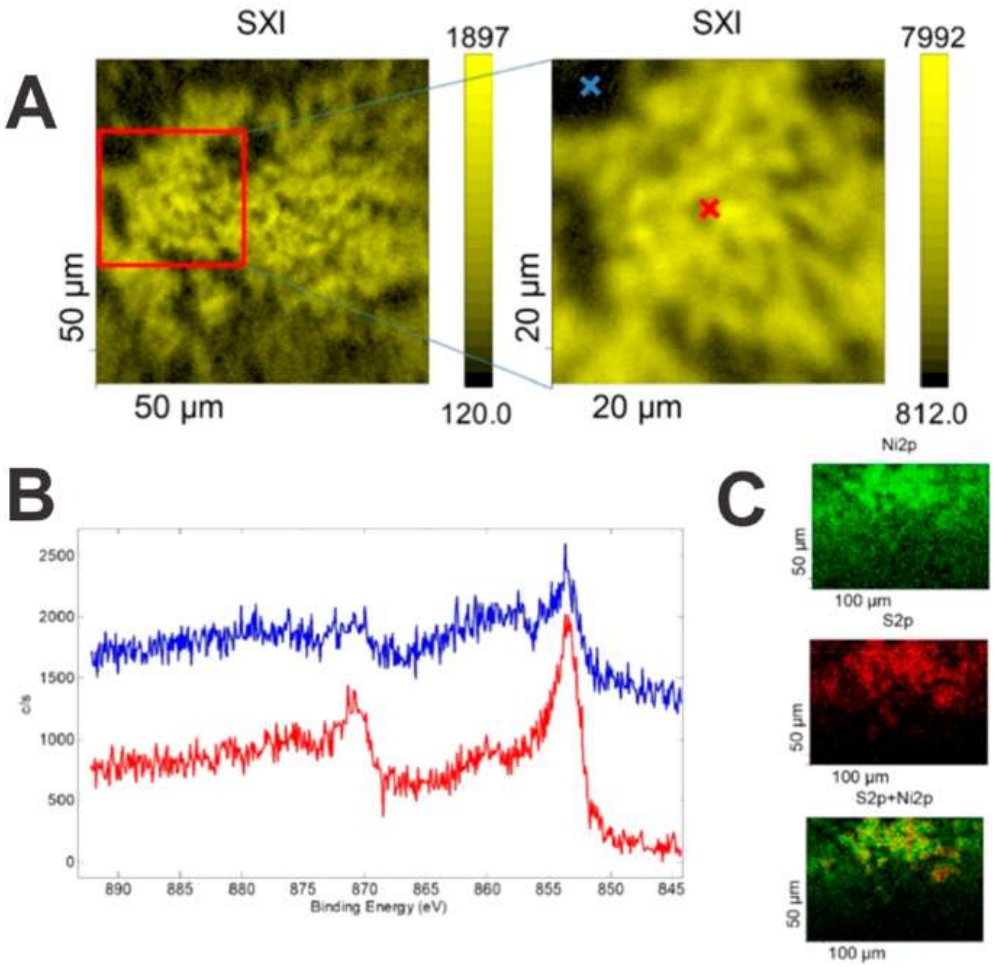

Figure 28. SXI (A) of uncycled **GC-2**, with the inset depicting examined areas and probing points marked by the colored x's for XPS (B), in which the red and blue traces correlate to the red and blue x's, respectively. (C) Elemental mapping (1000 × 700 µm), where nickel is green (top) and sulfur is red (middle) on the electrode. The overlay of the nickel and sulfur maps (bottom) confirms the catalyst location.

After conditioning, the XPS spectra of **GC-2** still display both the cationic nickel (Figure 27A) and anionic sulfur (Figure 27B). The fitting parameters for the

respective spectra can be found in Table 10 and Table 11. The measured nickel oxidation state after cycling is consistent with its binding energies (BEs) before cycling (Table 8 and Table 9). This rules out a noticeable nickel reduction to nickel metal nanoparticles[168–172]; however, nickel oxide nanoparticles with the same Ni 2p BEs cannot be totally ruled out. According to SXI and elemental mapping, we still observe a strong correlation between nickel and sulfur, as distributed on the electrode surface (Figure 29A-C). The red and blue x's in Figure 29A show the locations where data were collected. The red x clearly overlays on the deposited catalyst, whereas the blue x does not. This is substantiated in the XPS spectra for each location (Figure 29B). The red traces of both nickel (top) and sulfur (bottom) display the presence of both elements, whereas there is little to no detection for the blue trace, as seen with the uncycled electrode. Elemental mapping (Figure 29C) confirms that the location of nickel (top) coincides with that of anionic sulfur (middle) when overlaid (bottom). Note that, in order to satisfy the fitting, an additional (to higher sulfur oxidation states seen in the pristine sample) doublet of elemental sulfur (at about of 164 eV) was introduced.

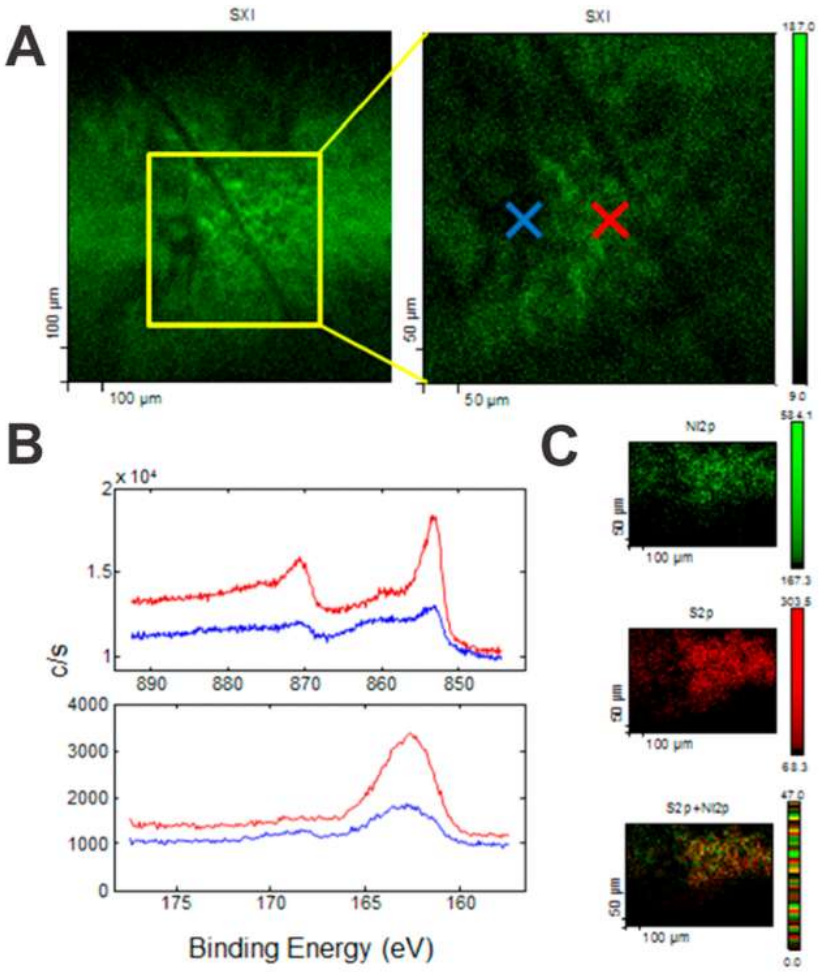

Figure 29. SXI (A) of the **GC-2** electrode after 1000 cycles, with the inset depicting examined areas and probing points marked by the colored x's for XPS (B), in which the red and blue traces correlate to the red and blue x's, respectively. (C) Elemental mapping (1000 × 700 um), where nickel is green (top) and sulfur is red (middle) on the electrode. The overlay image of the nickel and sulfur maps (bottom) confirms the catalyst location.

We noticed that the cycling results in a distribution of contrasting features across the scanned area. Consequently, multiple areas on the electrode surface were

subjected to elemental mapping using an increased lateral resolution (the scanned areas 200 × 100 vs 1000 × 700 μm), as shown in Figure 59. The data are consistent with observations found for larger scanned areas. The polarization curves (Figure 24) displayed a marginal decrease in the overall activity upon conditioning of the electrode past the point of peak activity, indicative of catalyst loss. The atomic percentage of nickel was determined via XPS, while only a fraction of the C 1s signal related to the C−F bonds in Nafion was included in the calculation. These bonds in Nafion are expected to be the least affected by cycling and the least affected by adventitious carbon contamination, so that the signal was used as a reference. The atomic percentage of nickel in the uncycled electrode was 18%, whereas the cycled compound displayed 13%. The loss of nickel over the conditioning process is consistent with the slight increase in the overpotential (Figure 24B) and Tafel slope (Figure 24E) due to the loss of catalyst from the electrode surface.

EIS was used to study the effect of conditioning on the electrical properties of the modified electrode surface. The impedance data were interpreted using an equivalent circuit model (Figure 60), consisting of the resistance of solution and wires (Rs) in series with an interfacial constant-phase element (CPE) and a charge-transfer resistance (Rc) circuit in parallel along with a Warburg element (W). The CPE is a circuit element used to replace a capacitor and is generally associated with a nonhomogenous surface and variable current density at the electrode. The impedance of the CPE is defined as in Equation 25 where Q is the magnitude of the CPE, j is the imaginary unit, ω is the angular frequency, and n

is the CPE exponent. The Warburg element was introduced to account for diffusion resistance within the crystalline domains, which are dominant prior to reductive cycling. Details are reported in Table 12.

$$Z_{CPE} = (j\omega)^{-n}/Q \qquad \textit{Equation 25}$$

Prior to conditioning, the Nyquist plots for **GC-1−GC-3** (Figure 61, Figure 62, and Figure 63, respectively) show large Rc values. The resistance for **GC-3**, 54800 Ω, is larger than those for **GC-1**, 25100 Ω, and GC-2, 18800 Ω. Following conditioning, the Rc values for **GC-1−GC-3** drop substantially to 270, 160, and 630 Ω, respectively. This dramatic decrease indicates excellent charge-transfer kinetics between the film and electrode attributed to a reorganization of the active sites to improve contact between the electrode and solution. This trend is consistent with the polarization curves in which **GC-3** displayed marginally worse metrics.

To further investigate the electrochemical performances of **GC-1−GC-3**, the electrochemical surface areas of the electrodes were approximated via cyclic voltammetry over a potential range where no faradaic processes were observed to occur (0.15−0.35 V vs RHE; Figure 64 and Figure 65). The approximate capacitance was obtained by plotting the average current density at 0.3 V versus RHE as a function of the scan rate and taking the slope (Figure 66 and Figure 67). When the determined capacitances for **GC-1−GC-3** are compared to that of GCE, relative roughness factors are obtained, which approximately express the available electrochemical surface area of each modified electrode relative to that of GCE. From this analysis, it was determined that, before conditioning, **GC-**

1−GC-3 have approximately 14, 17, and 8% of the electrochemical surface area of the bare GCE, respectively. However, following conditioning, **GC-1−GC-3** all have roughly 400% of the electrochemical surface area of the bare GCE. This evolution of electrode capacitances over the conditioning process suggests that very few active sites are available on the electrodes as deposited, fewer even than on the flat glassy carbon surface. However, the conditioning process exposes more active sites, which likely explains the improvement in the HER activity.

To further probe the surfaces of the modified electrodes, signals for the ferrocyanide/ferricyanide redox couple were recorded at various scan rates using the modified electrodes. Oxidation and reduction of the redox couple were observed for **GC-1** as deposited (Figure 68A), **GC-1** after conditioning to 300 cycles (Figure 68B), **GC-2** as deposited (Figure 68C), and GC-2 after conditioning to 200 cycles (Figure 68D. The maximum (for anodic sweeps) and minimum (for cathodic sweeps) currents were plotted against the square root of the scan rate (Figure 69). The slopes of these traces were used to solve the Randles−Sevcik equation for the electrochemical surface area available for redox of the ferricyanide couple, using previously reported diffusion coefficients[173]. The slopes of the current versus scan rate traces, as well as the calculated surface areas, are presented in

Table 13. For both **GC-1** and **GC-2**, the available surface areas increase following the conditioning process. These results appear to indicate a more permeable and accessible catalyst film following conditioning.

Furthermore, **GC-1−GC-3** were characterized in terms of the faradaic efficiency (Figure 70). All three modified electrodes exhibited approximately 100% faradaic efficiency. UV−visible (Figure 53) and Raman (Figure 54 and Figure 55) confirm translation of the intact molecular catalyst throughout the dropcasting, drying, and conditioning processes. Conditioning to peak activity produces a more permeable film, as demonstrated by ferrocyanide/ferricyanide experiments (Figure 68, Figure 69, and Table 13) and the measured capacitances of the modified electrodes (Figure 64, Figure 65, Figure 66, and Figure 67). The improvement in the overpotential caused by conditioning is attributed to perforation of the catalytic films by H_2 bubbles, as previously suggested by Konkena et al[174]. XPS studies confirmed the loss of catalyst from the surface during durability studies. Overall, conditioning creates a more open film morphology with more exposed active sites, resulting in improved HER activity up to a certain point. After this point (peak activity), further removal of the catalyst results in decreased activity. In summary, the nature of the catalyst is preserved throughout reductive cycling, and improvements in the HER activity result from H_2 bubbles creating a more permeable film

The combined surface characterization techniques confirm morphological changes of the catalyst coatings associated with a decrease in Rc upon exposure to reductive cycling. For modified electrodes **GC-1** and **GC-2**,

conditioning reorganizes the microcrystalline domains as an open-network arrangement, which ostensibly allows for greater solvent access and ion permeability. Despite **GC-3** displaying a different surface morphology, the overall performance is analogous to that of **GC-1** and **GC-2**. We postulate that this dynamic rearrangement gives rise to improved catalytic activity among the three complexes studied here. Minor differences in the catalytic performances of the three complexes are attributed to variations in their crystal-packing schemes.

4.4. CONCLUSIONS

The immobilization of active homogeneous HER catalysts on electrode surfaces has garnered recent attention. A fundamental aspect of these studies is the ability to translate homogeneous solution-phase activity to heterogeneous systems supported on an electrode. In homogeneous systems, the HER activity is largely dependent on the electronic structure of the catalyst, which dictates the reduction potential and interactions with a charged substrate. The physical structure can also be important, as demonstrated in catalysts with pendant amines that help orient the substrate for reduction. However, in heterogeneous systems derived from small-molecule catalysts, the physical structure is an essential component because it relates to catalyst−electrode interactions and charge transfer between the electrode, catalyst, and substrate.

In the current study, electronically similar HER catalysts were translated from homogeneous to heterogeneous solution. A remarkable feature of our system is the good stability of the surface-adhered catalysts without the inclusion of covalent linkers to the surface. The strong stacking interactions observed in the

crystal structures lead to robust interactions between the deposited films, dominated by microcrystal domains, and glassy carbon. The noncovalent interactions allow dynamic reorganization upon reductive cycling without changes in the molecular structure of the catalyst. As shown in Figure 30, initial cycling allows wetting of the catalyst surface and modest hydrogen evolution. The initially evolving hydrogen facilitates loss of crystallinity, leading to additional active sites and decreasing Rc. Prolonged reductive cycling leads to a loss of catalyst from the electrode surface and minimally decreases the HER activity. The results demonstrate the translation of a robust homogeneous catalyst to a solid support with no evidence of catalyst degradation or nano- particle formation.

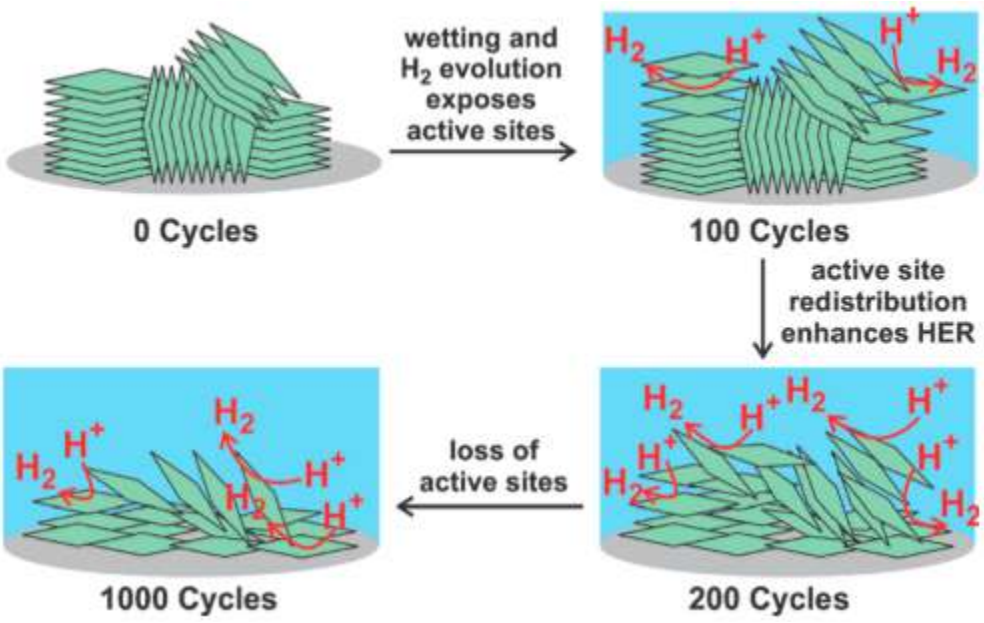

Figure 30. Conditioning via Reductive Cycling

5. PROTON EXCHANGE MEMBRANE FUEL CELL

The preceding two chapters deal with the design and evaluation of non-precious electrocatalysts for HER. Herein, the focus of the dissertation shifts away from ex-situ HER studies and toward the design and in-situ evaluation of proton exchange membrane fuel cells (PEMFCs) which use a structured cathode to achieve enhanced performance. Conventional Pt-based catalysts are employed in the work presented in Chapter 6. This chapter outlines fundamental aspects of PEMFC operation.

The PEMFC reaction (Equation 26, the opposite of water electrolysis) is comprised of the cathodic O_2 reduction (ORR, Equation 27) and anodic H_2 oxidation (HOR, Equation 28) half-reactions.

$$2H_2 + O_2 \rightarrow 2H_2O \qquad \textit{Equation 26}$$

$$O_2 + 4H^+ + 4e^- \rightarrow 2H_2O \qquad \textit{Equation 27}$$

$$2H_2 \rightarrow 4H^+ + 4e^- \qquad \textit{Equation 28}$$

In some cases, ORR can proceed with a ratio of two electrons per oxygen molecule, generating H_2O_2 as a product[175]. However, this predominantly occurs when carbon materials (without Pt) are used as catalysts. Since PEMFC work presented herein utilizes platinum-group metal catalysts for ORR, this possibility is omitted in subsequent sections. As is the case with electrolyzers, several types of fuel cells exist including proton exchange membrane, alkaline, and solid oxide[28]. Furthermore, some fuel cell types employ fuels such as hydrocarbons in

lieu of hydrogen. Fuel cells aside from the hydrogen/oxygen proton exchange membrane type fall outside of the scope of this work and will not be discussed herein. As with electrolyzer/HER systems, balance of plant components will not be discussed for PEMFCs in this dissertation.

The typical PEMFC device architecture is depicted in Figure 31. A PEMFC is an electrochemical device which leverages the exergonic oxidation of H_2 at the anode CL to produce an electrical current with O_2 reduction at the cathode balancing system charge transfer. Figure 32B shows the typical CL architecture. Carbon-supported Pt is the state-of-the-art cathode CL electrocatalyst. The anode catalyst is typically also carbon-supported Pt but may contain other PGMs such as Ir. Less-expensive non-precious catalysts exist, but current formulations are inferior to Pt in terms of efficiency, durability, and/or ease of fabrication which makes commercial utilization impractical. The CL also contains ionomer which serves as a binder and proton conduit. The state-of-the-art CL ionomer is perfluorosulfonic acid (PFSA, the most commonly utilized commercial formulation of which is Nafion). The simplest reaction site model stipulates that the anodic HOR and the cathodic ORR occur at the so-called *triple interface* of the electrically conductive catalyst particle, gas diffusion volume, and ion conducting ionomer (Figure 32C). However, the gas permeability of the ionomer thin film surrounding catalyst aggregates is significant[176], enabling reaction at active sites which are covered with ionomer.

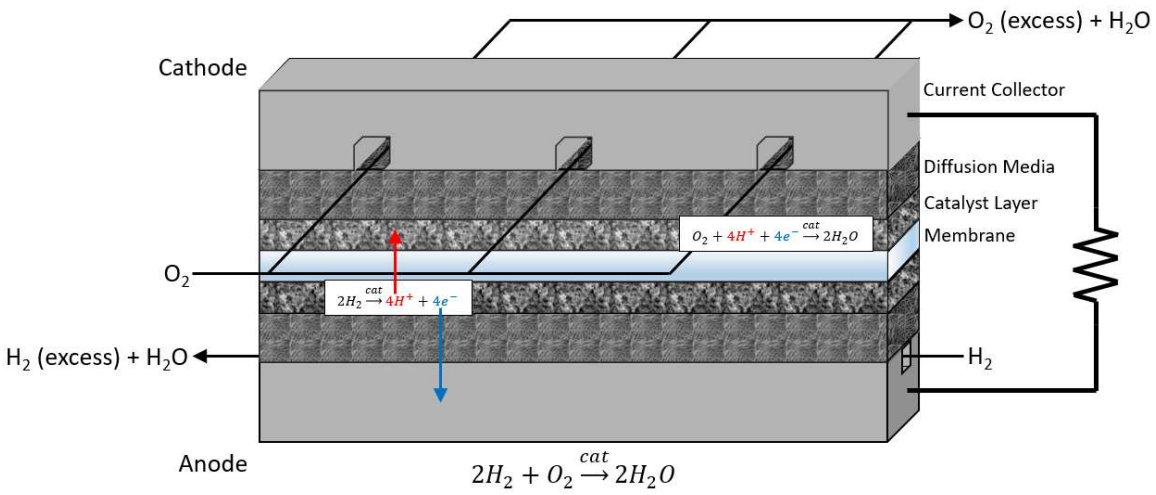

Figure 31. Simplified depiction of a PEMFC.

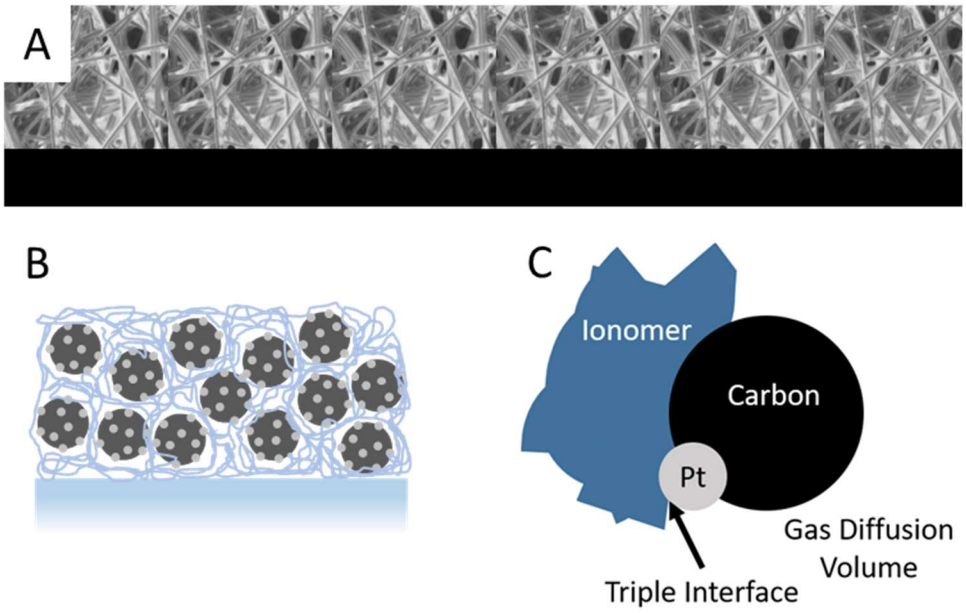

Figure 32. Simplified (A) diffusion media depiction showing PTL (top) and MPL (bottom); (B) catalyst layer depiction showing platinum (gray balls) supported on carbon (black balls) surrounded by ionomer (blue trace) attached to the membrane (bottom); (C) close-up view of triple-interface between catalyst aggregate (carbon and active Pt), gas diffusion volume, and ionomer

A PEM, also typically made of Nafion, as in the case of PEMWEs, selectively permits the passage of protons between electrodes while mitigating parasitic currents due to reactant gas and electron crossover. As in the PEMWE, the DM (also called gas diffusion layer, or GDL) bounds the CLs on the side opposite the PEM. In PEMFCs, the DM is typically comprised of a carbon slurry microporous layer (MPL, bottom black portion, Figure 32A) adjacent the CL and a carbon fiber porous transport layer (PTL, top portion, Figure 32A). Both DM components are typically hydrophobized with compounds such as polytetrafluoroethylene (PTFE).

The MPL improves the contact resistance between the GDL and CL, minimizes loss of catalyst to the GDL interior, protects the membrane from PTL fibers, and improves water management. The GDL serves as a conduit for reaction gas diffusion to the CL, conducts electrons and reaction heat, mechanically supports the membrane electrode assembly (MEA), and transports excess water away from the CL. Finally, introduction of reactant gases (H_2 and O_2 on the anode and cathode respectively) to the MEA occurs via the flow field (FF). The FF, commonly made of graphite or stainless steel, is a patterned feature adjacent or carved/pressed into the bipolar plate (BPP) – a conductive end plate that collects electrons on either side of the load. Higher voltage than what a single cell can provide is required for most real-world applications. In this case, several cells are configured end-to-end in a *stack* where the BPP separates and conducts electrons between adjacent cells.

Electrons (e^-) extracted from H_2 via HOR conduct through the anode CL, DM, and BPP; drive an external load; and then conduct through the cathode BPP and DM to the cathode CL. H^+ from HOR migrates through the anode CL ionomer, into the PEM, then into the cathode CL ionomer. At the cathode CL, H^+, O_2, and e^- combine to yield water. Flooding caused by excess water accumulation inhibits gas diffusion, slowing the reaction rate. Conversely, insufficient ionomer hydration inhibits proton conduction. Therefore, water management is critical to ensuring optimal PEMFC performance and stability.

5.1. STEADY-STATE PEMFC OPERATION

The polarization curve (plot of cell voltage as a function of current) is a practical and common way to represent the performance of a PEMFC. Figure 33 represents a typical PEMFC polarization curve. Thermodynamic, kinetic, Ohmic, and transport losses affect PEMFC performance as described in the following sections. In the vast majority of cases, cathodic ORR is the rate limiting half-reaction, so any losses at the anode are typically negligible unless the anode catalyst loading is very low and/or relatively inactive catalysts are used on the anode.

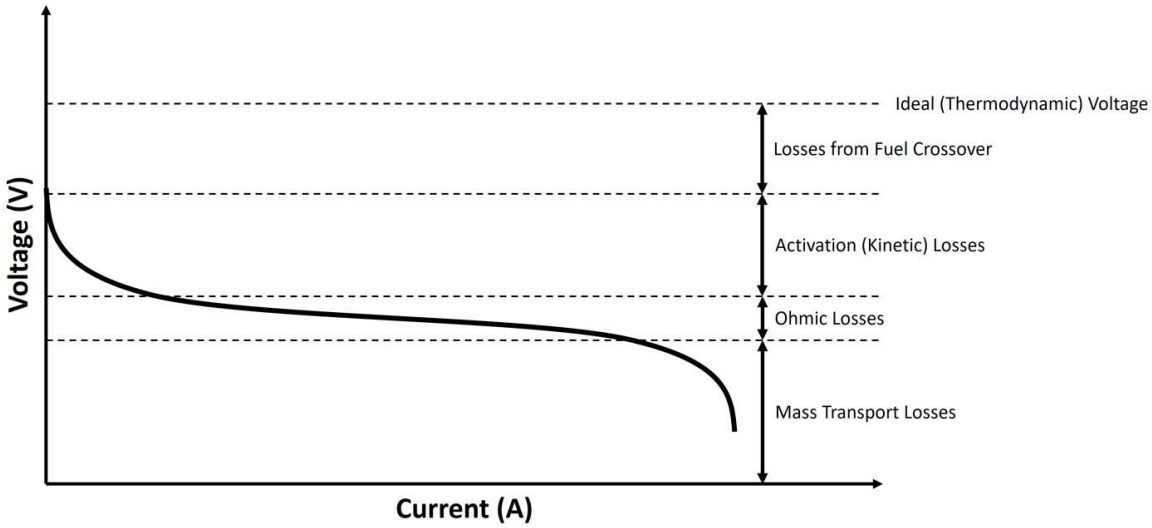

Figure 33. PEMFC polarization curve.

Steady-state operation assumes several factors including consistent cell hydration, constant current-voltage behavior, and consistent gas flow over time. Transient PEMFC operation is a significant consideration in applications including the start-up of PEMFCs at sub-freezing conditions and/or dead-ended

PEMFC operation (where there is no outlet stream from the cell). Additionally, fuel cell operation takes on a transient character during the “break-in” (conditioning) of the cell or as cell durability is adversely impacted over time due to phenomena including carbon corrosion, Ostwald ripening, coalescence, and membrane degradation. However, neither the deliberate introduction of transient conditions nor cell durability are studied herein. Therefore, a detailed discussion of transient fuel cell operation is beyond the scope of this dissertation and is omitted.

5.2. THERMODYNAMIC CONSIDERATIONS

For the PEMFC reaction, the Nernst equation which describes the ideal reversible voltage of the system is derived analogously to the case of HER (Chapter 2). However, for the PEMFC, $z = 2$, and the reaction quotient Q is determined using Equation 26. Making these changes, the PEMFC-specific form of the Nernst equation is given in Equation 29.

$$E = E^0 + \frac{RT}{2F} ln \frac{a_{H_2} a_{O_2}^{1/2}}{a_{H_2O}} \qquad \textit{Equation 29}$$

The standard reaction potential relates to the standard molar reaction free energy as in Equation 30.

$$E^0 = \frac{-\Delta \bar{g}_f^0}{zF} \qquad \textit{Equation 30}$$

where $\Delta \bar{g}_f^0$ is the difference in free energies of formation of reactants vs products as described by Equation 31. This relationship is analogous for enthalpy and entropy.

$$\Delta\bar{g}_f^0 = \sum(\bar{g}_f^0)_{products} - \sum(\bar{g}_f^0)_{reactants} = (\bar{g}_f^0)_{H_2O} - (\bar{g}_f^0)_{H_2} - \frac{1}{2}(\bar{g}_f^0)_{O_2} \quad \textit{Equation 31}$$

The standard changes in molar enthalpy ($\Delta\bar{h}_f^0$) and entropy ($\Delta\bar{s}_f^0$) define the standard change in molar free energy for component i as in Equation 32.

$$(\Delta\bar{g}_f^0)_i = (\Delta\bar{h}_f^0)_i - T(\Delta\bar{s}_f^0)_i \quad \textit{Equation 32}$$

The Gibbs' free energy term represents the electrical energy produced by the cell, the enthalpy term represents the *calorific value* – or energy liberated from simply burning the fuel, and the entropy term represents thermodynamic losses inherent in the PEMFC reaction. While the molar free energies are specific to standard conditions (25 °C, 1 atm) in this representation, two values are possible for $(\bar{g}_f^0)_{H_2O}$ depending on the phase of product water (liquid or vapor). For the production of water vapor where the latent heat of vaporization is lost (higher heating value), Equation 33 applies.

$$H_2 + \frac{1}{2}O_2 \xrightarrow{\Delta\bar{h}_f^0 = -241.83\frac{kJ}{mol}} H_2O(steam) \quad \textit{Equation 33}$$

For the case where the product is liquid water (lower heating value), Equation 34 applies.

$$H_2 + \frac{1}{2}O_2 \xrightarrow{\Delta\bar{h}_f^0 = -285.84\frac{kJ}{mol}} H_2O(liquid) \quad \textit{Equation 34}$$

where the difference between the two enthalpies (44.01 kJ mol^{-1}) is the molar vaporization of water. At typical PEMFC operating temperatures, the product water is liquid, so the corresponding lower heating value is used. The maximum (thermodynamic) efficiency of a PEMFC is determined by comparing maximum

useful electrical energy ($\Delta\bar{g}_f$) to the heat generated by simply combusting the reactants ($\Delta\bar{h}_f$) as in Equation 35.

$$\varepsilon_{max} = 100\% * \frac{\Delta\bar{g}_f}{\Delta\bar{h}_f} \quad \textit{Equation 35}$$

From the above equations, a maximum voltage and efficiency of 1.23 V and 83 % respectively are possible at standard conditions. However, depending on the application, it is atypical for a PEMFC to operate at standard conditions. The maximum efficiency under nonstandard conditions is found by first calculating the temperature-specific molar heat capacity at constant pressure ($\bar{c}_p$, Equation 36, Equation 37, and Equation 38),[177] molar enthalpy of formation $(\bar{h}_T)_i$ (Equation 39), and molar entropy of formation $(\bar{s}_T)_i$ (Equation 40).

For steam,

$$\bar{c}_p = 143.05 - 58.040T^{0.25} + 8.2751T^{0.5} - 0.036989T \quad \textit{Equation 36}$$

For H_2,

$$\bar{c}_p = 56.505 - 22222.6T^{-0.75} + 116500T^{-1} - 560700T^{-1.5} \quad \textit{Equation 37}$$

For O_2,

$$\bar{c}_p = 37.432 + 2.0102 * 10^{-5}T^{1.5} - 178570T^{-1.5} + 2368800T^{-2} \quad \textit{Equation 38}$$

$$(\bar{h}_T)_i = (\bar{h}_f^0)_i + \int_{298.15}^{T} \bar{c}_p dT \quad \textit{Equation 39}$$

$$(\bar{s}_T)_i = (\bar{s}_f^0)_i + \int_{298.15}^{T} \frac{1}{T}\bar{c}_p dT \quad \textit{Equation 40}$$

Equation 32 gives the free energy of formation for a given component at any temperature as long as each input value corresponds to the same temperature.

Similarly, the nonstandard analogue of Equation 31 gives the reaction free energy. Given the formation enthalpy of each component, the reaction enthalpy is calculated similarly to the reaction free energy (subtract reactant enthalpies from those of products) using Equation 41.

$$\Delta\bar{h}_f = \sum(\bar{h}_f)_{products} - \sum(\bar{h}_f)_{reactants} = (\bar{h}_f)_{H_2O} - (\bar{h}_f)_{H_2} - \frac{1}{2}(\bar{h}_f)_{O_2} \qquad \textit{Equation 41}$$

These relationships provide all the tools necessary to calculate the thermodynamic efficiency and maximum voltage of a cell at any temperature. For example, at 80 °C (a common benchmark operating temperature), the maximum operating voltage is 1.18 V, and the maximum efficiency is 80 %. Note that the maximum voltage is also governed by pressure as represented by component activity in Equation 29.

5.3. KINETIC LOSSES

As is the case with HER (Chapter 2), several irreversible losses are present in PEMFCs which limit the operating voltage to well below the reversible voltage calculated in the above section at a given reaction rate. Again, the difference between the operating voltage and the reversible thermodynamic voltage is referred to as the overpotential or overvoltage. Kinetic (activation) losses also affect PEMFC performance and refer to the loss of some amount of generated potential in order to drive the electrochemical reaction at the catalyst surface.

Applying the general redox reaction in Equation 7 to the PEMFC reaction (Equation 26), writing the rate equation (Equation 8), substituting in the Nernst

equation (Equation 9), and taking the derivative with respect to E, Equation 42 is obtained.

$$1 = \frac{RT}{2F}\left[\frac{d(lnk_r)}{dE} + \frac{d\left(ln\frac{1}{k_f}\right)}{dE}\right] \qquad \textit{Equation 42}$$

Equation 42 is the PEMFC-specific equivalent of Equation 10. It follows that for a PEMFC, Equation 11 and Equation 12 are replaced by Equation 43 and Equation 44 respectively.

$$\frac{RT}{2F}\frac{d(lnk_r)}{dE} = 1 - \alpha \qquad \textit{Equation 43}$$

$$\frac{RT}{2F}\frac{d\left(ln\frac{1}{k_f}\right)}{dE} = \alpha \qquad \textit{Equation 44}$$

The charge transfer coefficient α generally has a value around 0.5 for the PEMFC anode (hydrogen electrode) or 0.1 – 0.5 for the PEMFC cathode (oxygen electrode)[178]. Equation 45 is the form of Arrhenius' Law which describes the kinetics of the PEMFC cathode.

$$k_f = k_f^0 e^{\frac{-2\alpha E_a}{RT}} \qquad \textit{Equation 45}$$

The form of the Butler-Volmer equation for the PEMFC cathode surface is given by Equation 46.

$$i = i_0 \left(e^{\frac{-2\alpha \mathrm{F}\eta}{RT}} - e^{\frac{2(1-\alpha)\mathrm{F}\eta}{RT}} \right)$$ *Equation 46*

As the reaction is driven in the forward direction away from open circuit, the second term becomes insignificant, and the current can be approximated with Equation 47 – the Tafel equation.

$$i = i_0 e^{\frac{-2\alpha \mathrm{F}\eta}{RT}}$$ *Equation 47*

The PEMFC oxygen electrode (cathode) generally has an i_0 several orders of magnitude lower than that of the hydrogen electrode (anode) (i.e. $i_{0,c} \ll i_{0,a}$)[28]. Therefore, ORR is the rate-limiting PEMFC half-reaction, and anode overpotentials are insignificant as long as the anode catalyst loading and activity are sufficiently high as is typically the case with platinum group metal-based catalysts (non-precious PEMFC catalysts are not employed in the work presented in this dissertation). Subsequent discussions of PEMFC systems will focus exclusively on cathodic processes unless otherwise noted. In summary, PEMFC overpotentials due to kinetic losses at the cathode are described by Equation 48.

$$\eta_{kinetic} = \frac{-RT}{2\alpha \mathrm{F}} ln\left(\frac{i}{i_0}\right)$$ *Equation 48*

In addition to the irreversible losses related to driving the electrochemical reaction as described above, overpotentials related to fuel crossover and internal currents fall under the umbrella of kinetic losses. The purpose of the PEM is to selectively conduct protons from the PEMFC anode to the cathode. However, even state-of-the-art PEMs conduct a small electrical current. Furthermore,

PEMs are not perfectly gas impermeable. The result of these imperfections is a small parasitic current which effectively wastes electrons generated from the cell reaction and further increases the overpotential. To account for these parasitic currents, a crossover current term is added to the numerator of the logarithm in Equation 48 as shown in Equation 49.

$$\eta_{kinetic} = \frac{-RT}{2\alpha F} ln\left(\frac{i + i_{crossover}}{i_0}\right) \qquad \textit{Equation 49}$$

5.4. OHMIC LOSSES

In the PEMFC, the majority of Ohmic losses occur as protons are conducted through the PEM, but a small amount of energy is also lost due to imperfect contact at the interfaces between various cell components and within wires, BPPs, and other elements which make up the balance of the system. Overpotentials due to these losses are described by Ohm's Law (Equation 21).

In a PEMFC, Ohmic losses are highly dependent upon the degree of hydration of the PEM. A well-hydrated PEM will conduct protons more efficiently, whereas a drier cell will experience more pronounced resistive losses[179]. Another significant contribution to Ohmic losses is the percolation of protons throughout the cathode CL. These losses constitute the *sheet resistance* of the electrode. These losses are often neglected[180–182] – particularly at operation near or above 100 % RH. However, at lower humidification, these losses become important.

5.6. MASS TRANSPORT LOSSES

During PEMFC operation, the device can reach a high enough current density where oxygen supplied to the cathode is immediately depleted in the vicinity of

the catalyst surface. This process can be illustrated with the one-dimensional equation of continuity for a reactant species A in a mixture of A + B which diffuses to a surface and reacts (Equation 50).

$$D_{AB}\frac{d^2C_A}{dz^2} = kC_A = -r_A = \frac{i}{zF} \qquad \textit{Equation 50}$$

In PEMFCs where air is used as the cathode gas, A in Equation 50 refers to O_2, and B refers to N_2 – the balance gas. Although Equation 50 is an over-simplification which neglects convective mass transport, it demonstrates that the rate of the reaction is limited by the local supply of reactant gas to the active sites.

A popular empirical convention for modeling the overpotential due mass transport limitations[183–186] is presented in *Equation 51*.

$$\eta_{mt} = me^{ni} \qquad \textit{Equation 51}$$

Briefly, Equation 51 dictates that the mass transport overpotential is directly related to the concentration drop of reactant gases and inversely related to the accumulation of reaction byproducts (water). Physically, the term m correlates to the electrolyte conductivity, and n correlates to the porosity of gas diffusion pathways. At higher water content, the electrolyte is highly conducting, but the accumulation of water inhibits reactant diffusion through pores. At low water content, Ohmic losses become more dominant.

The total oxygen transport resistance (Equation 52) is the sum of both Fickian (R_F) and non-Fickian (R_{NF}) contributions[187–189].

$$R_{O_2} = R_F + R_{NF}$$ *Equation 52*

Fickian diffusion resistances are attributed to classical diffusion processes governed by concentration gradients assuming constant diffusion coefficients (i.e. Equation 50). *Molecular diffusion*, or the transport of reactant O_2 through a bulk volume of gas, falls under this umbrella. Fickian diffusion is limited by collisions between gas molecules which effectively slows the translation of a given molecule between two points, resulting in a lower diffusion coefficient. Fickian diffusion is typically the dominant mass transport mechanism in larger pores (>100 nm in diameter) such as those in the diffusion media or flow field channels. This type of diffusion is highly pressure-dependent.

Conversely, non-Fickian diffusion resistances becomes significant in smaller pore volumes. On smaller length scales (<100 nm), collisions between gas molecules and solid media (i.e. catalyst and support) become significant. Additionally, diffusion of gas molecules through ionomer or water films is governed by driving forces other than chemical potential such as molecular relaxation, polymer segment mobility, and interaction between the gas molecule and water/ionomer. Non-Fickian diffusion is considered to be pressure-independent, and a strong correlation exists between non-Fickian diffusion limitations and PEMFC performance at very high current densities[187]. As shown in Equation 53, non-Fickian diffusion resistance occurs within the MPL, CL, and locally at the Pt surface.

$$R_{NF} = R_{NF}^{MPL} + R_{NF}^{CL} + \frac{R_{O_2}^{Pt}}{r.f.}$$ *Equation 53*

where $r.f.$ is the roughness factor, or the product of Pt loading and electrochemically active surface area (ECSA). This relationship demonstrates that the Pt ECSA is a dominant factor in determining high-power PEMFC performance. The roughness factor and local diffusion resistance are commonly lumped together as $R_{ion}^{CL} = \frac{R_{O_2}^{Pt}}{r.f.}$ since a greater catalyst utilization will make local O_2 transport less limiting, reducing the apparent diffusion resistance caused by ionomer thin films. Further, the diffusion of O_2 through the CL ionomer film is significantly limited by the atypical properties of ionomer in nanometer-scale thin films[187,190,191]. One approach to address this problem is the design of novel electrode ionomers with bulk-like properties. Alternatively, simply using less ionomer in the cathode CL would attenuate this resistance. However, less ionomer in the CL provides less percolation volume for protons, making resistive losses more dominant. In the following chapter, we present function-segmented electrodes as a novel approach to address the interplay between these two factors.

6. IONOMER CHANNEL ARRAY FOR ENHANCED PERCOLATION IN PEMFC CATHODE CATALYST LAYERS

The tortuous and undifferentiated network of ionomer in the conventional proton exchange membrane fuel cell cathode catalyst layer imparts cell overpotentials related to inhibited chemical and charge percolation. Moreover, the ionomer itself exerts a poisoning effect on platinum active sites, adversely impacting oxygen reduction kinetics. Reducing electrode ionomer content to attenuate poisoning serves to exacerbate proton transport limitations, limiting the parameter space for tuning electrode composition to achieve enhanced performance. Here, we address this trade-off by patterning the proton exchange membrane with an array of ionomer channels which project into the cathode catalyst layer and serve as efficient conduits for proton transport, attenuating ionomer poisoning without adversely impacting electron or oxygen transport. Array electrodes impart an increase in mass activity of ~20 % for Vulcan carbon-supported Pt catalyst with *optimal* ionomer impregnation and enable the use of low-ionomer catalyst – increasing catalyst utilization by ~80 % thereby enabling fast oxygen reduction kinetics. Array electrodes increase cell performance by up to ~35 % in ionomer-rich catalyst or up to ~125 % in ionomer-deficient catalyst at low relative humidity. Further performance gains may be attained by supporting ionomer-free catalyst

Alexander J. Gupta[1,2], Gaoqiang Yang[1], Siddharth Komini-Babu[1], and Jacob Spendelow[1]
[1]Los Alamos National Laboratory, Los Alamos, NM 87545, United States
[2]University of Louisville, Louisville, KY 40292, United States
This research was supported by the Los Alamos National Laboratory Directed Research & Development (LDRD) program as well as the Million Mile Fuel Cell Truck (M2FCT) consortium.

on a dense array of thin ionomer channels and/or by utilizing high-performance catalysts based upon porous carbons.

6.1. INTRODUCTION

Conventional proton exchange membrane fuel cell (PEMFC) electrodes are homogeneous multi-phase porous networks[192] of ionomer, carbon-supported platinum (Pt), and void space which are randomly distributed on the microscale. This structure is created using methods such as ultrasonic spray coating, rod coating, or decal transfer to deposit the catalyst ink on the proton exchange membrane (PEM) or gas diffusion layer (GDL). Slow chemical transport is a key limiting factor for PEMFC operation at high power density[28].

Oxygen (O_2) transport limitations can be attributed to three factors: bulk molecular diffusion, Knudsen diffusion, and dissolution/diffusion in water and ionomer[189,193–197]. Molecular diffusion resistance is caused by the relatively slow diffusion of oxygen in air due to collisions between molecules in the gas mixture[194] and is highly dependent on pressure and temperature[195]. Knudsen diffusion resistance becomes significant in small void volumes and is caused by collisions between gas molecules and solid media[196]. Lastly, the diffusion coefficient of O_2 is much lower in water or ionomer than in air[197], so the reaction rate is significantly inhibited by ionomer-rich or flooded CLs.

The random distribution of CL ionomer, which serves as a conduit for protons (H^+), creates a tortuous charge transfer pathway which confers significant Ohmic losses within conventional cathode CLs[198], particularly when inlet gases possess a low degree of humidification. While a high ionomer content serves to decrease

H^+ transport resistance in the CL, resulting thicker ionomer films/channels[199] increase the separation and thus electrical contact resistance between catalyst particles[200,201] while also increasing the local O_2 diffusion resistance. Further, an ionomer content lower or higher than the optimal value for a given catalyst serves to decrease the catalyst utilization (mass activity) by isolating agglomerates from percolation of H^+ or electrons (e^-) respectively, effectively cutting off some of the catalyst from the three-phase reaction zone. Aside from the above considerations, it has been demonstrated that the sulfonate anions in Nafion and related ionomers exert a poisoning effect on Pt[202–206]. This poisoning effect entails a competitive inhibition mechanism caused by the electrochemical adsorption of sulfonate onto a Pt active site, blocking the adsorption of O_2. Optimization of I/C in conventional electrodes has been studied extensively to strike a balance between these factors[204,207,208]. For Vulcan carbon-supported Pt (used in this study), an optimal I/C of 0.5 has been reported[209,210]. The rigid requirement of an optimal I/C leaves very little room for tuning conventional electrode composition to improve the performance of a given catalyst.

The relationship between ink properties/deposition methods and percolation within the CL as well as utilization of catalyst at the interior of agglomerates has been studied extensively[211–216]. While these studies have furthered the understanding of highly active CL fabrication, gains have been somewhat incremental, and state-of-the-art PEMFCs are overwhelmingly driven by undifferentiated and tortuous CLs which suffer from the limitations detailed above. Conversely, theoretical studies suggest that ordered electrode structures

could attenuate these limitations by providing specialized domains for transport of H^+ or O_2, increasing catalyst utilization at high current densities[217–219].

Several efforts to improve catalyst utilization and decrease transport limitations by ordering the electrode to various degrees on various length scales have been reported in the literature[220,221,230–235,222–229]. Fang et al reported catalyst layers based on hierarchically ordered carbon supports[220–223] to enhance electrochemically active surface area (ECSA), provide additional pore volume for O_2 transport, enhance e^- transport and improve platinum Pt dispersion. Similarly, Tian et al supported Pt on an array of vertically aligned carbon nanotubes[233]. Jang[224,225], Prasanna[231], and Omosebi[230] patterned Nafion PEMs to improve the ionic contact between catalyst and PEM. Gruber[226] and Huang[227] deposited hierarchically-roughened Pt thin films on the GDL. Both Yakovlevl[228], Zeng[229], and Steinbach[232] supported Pt thin films on nanowire arrays to improve the mass-specific utilization of Pt. Lastly, Chong[235] and Yang[234] synthesized atomically ordered intermetallic nanoparticles with high mass activity.

The approaches taken in the above body of work all employ ordering of cathode CL components to improve upon some aspect of PEMFC performance. However, none of the aforementioned strategies give a function-differentiated cathode which attenuates the tradeoff between chemical transport limitations while conferring high activity. We postulate that this tradeoff can be circumvented in an electrode which uses a dense array of thin ionomer channels with bulk-like properties which have ionomer-free catalyst deposited in the interstitial spaces, providing domains dedicated to electron/oxygen transport or proton transport –

decreasing chemical transport lengths and reducing ionomer poisoning. The work detailed herein functions as a proof of concept to this end. Here, we introduce a cathode CL with catalyst deposited within an array of microscale Nafion channels which enhance H^+ transport between the CL and PEM without adversely impacting O_2 transport. The interplay between Nafion channels, ionomer content, electrode properties, and cell performance are explored in detail.

6.2. METHODS

6.2.1. MEA FABRICATION

Membrane electrode assemblies (MEAs) based on catalyst-coated Nafion channels were prepared as follows. Rectangular silicon templates, inscribed with a regular square array of 5-6 μm diameter cylindrical holes 10-13 μm in length with a pitch of 12 μm, with geometric area of 5 cm^2 were purchased from Smart Membranes. A Nafion NR211 PEM (Ion Power) was hot-pressed onto the template at 150 °C and 2000 lb for 10 min. The interface between the template and channel-imprinted PEM was etched away until the template and PEM detached by soaking in 2 M KOH overnight. The resulting K^+-form textured PEM was washed in deionized water (Millipore, 18.2 MΩ cm) for 20 min and dried at ambient conditions.

Cathode catalyst ink was prepared by combining TEC10V40E (Tanaka) VULCAN XC72-supported Pt catalyst, a mixture of 4:3 (v:v) H_2O:1-propanol in the ratio of 0.00234 g carbon per g liquids, and the quantity of D2020 Nafion dispersion (~20 wt% 1000 EW Nafion in water and 1-propanol, Chemours) necessary to achieve

the prescribed ionomer-to-carbon (I/C) ratio. The ink was homogenized via magnetic stirring for 20 min followed by bath ultrasonication for 20 min over ice.

The cathode catalyst was deposited on the channel-imprinted side of the PEM except where as-received (flat) NR-211 PEMs were used as control samples. Catalyst deposition was carried out using a Sono-Tek ultrasonic spray coater. The PEM was held in place with a vacuum plate (unheated), and the PEM surface outside the 5cm^2 active area was masked with a 0.001" Kapton film. For the cathode CL, the ink flow rate was set to 0.04 mL min^{-1} with 0.36 kPa shaping air pressure. Ink was sprayed until a cathode catalyst loading of ~300 μg_{Pt} cm^{-2} was confirmed via x-ray fluorescence (XRF, QUANT'X EDXRF Spectrometer).

The anode catalyst ink was prepared as above but with TEC10V20E (Tanaka) catalyst and I/C of 0.5 for all catalyst-coated membranes (CCMs). The anode catalyst layer was deposited by ultrasonic spray coating with a flow rate of 0.23 mL min^{-1} and shaping air pressure of 0.6 kPa over a vacuum hot plate heated to 95 °C until a loading of >100 μg_{Pt} cm^{-2} was confirmed via XRF. CCMs with cathode ink deposited on Nafion pillars were converted from K^+ to H^+ form by soaking in 0.5 M H_2SO_4 at 150 °C for 4 hr and then at ambient temperature overnight. The CCM was subsequently washed in deionized H_2O for 20 min and then dried at ambient conditions.

6.2.2. PEMFC TESTING

Single-cell testing was carried out using 50 cm^2 hardware (Fuel Cell Technologies) with graphite differential flow fields. The active testing area was reduced to 5 cm^2 to match the CCM active area using polyurethane gaskets. The

CCM was sandwiched between GDLs (Sigracet SGL 22BB) followed by the gasket material then flow fields then hardware, and the assembly was secured with 8 lubricated hexagonal bolts tightened with a torque wrench to 85 lb in.

Testing was conducted with a Scribner and Associates 850g fuel cell test station (10/50/100 series) equipped with potentiostat, auto multigas, and auxiliary temperature control unit. Cell conditioning was carried out via potentiostatic hold at 0 V under H_2/air (1000/3000 sccm) at 30 °C and 80 °C dew point for 90 min. A polarization curve was subsequently obtained by measuring the cell current at potentials ranging from 0.4 to 0.95 V for 4 min at each point at 80 °C and 100 % relative humidity (RH). The mass activity (MA) was then measured via potentiostatic hold at 0.9 V (iR-corrected) under H_2/O_2 for 15 min. H_2 crossover (0.5 V potentiostatic hold) and electrochemically-active surface area (HUPD ECSA, cyclic voltammetry between 0.1 and 1 V at 50 mV s^{-1}) were measured under H_2/N_2. The above testing constituted a single recovery cycle. 6 recovery cycles were conducted in total for each MEA after which the cell performance was stable.

PEMFC performance was evaluated at various temperatures, pressures, and RH with H_2 flowing over the anode and air, HelOx (21 % O_2, balance He), or half air (10.5% O_2, balance N_2) flowing over the cathode. At each condition, a polarization curve was measured as above; electrochemical impedance spectroscopy (EIS) was carried out at 200, 1000, 1500, and 2000 (where possible) mA cm^{-2}; and sheet resistance was quantified via EIS under H_2/N_2 with 0.5 V DC bias. Finally, the oxygen transport resistance (RO_2) was quantified by

flowing a dry O_2 mole fraction of 0.005, 0.01, or 0.015 (balance N_2) over the cathode and measuring the limiting current at 3.5, 7, 10.5, 14, 17.5, 21, 24.5, or 28 psi_g backpressure.

6.3. RESULTS AND DISCUSSION

6.3.1. ELECTRODE PROPERTIES

The array electrode fabrication process is detailed in Figure 34. After hot pressing and removal of the template, successful patterning of the Nafion NR-211 surface was confirmed via laser profilometry (Figure 71) and validated via SEM (Figure 34, bottom). The PEM surface is characterized by a regular square array of 10-11 μm cylindrical channel features 5-6 μm in diameter with ~12 μm inter-channel distance. After catalyst deposition using the spray coating parameters detailed above, the channels lean slightly but remain upright. Micrometer-scale cracks, caused by swelling of the channels during ink deposition and subsequent relaxation, are present in the catalyst material between pillars. To examine the effect of Nafion channels on the resulting electrode performance, array electrodes were compared with flat control electrodes. In-situ single-cell testing was carried out using MEAs with I/C = 0.15, 0.3, or 0.5 in the cathode CL. In the following subsections, the array electrodes are evaluated in terms of catalyst utilization, O_2 transport, and H^+ transport.

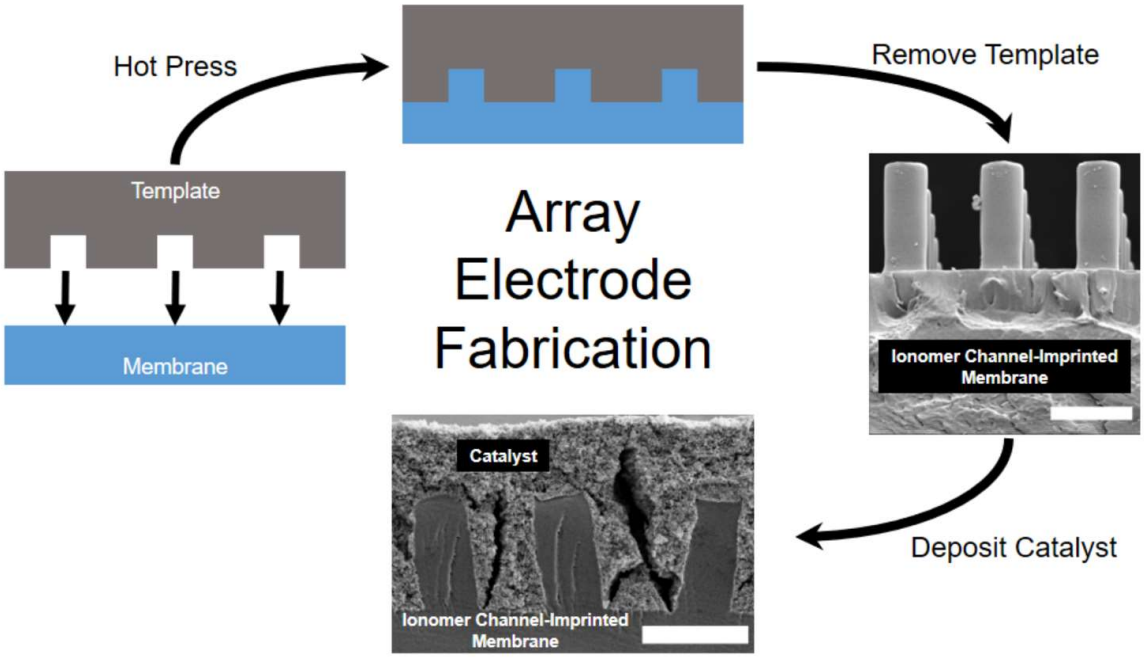

Figure 34. Schematic illustrating preparation of array electrodes. Scale bar width corresponds to 10 μm in SEM images.

H_2 crossover values for each MEA (Figure 72) are somewhat variable, although they are within the same order of magnitude. In particular, the crossover currents for the I/C = 0.15 array and I/C = 0.3 flat electrodes are relatively low. In general, the crossover current densities observed in this study are higher than those reported for the Nafion NR-211 PEM in the literature[236–238]. One possible explanation is that the somewhat higher crossover observed in this study results from the greater compression applied to the cell[239] in this work. The somewhat random variation of measured crossover currents suggests that texturing of the cathode side of the PEM to create channels did not have a significant adverse impact on the mechanical integrity of the PEM.

The ECSA as determined by the hydrogen underpotential deposition (HUPD) method[240] (Figure 73) is equivalent for each electrode and agrees with[241–245] published values for Vulcan carbon-supported Pt catalyst. It is important to note that the ECSA values in Figure 73 were measured under flooding conditions and therefore do not relate to the ionomer coverage. However, it can be inferred from the constant ECSA across all electrodes that neither deposition on the Nafion channel array nor variation of I/C alter agglomerate morphology to the extent that active sites are rendered inaccessible.

6.3.1.1. CATALYST UTILIZATION

The MA is compared for each electrode in Figure 35. The use of array electrodes confers a significant improvement in MA at each I/C. Notably, the MA of the I/C = 0.15 electrode improves by 83 %. The MAs of the I/C = 0.3 and 0.5 electrodes improve by 22 % and 16 % respectively.

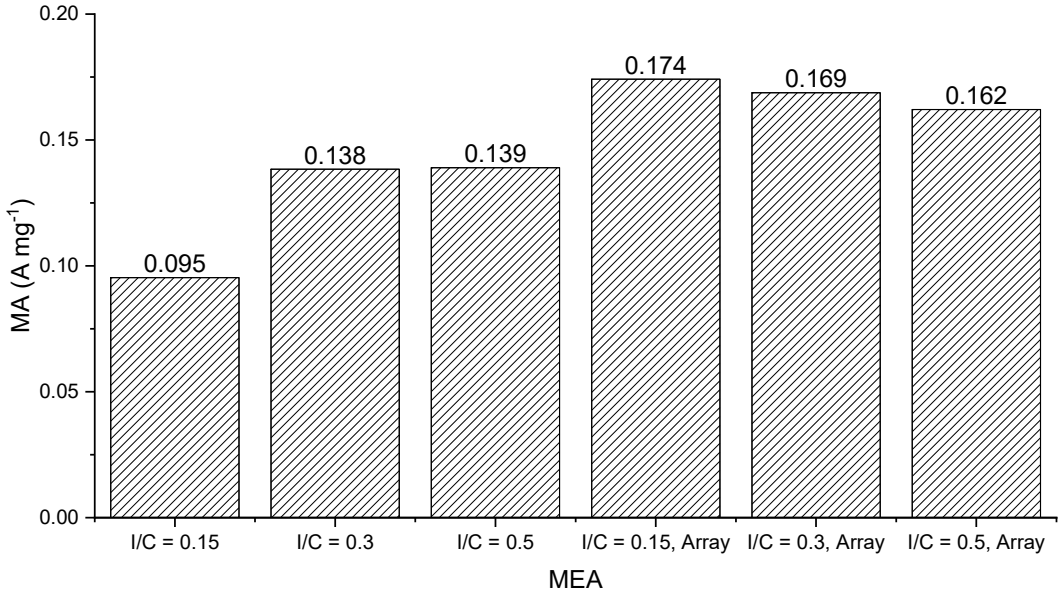

Figure 35. MA of Pt in the cathode CL of each MEA. Measured under H_2/O_2 at 0.9 V (HFR, Tafel, and crossover-corrected).

Garrick et al showed using CO displacement studies that the degree of sulfonate adsorption (ionomer poisoning) on the Pt surface increases asymptotically with increasing I/C [246]. The variation in MA between the electrodes in Figure 35 can be explained by the interplay between I/C, ionomer poisoning, and H^+ percolation. The very low MA exhibited by the I/C = 0.15 flat electrode is indicative of inhibited H^+ percolation caused by low ionomer coverage. Conversely, the similar MAs exhibited by the I/C = 0.3 and 0.5 flat electrodes suggests adequate H^+ percolation with electrode kinetics limited by ionomer poisoning. Implementation of ionomer channels in the I/C = 0.3 and 0.5 electrodes provides streamlined pathways for H^+ transport which moderately

improve the MA, albeit somewhat less so in the case of the relatively ionomer-rich I/C = 0.5 electrode. However, ionomer poisoning limits any further gains in terms of kinetic activity for the I/C = 0.3 and 0.5 electrodes. Finally, implementation of ionomer channels in the I/C = 0.15 electrode, which possesses a low degree of ionomer poisoning, ameliorates its significant H^+ transport limitations, causing this electrode to exhibit the best ORR kinetics out of the sample set considered in this study.

Studies on Vulcan carbon-based Pt indicate that the ionomer coverage, or portion of Pt material in contact with the H^+-percolating network, increases sharply from I/C = 0 and stabilizes around I/C = 0.375 [199,209] after which point the benefits reaped via connection of additional Pt to the H^+-percolating network by adding more ionomer is increasingly offset by kinetic losses from ionomer poisoning[246] and electronic isolation. In the absence of ionomer poisoning and electronic isolation, the addition of more ionomer would serve to decrease charge transfer resistance by increasing the effective cross-section of the H^+-conducting pathway and providing a shorter pathway between a given agglomerate and the membrane. It can be argued that the ionomer channels in the array electrode provide these benefits without conferring additional electronic isolation. However, this raises the question of ionomer poisoning by the channels themselves. In other words, why are kinetic improvements from enhanced H^+ percolation not offset by additional sulfonate adsorption from the channel Nafion as would be the case if the I/C were simply increased? Such behavior implies a difference in interfacial properties between the Pt surface and thin film vs. channel Nafion.

Studies by Shrivastava[247] and Kodama[248] indicate that ionomer poisoning is attenuated with increasing ionomer hydration due to the replacement of sulfonate groups with water at the Pt surface, enhancing local and interfacial O_2 diffusivity[249]. Importantly, these studies were carried out below 100 % RH, so interfacial water was provided from the ionomer itself and not as free liquid from the reactant gas stream. It has been demonstrated that water uptake/capacity is much lower in thin-film[250] than bulk-like[251] ionomer. Therefore, assuming the Nafion channels in the array electrodes maintain bulk-like character after hot pressing, it is possible that the channels cause less ionomer poisoning at the Pt surface than thin-film ionomer by providing additional interfacial water. However, this argument is somewhat speculative and merits further study.

Mass activity measurements show that the array electrode is a powerful tool capable of improving ORR kinetics by enhancing H^+ percolation without isolating agglomerates from e^- percolation or conferring substantial additional ionomer poisoning.

6.3.1.2. OXYGEN TRANSPORT

Characterization of the mass transport properties of each electrode was carried out using the limiting-current RO_2 method. The theory of this method is detailed in the literature[189]. Briefly, the concentration of O_2 in the cathode gas is reduced to the point where the concentration of O_2 is zero at the electrode surface at low voltage. The crossover-corrected limiting current (i_l, Figure 33) is measured at low voltage, and R_{O_2} is calculated using Equation 54.

$$R_{O_2} = C_{O_2,GC}\frac{4F}{i_l}$$ *Equation 54*

where F is Faraday's constant and $C_{O_2,GC}$ is the concentration of O_2 in the gas channels which is calculated from the humidity-corrected inlet gas composition. As noted previously (Equation 52), R_{O_2} is made up of pressure-dependent (Fickian) contributions (R_F, attributed to molecular diffusion in large pores such as in the GDL) and pressure-independent (non-Fickian) contributions (R_{NF}, attributed to Knudsen diffusion in the MPL and CL as well as diffusion of O_2 through water and/or ionomer thin-films in the CL, Equation 53).

The average R_{O_2} is plotted as a function of pressure in Figure 36. R_F is more or less the same around 0.004 s cm^{-1} kPa_{abs}^{-1} for each MEA. R_{NF} is within the same order of magnitude for all except the I/C = 0.15 flat electrode which exhibits a significantly higher value.

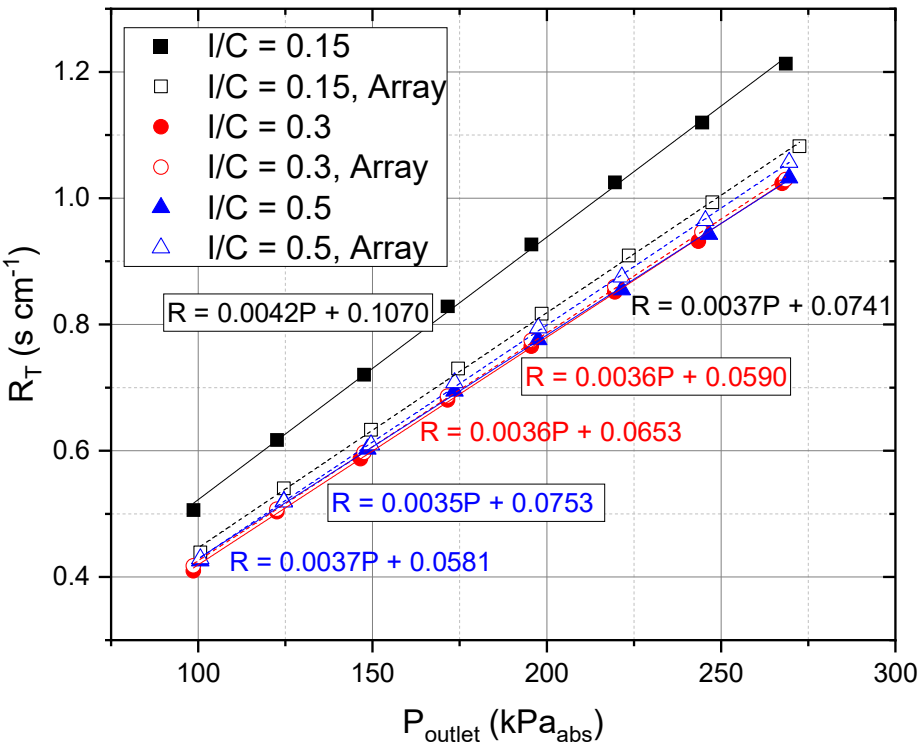

Figure 36. Average O_2 transport resistance as a function of pressure. Calculated from RO_2 limiting current. Boxed equations correspond to flat electrodes.

Recent work has demonstrated that the pore size distribution skews larger in CLs with low I/C [252]. The inverse relationship between I/C and pore size distribution gives a higher apparent O_2 diffusivity within low-I/C CLs due to reduced R_{Knud}^{CL}. It has been shown that the CL is thinner at very low I/C [209]. With the same torque applied to the cell bolts, a thinner CL will cause the GDL to be slightly less compressed, giving a smaller R_F [195]. However, the difference in CL thickness between the I/C = 0.15 and the I/C = 0.3 or 0.5 flat electrodes is likely sufficiently

small as to have a relatively minor impact pressure-dependent RO_2 behavior. The higher R_{NF} observed for the I/C = 0.15 flat electrode can be explained by R_{ion}^{CL}. Analysis by Nonoyama et al reveals that R_{ion}^{CL} (Equation 55) is sensitive to the O_2 permeability of the ionomer (ψ_{ion,O_2} – a function of ionomer properties and directly related to RH), the effective ionomer film thickness (δ_{ion}^{eff}), and the effective area of Pt in contact with ionomer (A_{ion}^{eff})[189].

$$R_{ion}^{CL} \propto \frac{1}{\psi_{ion,O_2}} \frac{\delta_{ion}^{eff}}{A_{ion}^{eff}} \qquad \textit{Equation 55}$$

The ionomer coverage of the I/C = 0.15 flat electrode is very low, as demonstrated by the poor MA (Figure 35). Therefore, this electrode has very low A_{ion}^{eff} which gives a high value of R_{ion}^{CL} and in turn R_{NF}. This phenomenon of high apparent R_{ion}^{CL} due to high O_2 flux per active site at low I/C has been observed previously[245]. The incorporation of Nafion channels at I/C = 0.15 proliferates the three-phase reaction zone throughout the CL, reducing the apparent R_{ion}^{CL} and causing the O_2 transport properties of the I/C = 0.15 array electrode to fall in line with those of the I/C = 0.3 and 0.5 electrodes.

The R_{O_2} plotted in Figure 36 is an average of the R_{O_2} measured at 0.5, 1, and 1.5 dry mole % O_2 in the cathode feed gas. The R_{O_2} at these O_2 concentrations are plotted in Figure 74, Figure 75, and Figure 76 respectively. The data largely mirrors the trends in Figure 36 with the I/C = 0.15 flat electrode exhibiting the highest RO_2 and the other electrodes having similar O_2 transport properties at low (Figure 74) and moderate (Figure 75) $C_{O_2,GC}$. However, at 1.5 % O_2 (Figure

76), differences in O_2 transport properties are magnified. R_F is highest for the I/C = 0.15 flat electrode, followed by the I/C = 0.15 array electrode, followed by the other electrodes. This difference can be attributed to larger pores within the I/C = 0.15 CLs[252] which slightly increase the prevalence of molecular diffusion[189]. Further, at 1.5 % O_2, the I/C = 0.3 and 0.5 array electrodes exhibit slightly higher R_{NF} than their flat counterparts. This difference may be attributed to the presence of more solid material within the CL which increases the overall electrode thickness, making Knudsen diffusion more prevalent[189]. For each MEA, R_{O_2}increases with $C_{O_2,GC}$, consistent with Equation 54.

From the preceding observations, array electrodes possess slightly higher Knudsen diffusion resistance than their flat counterparts, although this effect is negligible. Otherwise, O_2 transport is not significantly affected by the inclusion of Nafion channels in any of the MEAs tested here, except in the case of very low I/C where the channels enhance apparent local O_2 dissolution/diffusion.

6.3.1.3. PROTON TRANSPORT

EIS under H_2/N_2 was employed to examine H^+ transport within the CL. It has been shown[253,254] that PEMFCs under this condition ideally give a Warburg-like (45 ° curve in Nyquist representation) response at high frequency from which the sheet resistance (SR), representing Ohmic losses from H^+ transport in the CL, can be estimated. H_2/N_2 impedance spectra obtained at 80 °C and 150 kPa_{abs} are plotted in Nyquist representation in Figure 37. The data were fit to the equivalent circuit model in Figure 77. Qualitatively, the extent to which the impedance spectrum projects to higher Z' indicates higher SR, and the extent to

which the model (lines) tracks the data (symbols) qualitatively indicates the goodness of fit.

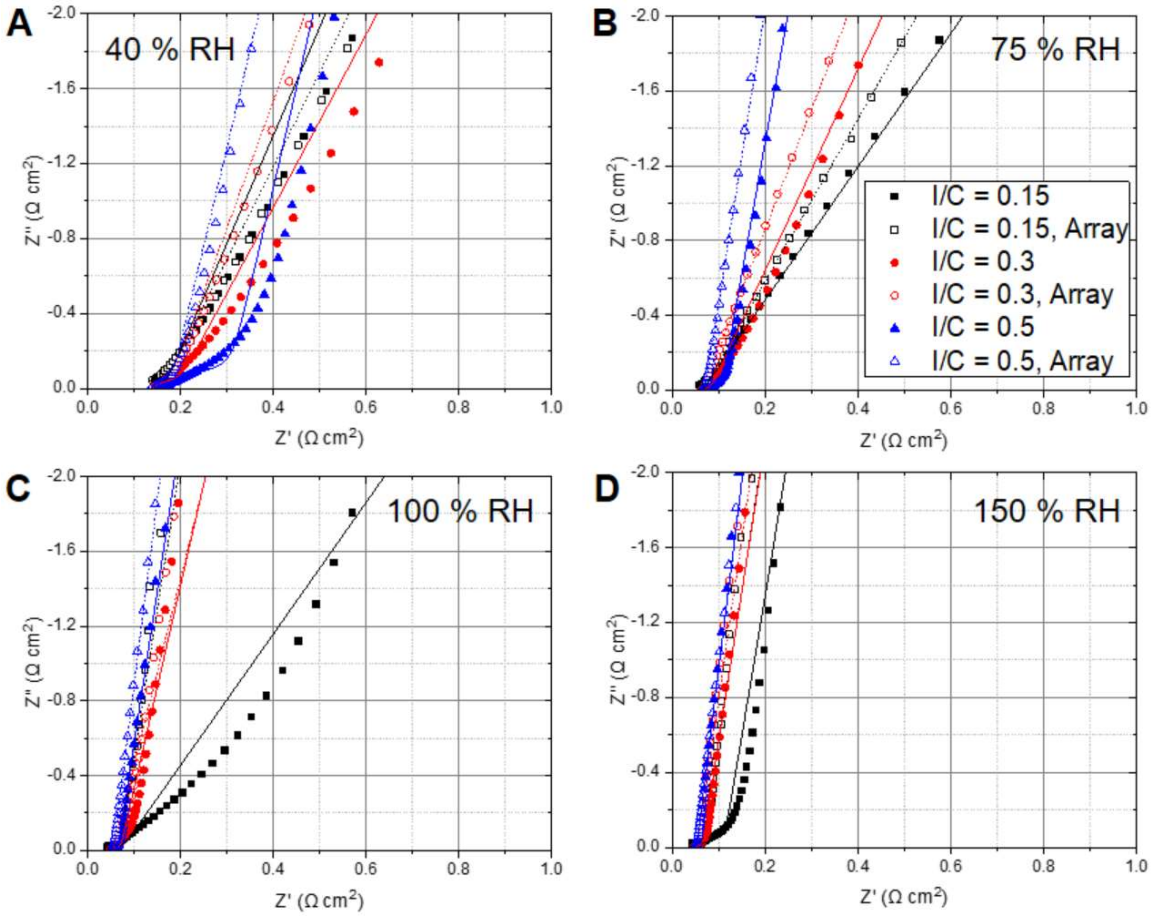

Figure 37. Nyquist representation of EIS at 0.5 V under H_2/N_2 at 80 °C, 150 kPa, and (A) 40 % RH, (B) 75 % RH, (C) 100 % RH, and (D) 150 % RH. Symbols represent raw data, and lines represent equivalent circuit fit (Figure 77).

At 40 % RH (Figure 37A), the I/C = 0.3 and 0.5 flat electrodes appear to have the highest SR, followed by I/C = 0.15 flat and array, followed by I/C = 0.3 array, followed by I/C = 0.5 array which appears to have the lowest SR. The quality of fit

appears relatively poor except for the I/C = 0.5 array electrode. At this RH, the incorporation of channels decreases the SR except for in the case of I/C = 0.15. At 75 % RH (Figure 37B), the incorporation of channels decreases the SR at each I/C, an inverse relationship exists between I/C and SR in all cases, and the fit appears to be reasonably good. At 100 (Figure 37C) and 150 % RH (Figure 37D), the impedance spectra converge, indicating similar and relatively low SR for all electrodes except for I/C = 0.15 flat which has much higher SR. At 250 kPa (Figure 79), the RH-dependent SR behavior is similar to that outlined above.

Issues with fitting the H_2/N_2 EIS data partially stem from the fact that the 45 ° (Warburg) region at high frequency is not readily apparent for all MEAs at all conditions. Figure 78 shows the same data as in Figure 37 but with the scale of axes narrowed to focus on the high-frequency region. From Figure 78, non-ideal behavior is generally observed more often at low I/C and/or low RH. Notably, the I/C = 0.15 array electrode exhibits apparent capacitive, as opposed to resistive, behavior at high frequency. This phenomenon has been observed previously in both PEMFC[253,254] and corrosion[255] systems and was attributed to a non-uniform current distribution on the electrode surface which introduces a frequency dependence to resistance. Applying this concept to the I/C = 0.15 array electrode, ionomer-deficient catalyst furthest away from ionomer channels exhibits high ionic resistance and only begins to participate in the reaction at low frequency or under direct current conditions. This implies that the majority of mass activity in this electrode is attributed to catalyst material in close contact with ionomer channels. A dense array of thin ionomer channels with low inter-

channel spacing and ionomer-free catalyst deposited in the interstitial volume may serve to increase catalyst utilization while further decreasing ionomer poisoning.

SR values calculated from the equivalent circuit fit are plotted in Figure 80A. The sum of squares in Figure 80B indicates a very poor fit to the equivalent circuit model for the I/C = 0.15 flat electrode, a relatively poor fit for the I/C = 0.3 flat electrode, a somewhat poor fit at 100 and 150 % RH for the I/C = 0.15 and 0.3 array electrodes, and a reasonably good fit for other electrodes/conditions, consistent with qualitative observations of Figure 37. From Figure 80A, the incorporation of pillars in I/C = 0.3 and 0.5 electrodes confers very low SR.

The most reliable parameters which describe the CL properties are obtained by the relatively good fit of the data at 75 % RH (Figure 37B) to the equivalent circuit model (Figure 77). From the model, τ, which constitutes a subunit of the Warburg element, corresponds to the characteristic time constant for H^+ transport within the CL. At 75 % RH, incorporation of Nafion pillars decreases τ by ~70 % for the I/C = 0.3 and 0.5 electrodes. The calculated τ is actually higher for the I/C = 0.15 array electrode than its flat counterpart, although this comparison is probably unreliable due to both the poor fit of the experimental data to the equivalent circuit model for the I/C = 0.15 flat electrode and the capacitive behavior of the I/C = 0.15 array electrode at high frequency.

These results demonstrate that ionomer channel arrays provide an avenue for rapid H^+ transport within the CL, attenuating SR. In the next section, the influence of electrode properties on cell performance will be examined.

6.3.2. ELECTRODE PERFORMANCE

Figure 38 shows the polarization behavior of each electrode under H_2/air at 80 °C and 150 kPa_{abs} backpressure. At all RHs, the ionomer channels confer a benefit to electrode performance, increasing the cell current density over a range of operating potentials. The relative improvement is greatest at low RH (Figure 38A and Figure 38B). The I/C = 0.15 flat electrode exhibits inferior performance at all conditions, owing to slow ORR kinetics as noted by comparatively large overpotentials at very low current densities and supported by MA data in Figure 35. Conversely, the I/C = 0.15 array electrode performs similarly to the I/C = 0.3 and 0.5 electrodes at high and moderate potentials, although its performance is diminished in the range of ~0.4 – 0.6 V where mass transport limitations are dominant at 100 and 150 % RH (Figure 38C and Figure 38D respectively).

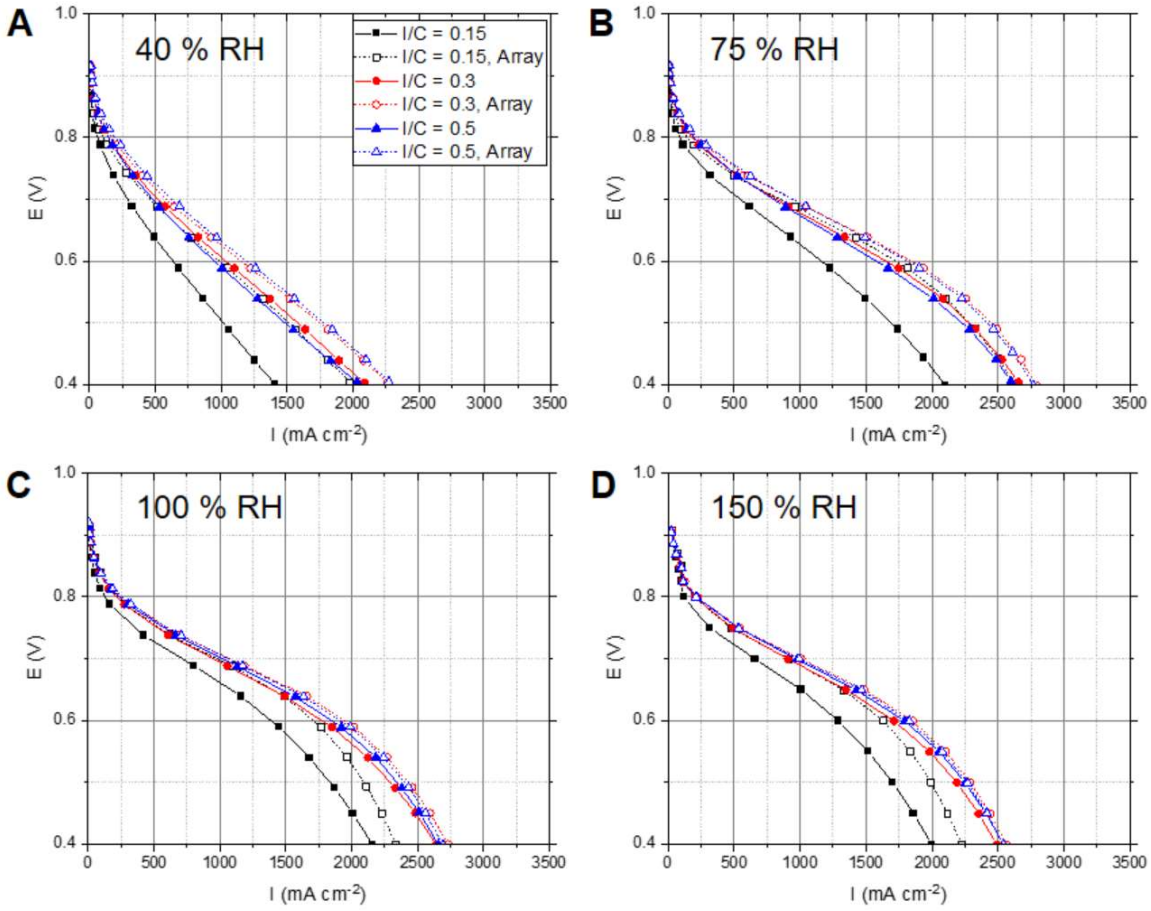

Figure 38. Polarization curves measured under H_2/air (1000/3000 sccm) at 80 °C; 150 kPa_{abs} outlet pressure; and (A) 40 % RH, (B) 75 % RH, (C) 100 % RH, or (D) 150 % RH.

The comparatively large difference in polarization behavior between the best-overall-performing flat and array electrodes (I/C = 0.3 and 0.5) at low RH correlates well with differences in SR at these conditions (Figure 37), indicating that the ionomer channels attenuate Ohmic losses related to ionomer dehydration. This is supported by the diminishing magnitude of improvement with increasing RH. As noted previously, thin-film CL ionomer has lower RH-

dependent water uptake and ionic conductivity[250] than the bulk ionomer[251] which makes up the membrane. In addition to ionomer channels decreasing the time constant for H^+ transport within the CL (discussed in the previous section), increased contact area with comparatively water-rich channels may improve agglomerate hydration at low RH.

The sharp drop in current density exhibited by the I/C = 0.15 array electrode from 75 to 100 % RH (Figure 38B and Figure 38C respectively) at low voltages is indicative of a high sensitivity to electrode hydration which adversely impacts RO_2 for this electrode. Qualitatively, array electrodes perform very well at 75 % RH (Figure 38B), indicating that incorporation of ionomer channels in the cathode has significant potential to improve the performance of PEMFCs where full humidification of gases is not always practical, i.e. automotive fuel cells[256].

Cell performance was also evaluated at elevated pressure (250 kPa_{abs}) and/or temperature (Figure 81). Trends in comparative electrode performance outlined above largely persist at higher pressure, with ionomer channels improving electrode performance and the I/C = 0.3 and 0.5 electrodes having the best performance overall. The performances of both I/C = 0.15 electrodes converge at 80 °C and 100 % RH (Figure 81B) at low potentials, again indicating a problem with removal of product water which inhibits O_2 transport at moderate-high RH in the I/C = 0.15 array electrode. This is supported by the superior sheet resistance observed for the I/C = 0.15 array electrode at 100 % RH as compared to the I/C = 0.3 electrodes (Figure 37C) which implies H^+ transport through free water and thus flooding within the CL. The nature of this effect is unknown and merits

further consideration, although it could possibly be attributed to atypical CL pore properties within the I/C = 0.15 array electrode or simply experimental error. The performance gap between pillar and flat electrodes is exacerbated at 94 °C and 65 % RH (Figure 81C), showing that improved catalyst utilization (Figure 35) allows array electrodes to reap additional benefits from increased reactant activity.

To qualitatively probe the effect of mass transport on electrode performance, additional polarization curves were measured in HelOx (Figure 82). The bulk diffusion coefficient of O_2 is higher in HelOx than in air, and differences in cell performance in air vs. HelOx are indicative of mass transport limitations caused by bulk molecular diffusion (R_F). The performance at low voltage is enhanced for all electrodes under HelOx (Figure 82) as opposed to air (Figure 38C), indicating that molecular diffusion limitations are non-negligible for these cells. Moreover, the performance gap between flat and pillar electrodes is widened under HelOx as opposed to air, indicating that molecular diffusion plays a greater role within the array electrodes. Although this notion is not supported by the relatively consistent R_F measured in limiting current R_{O_2} studies (Figure 36), the significantly higher $C_{O_2,GC}$ used in the HelOx studies increases the overall R_{O_2} (Equation 54), exacerbating minor differences in R_F which may not be visible at lower $C_{O_2,GC}$. Cracks formed within the CL of the array electrodes due to ionomer channel swelling during catalyst deposition (Figure 34) may serve as the locus of additional molecular diffusion within the CL.

Aside from the demonstrably lower Ohmic losses within the CL of the array electrodes (Figure 37), it is possible that the hot pressing required to create the ionomer channels (Figure 34) simply thins the PEM, decreasing its H^+ transport resistance. If so, a significant portion of performance gains in the array electrodes would not be attributable to the ionomer channels themselves. If present, such a difference would manifest as lower high-frequency resistance (HFR). The HFR of each MEA measured at each experimental condition is plotted in Figure 83. In general, the magnitude of the HFR is more or less the same for each MEA. However, the I/C = 0.15 flat sample tends to have slightly higher HFR over all experimental conditions. This could be related to poor ionic contact between the membrane and ionomer-deficient CL. As noted previously, the I/C = 0.15 array electrode exhibits atypical capacitive behavior at high frequency, so the estimation of HFR by either taking the real component of impedance at 5000 Hz or extrapolating the high-frequency component of the equivalent circuit fit to $Z'' = 0$ gives results which likely overestimate or underestimate the HFR of this MEA respectively. Regardless, estimates of this sample's HFR from these methods are included in Figure 83 and subsequent discussion.

To examine the contribution of HFR variations to electrode polarization behavior, the cell voltage was corrected for HFR and plotted as a function of current density in Figure 84. In every case, a significant improvement in cell activity persists for the I/C = 0.15 array electrode as compared to its flat counterpart. HFR correction of the I/C = 0.15 array electrode performance gives somewhat

strange polarization curves at some conditions due to the capacitive behavior of this sample at high frequency. Even after HFR correction, the performance improvement persists for the other electrodes with ionomer channels improving the current density by up to 100's of mA cm^{-2} at benchmark potentials – particularly at low RH. In conclusion, membrane properties do not significantly vary between MEAs.

EIS under H_2/air at 75 and 100 % RH is plotted for each MEA in Figure 85. The high-frequency capacitive behavior characteristic of the I/C = 0.15 array electrode is again apparent. From qualitative analysis of the EIS data, as expected, the reaction is dominated by activation kinetics at both 75 (Figure 85A) and 100 % RH (Figure 85C) at low current density, although improved electrode hydration at 100 % RH decreases the charge transfer resistance and HFR slightly. The I/C = 0.5 flat electrode exhibits very low charge transfer resistance and high HFR at 75 % RH and 200 mA cm^{-2} (Figure 37), which is consistent with the high HFR observed in Figure 83B. The nature of this effect is unclear. A second semi-circle at low frequency corresponding to mass transport resistance becomes apparent at higher current density (Figure 85B). At 100 % RH (Figure 85D), the I/C = 0.3 and 0.5 electrodes exhibit similar resistive character as at 75 % RH (Figure 85B), but both I/C = 0.15 electrodes show a dramatic increase in mass transport resistance, consistent with low-voltage polarization behavior (Figure 38C).

The absolute performances of each electrode at all testing conditions are compared in terms of power density at 0.7 V in Figure 39. At 0.7 V, a mixed ORR mechanism is present where the reaction rate is significantly influenced by

kinetic, Ohmic, and mass transport factors. In general, incorporation of ionomer channels in the cathode CL improves cell operation at this benchmark voltage. Due to enhanced electrode kinetics (Figure 35) and reduced Ohmic losses (Figure 37), the pillar electrodes outperform their flat counterparts under every condition.

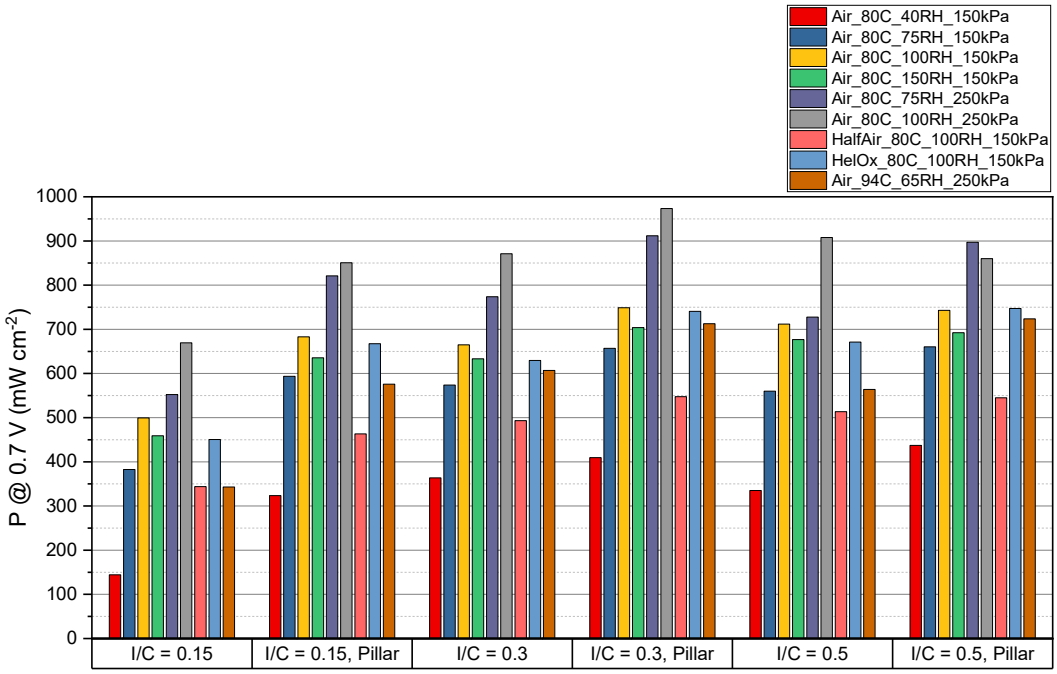

Figure 39. Comparison of power density at 0.7 V for each testing condition.

The bar chart representation of cell performance in Figure 39 is employed in Figure 86 and Figure 87 to further deconvolute the contributions of various losses to electrode performances at 0.8 and 0.6 V respectively. At 0.8 V, the effect of catalyst activation kinetics is more pronounced, but Ohmic losses are still considerable; reaction rate is represented here in terms of current density in

accordance with Department of Energy (DOE) performance targets[257]. At 0.6 V, the effects of R_{O_2} become more prominent, but Ohmic losses contribute to performance at this voltage as well.

Under air at 80 °C and 150 kPa_{abs}, ionomer channels improve the performance of electrodes at each I/C at both 0.8 and 0.6 V. Electrode performance is also improved by ionomer channels at 0.8 or 0.6 V and 250 kPa_{abs}. At 0.6 V (Figure 87), electrode performance under HelOx is approximately the same as under air for the flat electrodes, but somewhat higher for array electrodes under HelOx as opposed to air, again highlighting the enhanced role of molecular diffusion in array electrodes.

The I/C = 0.5 array electrode appears to have the best overall performance over the potentials and testing conditions explored here. However, the I/C = 0.3 pillar electrode generally exhibits better performance at high pressure. Although pillars significantly improve electrode performance at the standard testing condition of Air, 80 °, 100 % RH, and 150 kPa_{abs}, none of the electrodes here exceed the ultimate DOE performance target of 300 mA cm^{-2} at 0.8 V (Figure 86). However, the pillar electrodes perform favorably as compared with other Vulcan carbon-supported Pt-based electrodes reported in the literature[258–261].

Finally, the relative improvement conferred by array electrodes, calculated via comparison with flat electrode current density, at 0.8, 0.7, or 0.6 V is detailed in Figure 40A – C respectively. Most notably, incorporation of ionomer channels in the I/C = 0.15 electrode improves performance by ~70 % over a range of RH at 0.8 V, effectively conferring viability to low-I/C CLs. However, the magnitude of

this improvement diminishes at lower voltages, particularly as RH increases, as mass transport limitations become apparent. Further, supporting the I/C = 0.5 catalyst layer on ionomer channels enables performance gains of up to ~35 % beyond the optimized conventional flat electrode based upon commercial Vulcan carbon-supported Pt.

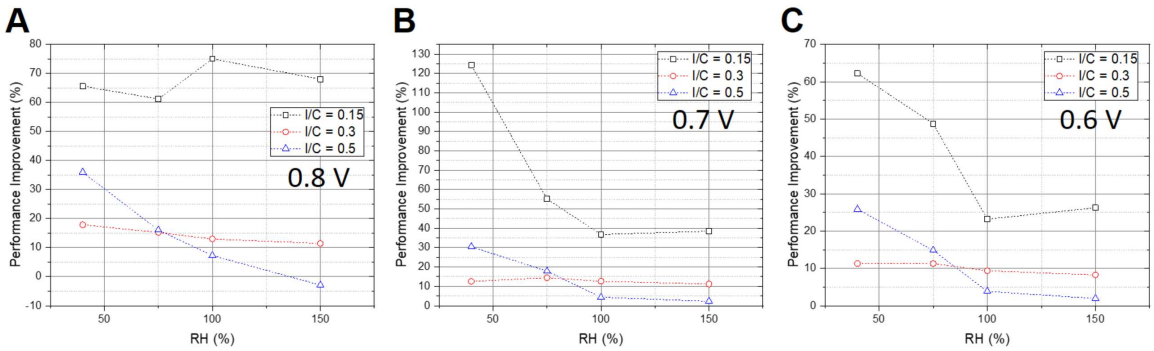

Figure 40. Relative performance improvement attained by using array as opposed to flat electrodes in the cathode CL under H_2/air at 80 °C; 150 kPa_{abs}; and (A) 0.8 V, (B) 0.7 V, or (C) 0.6 V.

6.4. CONCLUSIONS AND OUTLOOK

This work demonstrates the utility of an array electrode based upon ionomer channels for use in the PEMFC cathode catalyst layer. As demonstrated by sheet resistance measurements, the ionomer channels facilitate proton transport within the catalyst layer. Increased proton percolation confers a significant improvement in catalyst utilization without adversely impacting electron percolation, oxygen transport, or catalyst poisoning via sulfonate adsorption. Array electrodes based upon the *optimized* I/C = 0.5 Vulcan carbon-supported Pt catalyst layer exhibit

significantly higher performance than conventional electrode structures, particularly at low relative humidity. Moreover, the array electrode structure enables utilization of low-I/C catalyst material which exhibits high kinetic performance due to reduced sulfonate poisoning. Further gains in array electrode activity may be pursued by utilizing a dense array of thin (nanometer-scale diameter) ionomer channels with thin columns of catalyst material based upon Vulcan carbon deposited in the interstitial volume, eliminating the need for ionomer impregnation within the catalyst layer altogether and allowing for ORR to proceed in the absence of extraneous kinetic inhibition.

Although the Vulcan carbon-based catalyst employed in this study has favorable durability due to its high degree of graphitization[243] and good transport properties due to its surface-exposed active sites[216], its kinetic performance is much lower than that exhibited by high surface-area[216] or mesoporous[204] carbons because all of its Pt active sites are necessarily in contact with poisoning ionomer. The translation of array electrodes to catalyst layers based upon porous carbon types may enable record-breaking performance by allowing for a reduction in the relatively high optimal ionomer content required for these catalysts, improving percolation of reactants to Pt particles in primary pores and reducing the poisoning of surface active sites without sacrificing ionic conductivity. Furthermore, the benefits conferred by array electrodes may be applicable to other fuel cell types such as direct methanol, alkaline, etc.

REFERENCES

1. US Energy Facts Explained. *US Energy Inf. Adm.* (2021).

2. Ritchie, H. & Roser, M. Energy. *OurWorldInData.org* https://ourworldindata.org/energy (2020).

3. IEA. EIA: International Energy Outlook 2019 Presentation. *Int. Energy Agency* 18 (2019).

4. Halbouty, M. *Giant Oil and Gas Fields of the Decade, 1990-1999*. (American Association of Petroleum Geologists, 2003).

5. BP. *Statistical Review of World Energy*. (2021).

6. Helm, D. Peak oil and energy policy-A critique. *Oxford Rev. Econ. Policy* **27**, 68–91 (2011).

7. Tyndall, J. XXXVI. On the absorption and radiation of heat by gases and vapours, and on the physical connexion of radiation, absorption, and conduction.—The bakerian lecture. *London, Edinburgh, Dublin Philos. Mag. J. Sci.* **22**, 273–285 (1861).

8. Solomon, S. *et al.* IPCC, 2007: Climate Change 2007: The Physical Science Basis. Contribution of Working Group I to the Fourth Assessment Report of the Intergovernmental Panel on Climate Change. *Cambridge*

Univ. Press **4**, (2007).

9. Huber, M. & Knutti, R. Anthropogenic and natural warming inferred from changes in Earth's energy balance. *Nat. Geosci.* **5**, 31–36 (2012).

10. Lean, J. L. Cycles and trends in solar irradiance and climate. *Wiley Interdiscip. Rev. Clim. Chang.* **1**, 111–122 (2010).

11. Collins, M. *et al.* Long-term climate change: Projections, commitments and irreversibility. in *Climate Change 2013 the Physical Science Basis: Working Group I Contribution to the Fifth Assessment Report of the Intergovernmental Panel on Climate Change* vol. 9781107057 1029–1136 (2013).

12. NOAA National Centers for Environmental information, Climate at a Glance: Global Time Series. https://www.ncdc.noaa.gov/cag/ (2021).

13. Houghton, J. T., Jenkins, G. J. & Ephraums, J. J. Climate change: the IPCC scientific assessment. *Clim. Chang. IPCC Sci. Assess.* (1990) doi:10.2307/1971875.

14. Sherwood, S. C., Dixit, V. & Salomez, C. The global warming potential of near-surface emitted water vapour. *Environ. Res. Lett.* **13**, 104006 (2018).

15. IPCC SR 1.5°. Global warming of 1.5°C. An IPCC Special Report on the impacts of global warming of 1.5°C above pre-industrial levels and related global greenhouse gas emission pathways, in the context of strengthening the global response to the threat of climate change,. *Ipcc - Sr15* **2**, 17–20

(2018).

16. Cowtan, K. *et al.* Robust comparison of climate models with observations using blended land air and ocean sea surface temperatures. *Geophys. Res. Lett.* **42**, 6526–6534 (2015).

17. IPCC *et al. Climate Change 2021: The Physical Science Basis. Contribution of Working Group I to the Sixth Assessment Report of the Intergovernmental Panel on Climate Change*. *Cambridge University Press* https://elib.dlr.de/137584/ (2021).

18. UNEP CLIMATE ACTION. UNFCCC COP 21 Paris France - 2015 Paris Climate Conference. https://www.cop21paris.org/about/cop21 (2017).

19. *Renewable Power Generation Costs in 2020*. https://scholar.google.com/scholar?hl=en&as_sdt=0%2C32&q=%22Renewable+Power+Generation+Costs+in+2020%22&btnG= (2021).

20. Ould Amrouche, S., Rekioua, D., Rekioua, T. & Bacha, S. Overview of energy storage in renewable energy systems. *Int. J. Hydrogen Energy* **41**, 20914–20927 (2016).

21. Zhang, C. *et al.* Charging optimization in lithium-ion batteries based on temperature rise and charge time. *Appl. Energy* **194**, 569–577 (2017).

22. Thomas, C. E. Fuel cell and battery electric vehicles compared. *Int. J. Hydrogen Energy* **34**, 6005–6020 (2009).

23. Edwards, P. P., Kuznetsov, V. L. & David, W. I. F. Hydrogen energy.

Philos. Trans. R. Soc. A Math. Phys. Eng. Sci. **365**, 1043–1056 (2007).

24. IEA. *The Future of Hydrogen*. *The Future of Hydrogen* (2019). doi:10.1787/1e0514c4-en.

25. Zou, X. & Zhang, Y. Noble metal-free hydrogen evolution catalysts for water splitting. *Chem. Soc. Rev* **44**, 5148 (2015).

26. Mayyas, A. *et al. Manufacturing Cost Analysis for Proton Exchange Membrane Water Electrolyzers*. *National Renewable Energy Laboratory* https://www.nrel.gov/docs/fy10osti/72740.pdf. (2019).

27. H2@Scale | Department of Energy. *Hydrogen and Fuel Cell Technologies Office* https://www.energy.gov/eere/fuelcells/h2scale.

28. Larminie, J. & Dicks, A. *Fuel cell systems explained: Second edition*. *Fuel Cell Systems Explained: Second Edition* vol. 2 (J. Wiley Chichester, UK, 2013).

29. Shirvanian, P. & van Berkel, F. Novel components in Proton Exchange Membrane Water Electrolyzers (PEMWE): Status, challenges and future needs. *Electrochemistry Communications* vol. 114 106704 (2020).

30. Bertuccioli, L. *et al. Study on development of water electrolysis in the EU*. *Final Report in Fuel Cells and Hydrogen, Joint Undertaking* vol. 1 https://www.fch.europa.eu/sites/default/files/study electrolyser_0.pdf (2014).

31. Bernt, M., Siebel, A. & Gasteiger, H. A. Analysis of Voltage Losses in PEM

Water Electrolyzers with Low Platinum Group Metal Loadings. *J. Electrochem. Soc.* **165**, F305–F314 (2018).

32. Dumont, J. Graphite and Graphene Oxide Based PGM-Free Model Catalysts for the Oxygen Reduction Reaction. (2017).

33. Ooka, H., Huang, J. & Exner, K. S. The Sabatier Principle in Electrocatalysis: Basics, Limitations, and Extensions. *Frontiers in Energy Research* vol. 9 (2021).

34. Sabatier, P. La catalyse en chimi organique. https://scholar.google.com/scholar?hl=en&as_sdt=0%2C32&q=Sabatier%2C+F.+La+catalyse+en+chimie+organique%3B+Berauge%3A+Paris%2C+1920&btnG= (1920).

35. Trasatti, S. Work function, electronegativity, and electrochemical behaviour of metals. III. Electrolytic hydrogen evolution in acid solutions. *J. Electroanal. Chem.* **39**, 163–184 (1972).

36. Quaino, P., Juarez, F., Santos, E. & Schmickler, W. Volcano plots in hydrogen electrocatalysis-uses and abuses. *Beilstein J. Nanotechnol.* **5**, 846–854 (2014).

37. Lasia, A. Hydrogen evolution reaction. in *Handbook of Fuel Cells* vol. 2 (2010).

38. Gupta, A. *et al.* Intense pulsed light, a promising technique to develop molybdenum sulfide catalysts for hydrogen evolution. *Nanotechnology* **30**,

(2019).

39. Garcia-Navarro, J. C., Schulze, M. & Friedrich, K. A. Measuring and modeling mass transport losses in proton exchange membrane water electrolyzers using electrochemical impedance spectroscopy. *J. Power Sources* **431**, 189–204 (2019).

40. Bard, A. & Faulkner, L. *Electrochemical Methods: Fundamentals and Applications*. doi:10.1108/acmm.2003.12850eae.001.

41. Liang, S. *et al.* Au and Pt co-loaded g-C 3 N 4 nanosheets for enhanced photocatalytic hydrogen production under visible light irradiation. in *Applied Surface Science* vol. 358 304–312 (Elsevier B.V., 2015).

42. Crabtree, G. W., Dresselhaus, M. S. & Buchanan, M. The Hydrogen Economy. *Phys. Today* **57**, 39–44 (2004).

43. Xia, Y. *et al.* Engineering a highly dispersed co-catalyst on a few-layered catalyst for efficient photocatalytic H2 evolution: A case study of Ni(OH)2/HNb3O8 nanocomposites. *Catal. Sci. Technol.* **7**, 5662–5669 (2017).

44. Wang, M. *et al.* An amorphous CoS: X modified Mn0.5Cd0.5S solid solution with enhanced visible-light photocatalytic H2-production activity. *Catal. Sci. Technol.* **8**, 4122–4128 (2018).

45. Liang, S. *et al.* Constructing a MoS2 QDs/CdS core/shell flowerlike nanosphere hierarchical heterostructure for the enhanced stability and

photocatalytic activity. *Molecules* **21**, 213 (2016).

46. Merki, D., Fierro, S., Vrubel, H. & Hu, X. Amorphous molybdenum sulfide films as catalysts for electrochemical hydrogen production in water. *Chem. Sci.* **2**, 1262–1267 (2011).

47. Xiong, J. *et al.* An efficient cocatalyst of defect-decorated MoS2 ultrathin nanoplates for the promotion of photocatalytic hydrogen evolution over CdS nanocrystal. *J. Mater. Chem. A* **3**, 12631–12635 (2015).

48. Bromley, R. A., Murray, R. B. & Yoffe, A. D. The band structures of some transition metal dichalcogenides. III. Group VIA: Trigonal prism materials. *J. Phys. C Solid State Phys.* **5**, 759–778 (1972).

49. Verble, J. L., Wietling, T. J. & Reed, P. R. Rigid-layer lattice vibrations and van der waals bonding in hexagonal MoS2. *Solid State Commun.* **11**, 941–944 (1972).

50. Hinnemann, B. *et al.* Biomimetic hydrogen evolution: MoS2 nanoparticles as catalyst for hydrogen evolution. *J. Am. Chem. Soc.* **127**, 5308–5309 (2005).

51. Gopalakrishnan, D., Damien, D. & Shaijumon, M. M. MoS2 quantum dot-interspersed exfoliated MoS2 nanosheets. *ACS Nano* **8**, 5297–5303 (2014).

52. Lukowski, M. A. *et al.* Enhanced hydrogen evolution catalysis from chemically exfoliated metallic MoS2 nanosheets. *J. Am. Chem. Soc.* **135**,

10274–10277 (2013).

53. Eda, G. *et al.* Photoluminescence from chemically exfoliated MoS 2. *Nano Lett.* **11**, 5111–5116 (2011).

54. Devers, E., Afanasiev, P., Jouguet, B. & Vrinat, M. Hydrothermal syntheses and catalytic properties of dispersed molybdenum sulfides. *Catal. Letters* **82**, 13–17 (2002).

55. Cummins, D. R. *et al.* Catalytic Activity in Lithium-Treated Core-Shell MoOx/MoS2 Nanowires. *J. Phys. Chem. C* **119**, 22908–22914 (2015).

56. Bilgin, I. *et al.* Chemical Vapor Deposition Synthesized Atomically Thin Molybdenum Disulfide with Optoelectronic-Grade Crystalline Quality. *ACS Nano* **9**, 8822–8832 (2015).

57. Kappera, R. *et al.* Metallic 1T phase source/drain electrodes for field effect transistors from chemical vapor deposited MoS2. *APL Mater.* **2**, (2014).

58. Ponomarev, E. A., Neumann-Spallart, M., Hodes, G. & Lévy-Clément, C. Electrochemical deposition of MoS2 thin films by reduction of tetrathiomolybdate. *Thin Solid Films* **280**, 86–89 (1996).

59. Li, Q., Newberg, J. T., Walter, E. C., Hemminger, J. C. & Penner, R. M. Polycrystalline Molybdenum Disulfide (2H-MoS2) Nano- and Microribbons by Electrochemical/Chemical Synthesis. *Nano Lett.* **4**, 277–281 (2004).

60. Liu, K. K. *et al.* Growth of large-area and highly crystalline MoS 2 thin layers on insulating substrates. *Nano Lett.* **12**, 1538–1544 (2012).

61. Druffel, T., Dharmadasa, R., Lavery, B. W. & Ankireddy, K. Intense pulsed light processing for photovoltaic manufacturing. *Sol. Energy Mater. Sol. Cells* **174**, 359–369 (2018).

62. Dharmadasa, R., Jha, M., Amos, D. A. & Druffel, T. Room Temperature Synthesis of a Copper Ink for the Intense Pulsed Light Sintering of Conductive Copper Films. *ACS Appl. Mater. Interfaces* **5**, 13227–13234 (2013).

63. Dharmadasa, R., Lavery, B., Dharmadasa, I. M. & Druffel, T. Intense pulsed light treatment of cadmium telluride nanoparticle-based thin films. *ACS Appl. Mater. Interfaces* **6**, 5034–5040 (2014).

64. Lavery, B. W. *et al.* Intense Pulsed Light Sintering of CH3NH3PbI3 Solar Cells. *ACS Appl. Mater. Interfaces* **8**, 8419–8426 (2016).

65. Li, H. *et al.* From bulk to monolayer MoS 2: Evolution of Raman scattering. *Adv. Funct. Mater.* **22**, 1385–1390 (2012).

66. Frey, G. L., Tenne, R., Matthews, M. J., Dresselhaus, M. S. & Dresselhaus, G. Raman and resonance Raman investigation of MoS2 nanoparticles. *Phys. Rev. B - Condens. Matter Mater. Phys.* **60**, 2883–2892 (1999).

67. Bozheyev, F., Valiev, D. & Nemkayeva, R. Pulsed cathodoluminescence and Raman spectra of MoS2 nanocrystals at different excitation electron energy densities and laser wavelengths. *J. Lumin.* **188**, 529–532 (2017).

68. Weber, T., Muijsers, J. C. & Niemantsverdriet, J. W. Structure of

amorphous MoS3. *J. Phys. Chem.* **99**, 9194–9200 (1995).

69. Muijsers, J. C., Weber, T., Vanhardeveld, R. M., Zandbergen, H. W. & Niemantsverdriet, J. W. Sulfidation study of molybdenum oxide using moo3/sio2/si(100) model catalysts and mo-iv3-sulfur cluster compounds. *J. Catal.* **157**, 698–705 (1995).

70. Wang, H. W., Skeldon, P., Thompson, G. E. & Wood, G. C. Synthesis and characterization of molybdenum disulphide formed from ammonium tetrathiomolybdate. *J. Mater. Sci.* **32**, 497–502 (1997).

71. Ankireddy, K., Ghahremani, A. H., Martin, B., Gupta, G. & Druffel, T. Rapid thermal annealing of CH3NH3PbI3 perovskite thin films by intense pulsed light with aid of diiodomethane additive. *J. Mater. Chem. A* **6**, 9378–9383 (2018).

72. Chen, Z. *et al.* Core-shell MoO3-MoS2 nanowires for hydrogen evolution: A functional design for electrocatalytic materials. *Nano Lett.* **11**, 4168–4175 (2011).

73. Wu, Z. *et al.* MoS2 nanosheets: A designed structure with high active site density for the hydrogen evolution reaction. *ACS Catal.* **3**, 2101–2107 (2013).

74. Benck, J. D., Chen, Z., Kuritzky, L. Y., Forman, A. J. & Jaramillo, T. F. Amorphous molybdenum sulfide catalysts for electrochemical hydrogen production: Insights into the origin of their catalytic activity. *ACS Catal.* **2**, 1916–1923 (2012).

75. Xie, J. *et al.* Defect-rich MoS2 ultrathin nanosheets with additional active edge sites for enhanced electrocatalytic hydrogen evolution. *Adv. Mater.* **25**, 5807–5813 (2013).

76. Li, Y. *et al.* MoS2 nanoparticles grown on graphene: An advanced catalyst for the hydrogen evolution reaction. *J. Am. Chem. Soc.* **133**, 7296–7299 (2011).

77. Jaramillo, T. F. *et al.* Identification of Active Edge Sites for Electrochemical H 2 Evolution from MoS 2 Nanocatalysts. *Science (80-.).* **317**, 100–102 (2007).

78. Gupta, A. J. *et al.* Effect of Stacking Interactions on the Translation of Structurally Related Bis(thiosemicarbazonato)nickel(II) HER Catalysts to Modified Electrode Surfaces. *Inorg. Chem.* **58**, 12025–12039 (2019).

79. Hoffert, M. I. *et al.* Energy implications of future stabilization of atmospheric CO2 content. *Nature* **395**, 881–884 (1998).

80. Lewis, N. S. & Nocera, D. G. Powering the planet: Chemical challenges in solar energy utilization. *Proceedings of the National Academy of Sciences of the United States of America* vol. 103 15729–15735 (2006).

81. Park, J. H., Kim, S. & Bard, A. J. Novel carbon-doped TiO 2 nanotube arrays with high aspect ratios for efficient solar water splitting. *Nano Lett.* **6**, 24–28 (2006).

82. Khaselev, O. & Turner, J. A. A monolithic photovoltaic-

photoelectrochemical device for hydrogen production via water splitting. *Science (80-.).* **280**, 425–427 (1998).

83. Kim, T. W. & Choi, K. S. Nanoporous BiVO4 photoanodes with dual-layer oxygen evolution catalysts for solar water splitting. *Science (80-.).* **343**, 990–994 (2014).

84. Sivula, K., Le Formal, F. & Grätzel, M. Solar water splitting: Progress using hematite (α-Fe 2O3) photoelectrodes. *ChemSusChem* vol. 4 432–449 (2011).

85. Turner, J. A. A realizable renewable energy future. *Science* vol. 285 687–689 (1999).

86. Kibler, L. A. Hydrogen electrocatalysis. *ChemPhysChem* vol. 7 985–991 (2006).

87. Subbaraman, R. *et al.* Enhancing hydrogen evolution activity in water splitting by tailoring Li+-Ni(OH)2-Pt interfaces. *Science (80-.).* **334**, 1256–1260 (2011).

88. Di Giovanni, C. *et al.* Bioinspired iron sulfide nanoparticles for cheap and long-lived electrocatalytic molecular hydrogen evolution in neutral water. *ACS Catal.* **4**, 681–687 (2014).

89. Popczun, E. J., Read, C. G., Roske, C. W., Lewis, N. S. & Schaak, R. E. Highly active electrocatalysis of the hydrogen evolution reaction by cobalt phosphide nanoparticles. *Angew. Chemie - Int. Ed.* **53**, 5427–5430 (2014).

90. Tang, C., Pu, Z., Liu, Q., Asiri, A. M. & Sun, X. NiS2 nanosheets array grown on carbon cloth as an efficient 3D hydrogen evolution cathode. *Electrochim. Acta* **153**, 508–514 (2015).

91. Tian, J., Liu, Q., Cheng, N., Asiri, A. M. & Sun, X. Self-Supported Cu 3 P Nanowire Arrays as an Integrated High-Performance Three-Dimensional Cathode for Generating Hydrogen from Water. *Angew. Chemie* **126**, 9731–9735 (2014).

92. Ye, G. *et al.* Defects Engineered Monolayer MoS2 for Improved Hydrogen Evolution Reaction. *Nano Lett.* **16**, 1097–1103 (2016).

93. Yan, Y., Xia, B., Xu, Z. & Wang, X. Recent development of molybdenum sulfides as advanced electrocatalysts for hydrogen evolution reaction. *ACS Catalysis* vol. 4 1693–1705 (2014).

94. Popczun, E. J. *et al.* Nanostructured nickel phosphide as an electrocatalyst for the hydrogen evolution reaction. *J. Am. Chem. Soc.* **135**, 9267–9270 (2013).

95. Kong, D., Cha, J. J., Wang, H., Lee, H. R. & Cui, Y. First-row transition metal dichalcogenide catalysts for hydrogen evolution reaction. *Energy Environ. Sci.* **6**, 3553–3558 (2013).

96. Bonde, J., Moses, P. G., Jaramillo, T. F., Nørskov, J. K. & Chorkendorff, I. Hydrogen evolution on nano-particulate transition metal sulfides. *Faraday Discuss.* **140**, 219–231 (2008).

97. Merki, D. & Hu, X. Recent developments of molybdenum and tungsten sulfides as hydrogen evolution catalysts. *Energy and Environmental Science* vol. 4 3878–3888 (2011).

98. Straistari, T. *et al.* A Thiosemicarbazone–Nickel(II) Complex as Efficient Electrocatalyst for Hydrogen Evolution. *ChemCatChem* **9**, 2262–2268 (2017).

99. Haddad, A. Z., Cronin, S. P., Mashuta, M. S., Buchanan, R. M. & Grapperhaus, C. A. Metal-Assisted Ligand-Centered Electrocatalytic Hydrogen Evolution upon Reduction of a Bis(thiosemicarbazonato)Cu(II) Complex. *Inorg. Chem.* **56**, 11254–11265 (2017).

100. Rountree, E. S. & Dempsey, J. L. Reactivity of Proton Sources with a Nickel Hydride Complex in Acetonitrile: Implications for the Study of Fuel-Forming Catalysts. *Inorg. Chem.* **55**, 5079–5087 (2016).

101. Mejia-Rodriguez, R., Chong, D., Reibenspies, J. H., Soriaga, M. P. & Darensbourg, M. Y. The hydrophilic phosphatriazaadamantane ligand in the development of H 2 production electrocatalysts: Iron hydrogenase model complexes. *J. Am. Chem. Soc.* **126**, 12004–12014 (2004).

102. Straistari, T. *et al.* Influence of the Metal Ion on the Electrocatalytic Hydrogen Production by a Thiosemicarbazone Palladium Complex. *Eur. J. Inorg. Chem.* **2018**, 2259–2266 (2018).

103. Haddad, A. Z. *et al.* Proposed Ligand-Centered Electrocatalytic Hydrogen Evolution and Hydrogen Oxidation at a Noninnocent Mononuclear Metal-

Thiolate. *J. Am. Chem. Soc.* **137**, 9238–9241 (2015).

104. Dempsey, J. L., Brunschwig, B. S., Winkler, J. R. & Gray, H. B. Hydrogen evolution catalyzed by cobaloximes. *Acc. Chem. Res.* **42**, 1995–2004 (2009).

105. Merki, D., Vrubel, H., Rovelli, L., Fierro, S. & Hu, X. Fe, Co, and Ni ions promote the catalytic activity of amorphous molybdenum sulfide films for hydrogen evolution. *Chem. Sci.* **3**, 2515–2525 (2012).

106. Xiao, P. *et al.* Molybdenum phosphide as an efficient electrocatalyst for the hydrogen evolution reaction. *Energy Environ. Sci.* **7**, 2624–2629 (2014).

107. Callejas, J. F. *et al.* Electrocatalytic and photocatalytic hydrogen production from acidic and neutral-pH aqueous solutions using iron phosphide nanoparticles. *ACS Nano* **8**, 11101–11107 (2014).

108. Chen, W. F. *et al.* Hydrogen-evolution catalysts based on non-noble metal nickel-molybdenum nitride nanosheets. *Angew. Chemie - Int. Ed.* **51**, 6131–6135 (2012).

109. Lazarides, T. *et al.* Making hydrogen from water using a homogeneous system without noble metals. *J. Am. Chem. Soc.* **131**, 9192–9194 (2009).

110. Fukuzumi, S., Yamada, Y., Suenobu, T., Ohkubo, K. & Kotani, H. Catalytic mechanisms of hydrogen evolution with homogeneous and heterogeneous catalysts. *Energy Environ. Sci.* **4**, 2754–2766 (2011).

111. Ford, P. C. The Water Gas Shift Reaction: Homogeneous Catalysis by

Ruthenium and Other Metal Carbonyls. *Acc. Chem. Res.* **14**, 31–37 (1981).

112. Dubois, M. R. & Dubois, D. L. Development of molecular electrocatalysts for CO2 reduction and H2 production/oxidation. *Acc. Chem. Res.* **42**, 1974–1982 (2009).

113. Wiese, S., Kilgore, U. J., Dubois, D. L. & Bullock, R. M. [Ni(P Me2N Ph2) 2] (BF 4) 2 as an electrocatalyst for H 2 production. *ACS Catal.* **2**, 720–727 (2012).

114. Brown, A. P. & Anson, F. C. Molecular anchors for the attachment of metal complexes to graphite electrode surfaces. *J. Electroanal. Chem.* **83**, 207–213 (1977).

115. Bullock, R. M., Das, A. K. & Appel, A. M. Surface Immobilization of Molecular Electrocatalysts for Energy Conversion. *Chemistry - A European Journal* vol. 23 7626–7641 (2017).

116. Blakemore, J. D., Gupta, A., Warren, J. J., Brunschwig, B. S. & Gray, H. B. Noncovalent immobilization of electrocatalysts on carbon electrodes for fuel production. *J. Am. Chem. Soc.* **135**, 18288–18291 (2013).

117. Mann, J. A., Rodríguez-López, J., Abruña, H. D. & Dichtel, W. R. Multivalent binding motifs for the noncovalent functionalization of graphene. *J. Am. Chem. Soc.* **133**, 17614–17617 (2011).

118. Goff, A. Le *et al.* From hydrogenases to noble metal-free catalytic nanomaterials for H 2 production and uptake. *Science (80-.).* **326**, 1384–

1387 (2009).

119. Pantani, O., Anxolabéhère-Mallart, E., Aukauloo, A. & Millet, P. Electroactivity of cobalt and nickel glyoximes with regard to the electro-reduction of protons into molecular hydrogen in acidic media. *Electrochem. commun.* **9**, 54–58 (2007).

120. Berben, L. A. & Peters, J. C. Hydrogen evolution by cobalt tetraimine catalysts adsorbed on electrode surfaces. *Chem. Commun.* **46**, 398–400 (2010).

121. Lei, H. *et al.* Electrochemical, spectroscopic and theoretical studies of a simple bifunctional cobalt corrole catalyst for oxygen evolution and hydrogen production. *Phys. Chem. Chem. Phys.* **16**, 1883–1893 (2014).

122. Mondal, B. *et al.* Cobalt corrole catalyst for efficient hydrogen evolution reaction from H2O under ambient conditions: Reactivity, spectroscopy, and density functional theory calculations. *Inorg. Chem.* **52**, 3381–3387 (2013).

123. Rodríguez-Maciá, P. *et al.* Covalent Attachment of the Water-insoluble Ni(PCy2NPhe2)2 Electrocatalyst to Electrodes Showing Reversible Catalysis in Aqueous Solution. *Electroanalysis* **28**, 2452–2458 (2016).

124. Oughli, A. A. *et al.* Dual properties of a hydrogen oxidation Ni-catalyst entrapped within a polymer promote self-defense against oxygen /639/638/77/886 /639/638/161/893 /639/638/675 /120 /128 /140/131 article. *Nat. Commun.* **9**, (2018).

125. Tran, P. D. *et al.* Noncovalent Modification of Carbon Nanotubes with Pyrene-Functionalized Nickel Complexes: Carbon Monoxide Tolerant Catalysts for Hydrogen Evolution and Uptake. *Angew. Chemie* **123**, 1407–1410 (2011).

126. Zhang, W. *et al.* Translation of Ligand-Centered Hydrogen Evolution Reaction Activity and Mechanism of a Rhenium-Thiolate from Solution to Modified Electrodes: A Combined Experimental and Density Functional Theory Study. *Inorg. Chem.* **56**, 2177–2187 (2017).

127. Abe, T. *et al.* Highly Active Electrocatalysis by Cobalt Tetraphenylporphyrin Incorporated in a Nafion Membrane for Proton Reduction. *Polym. Adv. Technol.* **9**, 559–562 (1998).

128. Koca, A., Kalkan, A. & Bayir, Z. A. Electrochemical, in situ spectroelectrochemical, in situ electrocolorimetric and electrocatalytic characterization of metallophthalocyanines bearing four dioctylaminocarbonyl biphenyloxy substituents. *Electroanalysis* **22**, 310–319 (2010).

129. Koca, A., Kalkan, A. & Bayir, Z. A. Electrocatalytic oxygen reduction and hydrogen evolution reactions on phthalocyanine modified electrodes: Electrochemical, in situ spectroelectrochemical, and in situ electrocolorimetric monitoring. *Electrochim. Acta* **56**, 5513–5525 (2011).

130. Koca, A. Hydrogen evolution reaction on glassy carbon electrode modified with titanyl phthalocyanines. *Int. J. Hydrogen Energy* **34**, 2107–2112

(2009).

131. Koca, A. Copper phthalocyanine complex as electrocatalyst for hydrogen evolution reaction. *Electrochem. commun.* **11**, 838–841 (2009).

132. Grass, V., Lexa, D. & Savéant, J. M. Electrochemical generation of rhodium porphyrin hydrides. Catalysis of hydrogen evolution. *J. Am. Chem. Soc.* **119**, 7526–7532 (1997).

133. Anxolabéhère-Mallart, E., Costentin, C., Fournier, M. & Robert, M. Cobalt-bisglyoximato diphenyl complex as a precatalyst for electrocatalytic H2 evolution. *J. Phys. Chem. C* **118**, 13377–13381 (2014).

134. El Ghachtouli, S. *et al.* Monometallic cobalt-trisglyoximato complexes as precatalysts for catalytic H2 evolution in water. *J. Phys. Chem. C* **117**, 17073–17077 (2013).

135. Anxolabéhère-Mallart, E. *et al.* Boron-capped tris(glyoximato) cobalt clathrochelate as a precursor for the electrodeposition of nanoparticles catalyzing H 2 evolution in water. *J. Am. Chem. Soc.* **134**, 6104–6107 (2012).

136. Cherdo, S. *et al.* A nickel dimethyl glyoximato complex to form nickel based nanoparticles for electrocatalytic H2 production. *Chem. Commun.* **50**, 13514–13516 (2014).

137. Fang, M., Engelhard, M. H., Zhu, Z., Helm, M. L. & Roberts, J. A. S. Electrodeposition from acidic solutions of nickel bis(benzenedithiolate)

produces a hydrogen-evolving Ni-S film on glassy carbon. *ACS Catal.* **4**, 90–98 (2014).

138. Martin, D. J., McCarthy, B. D., Donley, C. L. & Dempsey, J. L. Electrochemical hydrogenation of a homogeneous nickel complex to form a surface adsorbed hydrogen-evolving species. *Chem. Commun.* **51**, 5290–5293 (2015).

139. McCarthy, B. D., Donley, C. L. & Dempsey, J. L. Electrode initiated proton-coupled electron transfer to promote degradation of a nickel(II) coordination complex. *Chem. Sci.* **6**, 2827–2834 (2015).

140. Wombwell, C. & Reisner, E. Synthesis, structure and reactivity of Ni site models of [NiFeSe] hydrogenases. *Dalt. Trans.* **43**, 4483–4493 (2014).

141. Jurss, J. W. *et al.* Bioinspired design of redox-active ligands for multielectron catalysis: effects of positioning pyrazine reservoirs on cobalt for electro- and photocatalytic generation of hydrogen from water. *Chem. Sci.* **6**, 4954–4972 (2015).

142. Haddad, A. Z., Garabato, B. D., Kozlowski, P. M., Buchanan, R. M. & Grapperhaus, C. A. Beyond metal-hydrides: Non-transition-metal and metal-free ligand-centered electrocatalytic hydrogen evolution and hydrogen oxidation. *J. Am. Chem. Soc.* **138**, 7844–7847 (2016).

143. Thompson, E. J. & Berben, L. A. Electrocatalytic Hydrogen Production by an Aluminum(III) Complex: Ligand-Based Proton and Electron Transfer. *Angew. Chemie - Int. Ed.* **54**, 11642–11646 (2015).

144. Sherbow, T. J., Fettinger, J. C. & Berben, L. A. Control of Ligand pKa Values Tunes the Electrocatalytic Dihydrogen Evolution Mechanism in a Redox-Active Aluminum(III) Complex. *Inorg. Chem.* **56**, 8651–8660 (2017).

145. Panetier, J. A., Letko, C. S., Tilley, T. D. & Head-Gordon, M. Computational Characterization of Redox Non-Innocence in Cobalt-Bis(Diaryldithiolene)-Catalyzed Proton Reduction. *J. Chem. Theory Comput.* **12**, 223–230 (2016).

146. West, D. X. *et al.* Copper(II) and nickel(II) complexes of 2,3-butanedione bis(N(3)-substituted thiosemicarbazones). *Polyhedron* **16**, 1895–1905 (1997).

147. Xie, D., King, T. L., Banerjee, A., Kohli, V. & Que, E. L. Exploiting Copper Redox for 19 F Magnetic Resonance-Based Detection of Cellular Hypoxia. *J. Am. Chem. Soc.* **138**, 2937–2940 (2016).

148. Spek, A. L. Structure validation in chemical crystallography. *Acta Crystallogr. Sect. D Biol. Crystallogr.* **65**, 148–155 (2009).

149. CrysAlis PRO (CCD and RED). (2013).

150. Dennington, R., Keith, T. & Millam, J. GaussView. (2009).

151. Sheldrick, G. M. A short history of SHELX. *Acta Crystallographica Section A: Foundations of Crystallography* vol. 64 112–122 (2008).

152. Blower, P. J. *et al.* Structural trends in copper (II) bis (thiosemicarbazone) radiopharmaceuticals. *Dalt. Trans.* **23**, 4416–4425 (2003).

153. Barnes, C. L. ORTEP -3 for Windows - a version of ORTEP -III with a Graphical User Interface (GUI) by J. Farrugia. *J. Appl. Crystallogr.* **30**, 568–568 (1997).

154. Vishnosky, N. Synthesis, characterization, and evaluation of metal complexes with cancer selective anti-proliferative effects and hydrogen evolution catalytic properties. Recommended Citation. (University of Louisville, 2019). doi:10.18297/etd/3220.

155. Jain, R., Mamun, A. Al, Buchanan, R. M., Kozlowski, P. M. & Grapperhaus, C. A. Ligand-Assisted Metal-Centered Electrocatalytic Hydrogen Evolution upon Reduction of a Bis(thiosemicarbazonato)Ni(II) Complex. *Inorg. Chem.* **57**, 13486–13493 (2018).

156. Dearling, J. L. J., Lewis, J. S., Mullen, G. E. D., Welch, M. J. & Blower, P. J. Copper bis(thiosemicarbazone) complexes as hypoxia imaging agents: Structure-activity relationships. *J. Biol. Inorg. Chem.* **7**, 249–259 (2002).

157. Walter, M. G. *et al.* Solar water splitting cells. *Chem. Rev.* **110**, 6446–6473 (2010).

158. Weber, M. F. & Dignam, M. J. SPLITTING WATER WITH SEMICONDUCTING PHOTOELECTRODES: EFFICIENCY CONSIDERATIONS. in *Advances in Hydrogen Energy* vol. 3 957–968 (The Electrochemical Society, 1984).

159. Dickinson, T., Povey, A. F. & Sherwood, P. M. A. Dissolution and passivation of nickel. An X-ray photoelectron spectroscopic study. *J.*

Chem. Soc. Faraday Trans. 1 Phys. Chem. Condens. Phases **73**, 327–343 (1977).

160. Descostes, M., Mercier, F., Thromat, N., Beaucaire, C. & Gautier-Soyer, M. Use of XPS in the determination of chemical environment and oxidation state of iron and sulfur samples: Constitution of a data basis in binding energies for Fe and S reference compounds and applications to the evidence of surface species of an oxidized py. *Appl. Surf. Sci.* **165**, 288–302 (2000).

161. Peisert, H., Chassé, T., Streubel, P., Meisel, A. & Szargan, R. Relaxation energies in XPS and XAES of solid sulfur compounds. *J. Electron Spectros. Relat. Phenomena* **68**, 321–328 (1994).

162. Marcus, P. & Protopopoff, E. Potential pH Diagrams for Sulfur and Oxygen Adsorbed on Nickel in Water at 25 and 300°C. *J. Electrochem. Soc.* **140**, 1571–1575 (1993).

163. Jiang, N. *et al.* Electrodeposited nickel-sulfide films as competent hydrogen evolution catalysts in neutral water. *J. Mater. Chem. A* **2**, 1907–19414 (2014).

164. Jiang, N. *et al.* Nickel sulfides for electrocatalytic hydrogen evolution under alkaline conditions: A case study of crystalline NiS, NiS2, and Ni3S2 nanoparticles. *Catal. Sci. Technol.* **6**, 1077–1084 (2016).

165. Suzuki, T., Uchinokura, K., Sekine, T. & Matsuura, E. Raman scattering of NiS2. *Solid State Commun.* **23**, 847–852 (1977).

166. Guillaume, F., Huang, S., Harris, K. D. M., Couzi, M. & Talaga, D. Optical phonons in millerite (NiS) from single-crystal polarized Raman spectroscopy. *J. Raman Spectrosc.* **39**, 1419–1422 (2008).

167. Cheng, Z., Abernathy, H. & Liu, M. Raman spectroscopy of nickel sulfide Ni3S2. *J. Phys. Chem. C* **111**, 17997–18000 (2007).

168. Biesinger, M. C., Payne, B. P., Lau, L. W. M., Gerson, A. & Smart, R. S. C. X-ray photoelectron spectroscopic chemical state Quantification of mixed nickel metal, oxide and hydroxide systems. *Surf. Interface Anal.* **41**, 324–332 (2009).

169. Fujimoto, T., Ogawa, S., Yoshida, T., Uchiyama, N. & Yagi, S. Hydrogen storage property of Ni nanoparticles fabricated by the gas evaporation method. in *Surface and Interface Analysis* vol. 46 1121–1124 (John Wiley and Sons Ltd, 2014).

170. Zhao, Y., E, Y., Fan, L., Qiu, Y. & Yang, S. A new route for the electrodeposition of platinum-nickel alloy nanoparticles on multi-walled carbon nanotubes. *Electrochim. Acta* **52**, 5873–5878 (2007).

171. Prieto, P. *et al.* XPS study of silver, nickel and bimetallic silver-nickel nanoparticles prepared by seed-mediated growth. *Appl. Surf. Sci.* **258**, 8807–8813 (2012).

172. Legrand, J., Taleb, A., Gota, S., Guittet, M. J. & Petit, C. Synthesis and XPS characterization of nickel boride nanoparticles. *Langmuir* **18**, 4131–4137 (2002).

173. Konopka, S. J. & McDuffie, B. Diffusion Coefficients of Ferri- and Ferrocyanide Ions in Aqueous Media, Using Twin-Electrode Thin-Layer Electrochemistry. *Anal. Chem.* **42**, 1741–1746 (1970).

174. Konkena, B. *et al.* Pentlandite rocks as sustainable and stable efficient electrocatalysts for hydrogen generation. *Nat. Commun.* **7**, (2016).

175. Chai, G. L., Hou, Z., Ikeda, T. & Terakura, K. Two-Electron Oxygen Reduction on Carbon Materials Catalysts: Mechanisms and Active Sites. *J. Phys. Chem. C* **121**, 14524–14533 (2017).

176. Li, J., Sambandam, S., Lu, W. & Lukehart, C. M. Carbon nanofibers 'spot-welded' to carbon felt: A mechanically stable, bulk mimic of lotus leaves. *Adv. Mater.* **20**, 420–424 (2008).

177. Van Wylen, G. J., Sonntag, R. E. & Dybbs, A. Fundamentals of Classical Thermodynamics (2nd Edition). *J. Appl. Mech.* **42**, 522–522 (1975).

178. Davies, C. *Electrochemistry, Newnes*. (1967).

179. Mann, R. F. *et al.* Development and application of a generalised steady-state electrochemical model for a PEM fuel cell. *J. Power Sources* **86**, 173–180 (2000).

180. Xu, H., Kunz, H. R. & Fenton, J. M. Analysis of proton exchange membrane fuel cell polarization losses at elevated temperature 120 °C and reduced relative humidity. *Electrochim. Acta* **52**, 3525–3533 (2007).

181. Büchi, F. N. & Scherer, G. G. In-situ resistance measurements of Nafion®

117 membranes in polymer electrolyte fuel cells. *J. Electroanal. Chem.* **404**, 37–43 (1996).

182. Andreaus, B. & Scherer, G. G. Proton-conducting polymer membranes in fuel cells - Humidification aspects. in *Solid State Ionics* vol. 168 311–320 (2004).

183. Berning, T. & Djilali, N. Three-dimensional computational analysis of transport phenomena in a PEM fuel cell - A parametric study. *J. Power Sources* **124**, 440–452 (2003).

184. Laurencelle, F. *et al.* Characterization of a Ballard MK5-E Proton Exchange Membrane Fuel Cell Stack. *Fuel Cells* **1**, 66–71 (2001).

185. Hamelin, J., Agbossou, K., Laperrière, A., Laurencelle, F. & Bose, T. K. Dynamic behavior of a PEM fuel cell stack for stationary applications. *Int. J. Hydrogen Energy* **26**, 625–629 (2001).

186. Al-Baghdadi, M. A. R. S. Modelling of proton exchange membrane fuel cell performance based on semi-empirical equations. *Renew. Energy* **30**, 1587–1599 (2005).

187. Kongkanand, A. & Mathias, M. F. The Priority and Challenge of High-Power Performance of Low-Platinum Proton-Exchange Membrane Fuel Cells. *Journal of Physical Chemistry Letters* vol. 7 1127–1137 (2016).

188. Spingler, F. B., Phillips, A., Schuler, T., Tucker, M. C. & Weber, A. Z. Investigating fuel-cell transport limitations using hydrogen limiting current.

Int. J. Hydrogen Energy **42**, 13960–13969 (2017).

189. Nonoyama, N., Okazaki, S., Weber, A. Z., Ikogi, Y. & Yoshida, T. Analysis of Oxygen-Transport Diffusion Resistance in Proton-Exchange-Membrane Fuel Cells. *J. Electrochem. Soc.* **158**, B416 (2011).

190. Greszler, T. A., Caulk, D. & Sinha, P. The Impact of Platinum Loading on Oxygen Transport Resistance. *J. Electrochem. Soc.* **159**, F831–F840 (2012).

191. Ohma, A. *et al.* Analysis of proton exchange membrane fuel cell catalyst layers for reduction of platinum loading at Nissan. in *Electrochimica Acta* vol. 56 10832–10841 (2011).

192. Biesheuvel, P. M., Fu, Y. & Bazant, M. Z. Diffuse charge and Faradaic reactions in porous electrodes. *Phys. Rev. E* **83**, 61507 (2011).

193. Beuscher, U. Experimental Method to Determine the Mass Transport Resistance of a Polymer Electrolyte Fuel Cell. *J. Electrochem. Soc.* **153**, A1788 (2006).

194. Vielstich, W., Lamm, A. & Gasteiger, H. Handbook of fuel cells. Fundamentals, technology, applications. (2003).

195. Baker, D. R., Caulk, D. A., Neyerlin, K. C. & Murphy, M. W. Measurement of Oxygen Transport Resistance in PEM Fuel Cells by Limiting Current Methods. *J. Electrochem. Soc.* **156**, B991 (2009).

196. Chan, S. H., Chen, X. J. & Khor, K. A. Cathode Micromodel of Solid Oxide

Fuel Cell. *J. Electrochem. Soc.* **151**, A164 (2004).

197. Ono, Y., Ohma, A., Shinohara, K. & Fushinobu, K. Influence of Equivalent Weight of Ionomer on Local Oxygen Transport Resistance in Cathode Catalyst Layers. *J. Electrochem. Soc.* **160**, F779–F787 (2013).

198. Liu, Y. *et al.* Determination of Electrode Sheet Resistance in Cathode Catalyst Layer by AC Impedance. *ECS Trans.* **11**, 473–484 (2019).

199. Ikeda, K., Nonoyama, N. & Ikogi, Y. Analysis of the Ionomer Coverage of Pt Surface in PEMFC. *ECS Trans.* **33**, 1189–1197 (2019).

200. Srinivasan, S., Manko, D. J., Koch, H., Enayetullah, M. A. & Appleby, A. J. Recent advances in solid polymer electrolyte fuel cell technology with low platinum loading electrodes. *J. Power Sources* **29**, 367–387 (1990).

201. Rho, Y. W., Velev, O. A., Srinivasan, S. & Kho, Y. T. Mass Transport Phenomena in Proton Exchange Membrane Fuel Cells Using O 2/He, O 2/Ar, and O 2/N 2 Mixtures: I. Experimental Analysis. *J. Electrochem. Soc.* **141**, 2084 (1994).

202. Kodama, K. *et al.* Catalyst Poisoning Property of Sulfonimide Acid Ionomer on Pt (111) Surface. *J. Electrochem. Soc.* **161**, F649–F652 (2014).

203. Shinozaki, K., Morimoto, Y., Pivovar, B. S. & Kocha, S. S. Suppression of oxygen reduction reaction activity on Pt-based electrocatalysts from ionomer incorporation. *J. Power Sources* **325**, 745–751 (2016).

204. Yarlagadda, V. *et al.* Boosting Fuel Cell Performance with Accessible

Carbon Mesopores. *ACS Energy Lett.* **3**, 618–621 (2018).

205. Masuda, T., Sonsudin, F., Singh, P. R., Naohara, H. & Uosaki, K. Potential-dependent adsorption and desorption of perfluorosulfonated ionomer on a platinum electrode surface probed by electrochemical quartz crystal microbalance and atomic force microscopy. *J. Phys. Chem. C* **117**, 15704–15709 (2013).

206. Subbaraman, R., Strmcnik, D., Stamenkovic, V. & Markovic, N. M. Three phase interfaces at electrified metal-solid electrolyte systems 1. study of the pt(hkl)-nafion interface. *J. Phys. Chem. C* **114**, 8414–8422 (2010).

207. Eguchi, M. *et al.* Influence of ionomer/carbon ratio on the performance of a polymer electrolyte fuel cell. *Polymers (Basel).* **4**, 1645–1656 (2012).

208. Shinozaki, K., Yamada, H. & Morimoto, Y. Relative Humidity Dependence of Pt Utilization in Polymer Electrolyte Fuel Cell Electrodes: Effects of Electrode Thickness, Ionomer-to-Carbon Ratio, Ionomer Equivalent Weight, and Carbon Support. *J. Electrochem. Soc.* **158**, B467 (2011).

209. Xie, J., Wood, D. L., More, K. L., Zawodzinski, T. A. & Smith, W. H. Influence of ionomer content on the structure and performance of PEFC membrane electrode assemblies. in *Proceedings - Electrochemical Society* vol. PV 2004-21 657–671 (2004).

210. Passalacqua, E., Lufrano, F., Squadrito, G., Patti, A. & Giorgi, L. Nafion content in the catalyst layer of polymer electrolyte fuel cells: Effects on structure and performance. *Electrochim. Acta* **46**, 799–805 (2001).

211. Suzuki, T., Tsushima, S. & Hirai, S. Effects of Nafion® ionomer and carbon particles on structure formation in a proton-exchange membrane fuel cell catalyst layer fabricated by the decal-transfer method. *Int. J. Hydrogen Energy* **36**, 12361–12369 (2011).

212. Berlinger, S. A., McCloskey, B. D. & Weber, A. Z. Inherent Acidity of Perfluorosulfonic Acid Ionomer Dispersions and Implications for Ink Aggregation. *J. Phys. Chem. B* **122**, 7790–7796 (2018).

213. Takahashi, S., Mashio, T., Horibe, N., Akizuki, K. & Ohma, A. Analysis of the Microstructure Formation Process and Its Influence on the Performance of Polymer Electrolyte Fuel-Cell Catalyst Layers. *ChemElectroChem* **2**, 1560–1567 (2015).

214. Kim, T. H., Yi, J. Y., Jung, C. Y., Jeong, E. & Yi, S. C. Solvent effect on the Nafion agglomerate morphology in the catalyst layer of the proton exchange membrane fuel cells. *Int. J. Hydrogen Energy* **42**, 478–485 (2017).

215. Liu, Y. *et al.* Proton Conduction and Oxygen Reduction Kinetics in PEM Fuel Cell Cathodes: Effects of Ionomer-to-Carbon Ratio and Relative Humidity. *J. Electrochem. Soc.* **156**, B970 (2009).

216. Park, Y. C., Tokiwa, H., Kakinuma, K., Watanabe, M. & Uchida, M. Effects of carbon supports on Pt distribution, ionomer coverage and cathode performance for polymer electrolyte fuel cells. *J. Power Sources* **315**, 179–191 (2016).

217. Hussain, M. M., Song, D., Liu, Z. S. & Xie, Z. Modeling an ordered nanostructured cathode catalyst layer for proton exchange membrane fuel cells. *J. Power Sources* **196**, 4533–4544 (2011).

218. Du, C. Y., Shi, P. F. & Yin, G. P. Numerical simulation of ordered catalyst layer in cathode of proton exchange membrane fuel cells. *Harbin Gongye Daxue Xuebao/Journal Harbin Inst. Technol.* **39**, 1645–1648 (2007).

219. Rao, S. M. & Xing, Y. Simulation of nanostructured electrodes for polymer electrolyte membrane fuel cells. *J. Power Sources* **185**, 1094–1100 (2008).

220. Fang, B. *et al.* Dense Pt Nanowire Electrocatalyst for Improved Fuel Cell Performance Using a Graphitic Carbon Nitride-Decorated Hierarchical Nanocarbon Support. *Small* **17**, (2021).

221. Fang, B., Kim, J. H., Kim, M., Kim, M. & Yu, J. S. Hierarchical nanostructured hollow spherical carbon with mesoporous shell as a unique cathode catalyst support in proton exchange membrane fuel cell. *Phys. Chem. Chem. Phys.* **11**, 1380–1387 (2009).

222. Fang, B. *et al.* High Pt loading on functionalized multiwall carbon nanotubes as a highly efficient cathode electrocatalyst for proton exchange membrane fuel cells. *J. Mater. Chem.* **21**, 8066–8073 (2011).

223. Fang, B., Kim, J. H., Kim, M. & Yu, J. S. Ordered hierarchical nanostructured carbon as a highly efficient cathode catalyst support in proton exchange membrane fuel cell. *Chem. Mater.* **21**, 789–796 (2009).

224. Jang, S. *et al.* Facile Multiscale Patterning by Creep-Assisted Sequential Imprinting and Fuel Cell Application. *ACS Appl. Mater. Interfaces* **8**, 11459–11465 (2016).

225. Cho, H. *et al.* Multiplex lithography for multilevel multiscale architectures and its application to polymer electrolyte membrane fuel cell. *Nat. Commun.* **6**, 8484 (2015).

226. Gruber, D., Ponath, N., Müller, J. & Lindstaedt, F. Sputter-deposited ultra-low catalyst loadings for PEM fuel cells. *J. Power Sources* **150**, 67–72 (2005).

227. Huang, T. W., Qayyum, H., Lin, G. R., Chen, S. Y. & Tseng, C. J. Production of high-performance and improved-durability Pt-catalyst /support for proton-exchange-membrane fuel cells with pulsed laser deposition. *J. Phys. D. Appl. Phys.* **49**, 255601 (2016).

228. Yakovlev, Y. V *et al.* Highly developed nanostructuring of polymer-electrolyte membrane supported catalysts for hydrogen fuel cell application. *J. Power Sources* **439**, 227084 (2019).

229. Zeng, Y. *et al.* Nano-engineering of a 3D-ordered membrane electrode assembly with ultrathin Pt skin on open-walled PdCo nanotube arrays for fuel cells. *J. Mater. Chem. A* **6**, 6521–6533 (2018).

230. Omosebi, A. & Besser, R. S. Ultra-low Mass Sputtered and Conventional Catalyst Layers on Plasma-etched Nafion for PEMFC Applications. *Fuel Cells* **17**, 762–769 (2017).

231. Prasanna, M. *et al.* Effects of platinum loading on performance of proton-exchange membrane fuel cells using surface-modified Nafion® membranes. *J. Power Sources* **160**, 90–96 (2006).

232. Steinbach, A. J. *Highly Active, Durable, and Ultra-low PGM NSTF Thin Film ORR Catalysts and Supports*. *DOE Hydrogen and Fuel Cells Program - 2019 Annual Progress Report* (2019).

233. Tian, Z. Q. *et al.* A highly order-structured membrane electrode assembly with vertically aligned carbon nanotubes for ultra-low Pt loading PEM fuel cells. *Adv. Energy Mater.* **1**, 1205–1214 (2011).

234. Yang, C.-L. *et al.* Sulfur-anchoring synthesis of platinum intermetallic nanoparticle catalysts for fuel cells. *Science (80-.).* **374**, 459–464 (2021).

235. Chong, L. *et al.* Ultralow-loading platinum-cobalt fuel cell catalysts derived from imidazolate frameworks. *Science (80-.).* **362**, 1276–1281 (2018).

236. Peron, J. *et al.* Properties of Nafion® NR-211 membranes for PEMFCs. *J. Memb. Sci.* **356**, 44–51 (2010).

237. Zhang, H., Li, J., Tang, H., Lin, Y. & Pan, M. Hydrogen crossover through perfluorosulfonic acid membranes with variable side chains and its influence in fuel cell lifetime. *Int. J. Hydrogen Energy* **39**, 15989–15995 (2014).

238. Adamski, M. *et al.* Highly Stable, Low Gas Crossover, Proton-Conducting Phenylated Polyphenylenes. *Angew. Chemie* **129**, 9186–9189 (2017).

239. Diedrichs, A., Rastedt, M., Pinar, F. J. & Wagner, P. Effect of compression on the performance of a HT-PEM fuel cell. in *Journal of Applied Electrochemistry* vol. 43 1079–1099 (2013).

240. Jerkiewicz, G. Electrochemical Hydrogen Adsorption and Absorption. Part 1: Under-potential Deposition of Hydrogen. *Electrocatalysis* **1**, 179–199 (2010).

241. Dillet, J. *et al.* Impact of flow rates and electrode specifications on degradations during repeated startups and shutdowns in polymer-electrolyte membrane fuel cells. *J. Power Sources* **250**, 68–79 (2014).

242. Tian, Z. Q., Jiang, S. P., Liang, Y. M. & Shen, P. K. Synthesis and characterization of platinum catalysts on multiwalled carbon nanotubes by intermittent microwave irradiation for fuel cell applications. *J. Phys. Chem. B* **110**, 5343–5350 (2006).

243. Tuaev, X., Rudi, S. & Strasser, P. The impact of the morphology of the carbon support on the activity and stability of nanoparticle fuel cell catalysts. *Catal. Sci. Technol.* **6**, 8276–8288 (2016).

244. Vengatesan, S. *et al.* High dispersion platinum catalyst using mesoporous carbon support for fuel cells. *Electrochim. Acta* **54**, 856–861 (2008).

245. Yakovlev, Y. V. *et al.* Ionomer content effect on charge and gas transport in the cathode catalyst layer of proton-exchange membrane fuel cells. *J. Power Sources* **490**, 229531 (2021).

246. Garrick, T. R., Moylan, T. E., Yarlagadda, V. & Kongkanand, A. Characterizing Electrolyte and Platinum Interface in PEM Fuel Cells Using CO Displacement. *J. Electrochem. Soc.* **164**, F60–F64 (2017).

247. Shrivastava, U. N., Fritzsche, H. & Karan, K. Interfacial and Bulk Water in Ultrathin Films of Nafion, 3M PFSA, and 3M PFIA Ionomers on a Polycrystalline Platinum Surface. *Macromolecules* **51**, 9839–9849 (2018).

248. Kodama, K. *et al.* Increase in adsorptivity of sulfonate anions on Pt (111) surface with drying of ionomer. *Electrochem. commun.* **36**, 26–28 (2013).

249. Kudo, K., Jinnouchi, R. & Morimoto, Y. Humidity and Temperature Dependences of Oxygen Transport Resistance of Nafion Thin Film on Platinum Electrode. *Electrochim. Acta* **209**, 682–690 (2016).

250. Kusoglu, A., Kwong, A., Clark, K. T., Gunterman, H. P. & Weber, A. Z. Water Uptake of Fuel-Cell Catalyst Layers. *J. Electrochem. Soc.* **159**, F530–F535 (2012).

251. Zawodzinski, T. A. *et al.* Water Uptake by and Transport Through Nafion® 117 Membranes. *J. Electrochem. Soc.* **140**, 1041–1047 (1993).

252. Salari, S., Stumper, J. & Bahrami, M. Direct measurement and modeling relative gas diffusivity of PEMFC catalyst layers: The effect of ionomer to carbon ratio, operating temperature, porosity, and pore size distribution. *Int. J. Hydrogen Energy* **43**, 16704–16718 (2018).

253. Lefebvre, M. C., Martin, R. B. & Pickup, P. G. Characterization of ionic

conductivity profiles within proton exchange membrane fuel cell gas diffusion electrodes by impedance spectroscopy. *Electrochem. Solid-State Lett.* **2**, 259–261 (1999).

254. Li, G. & Pickup, P. G. Ionic Conductivity of PEMFC Electrodes. *J. Electrochem. Soc.* **150**, C745 (2003).

255. Cheng, Q. & Chen, Z. The cause analysis of the incomplete semi-circle observed in high frequency region of EIS obtained from TEL-covered pure copper. *Int. J. Electrochem. Sci.* **8**, 8282–8290 (2013).

256. US Fuel Cell Council. Doe Cell Component Accelerated Stress Test Protocols for Pem Fuel Cells. (2007).

257. U.S. Department of Energy, D. C. C. A. S. T. DOE Technical Targets for Polymer Electrolyte Membrane Fuel Cell Components | Department of Energy. *Http://Www1.Eere.Energy.Gov/Hydrogenandfuelcells/Pdfs/Component_Durability_May_2010.Pdf* 1–8 https://www.energy.gov/eere/fuelcells/doe-technical-targets-polymer-electrolyte-membrane-fuel-cell-components (2010).

258. Spendelow, J. S. *Advanced Electro-Catalysts through Crystallographic Enhancement*. *2020 DOE Fuel Cell Technologies Office Annual Merit Review* https://www.hydrogen.energy.gov/pdfs/review19/fc161_spendelow_2019_o.pdf%0Ahttps://www.hydrogen.energy.gov/pdfs/review19/fc161_spendelow_2020_o.pdf%0Ahttps://www.hydrogen.energy.gov/pdfs/review18/fc161_sp

endelow_2018_o.pdf (2020).

259. Owejan, J. P., Owejan, J. E. & Gu, W. Impact of Platinum Loading and Catalyst Layer Structure on PEMFC Performance. *J. Electrochem. Soc.* **160**, F824–F833 (2013).

260. Haug, A. Novel ionomers and electrode structures for improved PEMFC electrode performance at low PGM loadings. *DoE Annual Merit Review* (2019).

261. Qiao, Z. *et al.* Atomically Dispersed Single Iron Sites for Promoting Pt and Pt3Co Fuel Cell Catalysts: Performance and Durability Improvements. *Process* (2021).

262. Johnson, D. ZView: a software program for IES analysis, version 2.8. (2002).

263. Hjalmarsson, P., Søgaard, M. & Mogensen, M. Electrochemical behaviour of (La1-xSrx) sCo1-yNiyO3-δ as porous SOFC cathodes. *Solid State Ionics* **180**, 1395–1405 (2009).

264. Li, Q. & Thangadurai, V. A comparative 2 and 4-probe DC and 2-probe AC electrical conductivity of novel co-doped Ce0.9-xRExMo0.1O 2.1-0.5x (RE = Y, Sm, Gd; X = 0.2, 0.3). *J. Mater. Chem.* **20**, 7970–7983 (2010).

265. Li, Q. & Thangadurai, V. Synthesis, structure and electrical properties of Mo-doped CeO 2-Materials for SOFCs. *Fuel Cells* **9**, 684–698 (2009).

266. Gore, C. M., White, J. O., Wachsman, E. D. & Thangadurai, V. Effect of

composition and microstructure on electrical properties and CO2 stability of donor-doped, proton conducting BaCe 1-(x+y)ZrxNbyO3. *J. Mater. Chem. A* **2**, 2363–2373 (2014).

267. Chinarro, E., Jurado, J. R., Figueiredo, F. M. & Frade, J. R. Bulk and grain boundary conductivity of Ca0.97Ti1-xFexO3-δ materials. *Solid State Ionics* **160**, 161–168 (2003).

APPENDIX

SUPPORTING INFORMATION FOR CHAPTER 3

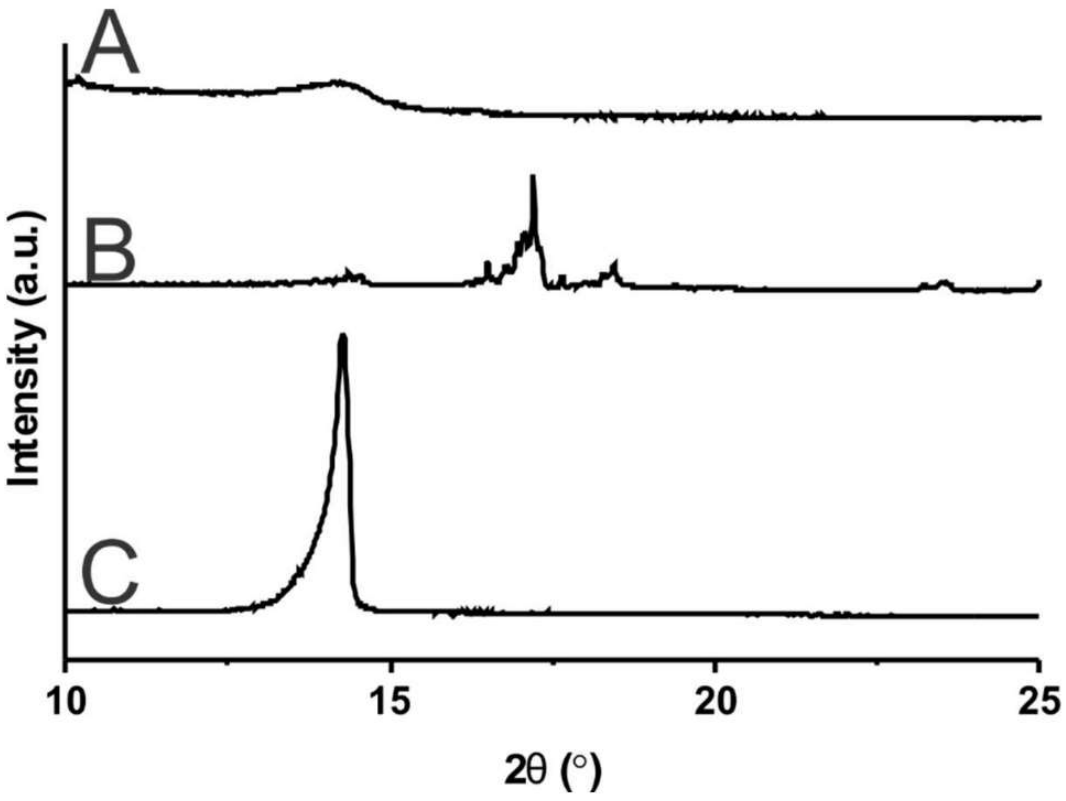

Figure 41. X-ray diffraction patterns for (A) IPL-MoS_2 on GCE, (B) ammonium tetrathiomolybdate powder, & (C) bulk MoS_2 powder

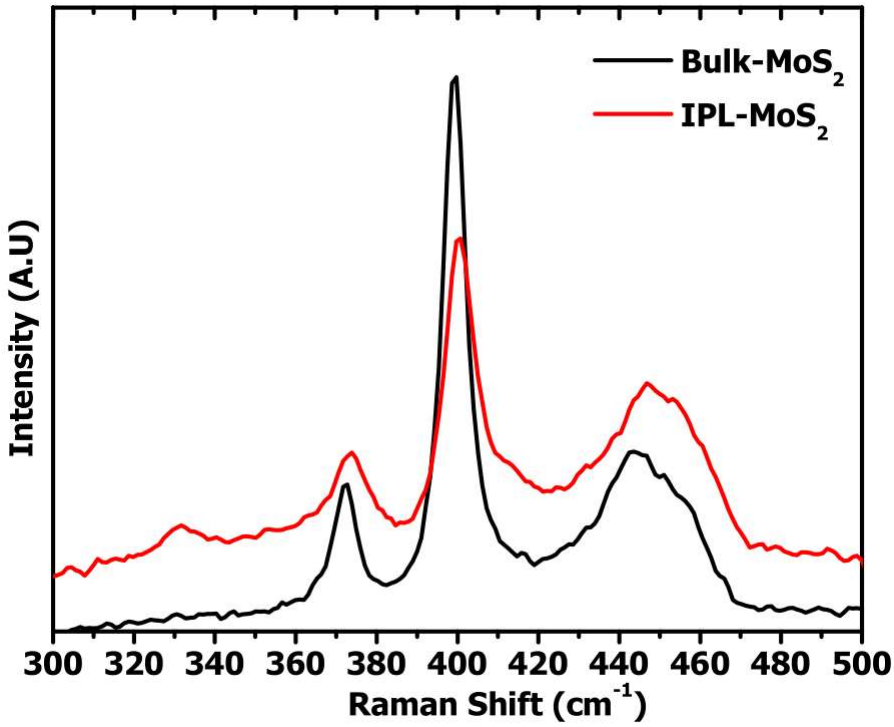

Figure 42. Raman spectra for bulk and IPL-MoS_2.

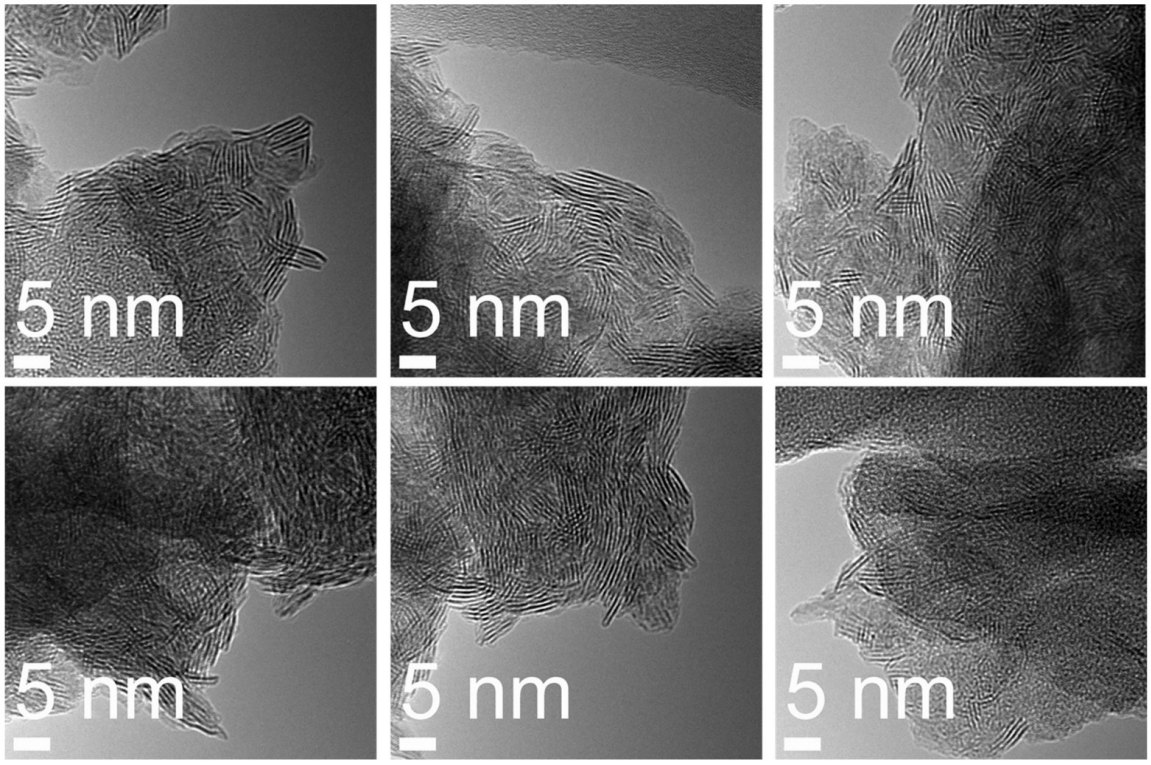

Figure 43. High resolution TEM images of IPL-MoS_2 nanosheets at different areas of the sample.

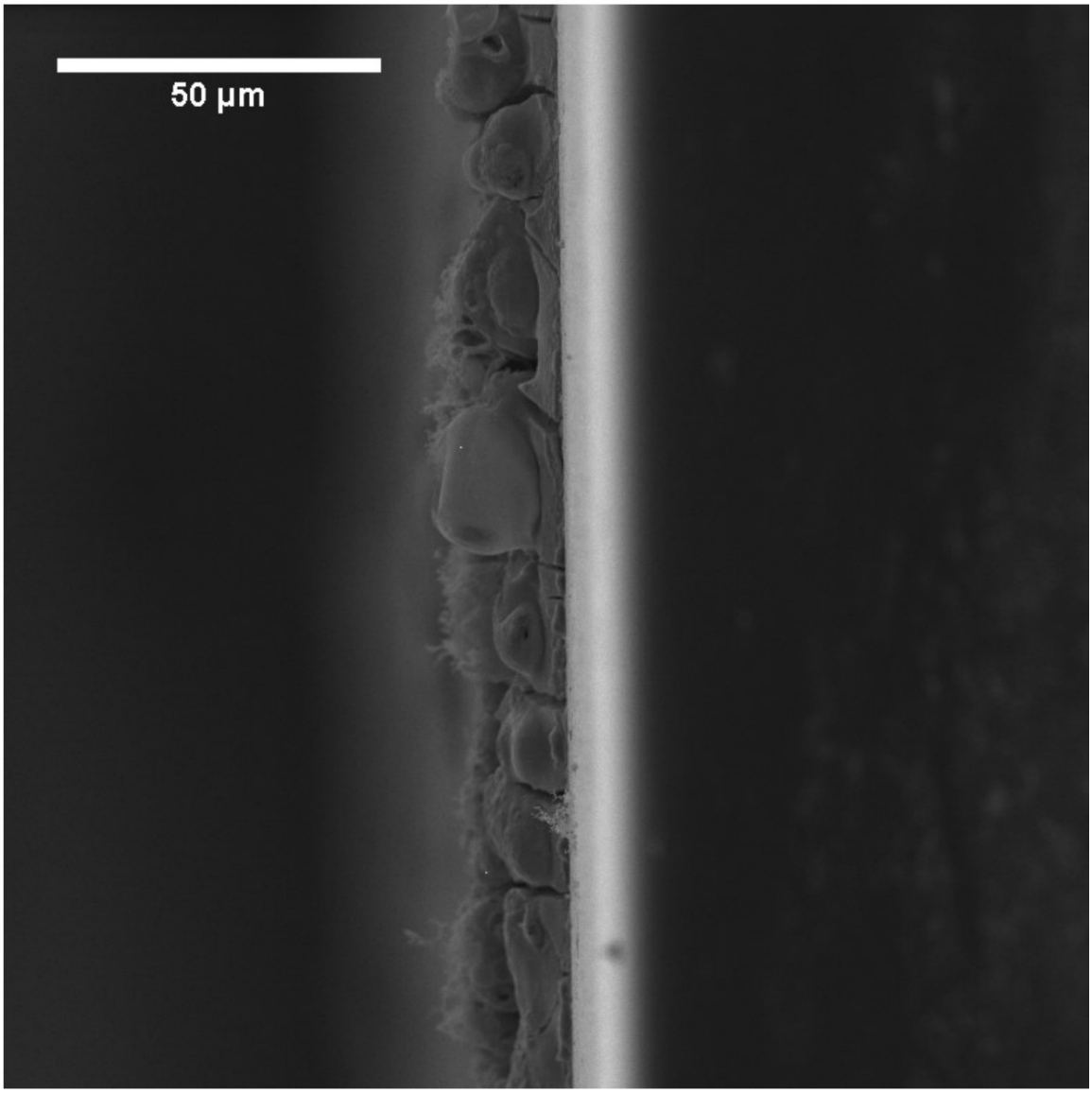

Figure 44. Cross-sectional SEM image of IPL-MoS_2 film (left) on the GCE surface.

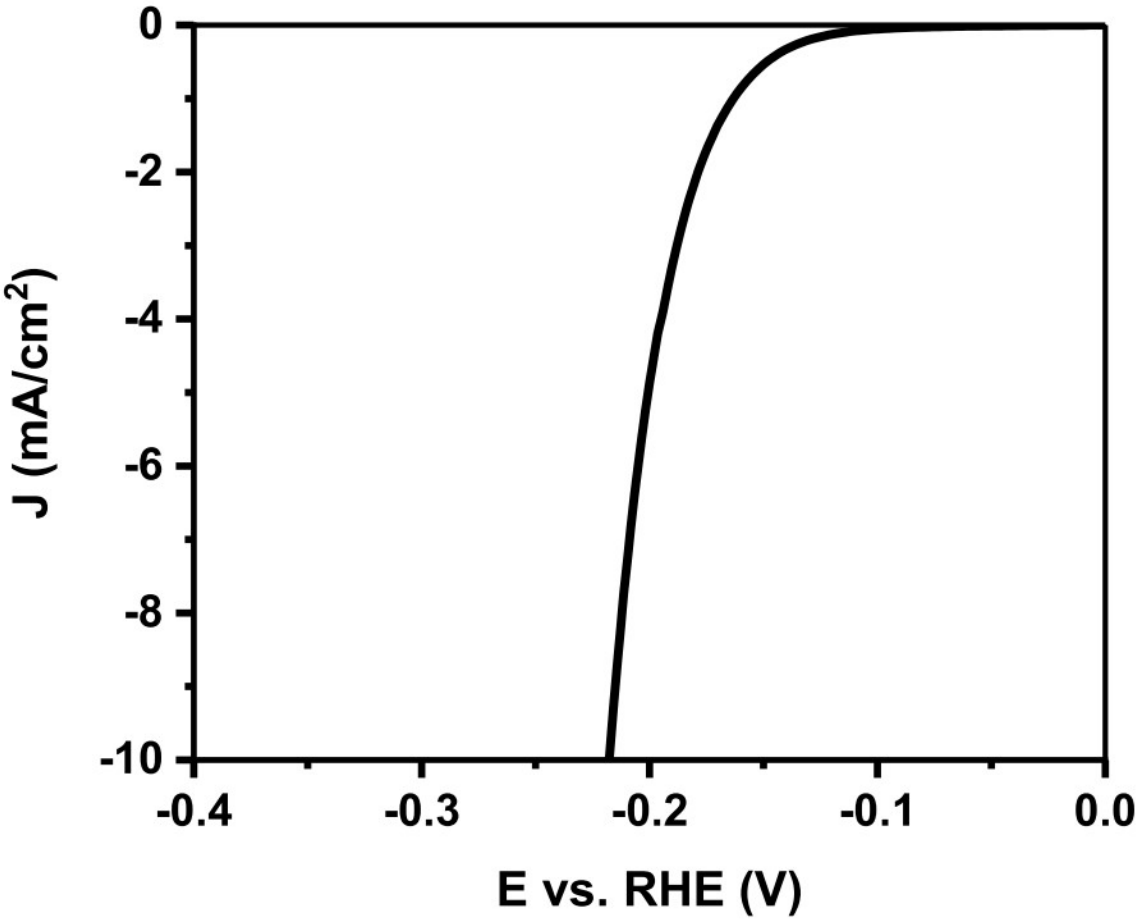

Figure 45. Polarization curve for IPL-MoS_2 on FTO-coated glass substrate.

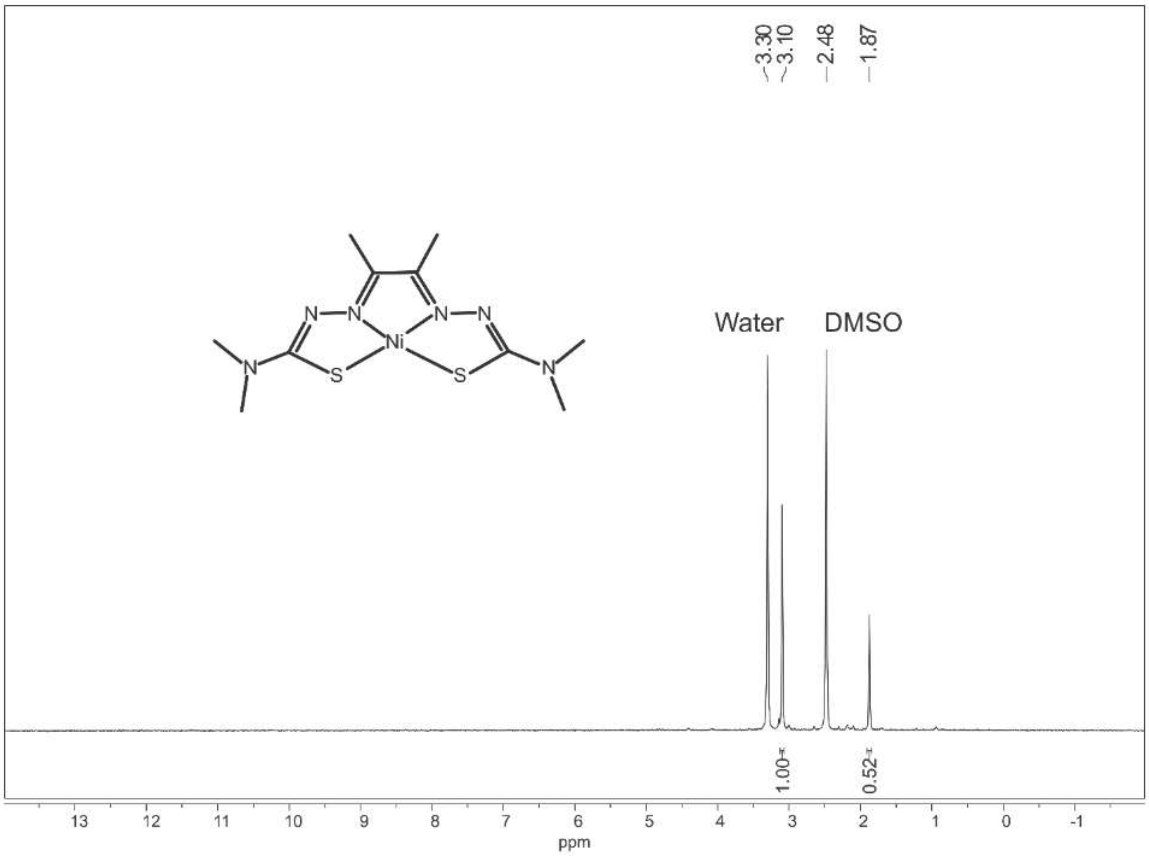

Figure 46. ^{1}H NMR (400 MHz) of **2** in DMSO-d_6. δ 1.87 (s, 6H) 3.10 (s, 12H)

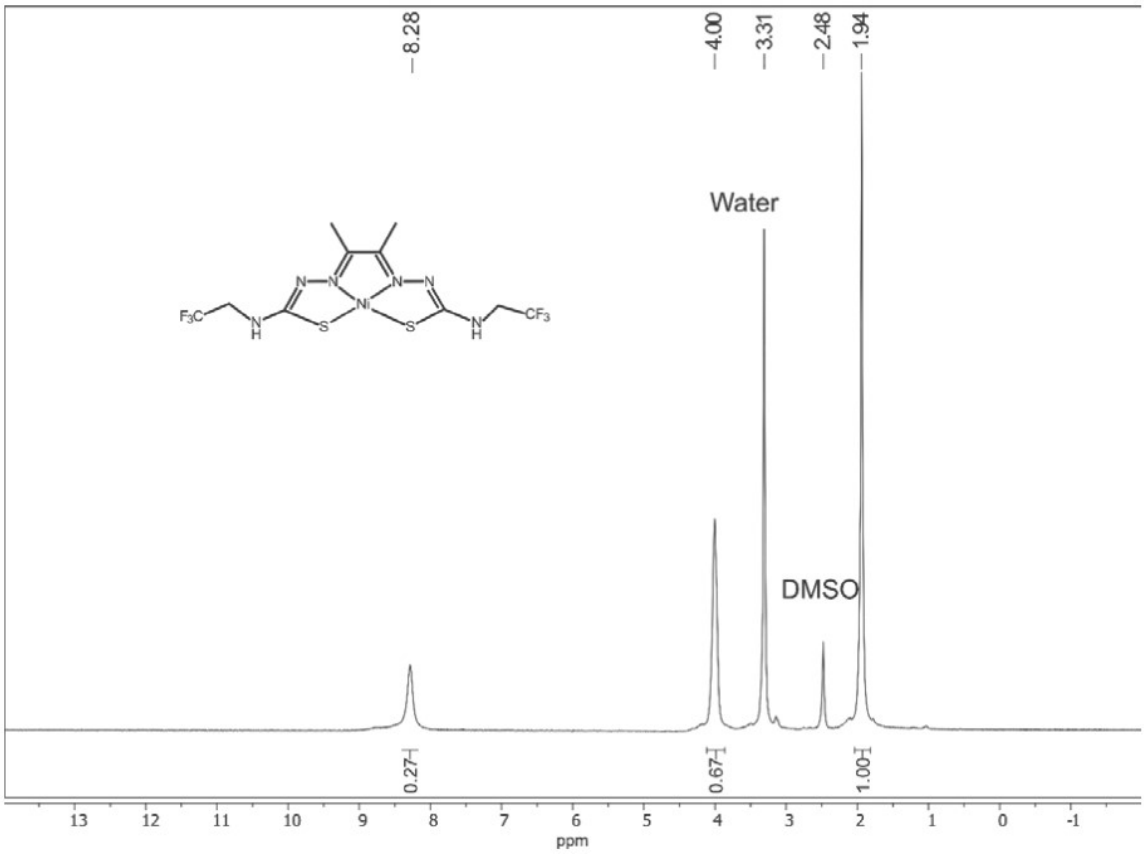

Figure 47. ^{1}H NMR (400 MHz) of **3** in DMSO-d_6. δ 1.94 (s, 6H) 4.00 (br, 4H) 8.28 (s, 2H)

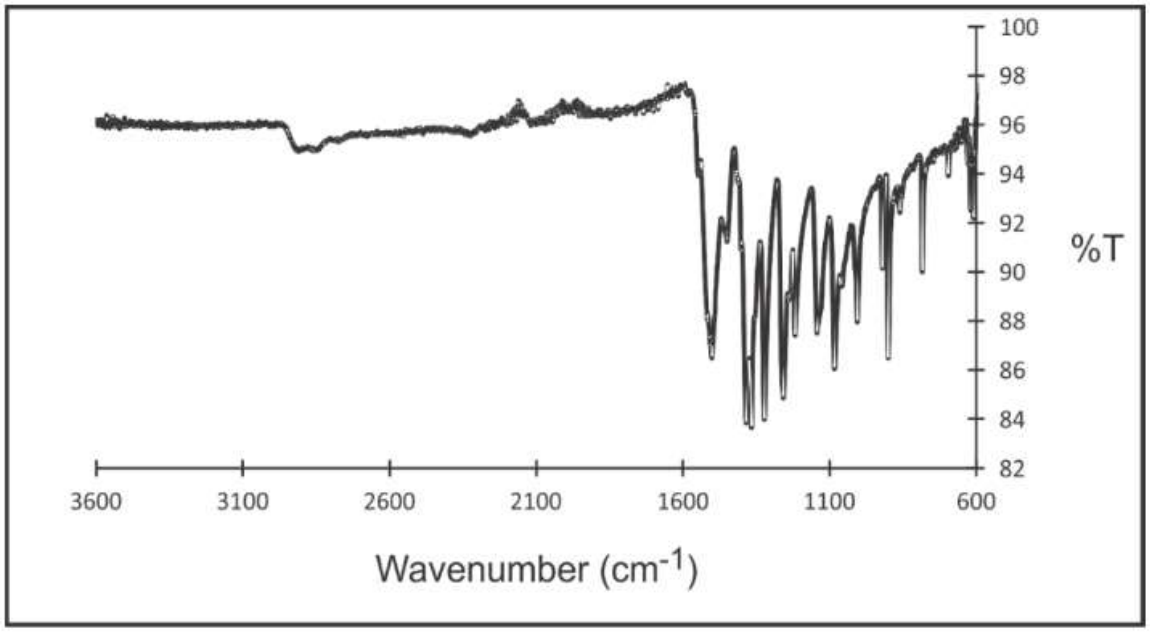

Figure 48. FTIR of **2** as a powder (ATR).

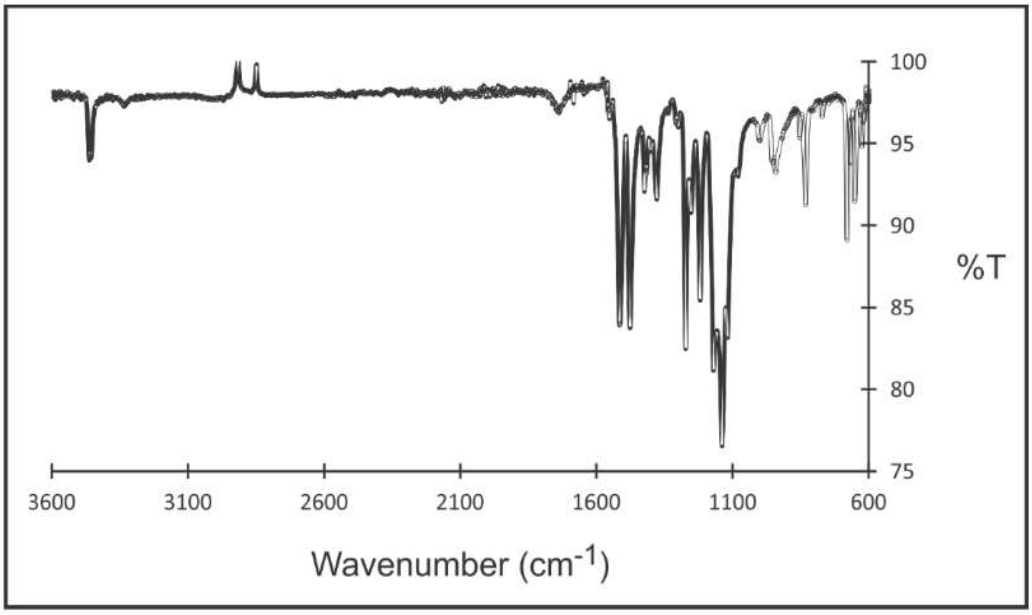

Figure 49. FTIR of **3** as a powder (ATR).

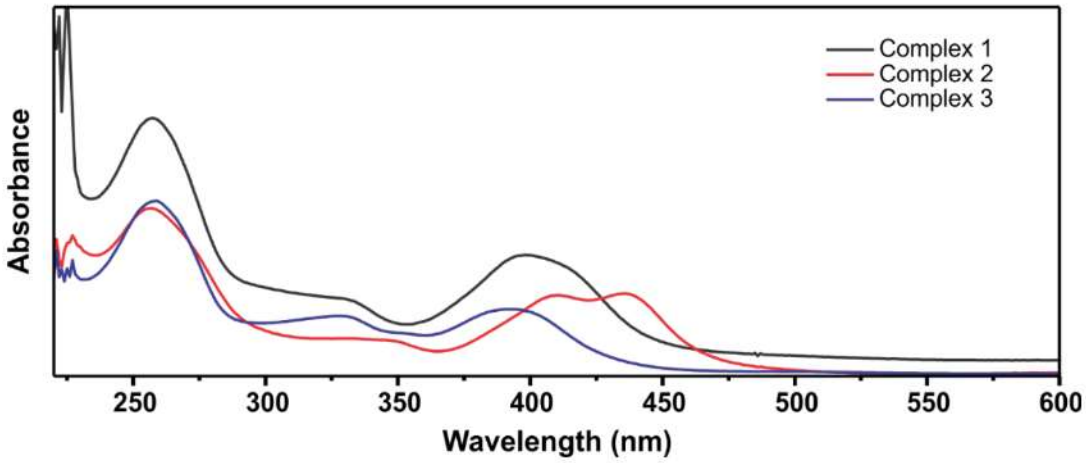

Figure 50. UV-visible spectra of **1 – 3** in acetonitrile.

Table 3

Crystal data and structural refinement for Complexes **2** and **3**.

Compound	NiATSDM (Complex **2**)	NiATSM-F_6 (Complex **3**)
Empirical formula	$C_{10}H_{18}N_6NiS_2$	$C_{10}H_{12}F_6N_6NiS_2$
Formula weight	345.13	453.09
Temperature (K)	100.2(6)	100(2)
Wavelength (Å)	0.71073	0.71073
Crystal system	Triclinic	Triclinic
Space group	P -1	P -1
Unit cell dimension	a = 7.33437(16)	a = 8.3598(10)
	b = 8.5595(2)	b = 9.4027(10)
	c = 11.6784	c = 13.5112(17)
	α = 103.865(2)	α = 109.467
	β = 98.2102(19)	β = 105.475(11)
	γ = 91.7205(18)	γ = 91.382(9)
Volume ($Å^3$)	702.92(3)	957.53(19)
Z	2	2
$\rho_{calcd.}$ (Mg/m^3)	1.631	1.571
Abs. coeff. (mm^{-1})	1.672	1.291
F(000)	360	456
Crystal colour, habit	Orange prism	Red-brown plate
Crystal size (mm^3)	0.40 x 0.34 x 0.18	0.41 x 0.08 x 0.01
Θ range data collection (°)	3.40 to 31.57	3.30 to 26.67
Index ranges	-10≤ h ≤ 10	-10≤ h ≤ 10
	-12 ≤ k ≤12	-11 ≤ k ≤11
	-17 ≤ l ≤ 17	-17 ≤ l ≤ 17
Reflections collected	19998	13904
Independent reflections	4702 [R(int) = 0.0217]	4031 [R(int) = 0.058]
Completeness to θ max	99.9 %	99.7%
Absorption correction	Multiscan	Multiscan
Max. and min. trans.	1.000 and 0.778	1.00 and 0.678
Refinement method	Full-matrix least-squares on F^2	Full-matrix least-squares on F^2
Data/restraints/params	4702/0/244	4031/0/288
Goodness-of-fit- on F^2	1.013	1.074
Final R indices	R1 = 0.0196	R1 = 0.0500
$[I>2\sigma(I)]^{a,b}$	wR2 = 0.0533	wR2 = 0.1099
R indices (all data)	R1 = 0.0211	R1 = 0.0647
	wR2 = 0.0545	wR2 = 0.1188
Largest difference peak and hole ($e \cdot Å^3$)	0.525 and -0.285	1.176 and -0.477

[a] $R1 = \Sigma||F_o| - |F_c||/\Sigma|F_o|$; [b] $wR2 = \{\Sigma[w(F_o^2 - F_c^2)^2]/\Sigma[w(F_o^2)^2]\}^{1/2}$; where $w = q/\sigma^2(F_o^2) + (qp)^2 + bp$. GOF = $S = \{\Sigma[w(F_o^2 - F_c^2)^2]/(n - p)\}^{1/2}$, where n is the number of reflections and p is the number of parameters refined.

Table 4

Selected bond distances (Å) and bond angles (°) for **1**[152], **2**, and **3**. [a]Metric parameters for **1** are reported according to the atom labeling scheme in Figure 19, which differs from prior structural report[152].

Bond distance	**1**[a]	**2**	**3**
Ni-N1	1.861(2)	1.8528(8)	1.854(3)
Ni-N3	1.855(2)	1.8580(8)	1.863(3)
Ni-S1	2.1546(6)	2.1617(3)	2.1542(11)
Ni-S2	2.1598(7)	2.1576(2)	2.1527(10)
S1-C5	1.767(3)	1.7665(9)	1.763(4)
N2-C5	1.315(3)	1.3222(12)	1.308(5)
N1-N2	1.378(3)	1.3694(11)	1.381(4)
N1-C1	1.303(3)	1.3038(11)	1.310(5)
C1-C3	1.489(4)	1.4857(13)	1.487(5)
C1-C2	1.470(3)	1.4658(13)	1.474(5)
N5-C5	1.339(3)	1.3456(12)	1.350(5)
N5-C7	1.449(3)	1.4570(13)	1.440(5)
Bond angle			
N1-Ni-S1	87.07(6)	87.09(3)	87.35(10)
N1-Ni-N3	83.59(9)	83.66(4)	83.65(13)
S2-Ni-S1	101.81(3)	102.019(10)	101.94(4)

Table 5

Bond distances and angles of complex **2**.

Atoms	Distance (Å)	Atoms	Angle (°)
Ni-N1	1.8528(8)	N1-Ni-N3	83.66(4)
Ni-N3	1.8580(8)	N1-Ni-S2	170.88(3)
Ni-S1	2.1617(3)	N3-Ni-S2	87.23(3)
Ni-S2	2.1576(2)	N1-Ni-S1	87.09(3)
S1-C5	1.7665(9)	S2-Ni-S1	102.019(10)
N1-C1	1.3038(11)	C5-S1-Ni	94.59(3)
N1-N2	1.3694(11)	C1-N1-N2	119.80(8)
N2-C5	1.3222(12)	C1-N1-Ni	115.46(6)
N5-C5	1.3456(12)	N2-N1-Ni	124.64(6)
N5-C8	1.4453(13)	C5-N2-N1	110.47(8)
N5-C7	1.4570(13)	C5-N5-C8	124.17(9)
C1-C2	1.4658(13)	C5-N5-C7	118.67(8)
C1-C3	1.4857(13)	C8-N5-C7	117.15(8)
		N1-C1-C2	112.75(8)
		N1-C1-C3	123.71(9)
		C2-C1-C3	123.52(8)
		C1-C2-C4	122.36(8)
		N2-C5-N5	116.74(8)
		N2-C5-S1	123.18(7)
		N5-C5-S1	120.06(7)

Table 6

Bond distances and angles of complex **3**.

Atoms	Distance(Å)	Atoms	Angle(°)
Ni-N1	1.854(3)	N1-Ni-N3	83.65(13)
Ni-N3	1.863(3)	N1-Ni-S2	170.63(10)
Ni-S2	2.1527(10)	N3-Ni-S2	87.12(9)
Ni-S1	2.1542(11)	N1-Ni-S1	87.35(10)
S1-C5	1.763(4)	S2-Ni-S1	101.94(4)
N1-C1	1.310(5)	C5-S1-Ni	94.17(13)
N1-N2	1.381(4)	C1-N1-N2	120.5(3)
N2-C5	1.308(5)	C1-N1-Ni	115.3(2)
N5-C5	1.350(5)	N2-N1-Ni	124.2(2)
N5-C7	1.440(5)	C5-N2-N1	109.8(3)
F1-C8	1.338(5)	C5-N5-C7	123.5(3)
F2-C8	1.339(4)	N1-C1-C2	112.6(3)
F3-C8	1.347(4)	N1-C1-C3	124.1(3)
C1-C2	1.474(5)	C2-C1-C3	123.3(3)
C1-C3	1.487(5)	C1-C2-C4	122.6(3)
		N2-C5-N5	119.3(3)
		N2-C5-S1	124.4(3)
		N5-C5-S1	116.2(3)
		N5-C7-C8	111.7(3)
		F1-C8-F2	106.7(3)
		F1-C8-F3	106.7(3)
		F2-C8-F3	106.0(3)
		F1-C8-C7	112.6(3)
		F2-C8-C7	111.4(3)
		F3-C8-C7	112.8(3)

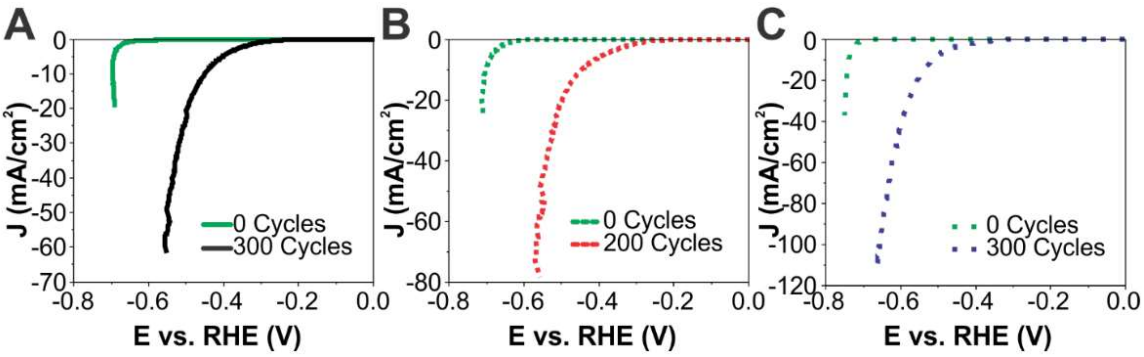

Figure 51. Effects of reductive cycling from 0 to -0.8 V vs. RHE at 50 mV/s on the performance of the three modified electrodes. Vertical scale is expanded to show peak cathodic current for each electrode. (A) Polarization curves for **GC-1** which exhibits peak HER performance after 300 cycles. (B) Polarization curves for **GC-2** which exhibits peak HER performance after 200 cycles. (C) Polarization curves for **GC-3** which exhibits peak HER performance after 300 cycles.

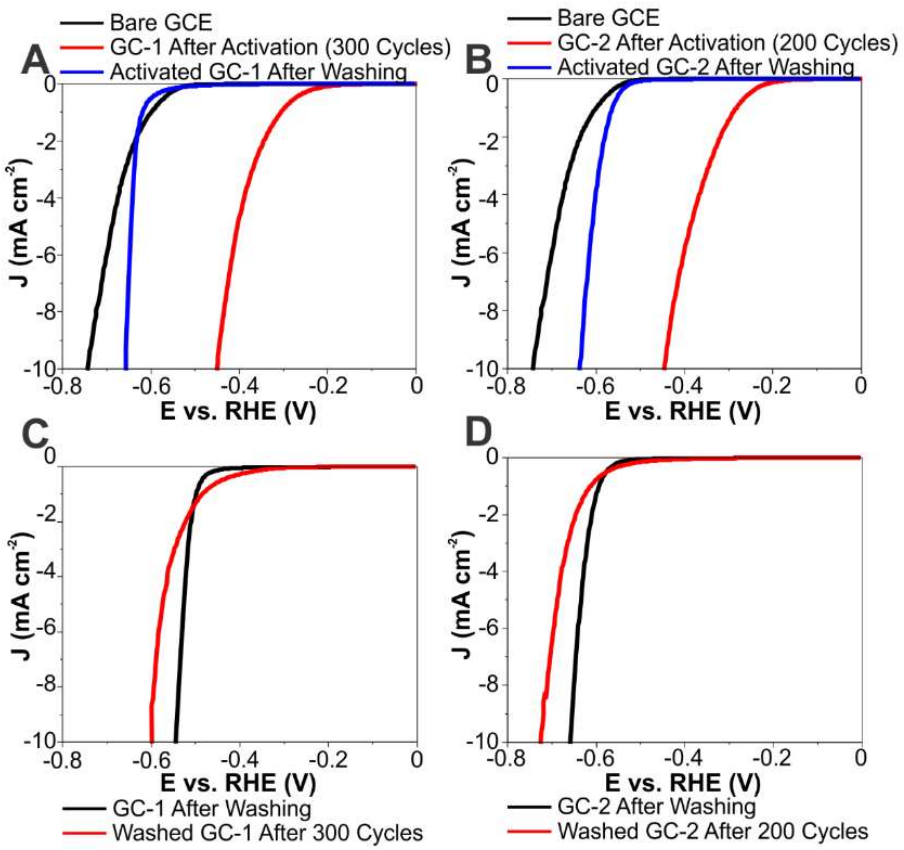

Figure 52. Effect on HER performance of dipping modified electrodes in acetonitrile for 30 seconds at 800 RPM rotation. (A) **GC-1** conditioned to peak activity (300 cycles, red trace) and then washed in acetonitrile (blue trace) and compared to bare glassy carbon electrode (black trace). (B) **GC-2** conditioned to peak activity (200 cycles, red trace) and then washed in acetonitrile (blue trace) and compared to glassy carbon (black trace). (C) **GC-1** washed in acetonitrile before any conditioning (black trace) and subsequently conditioned to 300 cycles (red trace). (D) **GC-2** washed in acetonitrile before any conditioning (black trace) and subsequently conditioned to 200 cycles (red trace).

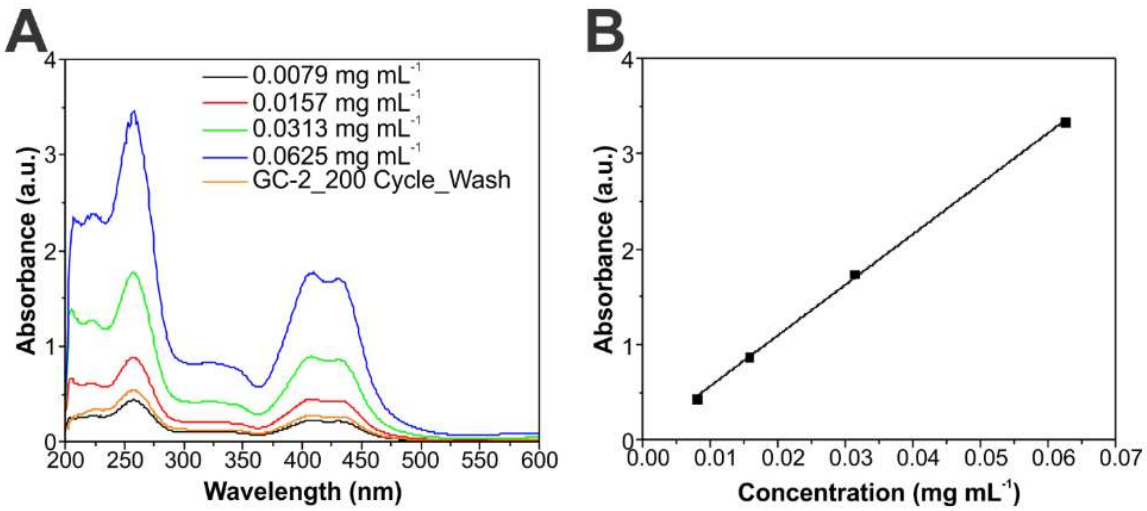

Figure 53. UV-Visible Spectroscopy data for complex **2** in solution. (A) UV-Vis spectra for complex **2** in acetonitrile solutions of known concentration and of unknown concentration after being washed off **GC-2** after conditioning to peak activity (200 cycles). (B) Calibration curve constructed from measured absorbances and known concentrations of standard acetonitrile solutions of **2**.

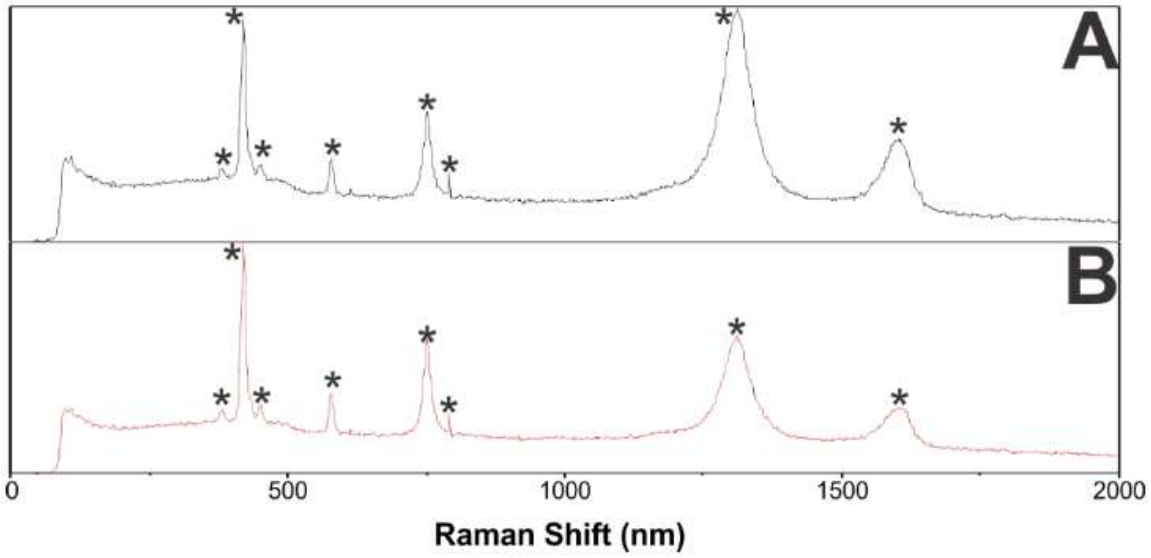

Figure 54. Raman spectra of various electrodes and organic solutions with bands labelled. Raman spectrum of (A) Glassy carbon electrode with Nafion film. (B) Bare glassy carbon electrode. Peaks labelled with * are attributed to the glassy carbon electrode.

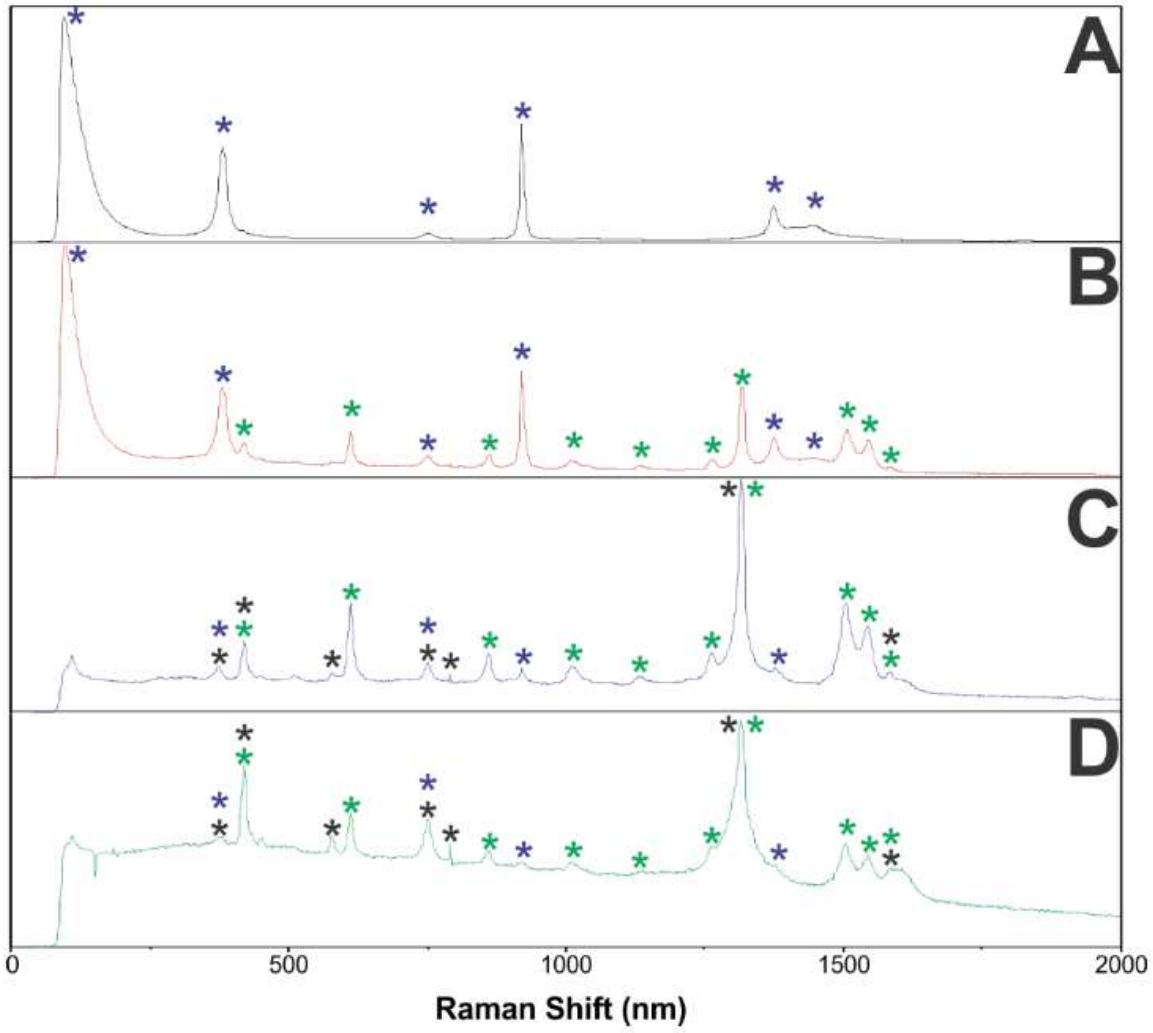

Figure 55. Raman spectra of various electrodes and organic solutions with bands labelled. Raman spectrum of (A) Acetonitrile. (B) Complex **2** in acetonitrile ink with Nafion. (C) **GC-2** as deposited. (D) **GC-2** after conditioning to peak activity (200 cycles). Peaks labelled with * are attributed to the glassy carbon electrode. Peaks labelled with * are attributed to acetonitrile. Peaks labelled with * are attributed to complex **2**.

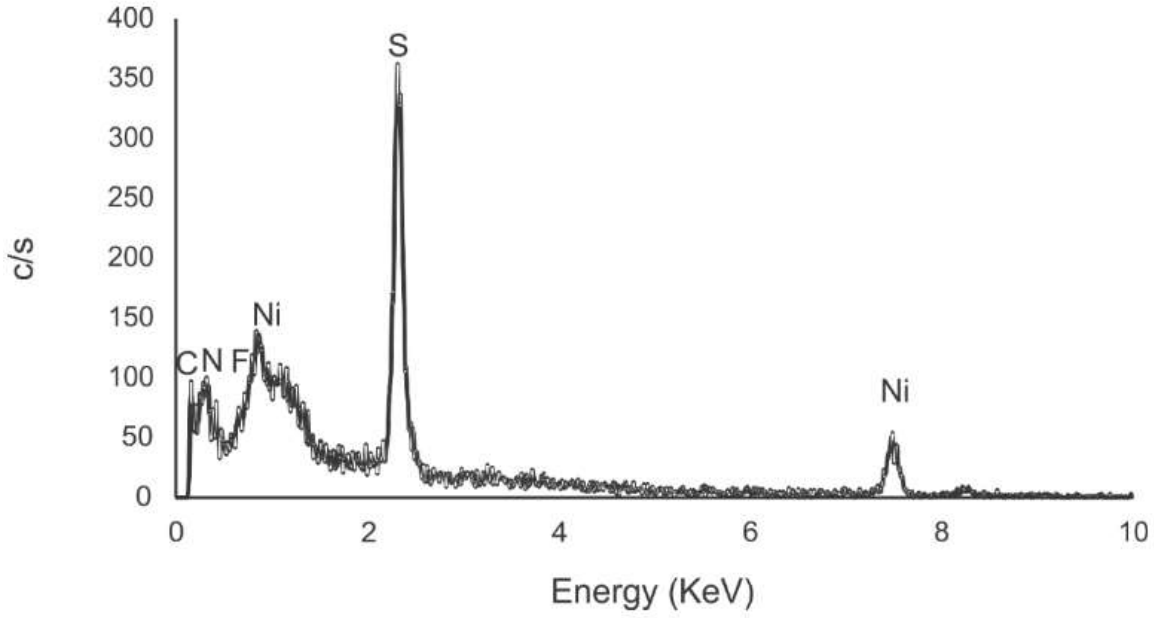

Figure 56. EDS of **GC-2** before reductive cycling.

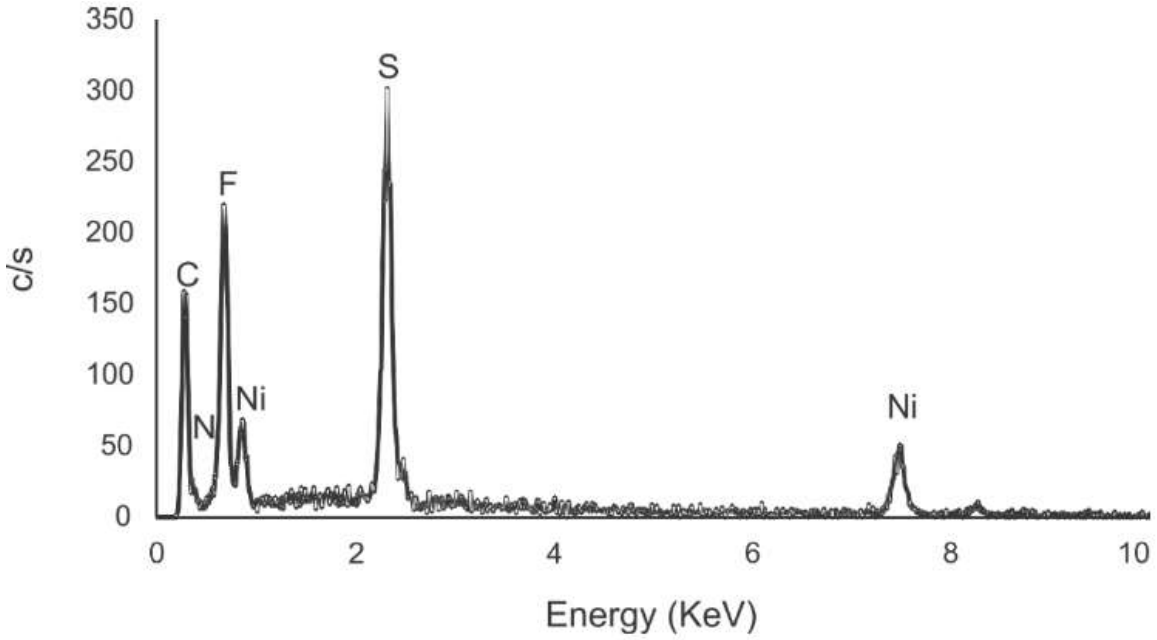

Figure 57. EDS of **GC-2** after 1000 cycles.

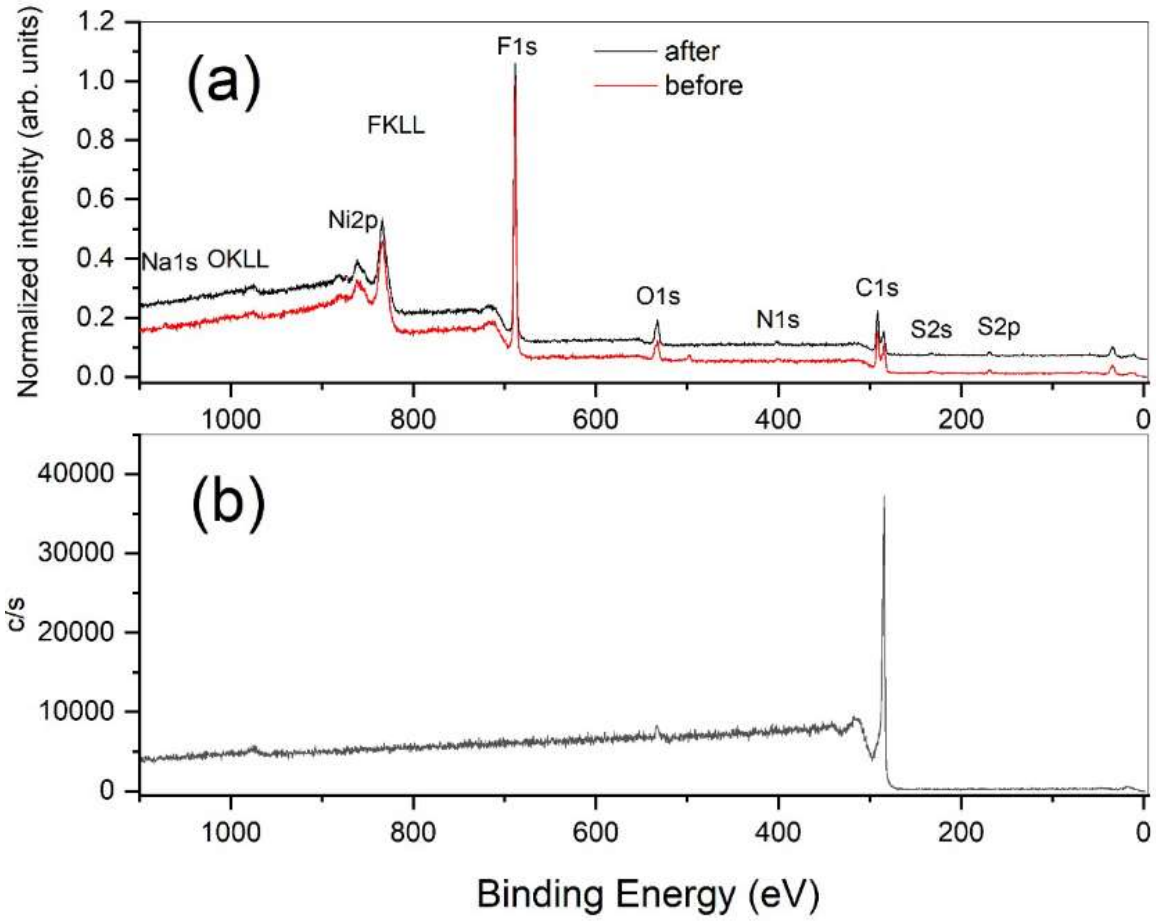

Figure 58. Survey scans of the **GC-2** electrode before (red) and after (black) conditioning to 1000 cycles (a) and of a pristine GCE (b).

Table 7

Atomic % of Ni2p, S2p and Ni1s before and after conditioning (1000 cycles).

	N1s, at%	S2p, at%	Ni2p, at%
Before	61.3	26.74	11.96
After	66.74	23.35	9.91

Table 8

XPS fitting parameters for nickel (Figure 27A).

Band	Pos	PosSep	B_FWHM	FWHM	Height	%Gauss	Area	%Area	ChiSquared
1	853.38	0	3.12	3.12	1459	80	5309	37.12	1.94
2	859.24	5.86	6.72	6.72	482	80	3775	26.4	
3	870.81	17.43	3.37	3.37	675	80	2654	18.56	
4	876.33	22.95	6.39	6.39	344	80	2564	17.93	

Table 9

XPS fitting parameters for sulfur (Figure 27B).

Band	Pos	PosSep	B_FWHM	FWHM	Height	%Gauss	Area	%Area	ChiSquared
1	162.93	0	2.6	2.6	211	80	640	56.12	1.35
2	164.13	1.2	2.6	2.6	109	87	320	28.06	
3	168.33	5.4	2.7	2.7	37	70	120	10.54	
4	169.53	6.6	2.65	2.65	19	70	60	5.27	

Table 10

XPS fitting parameters for nickel (Figure 27A).

Band	Pos	PosSep	B_FWHM	FWHM	Height	%Gauss	Area	%Area	ChiSquared
1	853.31	0	2.84	2.84	6436	90	20406	29.53	2.81
2	858.1	4.79	8.79	8.79	2405	90	23572	34.11	
3	870.58	17.28	3.96	3.96	2656	90	11718	16.95	
4	876.2	22.89	8.94	8.94	1346	90	13417	19.41	

Table 11

XPS fitting parameters for sulfur (Figure 27B).

Band	Pos	PosSep	B_FWHM	FWHM	Height	%Gauss	Area	%Area	ChiSquared
1	162.32	0	2.57	2.57	1571	100	4293	51.15	1.71
2	163.52	1.2	2.57	2.57	718	80	2146	25.57	
3	164.48	2.16	3.2	3.2	221	60	895	10.66	
4	165.68	3.36	3.2	3.2	116	71	447	5.33	
5	168.22	5.9	2.7	2.7	124	70	408	4.86	
6	169.42	7.1	2.7	2.7	65	79	204	2.43	

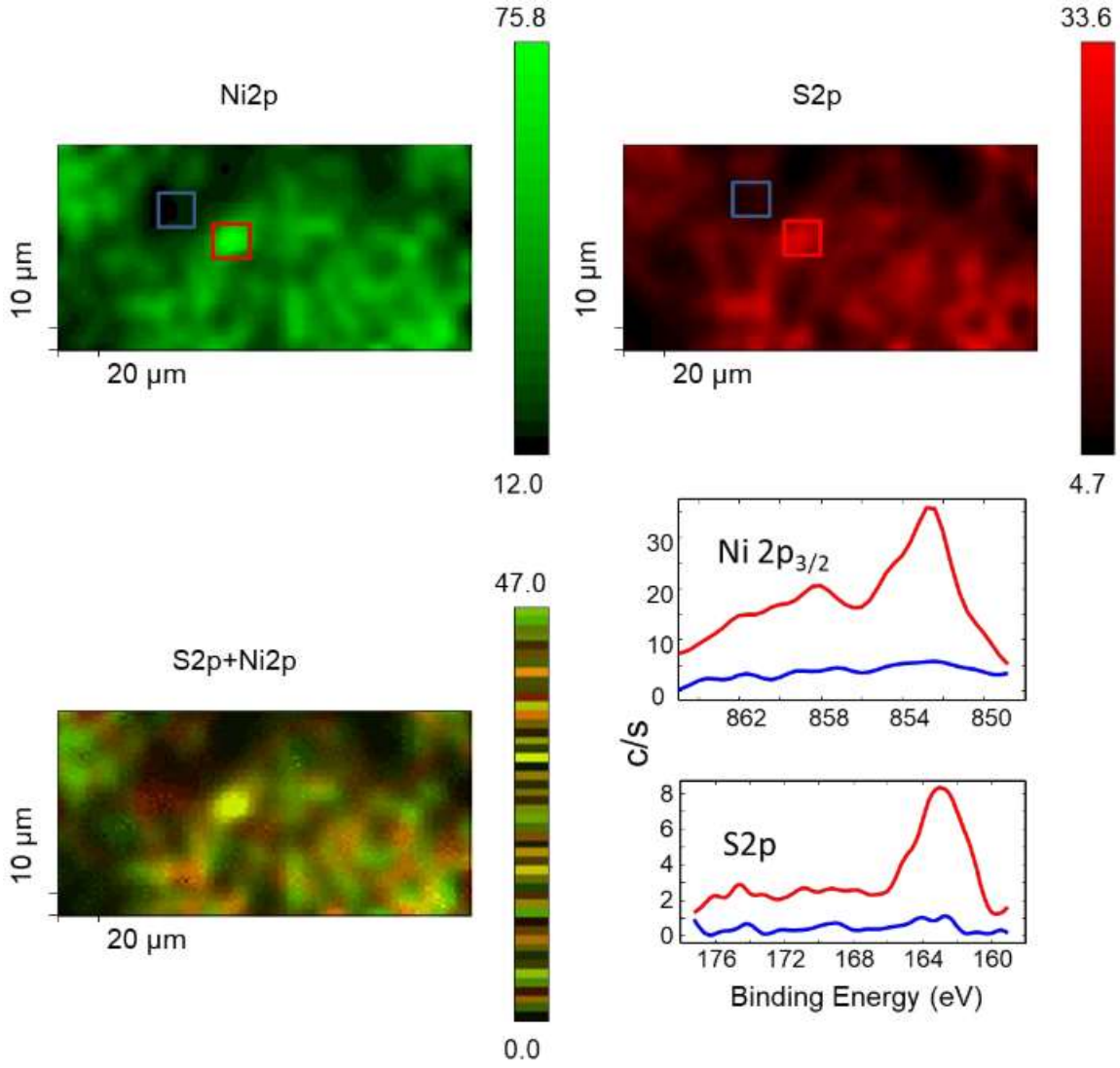

Figure 59. Elemental mapping of nickel and sulfur. Elemental mapping of nickel (top left), sulfur (top right), and an overlay of both (bottom left) at 200 × 100 µm scanned area and XPS spectra (right bottom) in which the red trace and blue trace correspond to the pixels integrated through red and blue squares respectively.

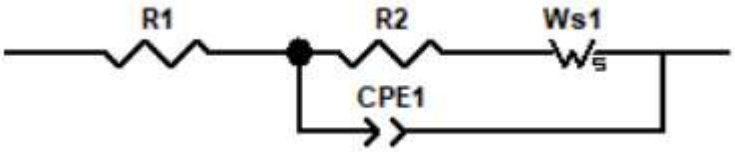

Figure 60. Equivalent circuit model used to fit EIS data.

Table 12

Parameters obtained by fitting frequency response analysis (FRA) data to simulated RCW circuit. Zview software[262] was used to fit data. Q is the magnitude of the CPE, Rc is the charge transfer resistance, Rs is approximate solution resistance, n is the CPE exponent, and C is the capacitance.

Capacitance values were calculated using $C = R_C^{\frac{1-n}{n}} * Q^{\frac{1}{n}}$.[263–267]

GC	1			2			3		
# Cycles	0	300	1000	0	200	1000	0	300	1000
Q (F s^{n-1})	2.43E-6	4.52E-6	4.46E-6	2.63E-6	6.10E-6	6.33E-6	3.55E-5	3.20E-5	5.14E-5
R_c (Ω)	25099	270	374	18843	158	374	54764	631	1093
R_s (Ω)	26.22	20.12	17.99	16.80	15.09	13.9	11.14	6.44	5.78
N	0.908	0.929	0.913	0.916	0.893	0.864	0.951	0.729	0.717
C (F)	1.83E-6	2.71E-6	2.43E-6	2.00E-6	2.65E-6	2.49E-6	3.67E-5	7.52E-6	1.66E-5
χ^2	0.00015	0.00121	0.00141	0.00072	0.00057	0.00057	0.03272	0.00163	0.00434

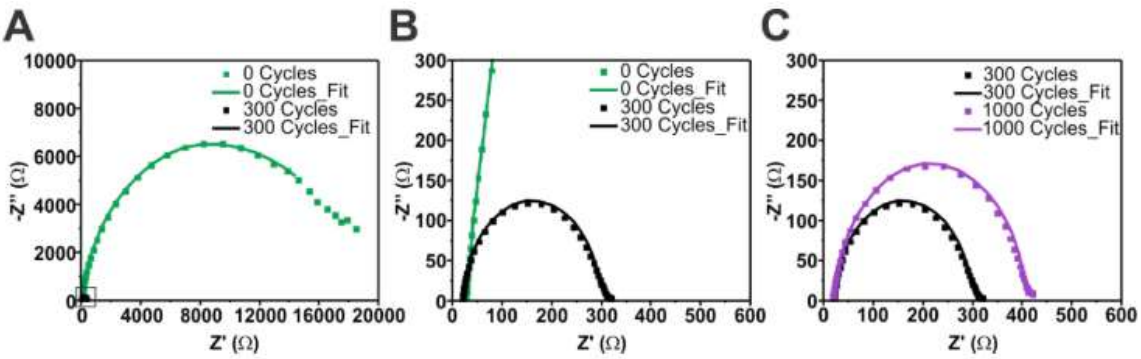

Figure 61. Nyquist plots showing the effects of reductive cycling from 0 to -0.8 V vs. RHE at 50 mV/sec on the impedance of **GC-1**. Solid traces represent fitted impedance data, while dotted traces represent actual data. (A) Nyquist plot showing impedance at 0 cycles (before any reductive cycling) and after 300 cycles (peak activity, in small frame). (B) The same data as in (A), but with axes scaled down to show impedance after 300 cycles in greater detail. (C) Comparison of Nyquist plots for **GC-1** after 300 cycles and 1000 cycles.

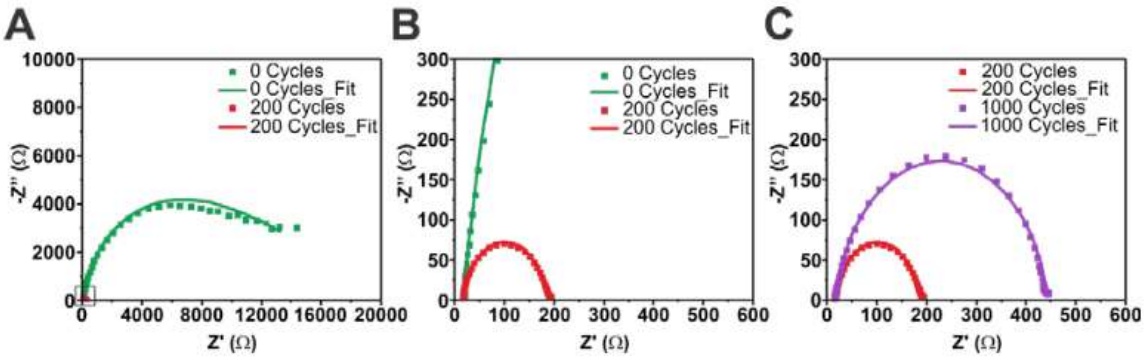

Figure 62. Nyquist plots showing the effects of reductive cycling from 0 to -0.8 V vs. RHE at 50 mV/sec on the impedance of **GC-2**. Solid traces represent fitted impedance data, while dotted traces represent actual data. (A) Nyquist plot showing impedance at 0 cycles (before any reductive cycling) and after 200 cycles (peak activity, in small frame). (B) The same data as in (A), but with axes scaled down to show impedance after 200 cycles in greater detail. (C) Comparison of Nyquist plots for **GC-2** after 200 and 1000 cycles.

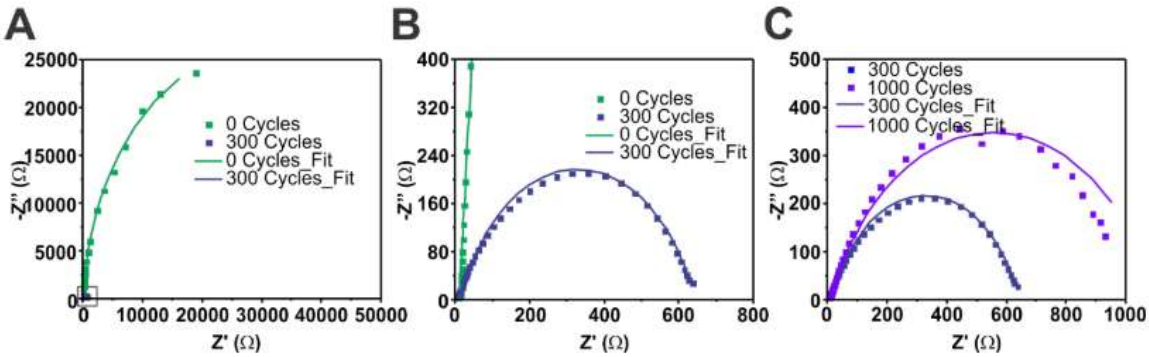

Figure 63. Nyquist plots showing the effects of cycling from 0 to -0.8 V vs. RHE at 50 mV/sec on the impedance of **GC-3**. Solid traces represent fitted impedance data, while dotted traces represent actual data. (A) Nyquist plot showing impedance at 0 cycles (before any reductive cycling) and after 300 cycles (peak activity, in small frame). (B) The same data as in (A), but with axes scaled down to show impedance after 300 cycles in greater detail. (C) Comparison of Nyquist plots for **GC-3** after 300 and 1000 cycles.

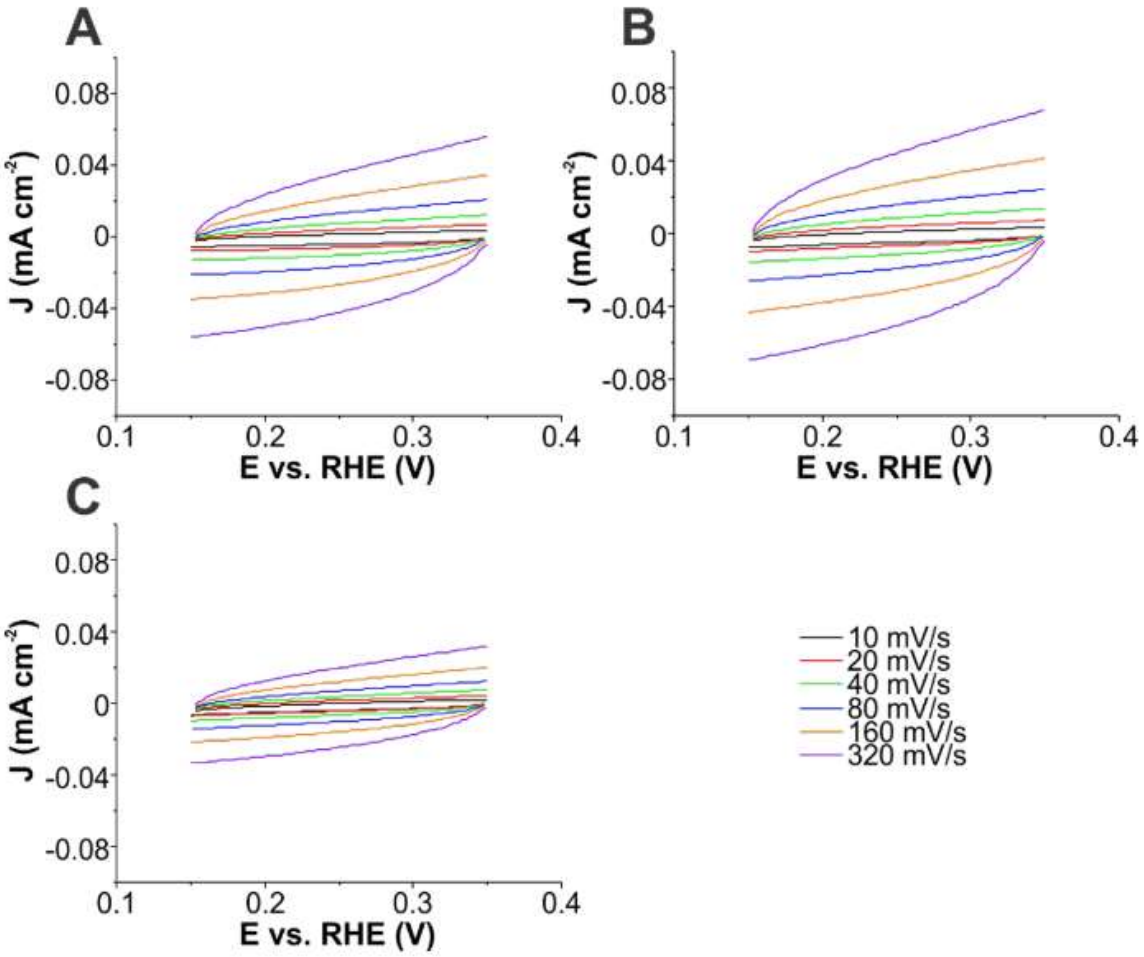

Figure 64. Cyclic voltammetry plots showing the capacitive effects of varying scan speed over a non-Faradaic potential range for **GC 1 – 3** as-deposited. (A) **GC-1** at 0 cycles. (B) **GC-2** at 0 cycles. (C) **GC-3** at 0 cycles

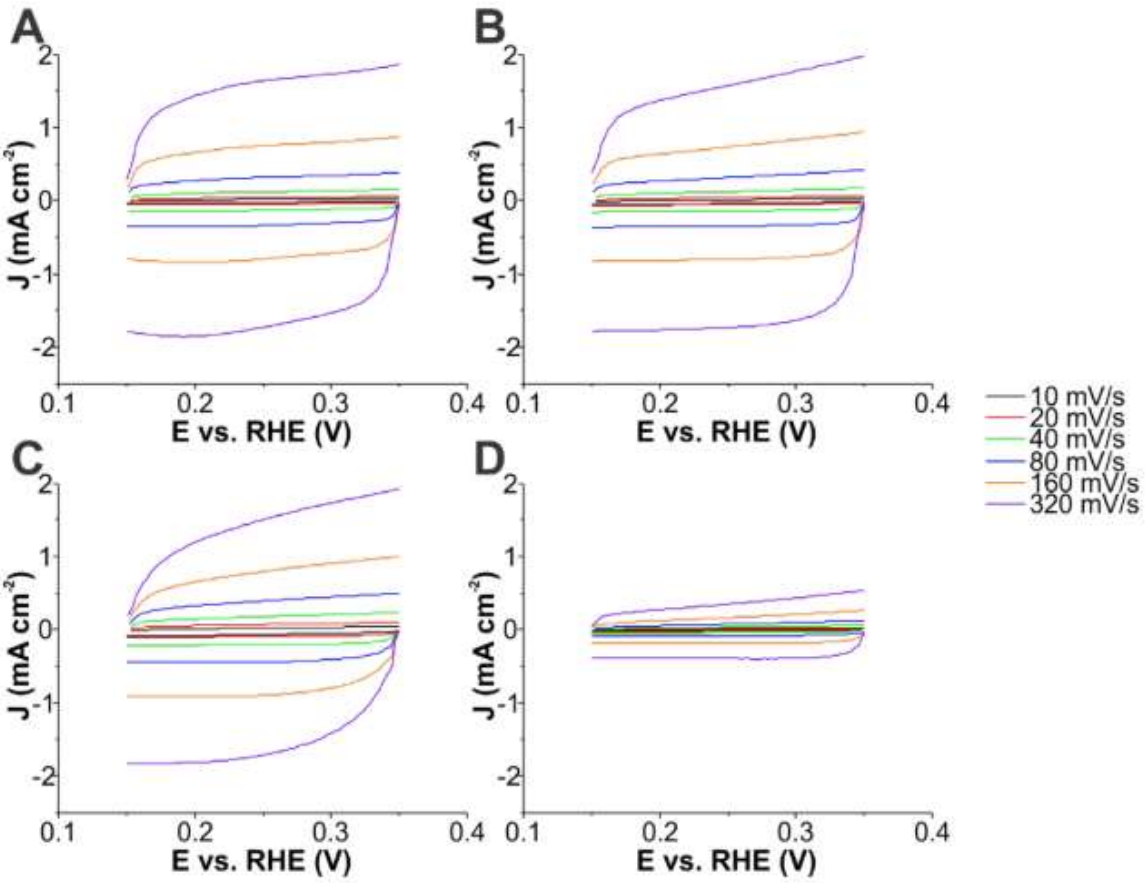

Figure 65. Cyclic voltammetry plots showing the capacitive effects of varying scan speed over a non-Faradaic potential range for **GC 1 – 3** after cycling to peak activity. (A) **GC-1** after 300 cycles. (B) **GC-2** after 200 cycles. (C) **GC-3** after 300 cycles. (D) Bare glassy carbon electrode.

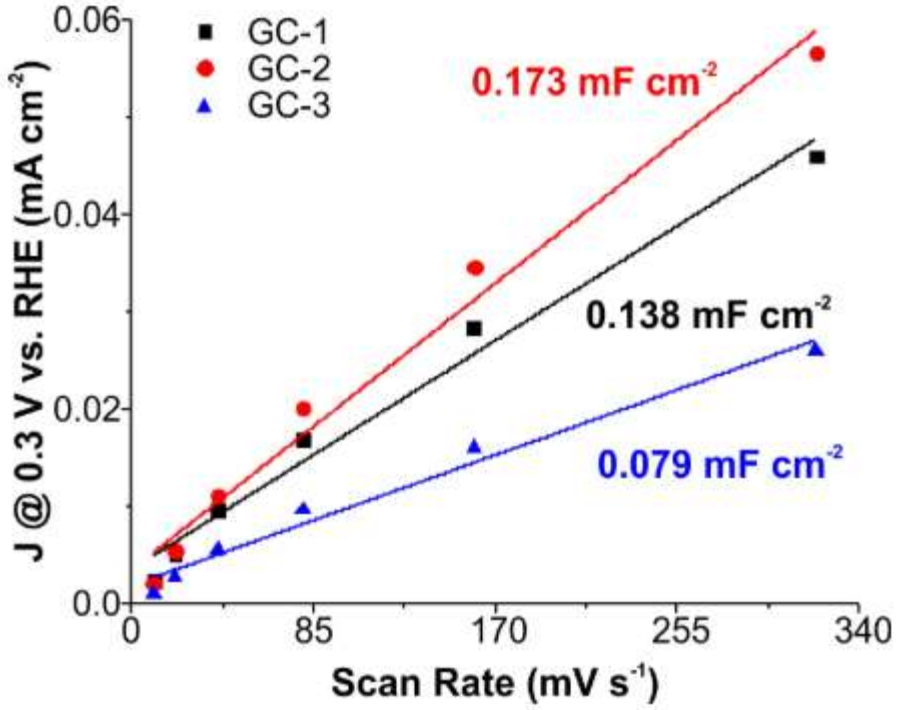

Figure 66. Plot of average current density at 0.3 V vs. RHE as measured during anodic sweep as a function of scan rate for as-deposited electrodes. Slopes of the traces give the approximate capacitances of each modified electrode per unit geometric area (denoted in the same color as the corresponding trace).

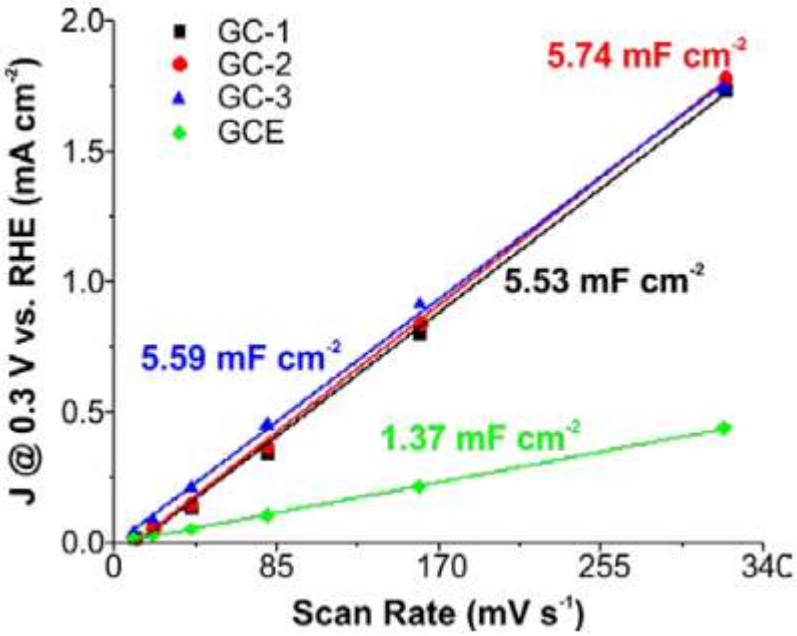

Figure 67. Plot of average current density at 0.3 V vs. RHE as measured during anodic sweep as a function of scan rate for **GC 1 – 3** after cycling to peak activity. Slopes of the traces give the approximate capacitances of each modified electrode per unit geometric area. The black trace corresponds to **GC-1** after 300 cycles, the red trace corresponds to **GC-2** after 200 cycles, and the blue trace corresponds to **GC-3** after 300 cycles.

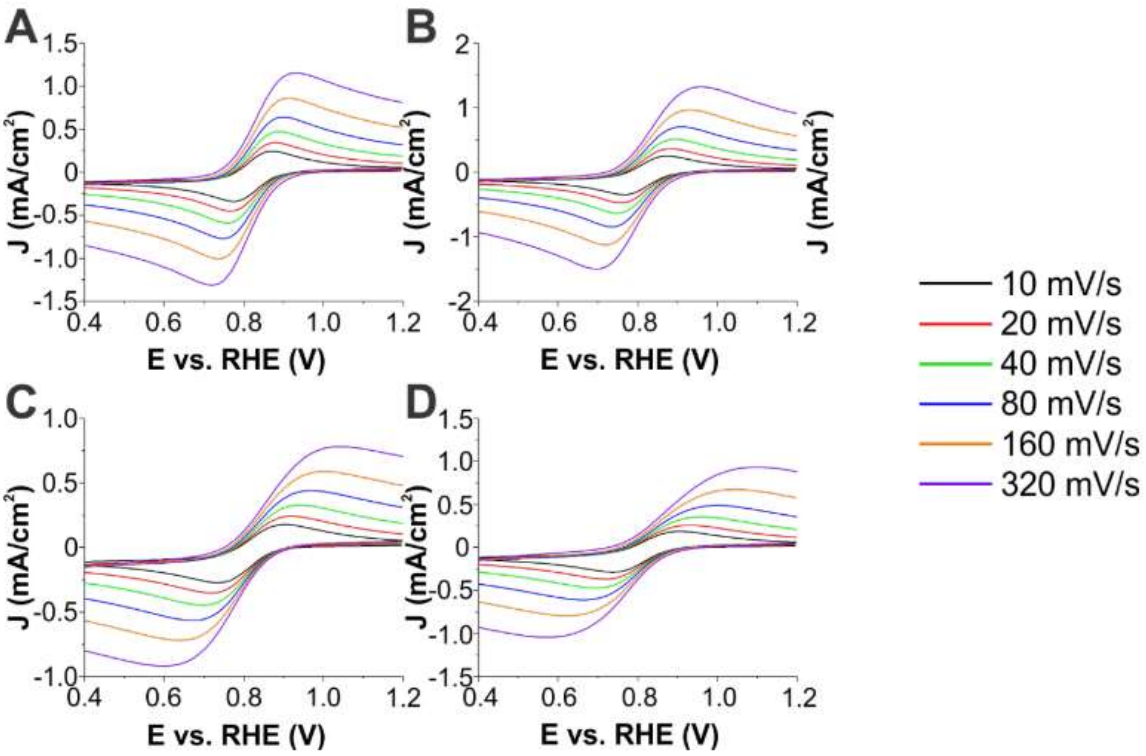

Figure 68. Oxidation (top peak) and reduction (bottom peak) of ferricyanide redox couple at 5 mM in 0.1 M potassium nitrate solution. (A) **GC-1** as-deposited. (B) **GC-1** after conditioning to 300 cycles. (C) **GC-2** as-deposited. (D) **GC-2** after conditioning to 200 cycles.

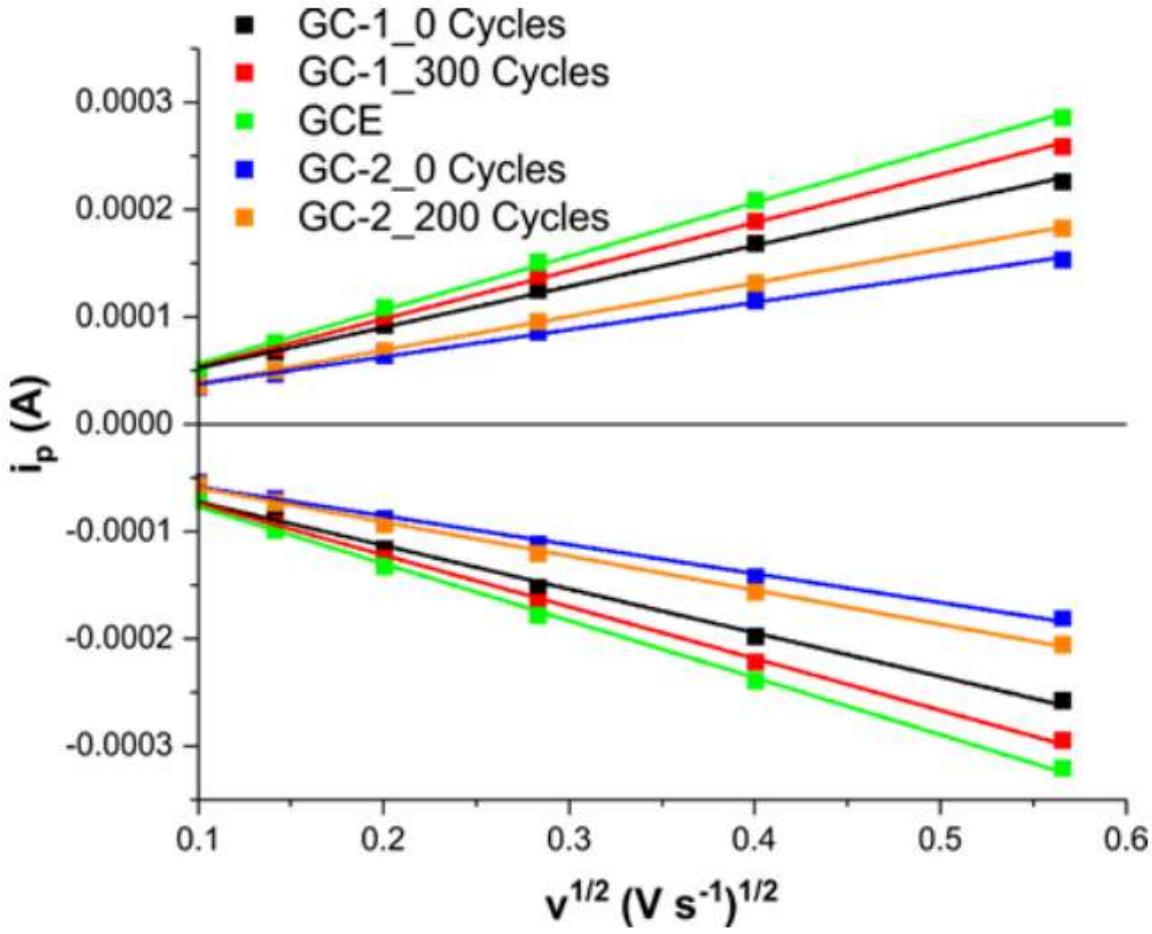

Figure 69. Plot of maximum current (top, for anodic sweeps) and minimum current (bottom, for cathodic sweeps) associated with ferricyanide reduction/oxidation cyclic voltammetry experiment as a function of the square root of scan rate.

Table 13

Slopes of the traces of maximum/minimum current densities as a function of the square root of scan rate for ferricyanide oxidation/reduction experiments as well as areas calculated from the Randles-Sevcik equation.

	Anodic		Cathodic	
Material	**Slope**	**Area (cm^2)**	**Slope**	**Area (cm^2)**
GC-1_300 Cycles	$4.5x10^{-4}$	0.12	$-4.8x10^{-4}$	0.14
GC-1_0 Cycles	$3.8x10^{-4}$	0.11	$-4.1x10^{-4}$	0.12
GC-2_200 Cycles	$3.1x10^{-4}$	0.09	$-3.2x10^{-4}$	0.09
GC-2_0 Cycles	$2.5x10^{-4}$	0.07	$-2.7x10^{-4}$	0.08

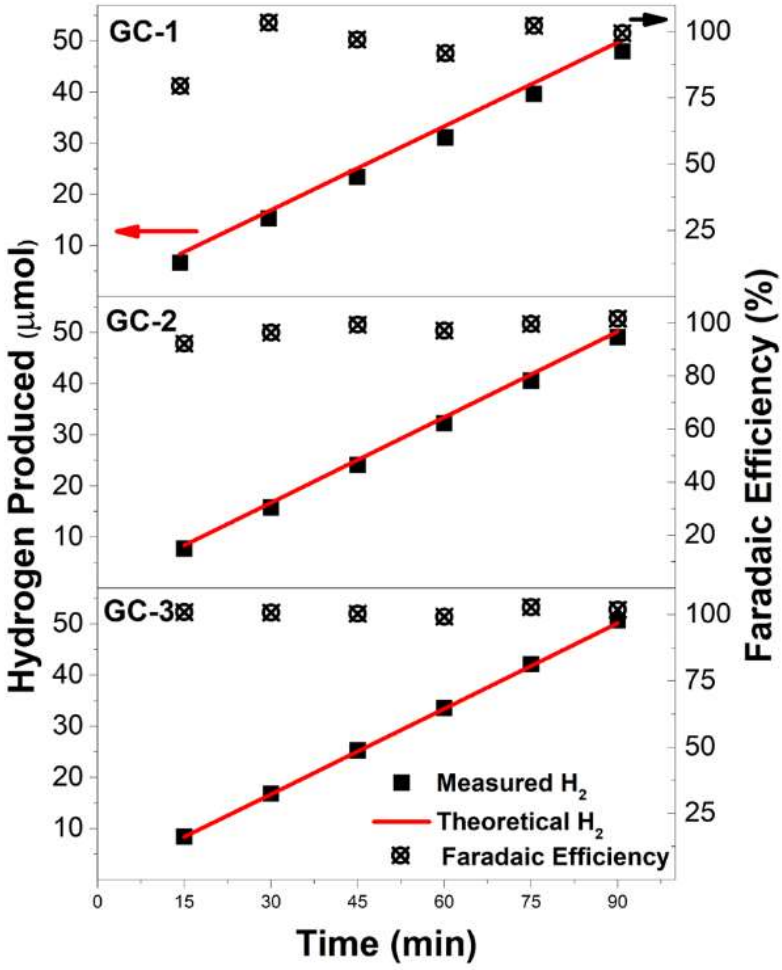

Figure 70. Plot of theoretical hydrogen, measured hydrogen, and Faradaic efficiencies for **GC 1 – 3** after cycling to peak activity. Theoretical H_2 is calculated from the coulombs of charge passed during the experiment. Measured H_2 was detected via gas chromatography. The Faradaic efficiency was calculating by comparing these two values. **GC 1 – 3** were evaluated after 300, 200, and 300 cycles respectively.

SUPPORTING INFORMATION FOR CHAPTER 6

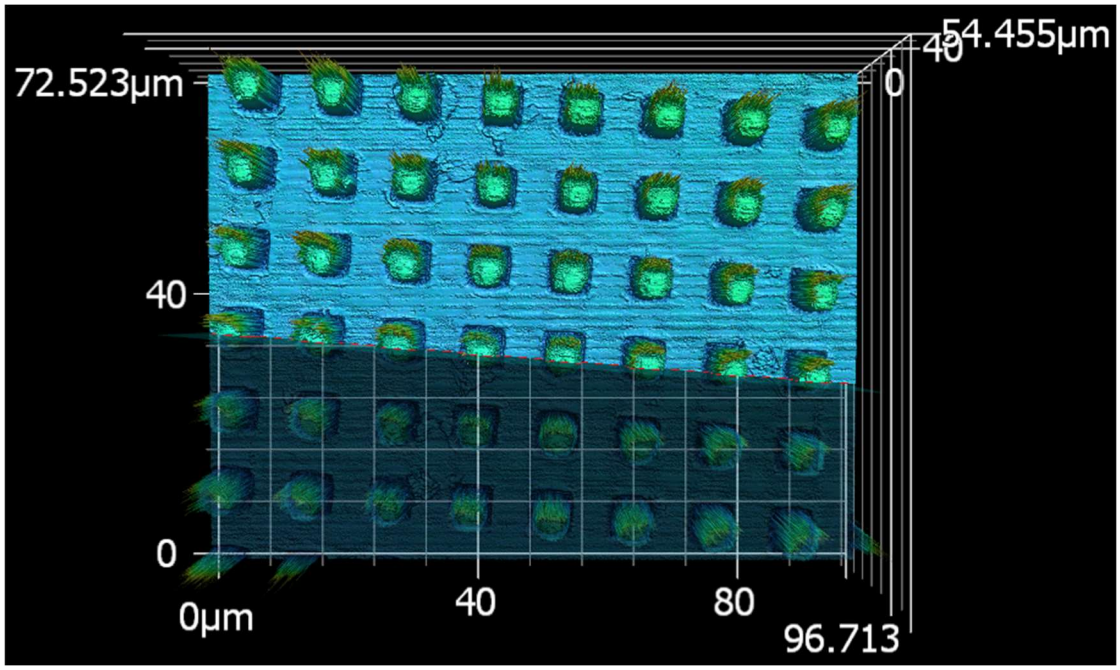

Figure 71. Surface topographical map of textured Nafion NR-211 PEM showing pillars on surface after hot pressing and removal of template. Obtained via laser profilometry.

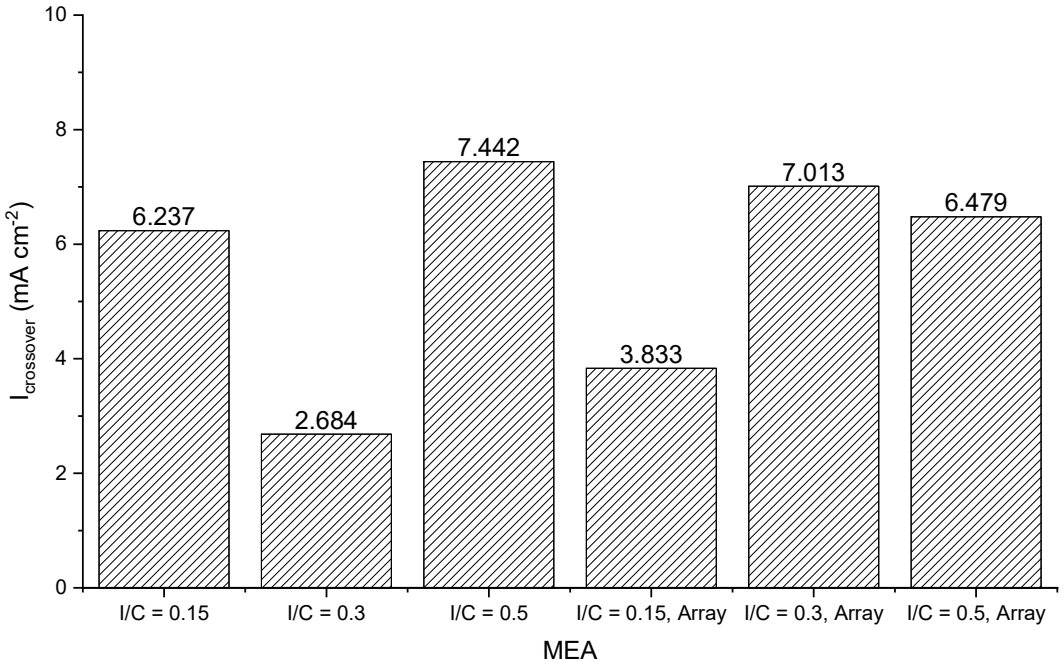

Figure 72. H_2 crossover measured at 0.5 V for each MEA.

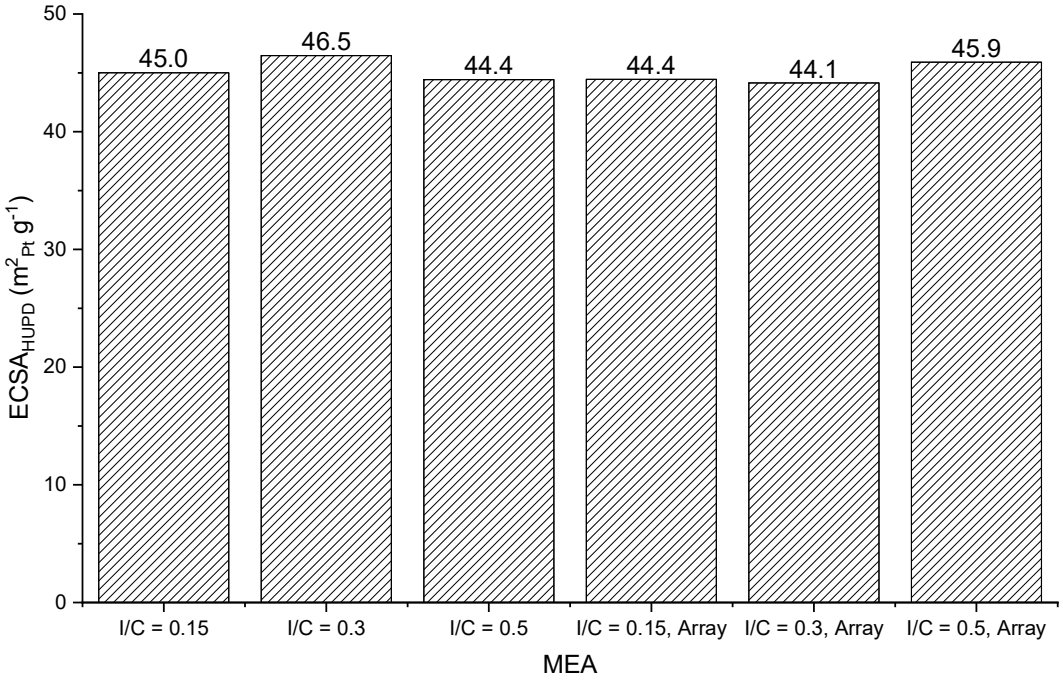

Figure 73. ECSA as determined by HUPD for Pt in the cathode CL of each MEA.

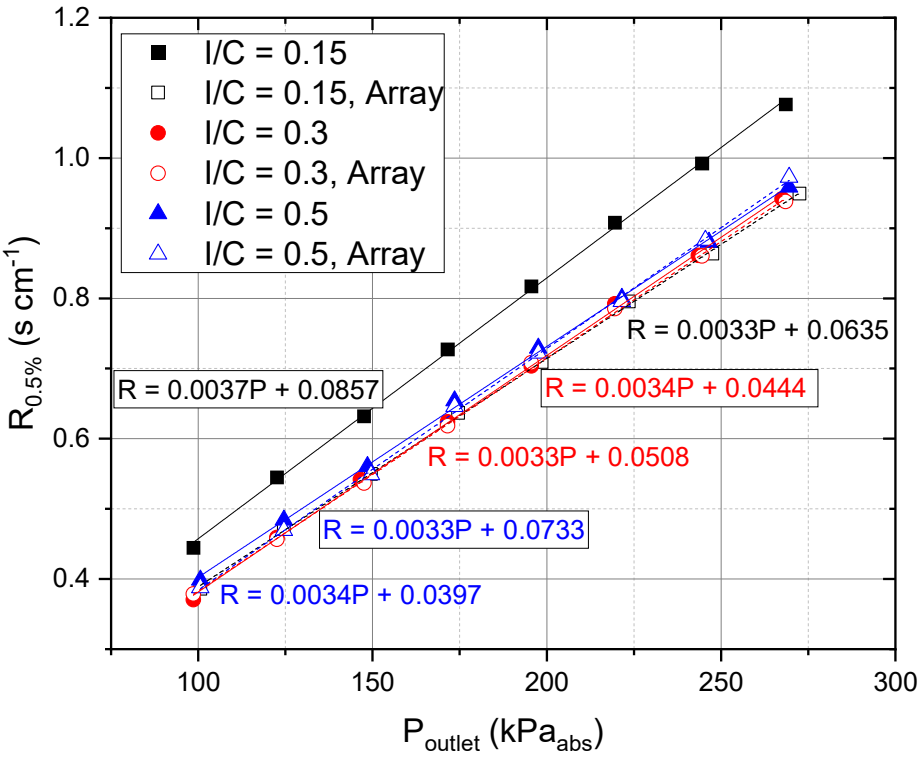

Figure 74. O_2 transport resistance in 0.5 % O_2 (balance N_2) as a function of pressure. Calculated from RO_2 limiting current. Boxed equations correspond to flat electrodes.

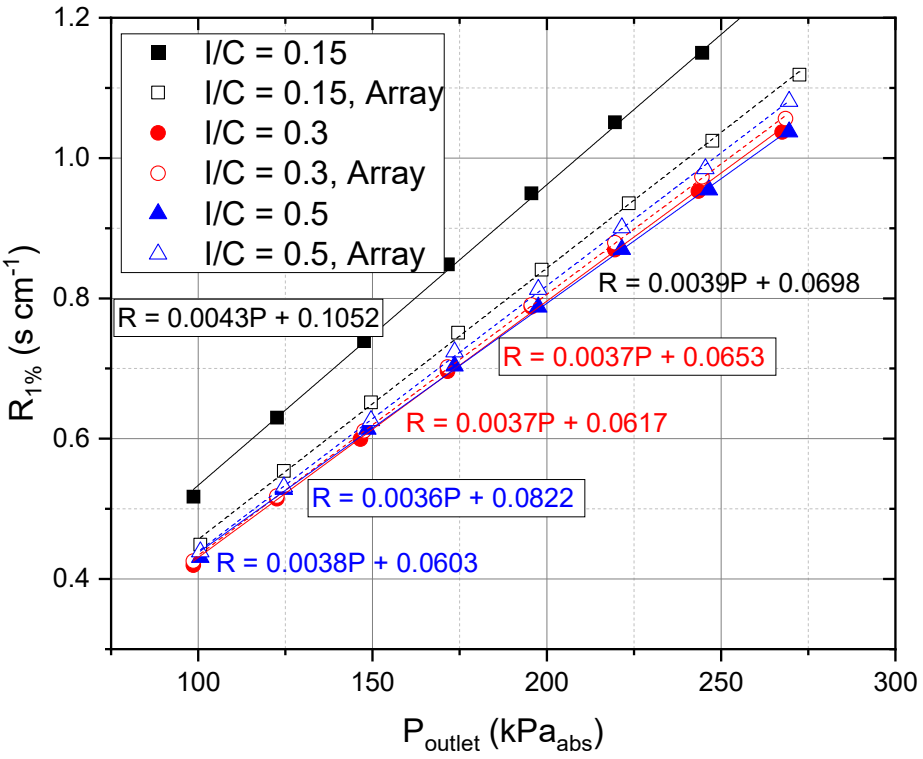

Figure 75. O_2 transport resistance in 1 % O_2 (balance N_2) as a function of pressure. Calculated from RO_2 limiting current. Boxed equations correspond to flat electrodes.

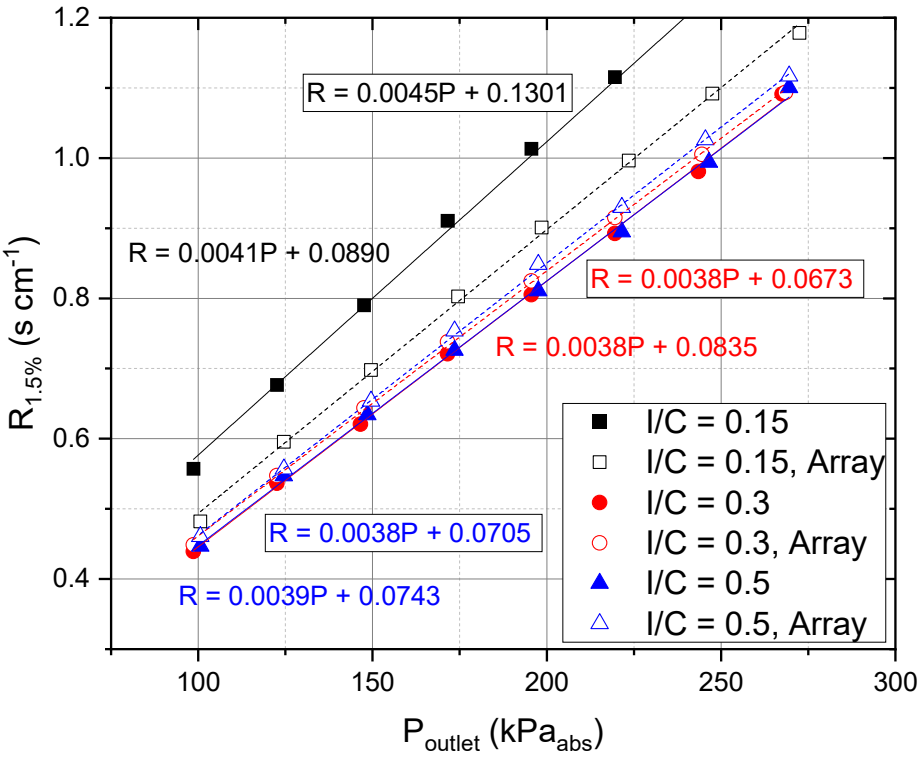

Figure 76. O_2 transport resistance in 1.5 % O_2 (balance N_2) as a function of pressure. Calculated from RO_2 limiting current. Boxed equations correspond to flat electrodes.

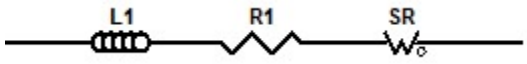

Figure 77. Equivalent circuit used to fit H_2/N_2 EIS data.

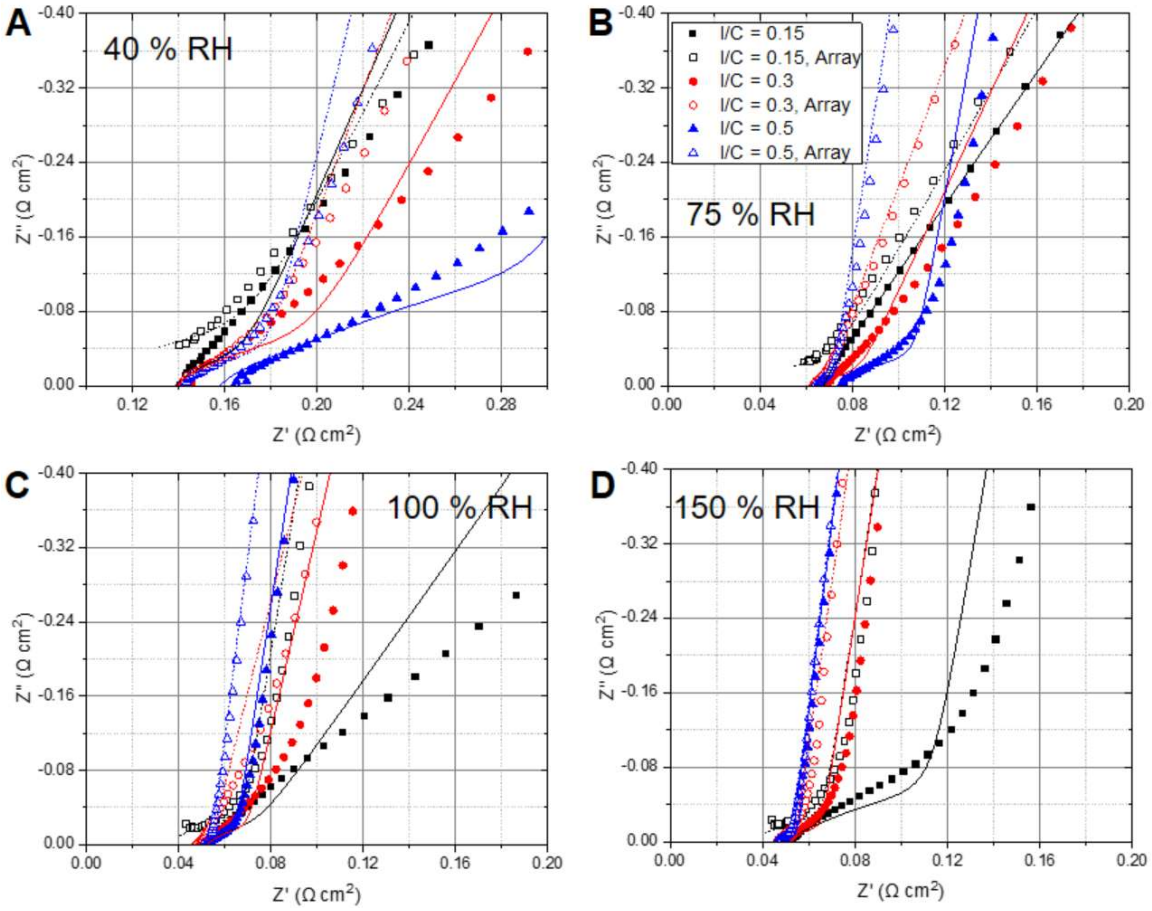

Figure 78. Zoomed-in view of data in Figure 37 focusing on high-frequency behavior.

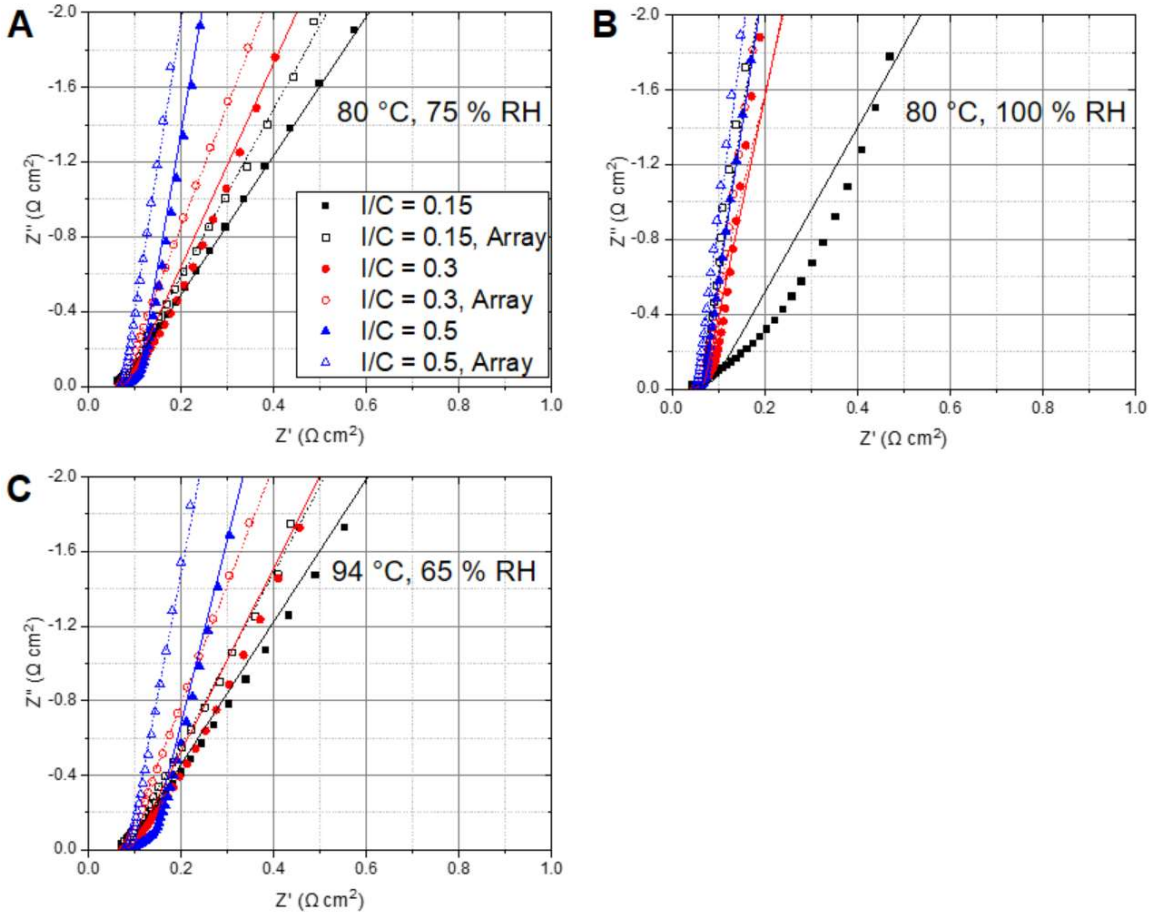

Figure 79. Nyquist representation of EIS at 0.5 V under H_2/N_2 at 250 kPa, (A) 80 ° C, and 75 % RH; (B) 80 ° C, and 100 % RH; (C) 94 °C, and 65 % RH. Symbols represent raw data, and lines represent equivalent circuit (Figure 77) fit.

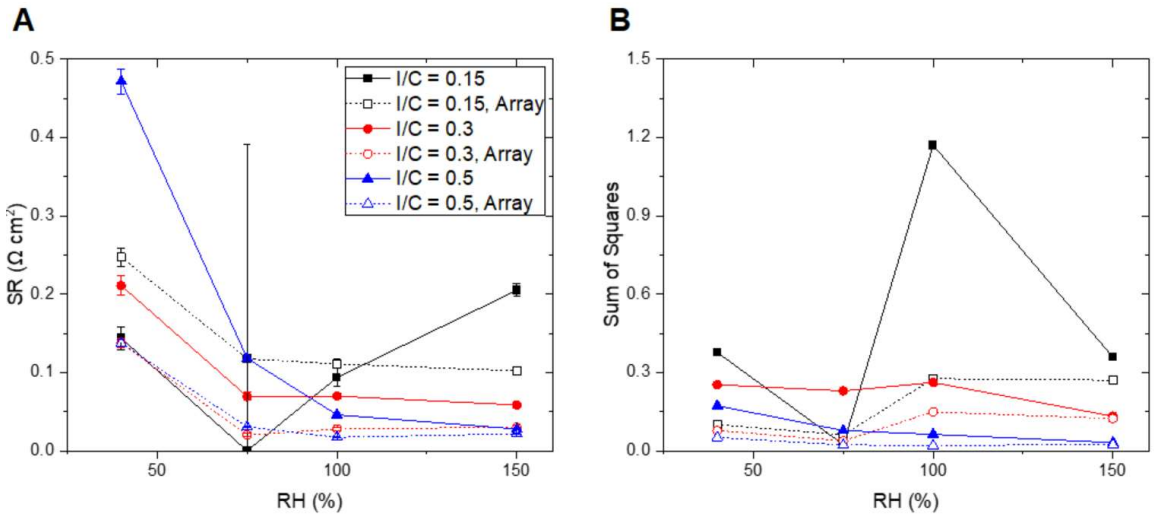

Figure 80. Results of fitting H_2/N_2 EIS data at 80 °C and 150 kPa (Figure 37) as a function of RH to the equivalent circuit in Figure 77. (A) Calculated SR. (B) sum of squares indicating goodness of fit.

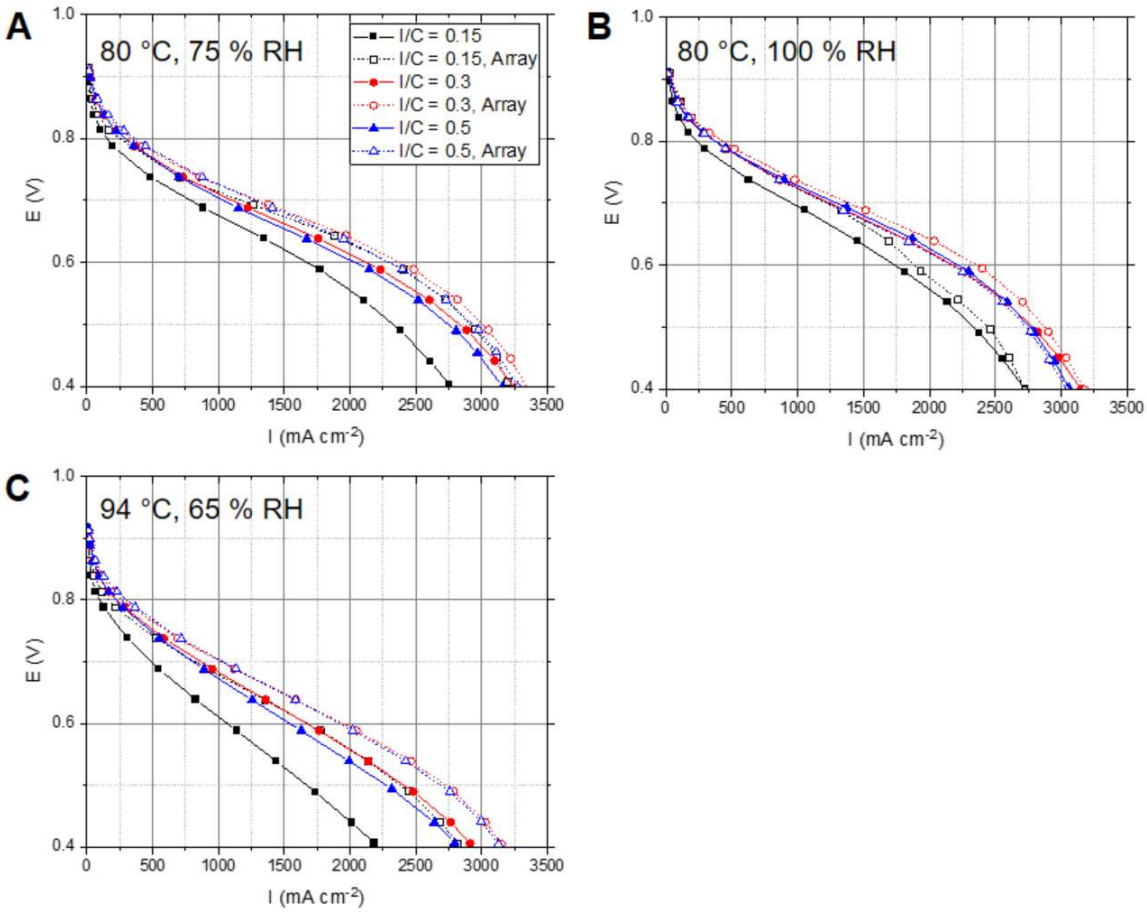

Figure 81. Polarization curves measured under H_2/air (1000/3000 sccm) at 250kPa and (A) 80 °C and 75 % RH, (B) 80 °C and 100 % RH, or (C) 94 °C and 65 % RH.

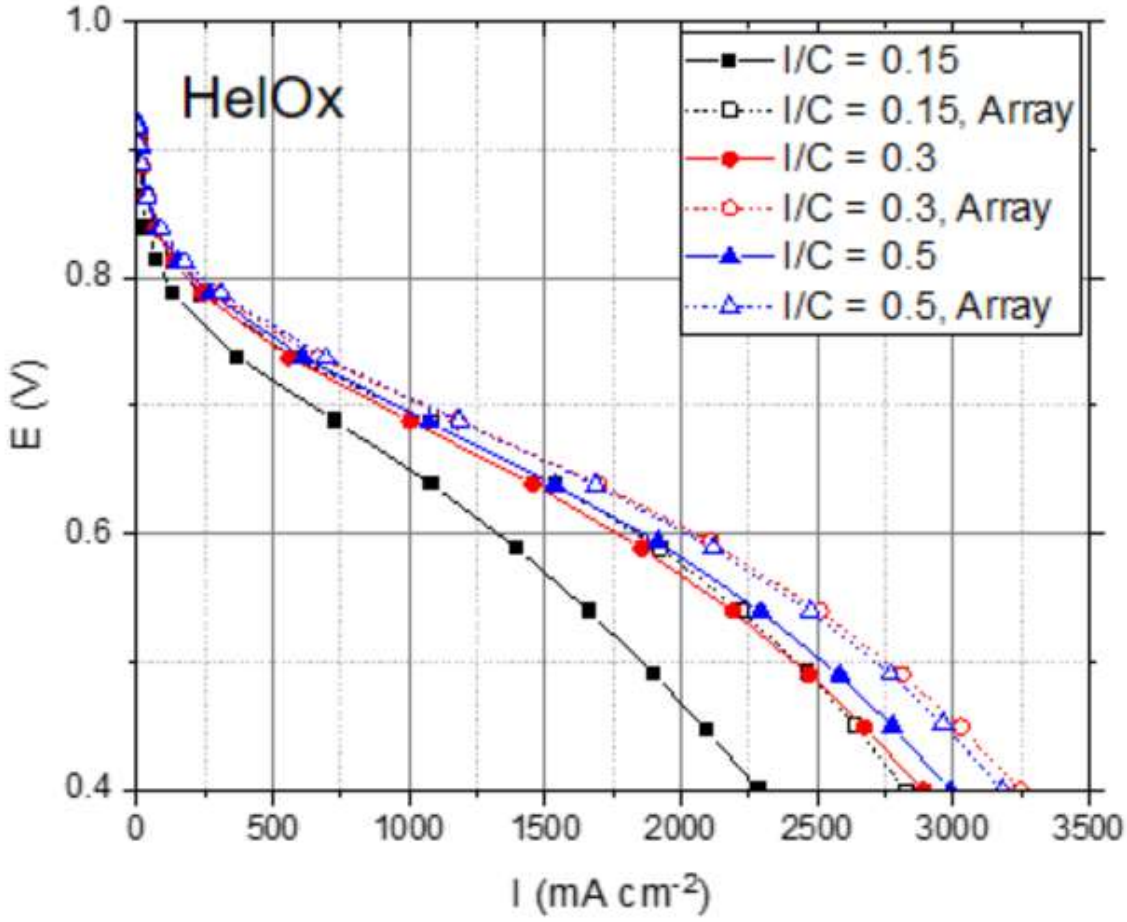

Figure 82. Polarization curves measured at 80 °C, 100% RH, and 150 kPa_{abs} in H_2/HelOx.

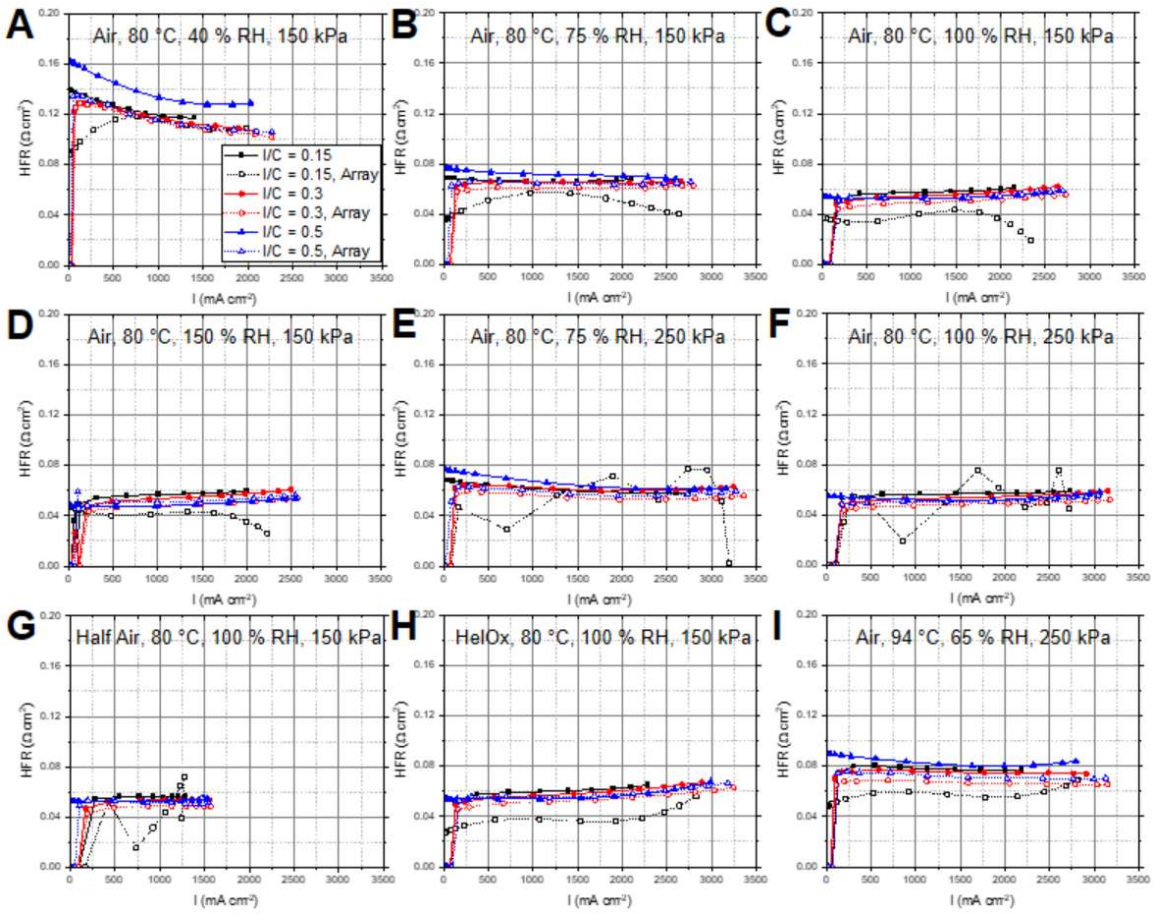

Figure 83. HFR of each MEA plotted at each experimental condition.

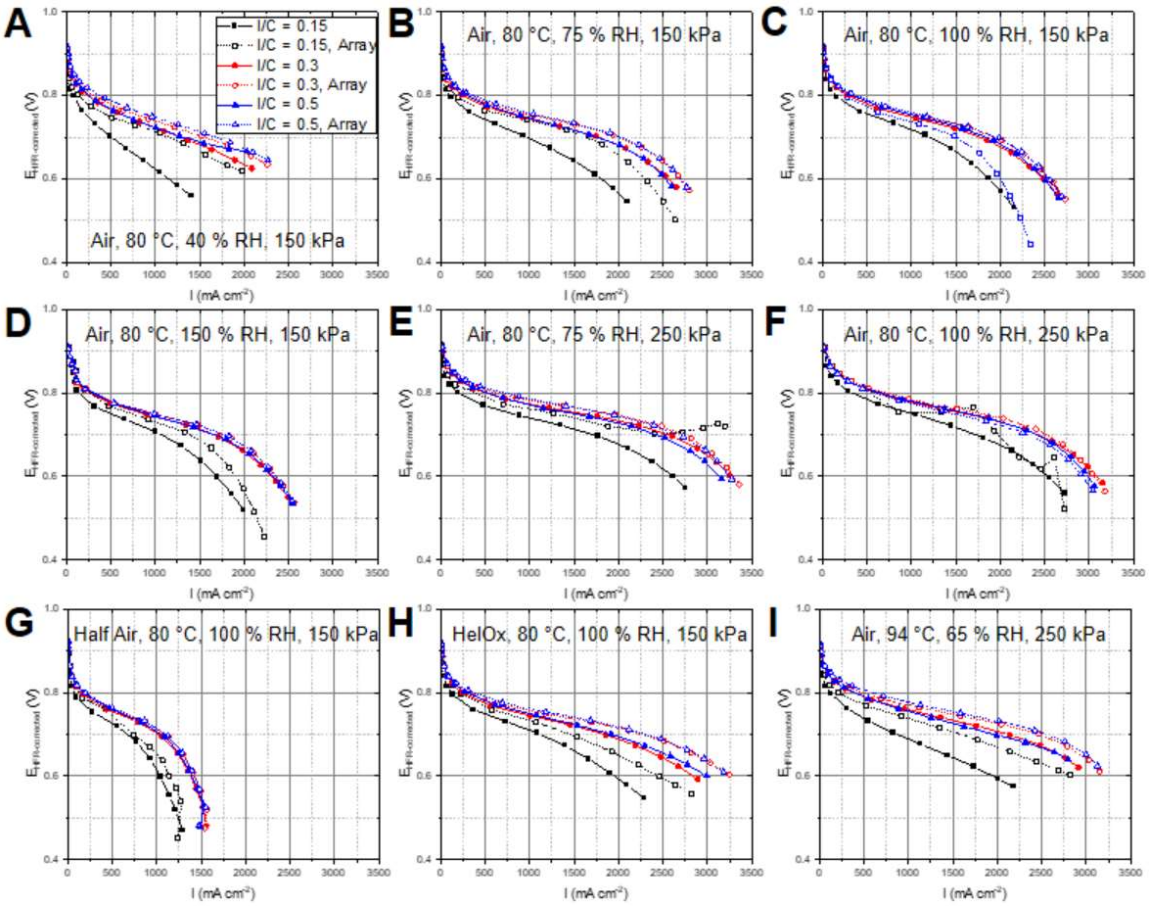

Figure 84. Polarization curves for each MEA at each experimental condition with cell voltage corrected for HFR.

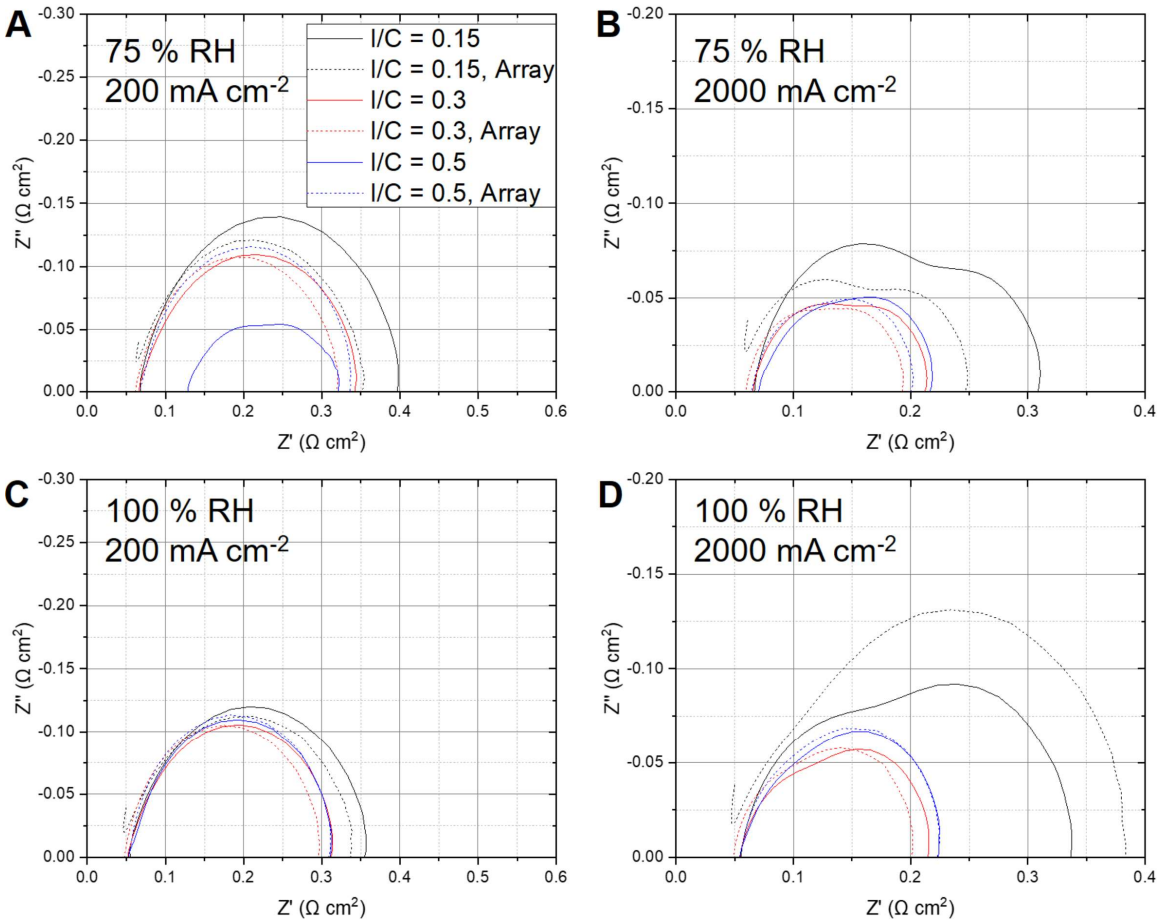

Figure 85. H_2/air EIS for each MEA at 150 kPa_{abs} and (A) 75 % RH and 200 mA cm^{-2}, (B) 75 % RH and 2000 mA cm^{-2}, (C) 100 % RH and 200 mA cm^{-2}, and (D) 100 % RH and 2000 mA cm^{-2}.

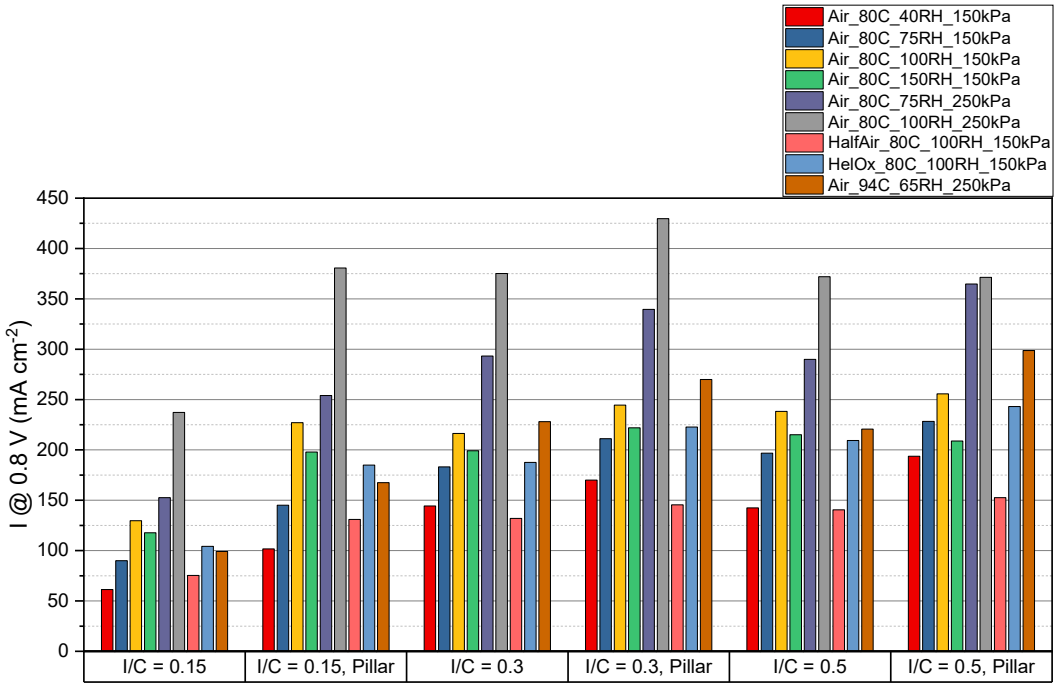

Figure 86. Comparison of current density at 0.8 V for each testing condition.

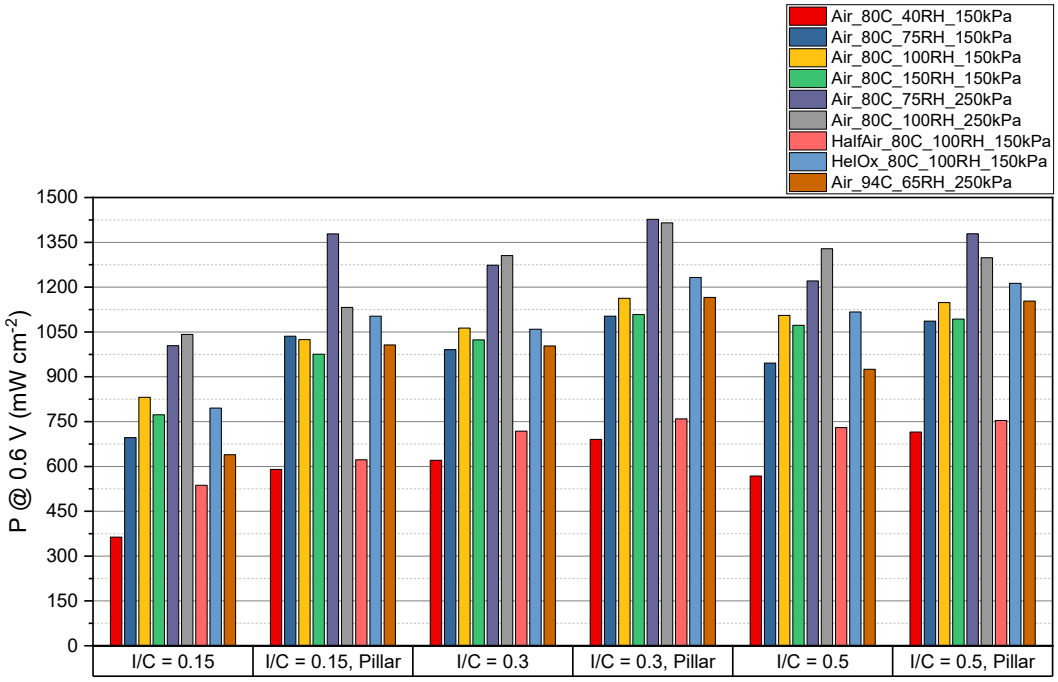

Figure 87. Comparison of power density at 0.6 V for each testing condition.

CURRICULUM VITA

NAME:	Alexander Jiya Gupta
ADDRESS:	2302 37th Street
	Apartment A
	Los Alamos, NM 87544
	United States
EMAIL:	ajgupta@lanl.gov
PHONE:	(270) 993-5755
DOB:	Columbia, Missouri – April 27, 1993
CITIZENSHIP:	U.S. Citizen

EDUCATION:	Ph.D., Chemical Engineering
	University of Louisville, Louisville, KY
	2017 – 2022
	B.S., Biochemistry
	University of Louisville, Louisville, KY
	2011 – 2016
PROFESSIONAL EXPERIENCE:	Graduate Research Assistant
	Los Alamos National Laboratory
	2020 – Now
	Laboratory Manager / Graduate Research Assistant

University of Louisville

2017 – 2020

Research Assistant

University of Louisville

2016 – 2017

TEACHING EXPERIENCE: Undergraduate Teaching Assistant

General Chemistry

University of Louisville

2014 – 2015

AWARDS: Student Grant

Metal Powder Industries Federation

2019

Third-Place Poster Prize

RE3 Workshop

2017

University Fellowship

University of Louisville

2017

Dean’s Scholar

University of Louisville

2016

Cum Laude

University of Louisville

2016

Trustees Scholarship

University of Louisville

2011

PROFESSIONAL SOCIETIES: Member

American Chemical Society

2014 – Now

CREDENTIALS: Green Belt

Institute of Industrial and Systems Engineers

2019 – Now

PUBLICATIONS: Gupta, A. et al. Ionomer channel array for enhanced percolation in PEMFC cathode catalyst layers (in process).

Gupta, A. et al. Heteropoly acid-doped Nafion membrane for prolonged PEFC operation at subzero temperature. (in process).

Gupta, A. et al. PEFC operation at subzero temperature: current understanding, challenges, and mitigating strategies. (in process).

Saraei, N. et al. Small molecule crystals with 1D water wires modulate electronic properties of surface water networks. *Appl. Mater. Today* **22**, 100895 (2021).

Ghahremani, A. H. et al. Rapid fabrication of perovskite solar cells through intense pulse light annealing of SnO2 and triple cation perovskite thin films. *Mater. Des.* **185**, (2020).

Gupta, A. J. et al. Effect of Stacking Interactions on the Translation of Structurally Related Bis(thiosemicarbazonato)nickel(II) HER Catalysts to Modified Electrode Surfaces. *Inorg. Chem.* **58**, 12025–12039 (2019).

Saraei, N. et al. Water wire clusters in isostructural Cu(II)and Ni(II)complexes: Synthesis, characterization, and thermal analyses. *Inorganica Chim. Acta* **492**, 268–274 (2019).

Gupta, A. et al. Intense pulsed light, a promising technique to develop molybdenum sulfide catalysts for hydrogen evolution. *Nanotechnology* **30**, (2019).

Zhang, C. et al. Highly Efficient and Durable Electrocatalyst Based on Nanowires of Cobalt Sulfide for Overall Water Splitting. *ChemNanoMat* **4**, 1240–1246 (2018).

PRESENTATIONS: Gupta, A., Analysis of Fuel Cell Catalyst Layers using Atomic Force Microscopy. *Center for Integrated Nanotechnology Annual Meeting*, poster, (2020).

Gupta, A., Hydrogen Energy: Production and Utilization for a Green Economy. *University of Louisville Chemical Engineering Department Seminar*, invited seminar, (2020).

Gupta, A., et al. Advanced Corrosion Studies of Laser-Powder Bed Processed 420 Stainless Steel. *KY Nanotechnology and Additive Manufacturing Symposium*, poster, (2019).

Gupta, A., et al. Advanced Corrosion Studies of Laser-Powder Bed Processed 420 Stainless Steel. *Additive Manufacturing with Powder Metallurgy Conference*, technical talk & poster, (2019).

Gupta, A., et al. Highly Defective MoS2 in Millisecond Time Scale using Intense Pulsed Light for Enhanced Hydrogen Evolution Catalysis. *Speed Research Exposition*, poster, (2018).

Gupta, A., et al. Catalysts for Hydrogen Evolution Reaction using Intense Pulsed Light. *Renewable Energy & Energy Efficiency (RE3) Workshop*, poster, (2017)